N° d'ordre: 2266

THESE
(LABEL EUROPEEN)

Présentée à

l'Université des Sciences et Technologies de Lille

pour obtenir le titre de

DOCTEUR DE L'UNIVERSITE
Spécialité: ELECTRONIQUE

par

Jorge CARBONELL OLIVARES

ELECTROMAGNETIC ANALYSIS OF ACTIVE AND PASSIVE DEVICES FOR SPACE APPLICATIONS

(ANALYSE ELECTROMAGNETIQUE DE COMPOSANTS ACTIFS ET PASSIFS POUR DES APPLICATIONS SPATIALES)

soutenue le 8 Juin 1998 devant la commission d'examen.

Membres du jury:
M. P. Kennis
M. D. Lippens
M. O. Vanbésien
M. M. Baquero
M. E. Kollberg
M. J.M. Lourtioz
M. G. Beaudin
M. M. Favreau

a mis padres,
a mis abuelos,
a María y Alberto,

a Eva.

ACKNOWLEDGMENTS / REMERCIEMENTS

Ce travail a été effectué au Laboratoire Central de l'Institut d'Electronique et de Microélectronique du Nord dirigé par Monsieur G. Salmer. Je le remercie de m'avoir accueilli dans ce laboratoire.

Je remercie Monsieur P. Kennis, Professeur à l'Université de Lille, qui me fait l'honneur de présider cette commission d'examen.

Je voudrais remercier spécialement Monsieur Didier Lippens en tant que Directeur de ce travail. Son intérêt pour ce projet, son amabilité et sa capacité de motivation ont fait de ces quelques années à Lille une période extrêmement enrichissante. Qu'il trouve ici ma plus profonde reconnaissance et gratitude.

Bien sûr, mes sincères remerciements pour Monsieur Olivier Vanbésien, Co-Directeur de ce travail, pour avoir été toujours disponible, pour avoir apporté tout son intérêt, sa patience et ses conseils au long de cette thèse. Merci, surtout, d'être devenu un ami.

Je suis particulièrement reconnaissant à Monsieur M. Baquero, de l'Université Polytechnique de Valencia, d'avoir suivi ce travail avec intérêt et d'en être le rapporteur. Mes plus vifs remerciements aussi pour Monsieur E. Kollberg, de l'Université de Chalmers à Göteborg, et Monsieur J.M. Lourtioz, de l'Institut d'Electronique Fondamentale de Paris, pour avoir accepté de juger ce travail et d'en être les rapporteurs.

Je remercie également Monsieur G. Beaudin, Ingénieur de Recherche à l'Observatoire de Paris, et Monsieur M. Favreau, Ingénieur à Matra Marconi Space à Toulouse, qui me font l'honneur de participer à ce jury.

Je voudrais remercier chaleureusement Mesdames Sylvie Lepilliet et Elisabeth Delos ainsi que Monsieur Patrick Mounaix, pour avoir apporté leur savoir et leur temps, chaque fois que cela a été nécessaire.

Ma reconnaissance aussi envers Messieurs Xavier Mélique et Reynald Havart, pour avoir fourni de leur travail des éléments importants inclus dans ce travail. Aussi à Mademoiselle Marta Fernández et Monsieur Samuel Boret pour leur aide.

Je ne peux pas oublier Messieurs Rafael Rincón, Javier Mateos et Xavier Oriols pour avoir rendu cette période beaucoup plus agréable en et en dehors du laboratoire.

Mon plus gentil merci à Mademoiselle Valérie Duez, avec laquelle j'ai eu le plaisir de partager beaucoup d'heures en salle de calcul ou dans le bureau. Merci, pour m'avoir fait sourire quand j'en avais vraiment besoin.

Mes remerciements à Messieurs Ludovic Burgnies, Eric Lheurette, Jérome Danglot, Olivier Dupuis pour leur sympathie et leur soutien, de la même manière aux différentes personnes que j'ai eu le plaisir de connaitre dans le laboratoire.

Je voudrais aussi remercier Monsieur Michel Sénéchal qui a su se montrer toujours disponible pour résoudre d'innombrables problèmes informatiques.

Je tiens à remercier Monsieur J.P. Dehorter qui a assuré la qualité de la reproduction de ce manuscrit.

Je ne veux pas oublier non plus à Mesdemoiselles Andrea Moreira et Lucia Fernández pour avoir su me supporter les soirs des mois de rédaction.

Surtout, merci à ceux qui n'étant pas physiquement avec moi à Lille m'ont donné leur soutien au long de ces années. Je pense particulièrement à ma famille et à mes amis.

INDEX

GENERAL INTRODUCTION

GENERAL INTRODUCTION:

During the last decades, the subject of climate change, and particularly the possibility of changes which may occur faster than the ability of ecosystems to adapt, have been the subject of public debate and scientific investigation. It is widely accepted that monitoring and studying our environment on the scale of the planet requires precise and global geophysical measurements from space. A complex system like the Earth's atmosphere and oceans, interacting on a wide range of temporal and spatial scales, is realistically impossible to fully monitor or measure within practical constraints. However, great efforts are undertaken to describe specific phenomena like the ozone depletion or the greenhouse effects. Currently, for these and other applications like radioastronomy, with the study of planets, comets and galactic structures, vehicular sensing, collision avoidance systems or even high performance communication systems, the use of millimeter and submillimeter wave technologies becomes more and more significant.

From the system side, heterodyne receiver technology was widely used in the millimeter and submillimeter frequency bands. Conventionally, Gunn diodes are currently employed as solid state sources, whereas Schottky barrier and Schottky varactor are used for providing mixing and multiplying functions, respectively, at room temperature. However, recent advances in technology, Computer Aided Design and characterization techniques have strongly modified this context. Concerning the technology, two new issues have now emerged.

First of all, the possibility to use semiconductor heterostructures, rather than the conventional Metal-Semiconductor homojunction, offer a large flexibility in the device design. In particular, the Heterostructure Barrier Varactor (HBV) has demonstrated promise for high efficiency frequency multipliers because of its symmetric capacitance-voltage characteristic or the possibility of stacking different devices on the same epitaxy. The HBV only generates odd harmonics of the pump signal and hence there is no need for idler circuits. Also, power capabilities may be improved in a twofold manner, by epitaxialy stacking different devices on the same wafer or by planar integration with monolithic procedures.

Second, the search towards improved performance leads to an effort in the electromagnetic side, with the possibility of describing the rather complex interaction of the active device with the embedding circuit in a system. This system will usually include different passive devices, and in the case of a frequency multiplier the analysis refers to waveguiding structures combined with planar technologies. Moreover, transmission lines, filtering or switching structures and antennas may be key elements in any high frequency electromagnetic analysis.

At last, and in parallel to the evolution of the technological or characterization facilities, computer aided design (CAD) techniques have received much interest in the last decade. Full wave analysis techniques offer an invaluable way to design prototypes for critical applications, and the effort of applying these techniques to high frequency systems is now widely recognized.

Within this scope, this research has focused on the electromagnetic analysis of active and passive devices for space applications.

The first chapter will briefly review different aspects of millimeter wave technologies. Active devices employed in non-linear electronic functions like mixing or harmonic multiplying are outlined. Also, this introductory chapter analyzes different passive technologies for planar transmission lines with the aim of reducing losses and dispersion at

high frequencies. Finally, open or quasi-optical systems are introduced with special emphasis on radiating elements combined with active devices.

The second chapter analyzes the HBV devices fabricated at IEMN for a frequency tripler application from 83 to 250 GHz. Our own contribution concerns the electromagnetic behavior of a multiplier block including an active device, integrated in a flip chip technology in a crossed waveguide mount. Full wave analysis is applied to study this complex structure including the embedding of the active devices. This analysis tries to get an insight into the influence of the integration techniques, notably the parasitics generated by the airbridge, as well as into the multiplier cell itself. Part of this work was performed in the framework of a European Space Agency contract #9777 for Millimeter Wave Critical Sounder Technologies.

The third chapter deals with the electromagnetic characteristics of micromachined technologies developed at the IEMN. In particular, we have analyzed transmission lines on dielectric membranes in terms of their electromagnetic behavior. The application of this technology to filter structures is also developed for frequencies in the millimeter wave spectrum. MicroElectroMechanical Systems (MEMS) fabricated by micromachining techniques are also investigated, with the aim of designing high frequency switches with different topologies.

Finally, the fourth chapter deals with emerging technologies applied to the millimeter wave frequencies, with the study of photonic band gap materials. The focus of this study is mainly on the understanding of the influence of finite dimensions structures, altogether with some applications of these structures as microresonators and reflectors for dipole antennas.

CHAPTER I:

APPLICATION PROSPECTS AT MILLIMETER AND SUBMILLIMETER WAVE FREQUENCIES

CHAPTER 1: APPLICATION PROSPECTS AT MILLIMETER AND SUBMILLIMETER WAVE FREQUENCIES.

In this first chapter, we will try to generalize critical technologies for millimeter and submillimeter systems. These frequency bands, rich in opportunities both for remote sensing applications and for emergent industrial and commercial activities, are aimed to play an important role in present and future research projects. At the moment, spacecraft applications are mainly based on the use of heterodyne receivers. The front ends of this type of systems integrate different devices and subsystems ranging from the antenna to the intermediate frequency signal processing and going through the whole receiving set. We will overview different parts of it, including active devices for mixing and frequency multiplying, integrated propagation structures, radiating elements and, briefly, array configurations and open systems.

1.1 Millimeter and Submillimeter receivers.

1.1.1 Monitoring the environment.

Different remote sensing instruments are currently being designed and tested to operate at high frequencies for environment control and radioastronomy applications. Among them, let us mention from the European Space Agency (ESA), projects like FIRST (Far Infrared and Submillimeter Telescope) with critical subsystems from 500 GHz to 1.2 THz and at 1.7 THz, Envisat (Environment Satellite) with payload modules in the lower millimeter and infrared spectra, or MASTER-SOPRANO (Submillimeter Observation PRocesses in the Atmosphere Noteworthy for Ozone) with two instruments at 200, 325 and 350 GHz, for the first, and 210, 440 and 640 GHz for the second.

The goals of these scientific missions are numerous and cover a large part of the electromagnetic spectrum ranging from the microwave frequencies to the ultraviolet, in which the Earth's atmosphere is rich in information about its molecular components. We can see in Figure 1.1 the absorption spectrum through the atmosphere with particular emphasis to the absorption lines of some molecules. Also are indicated the solar emission, and the payload modules of Envisat, both in frequency and wavelength scales.

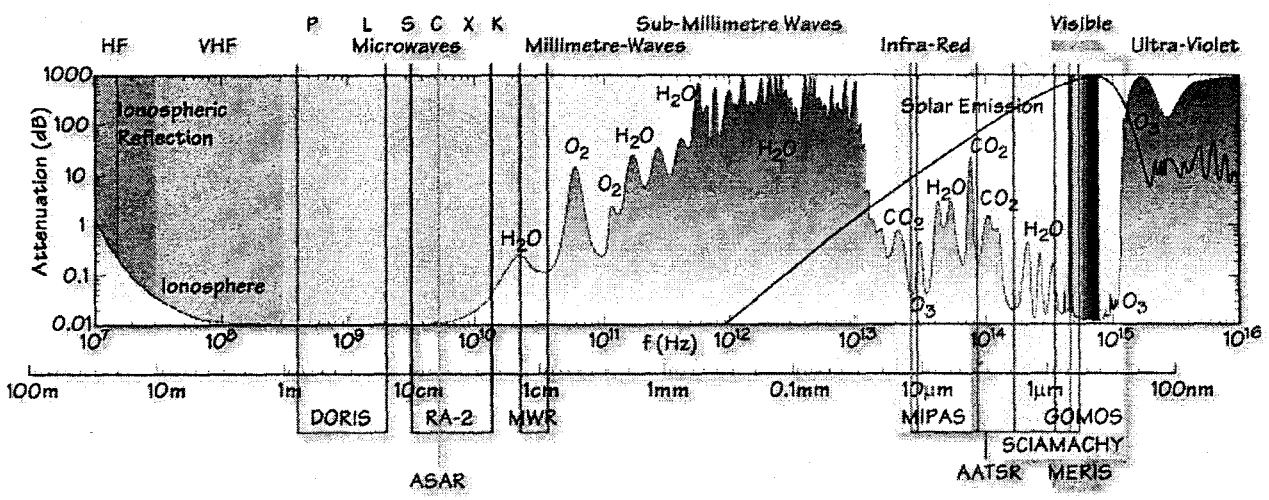

Figure 1.1: Absorption spectrum of the Earth's atmosphere, including the payload instruments of Envisat.

To explore the millimeter and submillimeter electromagnetic spectrum, two main kinds of receivers have been proposed, direct (or incoherent) detection techniques and heterodyne (or coherent) detection. This part of the spectrum lies between what traditionally can be regarded as the radio and infrared domains and the possibility of making two different approaches stems from this fact. Direct detection can be used as a downwards extension of the infrared approach, and on the other hand, heterodyne detection is a traditional means of detection at microwave frequencies. Both have specific limitations, but the main difference between them is based on the preservation or not of the phase information, as well as achievable sensitivity. In the following, we are going to briefly report on their basic schemes.

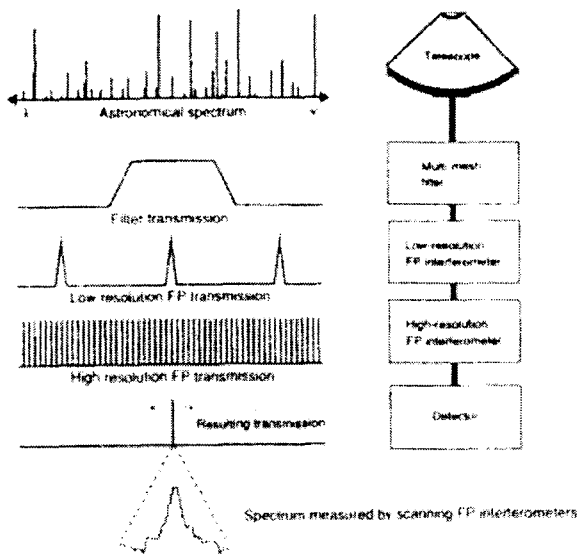

Figure 1.2: Principle of a direct detection system.

Figure 1.2 depicts the basic procedure to realize a direct detection system. We can see the receiver elements as well as the resulting signal spectrum after each step. Spectroscopy must be done by separating individual frequency components in the incoming signal before detection. The spectral bandwidth is reduced by a succession of filters and interferometers. Fourier transform instruments apart, incoherent systems measure one frequency channel per detector, requiring a scanning from the predetection filter to obtain a large spectrum. On the other hand, direct detection systems, because of the lack of phase sensitivity can detect much lower signal levels than coherent detectors, [Beaudin96].

With respect to heterodyne receivers, two parts are typically defined, a front-end, consisting of a heterodyne mixer which converts a high frequency band from a center frequency to a lower one without degrading the spectral information within the band, and a separate detector back-end, which gives the spectrum of the lower frequency band. We will see in further detail a basic configuration of this type of receiver in section 1.2.

The choice between a direct or heterodyne receiver will depend on the targeted application, and the decision has to be carefully analyzed in terms of operating frequency, technological achievability, capability and required sensitivity. A table is given in Figure 1.3 showing the best adapted technology for detection systems in a double scale taking into account operating frequencies and required resolution.

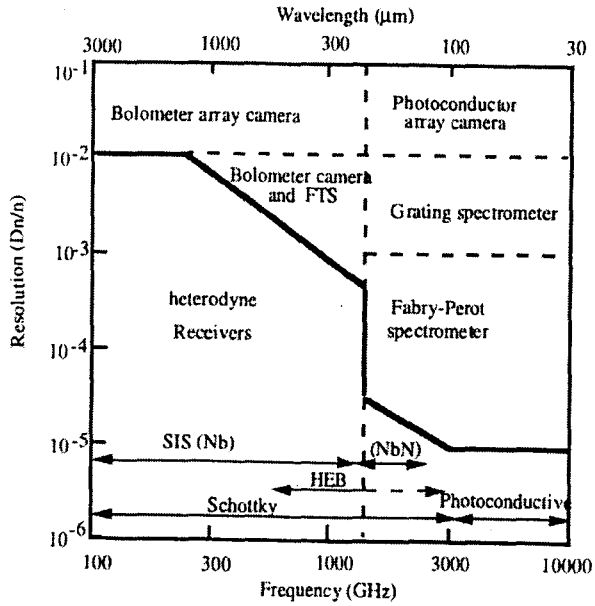

Figure 1.3: Devices and system technologies employed at millimeter and submillimeter frequencies.

1.1.2 Basic configuration of a heterodyne receiver.

For applications requiring both high sensitivity and high spectral resolution, the heterodyne approach is often preferred. A synoptic description of such kind of receiver is shown in Figure 1.4.

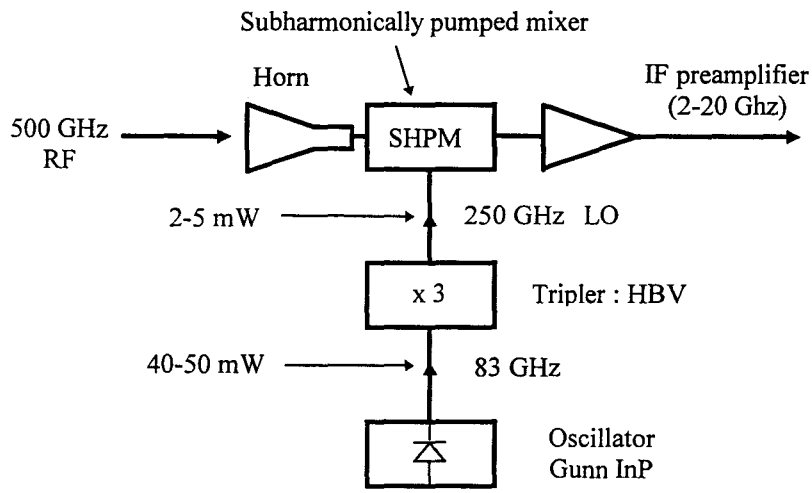

Figure 1.4: Schematic description of a heterodyne receiver.

The heterodyne receiver is based on the use of a strongly non-linear device which performs the mixing function. The first element in the front end is a low loss coupling structure, generally a waveguide feed horn or a planar antenna, which couples the incident radiation at a frequency f_s. Also, a local oscillator source at frequency f_{ol}, direct or multiplied from a fundamental source, is used to pump the mixer where a signal is generated by beating both incoming frequencies [Maas93]. Because of the non-linearity of the mixer device (any non-linearity will do it in principle) different harmonic products are generated and then filtered to obtain the required output frequency. Depending on the type of non-linearity of the device, several output frequencies can be selected. We

will comment briefly, on the different alternatives usually employed in millimeter wave heterodyne receivers. Table 1.1 summarizes the conventional possibilities for the mixer and the local oscillator elements, which in terms of electromagnetic analysis are directly comparable, in crossed waveguide mounts as well as in quasi-optical configurations. The purpose of this thesis being electromagnetic analysis of different receiver technologies, we will focus more precisely on a multiplier application in the second chapter.

type of mixer	*output frequency*
basic mixer	$f_i = f_s - f_{ol}$
subharmonically pumped mixer	$f_i = 2f_{ol} - f_s$
local oscillator	*generated frequency*
direct generation	$f_{ol} = f_{fundamental}$
frequency multipliers (n: order of the multiplier)	$f_{ol} = f_{fundamental} \times n$

Table 1.1: Conventional alternatives for mixer and local oscillator elements.

For a basic mixer, the output intermediate frequency, $f_i = f_s - f_{ol}$, is the one transmitted to the next stage, and other terms like DC, fundamental frequencies and the rest of harmonics are filtered before reaching the detector. For this purpose, the local oscillator frequency has to be very close to that of the observed signal, due to the limited bandwidth at intermediate frequency. The two parameters used to characterize the performance of the mixer are the noise temperature T_n and the conversion loss L_o. The latter gives the difference between the input and output power levels, whereas noise temperature is important to evaluate the minimum detectable power. Mixers cooled at cryogenic temperatures have very low noise temperatures, and hence can be used in astronomy applications where sensitivity is a key figure of merit.

However, for very high frequency applications, it can be difficult to obtain a fundamental frequency local oscillator, because of minimum power requirements or excessive noise. In these cases, it may be wise to use a mixer that is pumped at half the LO frequency, and to mix the incoming signal with the second harmonic of the oscillator. These subharmonically pumped mixers can have remarkably good conversion performance, often only few decibels worse than comparable fundamental mixers. Even with greater conversion loss, a subharmonically pumped mixer often provides the best performance when all these other factors, especially LO noise and power are considered.

It is possible to achieve a subharmonic operation with a single diode-mixer, nevertheless, there are usually interfering signals from other harmonics which can be troublesome in many critical applications. A better method is to employ a pair of anti-parallel diodes like in the configuration shown in Figure 1.5.

If the diodes are identical, this circuit has no fundamental mixing response. The RF and LO voltages are applied to the diode pair, and filters are used to separate the different frequencies. Since the RF and LO frequencies differ by approximately a factor of two, the filters are rarely difficult to realize.

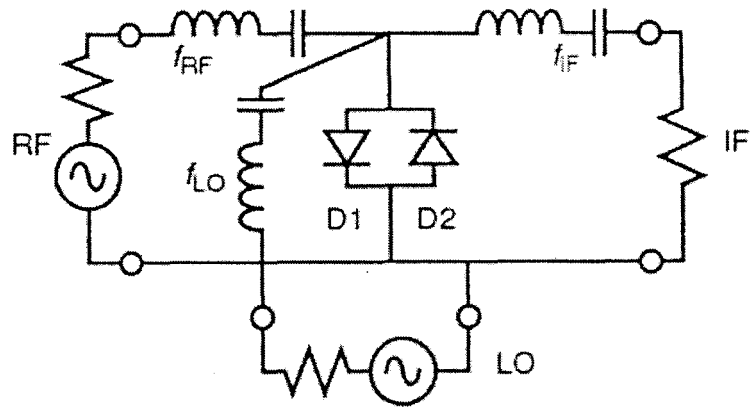

Figure 1.5: Schematic of a subharmonically pumped mixer.

The key issue when going up to millimeter and submillimeter frequencies, is the availability of reliable local oscillator sources to generate enough power levels at those frequencies. This can be achieved either by direct generation or by frequency multiplying of a lower fundamental source.

In the first case, different approaches can be considered, but for our purposes only solid state devices will be reviewed. Actually, traveling wave tubes and related devices are omitted because they are bulky, expensive or inappropriate for space borne and commercial applications, even if available powers are very important.

Different solid state devices can be integrated with a micromachined transmission line system, and can operate at room temperature. Devices and systems operating up to 40 GHz and above are commercially available, with laboratory examples of integrated circuits operating up to 170 GHz [Eisele95]. These systems are in general advanced developments of conventional electronics where reduced dimensions or sophisticated layer structures are used for operation beyond 100 GHz. Most of these devices may be broadly classified as "transit time devices" [Chamberlain97] and include such familiar examples as Bipolar Junction Transistor (BJTs), Heterojunction Bipolar Transistors (HBTs), Field Effect Transistors (FETs) High Electron Mobility Transistors (HEMTs) and Transferred Electron (Gunn) devices. In all of these, the time taken for carriers (usually electrons) to move a characteristic distance determines the maximum frequency of operation. The pertinent distance is the base width for BJTs, the gate length for FETs and the length of the active region for Gunn devices. A particular case is the Resonant Tunneling Diode, considered as the fastest electronic device and for which a frequency as high as 712 GHz has been demonstrated using a AlSb/InAs/AlSb double barrier structure [Brown91].

At much higher frequencies, typically around several Terahertz, where no fundamental sources are available, we again have well-developed solid-state sources such as infra-red lasers and Light Emitting Diodes (LEDs). The interband lead-salt semiconductor lasers [Horikoshi85] represent the long-wavelength limit of such devices. These devices may be classified as "transition devices", since the charge carriers undergo a transition from a higher to a lower energy state with the direct emission of radiation at a frequency f given by E = hf, where E is the energy state gap.

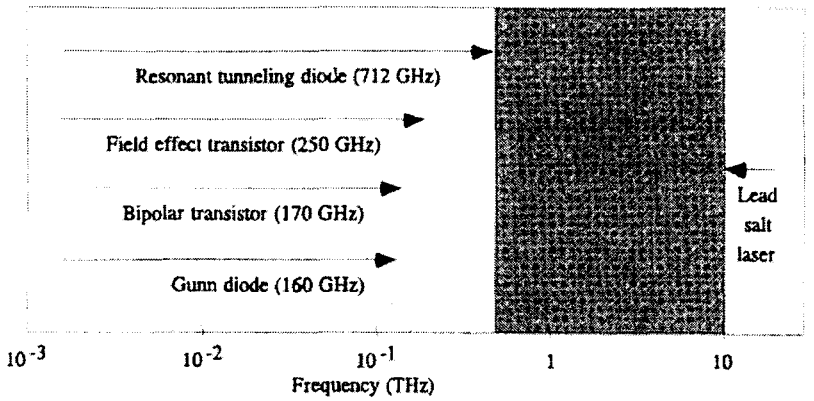

Figure 1.6: Frequency capability of conventional fundamental solid state sources.

In between the frequency bands covered by "electronic" and "optical" solid-state devices, there exists a range of frequencies that can be reached with harmonic multiplication of an "electronic" source or by down-converting an "optical" signal. As we stated before, we are going to point out some of the basic characteristics of frequency multipliers, and in particular those taking benefit of a diode as the non-linear element [Faber95]. Other devices used in frequency multipliers are FETs or HEMTs and the possibility of low conversion loss (or even conversion gain) is their potential advantage. This has already been demonstrated at microwave frequencies, and great efforts are currently under progress to reach output frequencies higher than 100 GHz.

Generally, diode frequency multipliers can be classified into two categories: varistors or varactors. In the first case, frequency multiplication is performed by a non-linear resistance or conductance with a consequent poor conversion efficiency but a very large potential bandwidth. The limit conversion efficiency can be estimated to be $1/n^2$, where n is the order of the output harmonic [Page56]. In the second case, a nonlinear reactive element (usually a non-linear capacitance) is used. Varactor frequency multipliers have high potential conversion efficiency (the theoretical low-frequency limit is 100%, i.e. no conversion loss at all) [Manley56], but they exhibit a narrow fixed-tuned bandwidth and higher sensitivity to operating conditions. Varactor frequency multipliers will require input and output tuning, or impedance matching, in order to cancel reactive power components with the consequent limitation in bandwidth. We will discuss on this issue and on other practical limitations in the next chapter.

1.2 Integration of active devices for heterodyne mixing and frequency multiplication.

When we move from the system side to the active device level, the key point is the integration of this device in a system that usually includes different passive elements. Nowadays, planar devices offer the opportunity of taking advantage of their ruggedness, reliability and technological maturity with respect to whisker contacted diodes, known to be fragile in adverse environments. If the first realizations date from the beginning of the decade [Bishop87, Garfield91], more and more planar integrated devices are used both in critical space-borne applications and in emerging commercial activities.

In the past, whisker contacts were the only means of introducing a diode in a waveguide system, see Figure 1.7. Nowadays, planar diodes are extensively used in crossed waveguide mounts in flip chip technology. A viewgraph of such a mount is shown in Figure 1.8, with an inset of a diode contacted by the airbridge technique.

Normally, the device chip is inserted in the output waveguide and the output frequency is coupled to it by the whole complex structure, metallic pads, high permittivity substrate and

eventually any strip or soldering procedure to hold the device within the waveguide. This leads to a complex electromagnetic problem which needs to be treated by full-wave EM analysis, as we will see in detail in Chapter 2.

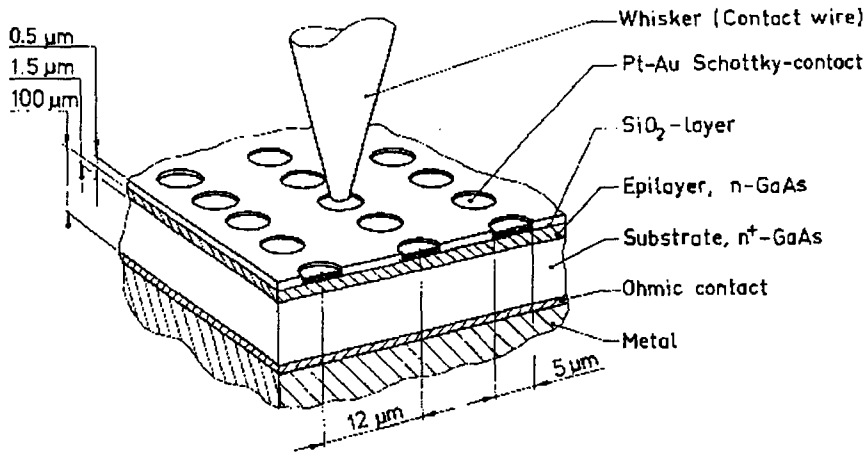

Figure 1.7: Whisker contacted diode.

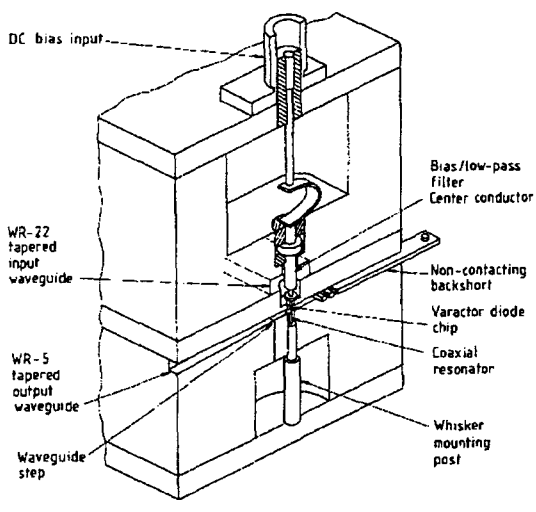

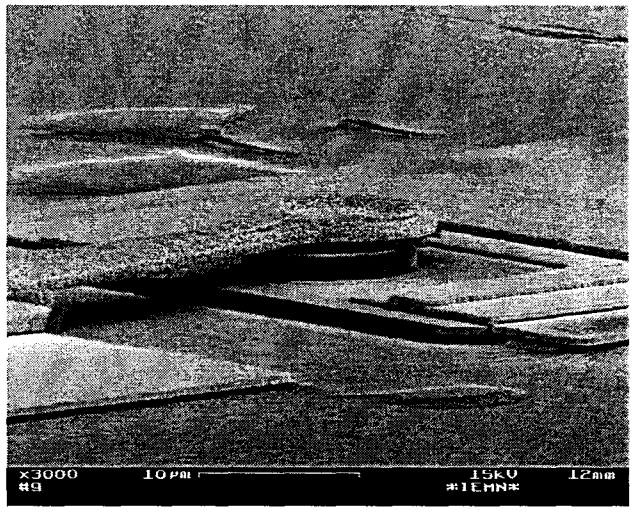

Figure 1.8: Crossed waveguide mount for frequency multiplication and planar diode integrated by an airbridge.

The University of Virginia (UVA) was the first to integrate planar devices in this kind of waveguide mounts [Bradley92]. In principle Schottky diodes where fabricated and tested [Rausch93], but more recently, Heterostructure Barrier Varactors (HBVs) have been a subject of interest [Jones96]. This technique is known as the surface channel technique. Nevertheless, in the IEMN, we have been working with a double mesa technique to integrate HBVs. Both procedures are schematically represented in Figure 1.9. Major differences come from the technological steps with the masks, the order of the procedures and finally, the planarity or not of the airbridge.

The surface channel technique creates a deep etch to reduce the parasitic capacitance between the two contact pads, whereas the IEMN procedure permits one to metallize both pads

directly on the semi-insulating GaAs substrate, with the associated benefit of reduced access resistance and low loss associated circuits.

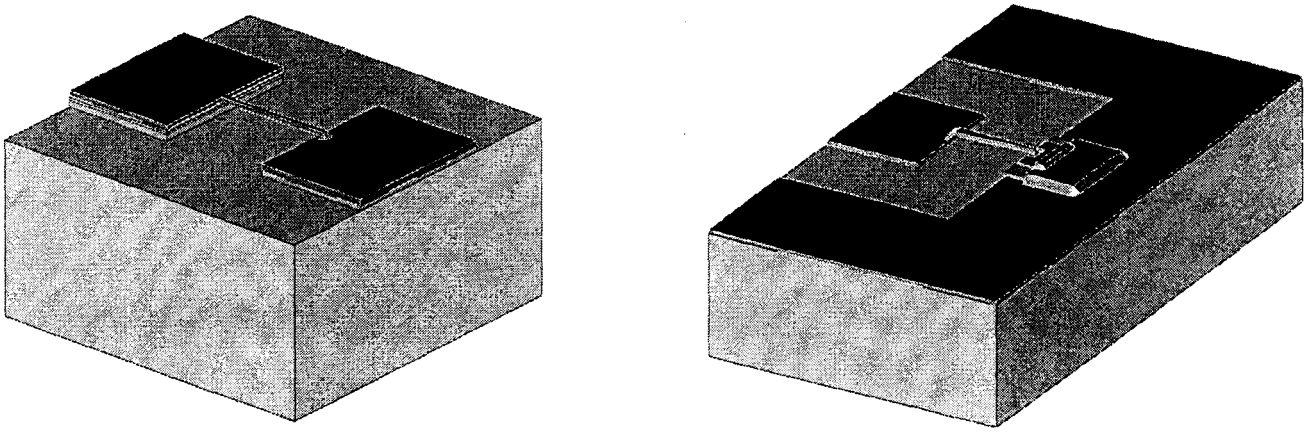

a. b.

Figure 1.9: Surface channel (UVA), a., and Double mesa (IEMN), b., airbridge techniques.

1.2.1 Mixer devices.

Although in theory, any non-linear or rectifying device can be used as a mixer, only a few devices satisfy the practical requirements of mixer operation. Any device used as a mixer must have a strong non-linearity, uniform electrical properties and an adequate frequency response. MESFET and HEMT mixers apart, two non-linear diodes are currently employed in millimeter and submillimeter receivers, the Schottky diode and the SIS (Superconductor - Insulator - Superconductor) diode.

1.2.1.1 Schottky diode.

The non-linear device most often used for mixing is the Schottky barrier diode, a device consisting of a rectifying metal to semiconductor junction. The successful development of good-quality Schottky barriers on GaAs semiconductors has been responsible for dramatic improvement in millimeter and submillimeter mixers throughout the last decade. GaAs is decidedly superior to Silicon for high-frequency mixers because of its higher electron mobility and saturation velocity. A good summary of the operation principle of Schottky mixer diodes is given in [Maas93]. State of the art results have demonstrated operation frequencies for planar diodes up to 250 GHz [Gearhart94] or 205 GHz [Siegel92], in waveguide systems and in open structure, respectively. Recently, planar diodes have been tested up to 1 THz [Hesler95], but whisker contacted diodes have been used for measurements up to the record of 30 THz [Hübers92].

1.2.1.2 SIS junction.

When detected power levels are extremely low, SIS mixers are presently the most sensitive alternative for low noise receivers in the frequency range from about 75 GHz to about 1 THz. They are also known as the "quasi-particle" mixers, because the conduction current in these junctions relies on a tunnel effect through the potential barrier created by the insulator. This effect creates a strong resistive non-linearity that characterizes the operation of this device [Kollberg97].

Moreover, the decrease of the operation temperature tends to limit strongly the noise in the device, which is the most important parameter to evaluate its sensitivity. State of the art results have reported noise temperatures of 200 K for 795 GHz operation frequency [Kooi96] and 1000 K at 1 THz [Gao96]. In both cases, SIS junctions are fabricated with Niobium technology. At the present time, only low temperature (< 10 K) superconductors have been used, so cryogenic cooling at liquid helium temperature (4 K) is required to operate these devices. This considerably limits the application of SIS devices for long duration space applications such as investigation of the atmosphere.

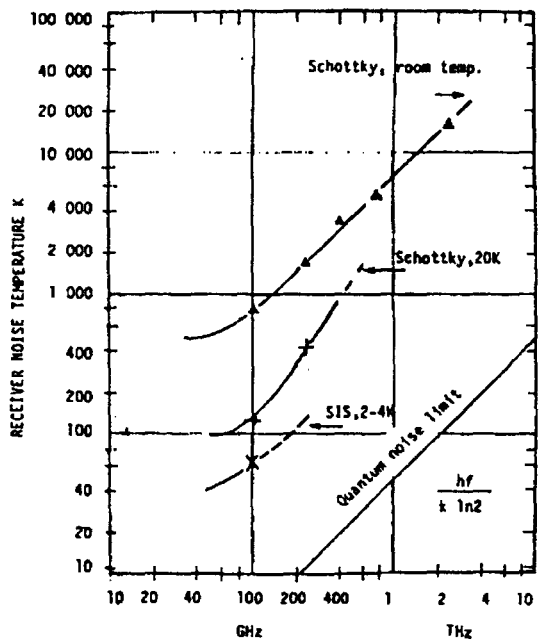

Figure 1.10: Resolution for different receiver systems.

1.2.2 Semiconductor diodes for frequency multipliers.

Up to now, the standard device for frequency multiplication has been the Schottky barrier diode but novel devices have been developed during the last decade offering promising performance, even becoming a real alternative. If Schottky multipliers have been a reliable means of generating power above 100 GHz, with still further developments under progress, some limitations like parasitics series impedance, velocity saturation in the semiconductor or the need for idlers in high order multipliers have lead to research efforts on other devices. Among them we can mention those based on semiconductor heterostructures which offer several degrees of freedom in their design. In particular we will present some of the characteristics of the HBV operation, but we will have deeper insight into this device in Chapter 2.

1.2.2.1 Schottky diode.

Schottky Barrier Varactors (SBVs) are the most widely employed diodes for frequency multiplication. High quality junctions, sometimes with diameters below 1 μm, have been successfully developed making frequency multipliers feasible even at frequencies greater than 1 THz.

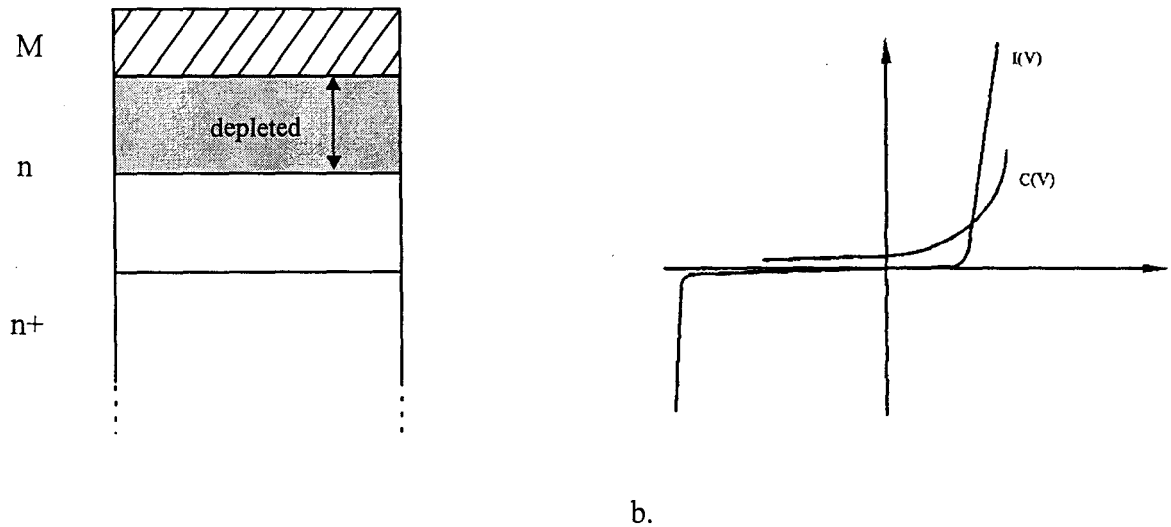

a. b.

Figure 1.11: Schottky Barrier diode, a.) epitaxial structure, b.) C_V and I_V characteristics.

In practice, Schottky diodes consist of a junction between a metal (M) and a lightly doped thin epitaxial layer (n) grown on a heavily doped buffer layer (n+). This M-n-n+ structure allows the epitaxial layer to be used for the junction and the heavily doped region to minimize series resistive losses. The non-linear junction shown in Figure 1.11 is the rectifying metal-semiconductor contact with the surface of the metal defining the upper edge of the diode junction. Under reverse bias, the SBV exhibits a progressive depletion in the vicinity of the M-n junction, which tends to lower the capacitance of the junction. In Figure 1.11 typical I_V, which determines the amplitude of the pump signal, and C_V characteristics, for varactor operation, for a SBV are shown.

If theoretically an ideal efficiency of 1 can be expected [Manley56], in practice, different parameters, like the series resistance, current saturation phenomena or other extrinsic elements, limit its values to several tens of percent at the lower millimeter band or several percent at submillimeter wave frequencies. A reasonable efficiency of 30 % can be expected up to 100 GHz, but 3.3 % has been reported at 800 GHz [Crowe96].

1.2.2.2 Heterostructure Barrier Varactor (HBV).

In contrast to Schottky varactors, where the limiting factor for conduction was the metal-semiconductor potential barrier, in the case of HBVs, the operation principle is based on a heterostructure blocking barrier, obtained by creating a potential discontinuity in the conduction band, as shown in Figure 1.12.

The HBV, first proposed by E. Kollberg and A. Rydberg [Kollberg89], has received considerable attention as a promising device for high efficiency frequency multiplication at millimeter and submillimeter wavelengths because of its attractive device characteristics and flexible design parameters. A single barrier HBV consists of a large band gap semiconductor sandwiched between symmetric moderately doped modulation regions of smaller band gap material such that the device has an evenly symmetric nonlinear capacitance-voltage characteristic (C_V) relationship about zero bias. This evenly symmetric device C_V characteristic eliminates the even harmonic components from the output current waveform. High efficiency frequency multiplier circuits, which do not require DC bias and which require fewer idlers than the standard Schottky-barrier varactor multipliers, can then be realized. These device characteristics make the HBV an

ideal device for use in high rank frequency multipliers, broad-band frequency multipliers and quasi-optical tripler arrays. The HBV is ideally suited for use as the multiplier element in a quasi-optical tripler array since no idlers are required for frequency tripling and dc bias is not required for the individual elements in the array.

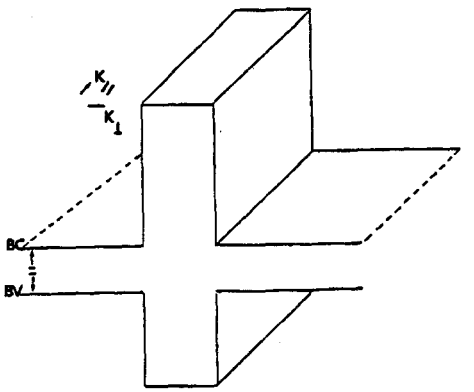

Figure 1.12: Band structure for a basic HBV diode.

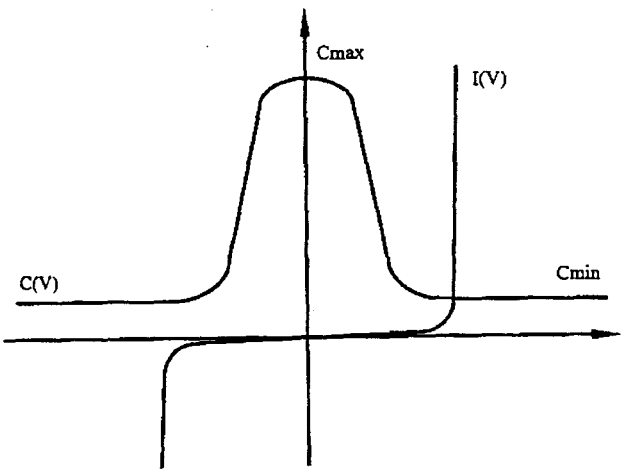

Figure 1.13: C_V and I_V characteristics of an HBV device.

By epitaxially stacking several single-barrier HBVs in series, [Lheurette96, Krishnamurthy96], further advantages are obtained including increased device impedances for a given device area, higher device cutoff frequencies due to reduced device capacitances, higher power handling capabilities due to the sharing of the pump power over several series devices, and increased heat dissipation capabilities for a given capacitance modulation range due to increased device areas. Also, HBVs have degree of design flexibility since semiconductor alloy compositions and doping profiles, barrier thicknesses, device geometries and areas can be easily varied. Ultimately, the design flexibility and the attractive device characteristics of the HBV suggest that a high efficiency frequency multiplier with excellent device/circuit impedance matching and near-optimum C_V relationship can be achieved with a single device.

We will have a deep insight into the HBV structures employed in this research and into its application to a tripler circuit to 250 GHz in the next chapter. Nevertheless let us mention that

remarkable performances have been obtained for tripler circuits with up to 2 mW (2.5 % efficiency) at 252 GHz [Jones97].

1.3 Integrated propagation structures and transmission lines.

The need to integrate the active devices into a circuit, makes the analysis and design of millimeter and submillimeter wave transmission lines an important issue. Although the majority of integrated circuits have been fabricated using microstrip lines, alternative transmission media which would present potential advantages over the microstrip or supplement it, have been and still are under investigation. Because of the high operation frequencies, effects that can be considered secondary for lower frequency bands, here become critical. Among them are losses, circuit discontinuities, generation of leaky waves, multimoding or radiation. Besides the microstrip line, other planar transmission lines have been classically considered such as the inverted stripline or the coplanar waveguide. More recently, micromachined transmission lines fabricated on thin dielectric membranes have demonstrated outstanding performance at higher frequencies with respect to conventional planar lines.

Unfortunately, since the dielectric material does not surround completely the conducting strips and no pure TEM mode exists, there are no simple closed-form expressions that can be derived for the field distribution or the characteristics of planar transmission lines. In that sense, micromachined transmission lines are closest to the ideal conditions if the dielectric membrane is sufficiently thin compared to the wavelength.

1.3.1 Planar transmission lines.

Three alternatives of planar transmission lines are presented in Figure 1.14, showing the schematic cross section of these lines and the E-field patterns of the dominant mode in each case.

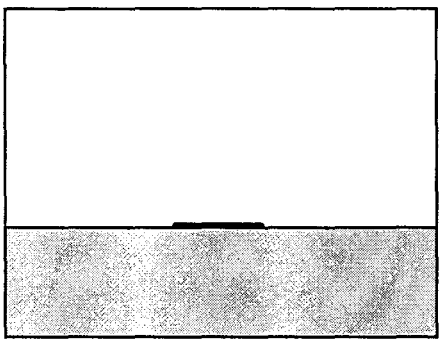

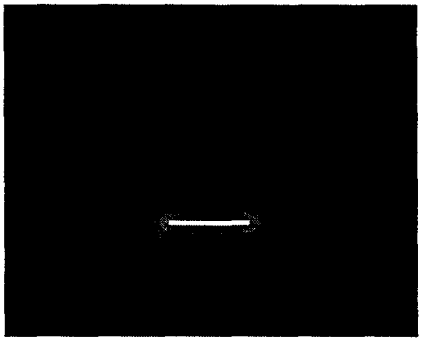

a. microstrip line.

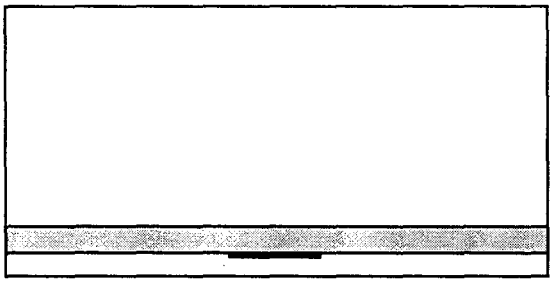

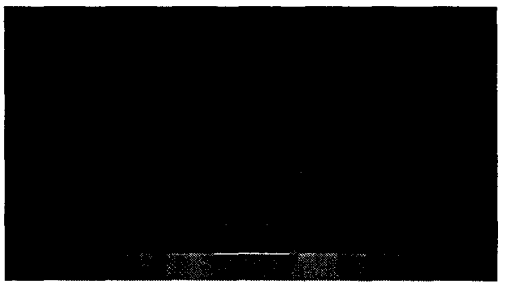

b. inverted stripline.

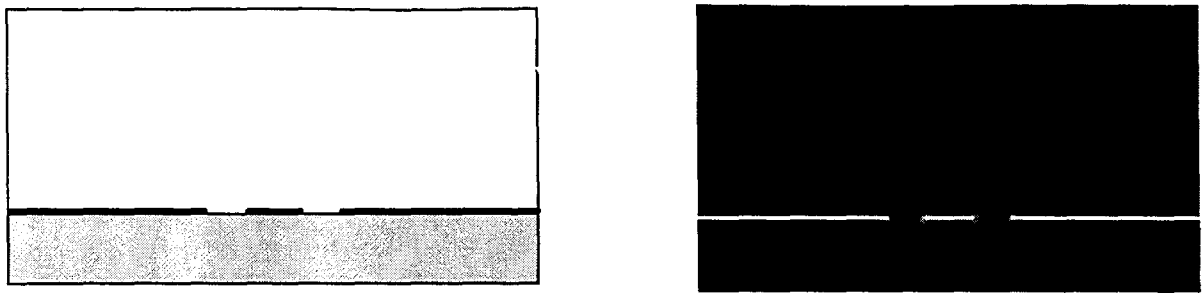

c. coplanar waveguide.

Figure 1.14: Planar transmission lines with dominant mode E-field patterns.

1.3.1.1 Microstrip line.

The microstrip line is by far the most extensively characterized transmission medium for planar circuits, from microwaves to millimeter waves. All the necessary formulas for the characteristic impedance, effective dielectric constant, attenuation per unit length and typical discontinuities can be found in [Gupta79], with quasi-static models as well as full-wave analysis techniques. Microstrip lines are often the preferred option for monolithic integration, however, if it is relatively easy to introduce series elements, it is necessary to use via holes in the substrate for shunt connections.

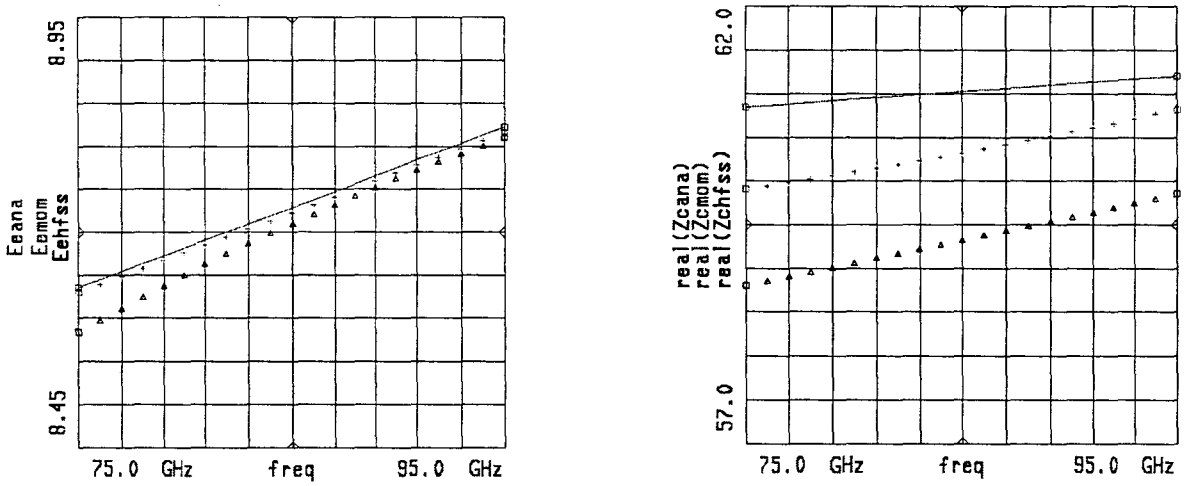

Figure 1.15: Effective dielectric constant and characteristic impedance variations for a microstrip transmission line at millimeter wave frequencies.

In the millimeter and submillimeter spectrum, dispersion occurs and this affects ε_{eff} and Z_o. To illustrate this effect, a comparison between full-wave simulation tools and well known analytical models is done in Figure 1.14, in terms of effective dielectric constant and characteristic impedance. The geometry of the microstrip is also given in this Figure. The planar waveguide model, [Kompa75], combined with a calculation of the effective dielectric permittivity [Kobayshi88], is in good agreement with the method of moments (MoM) and the finite element method (FEM), employed in Momentum and HFSS respectively, both from Hewlett-Packard, [Momentum95, HFSS95]. Later in this thesis, we will make some comments on these commercial simulators (see also Appendix A).

For practical purposes, when operation frequencies are increased, the main problems are unacceptable losses and the excitation of hybrid modes. In particular, surface waves can propagate in high permittivity substrates in the upper millimeter wave band. For the line described in Figure 1.15 analytical models as well as full wave analysis predict a cut-off frequency for the first high order mode around 250 GHz. On the other hand, simple formulas giving the attenuation of microstrip lines at high frequencies do not exist. This attenuation is caused by three mechanisms: conductor losses, dielectric losses and radiation losses. The former is the dominant component, but it depends to a large extent on conductor surface roughness, which can vary from substrate to substrate. It also depends upon the behavior of current crowded near the edge of etched conductor, and skin effects cannot be neglected. At the same time, increasing frequency raises the importance of dielectric losses, because the fields tend to be more concentrated in the dielectric substrate [Collin92], and also of radiation losses coming from line discontinuities. Anyway, radiation is usually a much lower losses factor than conductor or dielectric losses.

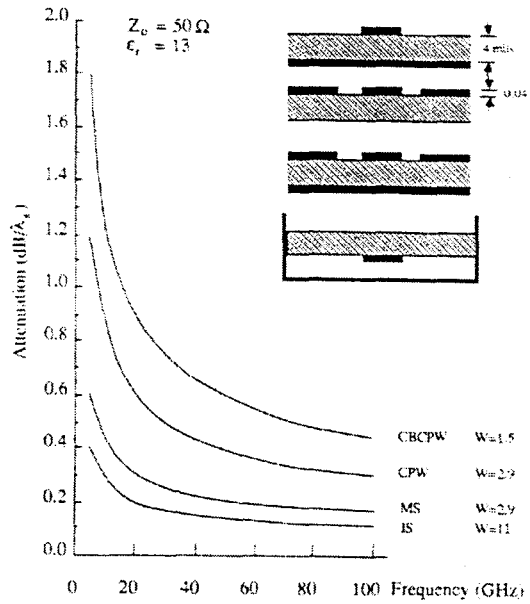

Figure 1.16: Comparison of losses for different planar transmission line technologies, [Itoh89].

Figure 1.16 shows a comparison of losses (conductor and dielectric) for different planar transmission line technologies [Itoh89]. For a given impedance value (Z_0 = 50 Ω), the width of the active line is varied keeping constant the substrate permittivity and thickness (ε_r = 13 for GaAs and h = 100 μm), and the metallization thickness (t = 1 μm). The inverted stripline has the lowest losses (note also that we have a strip width of w = 270 μm for Z_0 = 50 Ω), and for this configuration losses in the microstrip line are found to be lower than those of the coplanar waveguide, but generally the latter can have less losses than the microstrip at higher impedances.

1.3.1.2 Inverted stripline.

Figure 1.14b shows the cross section of the inverted stripline, usually this configuration is placed inside a waveguide, and in this case it can also be considered as a suspended stripline. This structure provides a way to reduce the attenuation in a microstrip at higher frequencies and yet retain some of the features of the microstrip line such as the quasi-TEM nature of the dominant mode propagation. From the analysis point of view, this configuration and the microstrip can be

treated in a unified manner as strip transmission lines containing multiple layers of dielectric materials.

This configuration can have a number of useful features. First the attenuation due to the dielectric material is reduced, because the substrate is used for supporting the strip and the larger part of the electromagnetic field is located in the air, as it is shown in Figure 1.14b . The losses characteristics are compared in Figure 1.15. This also makes the modal dispersion weak and the effective dielectric constant relatively small. The low dispersion nature is useful for broad-band applications and the low effective dielectric constant relaxes the mechanical tolerance of the structure since the physical size is larger. Second, it is possible to use both sides of the substrate. Coupled lines on both sides can be suited for filter applications and an antenna patch can be coupled to a feeding line through the substrate. On the other hand, there is a lower limit to the realizable characteristic impedance in the case of a shielded inverted stripline. This is because the size of the shielding enclosure, which limits the maximum size of the strip, is designed in such a way that the higher order waveguide-type modes are cut off. Also, shunt elements, like in the microstrip, are difficult to integrate in the line and there is not much information on discontinuities in the literature.

1.3.1.3 Coplanar waveguide.

The coplanar waveguide (CPW) was invented by Wen, [Wen69], as a planar transmission line which is made of a center strip on the surface of a substrate with two ground planes adjacent and parallel to the strip (see Figure 1.14c). Even if the coplanar waveguide has been used much less frequently than the microstrip line, with the advent of monolithic millimeter-wave integrated circuits, there has been a renewed interest in it [Jackson86]. All three conductors in the CPW are on the same side of the substrate, and this eliminates the need for via holes and thus simplifies the fabrication process. Since the dominant mode is quasi-TEM, there is no low frequency cut off and in the ideal form, when semi-infinite ground planes and a semi-infinitely thick substrate are analyzed, this mode is a balanced mode. Practical realizations of CPW deviate from the ideal structure in a number of ways. First, in most cases, the substrate cannot be considered infinitely thick. Second, the ground conductors have finite widths and third, the finite substrate may have a conducting back plate. A rigorous study of these practical configurations is done in [Riaziat90]. At millimeter wave frequencies and on high permittivity substrates, the radiation of unwanted parasitic modes can be a problem. For open structures, these parasitic modes are free-space waves and surface modes, whereas for conductor backed structures, the most likely mode to be excited is a parallel plate transmission line mode [Jackson89]. At the same time, since there are gaps on both sides of the center strip in the coplanar waveguide, this configuration may be considered as two coupled slot lines. The coupled slot line mode may be excited in the CPW as an unbalanced mode if the symmetry of the structure is broken. To prevent excitation of the coupled slot line mode, air bridges between the two ground planes are often used so that the RF potentials of the two ground planes are kept equal. Losses has also been analyzed by means of quasi-static models [Gopinath82, Gupta79] or with full-wave methods [Jackson89], including radiation from discontinuities. The major contribution is also found to be conductor losses.

1.3.2 Micromachined transmission lines.

We have seen, in the previous section, that planar transmission lines present severe drawbacks at millimeter and submillimeter wave frequencies. They essentially stems from the fact that substrate thickness becomes comparable to the guided wavelength, generating higher order mode propagation as well as increased losses in the substrate. To solve this problem, while keeping the advantages of ease of integration of planar transmission lines, membrane supported structures have emerged as a novel and promising technology.

Micromachined or membrane transmission lines were first analyzed by the University of Michigan [Dib91], at the beginning of the decade. This technology was based on silicon micromachining. Later, membrane structures on GaAs substrates were demonstrated at the IEMN [Salzenstein96]. Figure 1.17 shows the schematics of both technologies for CPW supported on membrane.

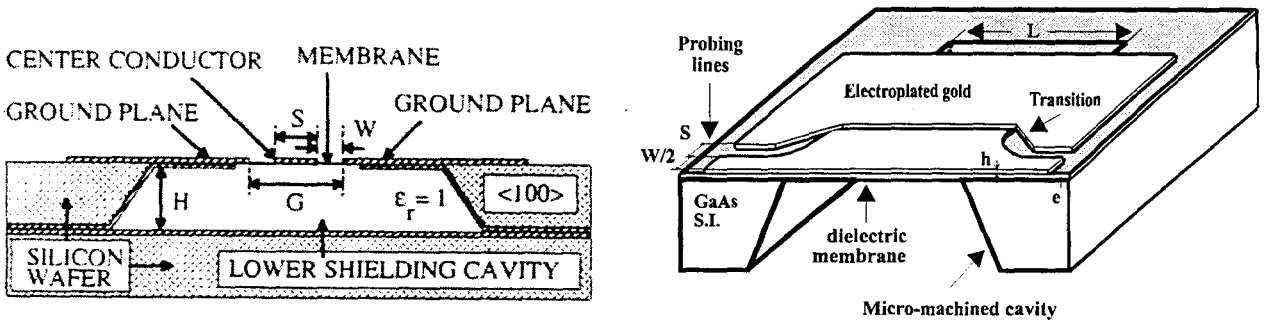

Figure 1.17: Schematics of a CPW micromachined on Silicon technology (a) and on GaAs technology (b).

The potential advantages of these lines stem from the fact that metallic strips are suspended in an almost homogeneous medium. In terms of propagation this means that we have an almost pure TEM wave, with no dispersion up to very high frequencies. The membranes employed have to be very thin (in the order of 1 μm), and thus only a small fraction of the electromagnetic energy is confined within the membrane. On these basis, we can obtain a very low effective dielectric constant, comparable to that of free space propagation (ε_{eff} = 1.08), and as a consequence a very high phase velocity (v_φ= 2.9 10^8 m.s^{-1}) [Salzenstein96]. Losses can be reduced practically to the conductor contribution and if a shielding of the structure is done [Katehi93], radiation losses can also be eliminated.

Two main kinds of dielectric membranes exist in thin film technology, silicon nitride (Si_3N_4) and polyimide membranes. The fabrication process is basically divided into a front-side processing, for the dielectric and metal strip depositions, and a back-side processing, for the bulk micromachining of a cavity under the membrane. We will describe more in detail the fabrication steps in Chapter 3.

The potential applications of membrane technology are the fabrication of non dispersive transmission lines far inside the submillimeter wave spectrum as well as other passive components, like filters or resonators. Membranes can also support planar antennas allowing high operation frequencies with improved radiation efficiencies because of the lack of thick substrate (no surface waves are radiated into the substrate). Finally, mechanical properties of a membrane structure can also be exploited, in particular, for switching purposes as we will see in Chapter 3.

1.4 Integrated radiating elements and open systems.

When operation frequencies are in the upper range of the submillimeter wave spectrum, power levels become extremely low. The natural trend has then been to combine output power from individual devices and thus to create array systems. In the same way we saw for frequency multipliers, if traditionally the Schottky diode has been and still is the reference device [Hacker92], novel structures, like again the HBV, are replacing the former because of their simpler (no bias or idlers are required) operating conditions [Shalaan97a].

1.4.1 Antennas for millimeter and submillimeter wave operation.

Planar antennas are the most widely used and realistic solution to couple an incident radiation to a millimeter or submillimeter wave receiver. Monolithic receivers integrate a planar antenna to a mixer diode by means of a matching network. They are an attractive solution for the millimeter-wave frequency range (< 300 GHz) and currently the only practical solution for the submillimeter-wave region (300 GHz - 3 THz). Different types of technologies are usually employed in practice. The most common solution is the use of antennas on thick dielectric substrates (dipoles, slots, bow-ties, etc.). More recently, antennas on thin dielectric membranes or in the presence of photonic band gap materials appear to be a new subject of interest. An extensive review of the two former types can be found in [Rebeiz92]. For the latter, different research groups are currently working on it [Yang97, Sigalas96].

1.4.1.1 Antennas on thick dielectric substrates.

A great variety of active antenna configurations, including an active device and an antenna, have been developed which are suitable for active power combining arrays. Some commonly used designs are illustrated in Figure 1.18.

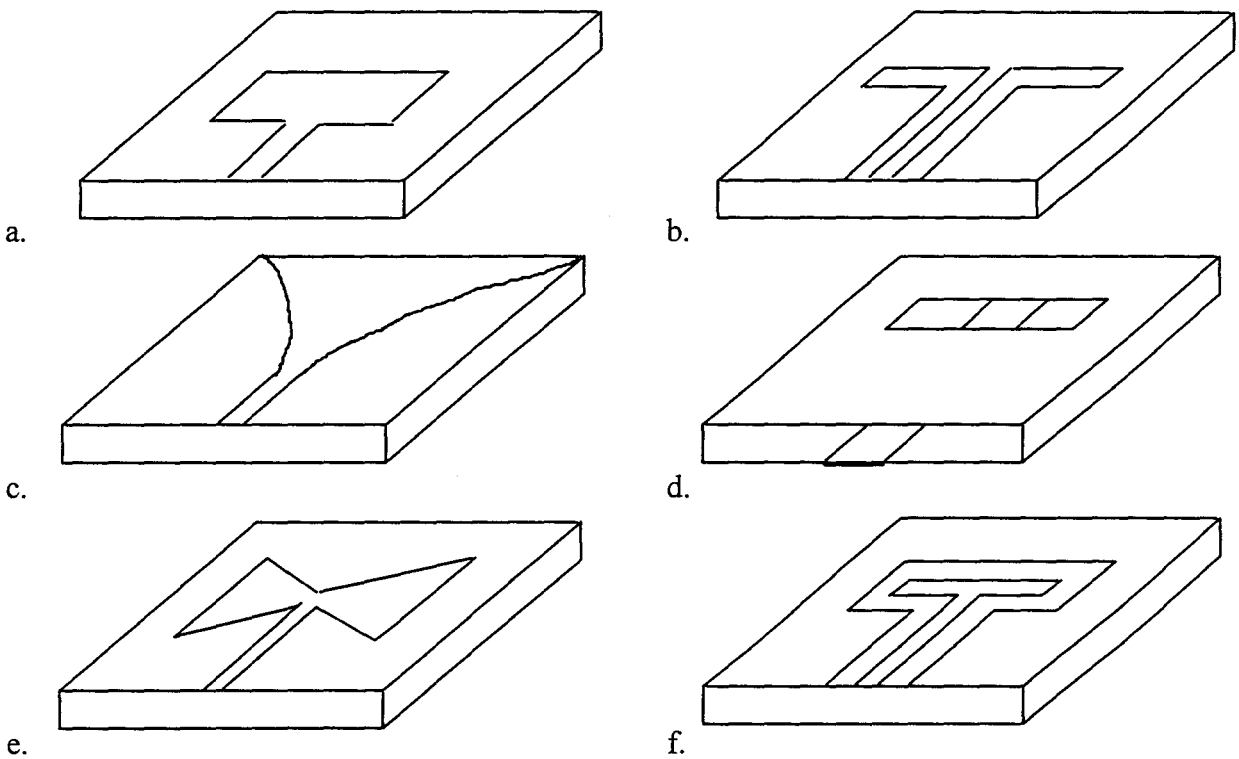

Figure 1.18: Planar antennas on thick dielectric substrates, a.) patch antenna, b.) CPW-fed slot antenna, c.) tapered slot antenna, d.) microstrip fed slot, e) bow-tie antenna, f.) CPW-fed folded slot.

Planar antennas have suffered from two limitations, first, poor radiation patterns and low coupling efficiencies as a consequence of the excitation of surface-waves on the dielectric substrate, and second, narrow bandwidths because of their limited size and resonant nature. Typical gain for these antennas is around 6 dB [Balanis82]. Some approaches to conceive broadband planar antennas are the bow tie antenna, spiral and log periodic antennas. These structures have geometries that can be specified by angles instead of resonant lengths.

To optimize performance in the presence of substrate modes, a careful choice of the substrate has to be done in terms of dielectric permittivity and thickness. If not optimized, the fraction of power radiated by a planar dipole (or slot) in the substrate can be up to a factor of ε_r ($\varepsilon_r^{3/2}$), ε_r being the permittivity of the substrate, larger than the power into the free space. Hence dipoles on GaAs ($\varepsilon_r = 13$) radiate only 2% of their power into free space, and for power radiated into the substrate, a large fraction is in the form of trapped waves propagating at angles larger than the critical angle [Alexopoulos83].

The substrate mode problem can be eliminated if the dielectric thickness is made infinite, i.e., the antenna is placed on a semi-infinite substrate. However, infinite dielectric substrates cannot be obtained in practice, but the best way to synthesize them is to use a lens of the same dielectric constant attached to the antenna substrate, hence the name "substrate lens". This approach eliminates substrate mode losses, but it requires a matching layer to reduce reflection losses at the air-dielectric interface [Rebeiz92]. This technique has been extensively used because of its simple construction and robustness. An antenna on a substrate lens is shown in Figure 1.19.

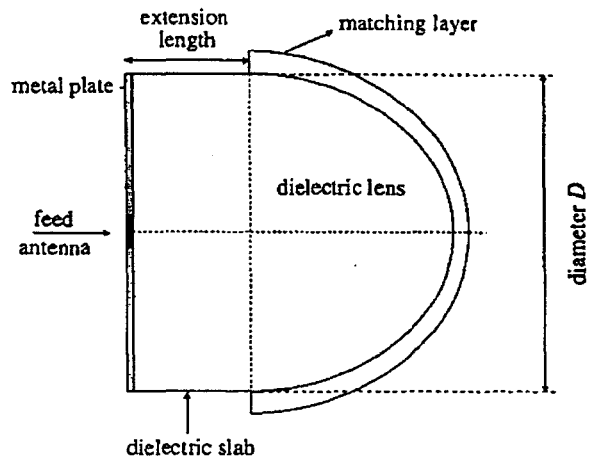

Figure 1.19: Lens configuration to reduce substrate moding problems.

1.4.1.2 Novel antenna configurations.

Basically, novel antenna configurations include antennas on thin dielectric membranes and antennas combined with photonic band gap materials (PBGs). Actually, both solutions tend to preclude the generation of substrate modes by means of suspending metallic patches on the membrane for the former, or by preventing the propagation of any radiated wave in the substrate for the latter. Membrane technologies will be analyzed in the third chapter, whereas PBGs and their combination with dipole antennas will be studied in the fourth chapter.

The membrane approach is the opposite solution with respect to substrate lenses. Here the substrate is removed to metallize the antenna on the dielectric membrane. It is so thin compared to free-space wavelength, that the antenna effectively radiates in free space. Dielectric losses are eliminated and the geometry can almost be scaled according to free-space conditions. The antenna can be coupled to the active device which is integrated in the surrounding Si or GaAs substrate [deLange96, Rahman96].

Figure 1.20 shows a micromachined horn antenna which consists of a dipole antenna suspended on a membrane inside a pyramidal cavity etched in silicon, several wafers are machined and then stacked to form a horn. Usually, the horn walls are metallized to reduce losses. Gain of this kind of antennas is close to 13 dB, with a relative bandwidth of up to 20%, depending on the feeder position, at 94 GHz [Ahmad91]. Planar millimeter-wave patches on SiN_x membranes have also been reported for automotive systems at 77 GHz [Stotz96]. In this case, an array of microstrip patches is used, showing good and predictable radiation characteristics.

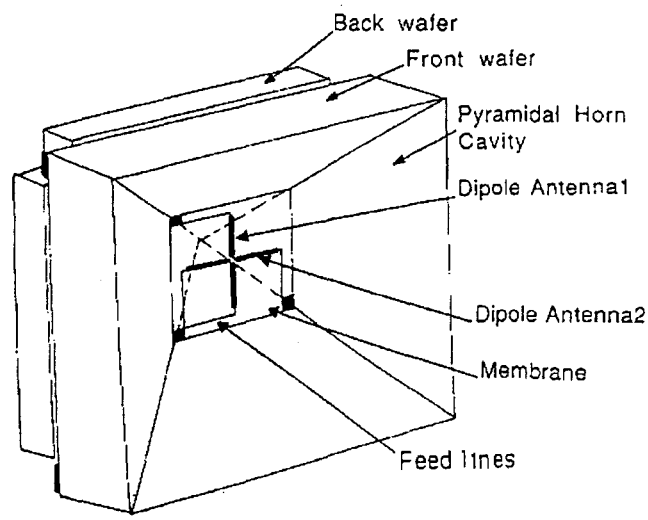

Figure 1.20: Micromachined horn antenna [Ahmad91].

On the other hand we also have antennas combined with PBGs. A PBG material or photonic crystal is an artificial material made of periodic implants within a surrounding medium [Yablonovitch93]. Electromagnetic wave propagation through such a medium is affected by the scattering and diffraction properties of periodic elements. Planar periodic printed conducting strips or patches on materials have already had important applications in frequency selective surfaces (FSS). Since electromagnetic waves can be highly directional in PBG materials, it is conceivable that antennas combined PBG materials will have many unique characteristics [Brown93, Cheng95].

Owing to the fact that these artificial materials have forbidden band gaps where no power should be transmitted into the crystal, all power should be radiated to free space (if no evanescent modes are present). A study of dipole antennas combined with metallic PBGs acting as reflectors is developed in chapter four with special attention to the position of the dipole with regard to the PBG. The main feature is the lobe engineering of the resulting system.

1.4.2 Quasi optical arrays for power combining.

To satisfy typical power requirements, the power from numerous individual devices must be added coherently. Many circuit-based power combining techniques have been proposed, but they usually face difficulties at millimeter-wave frequencies where a large number of devices must be combined and transmission losses are more important. Quasi-optical power combining methods address these limitations, in the sense that they can accommodate a large number of devices conveniently, [York 97].

High losses associated with circuit combining schemes can be avoided using antenna arrays for power combining. In principle, the power combining efficiency of a quasi-optical combiner can be extremely high, since the energy is combined in a low-loss dielectric medium (air). Since the

combining losses are reduced, the technique is well suited for combining a large number of devices or circuits, as required for millimeter-wave systems. Some problems typically encountered with this approach are imperfect radiation efficiency of planar antenna structures, and energy loss associated with the difficulty in collecting all of the generated output power. In this case, lenses or reflective optics can be used to focus the input signal onto the array, and also focus the output energy to improve collection efficiency. The natural configuration for such a system is therefore a Gaussian-beam waveguide, with the array placed in the beam waist where the phase front is planar. An important challenge is then electromagnetic design of the array receiving and transmitting surfaces and associated active circuitry to couple efficiently to the dominant mode. Actually, even if a very large amount of high performance devices is combined, the key issue is to efficiently couple the incident beam by any matching technique.

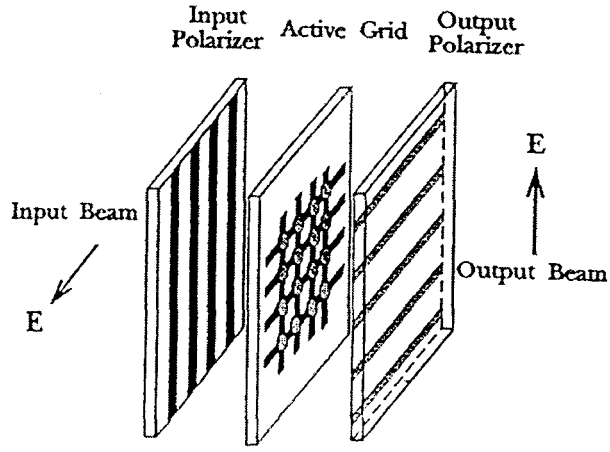

Figure 1.21: Quasi-optical combining scheme.

Figure 1.21 illustrates a quasi-optical combining scheme. The active array is sandwiched between two grid polarizers. This concept can be applied to amplifiers, mixers and multipliers with minor variations.

A variety of array components have been designed, but most of them can be classified in two categories, grids or active arrays. The two approaches are compared in Figure 1.22. Work from D. Rutledge is essentially based on the concept of an 'active' Frequency Selective Surface (FSS) formed from a tight metal mesh loaded with active non-linear devices, with a mesh period that is typically small compared to a wavelength [Hacker92]. Alternatively, the active-array approach is an extension of classical antenna array systems, where each cell of the array is independent and contains a conventional planar antenna structure integrated with the appropriate circuitry, and the cell size is typically a half-wavelength square [Shaalan97b]. This distinction is often made to distinguish between methods for analysis, to emphasize on the array periodicity or on the type of radiating structure. Grids typically involve elementary antennas with simple geometric shapes, analyzed using methods associated with infinite periodic structures, whereas active arrays use common analytical techniques developed for planar circuits and phased arrays.

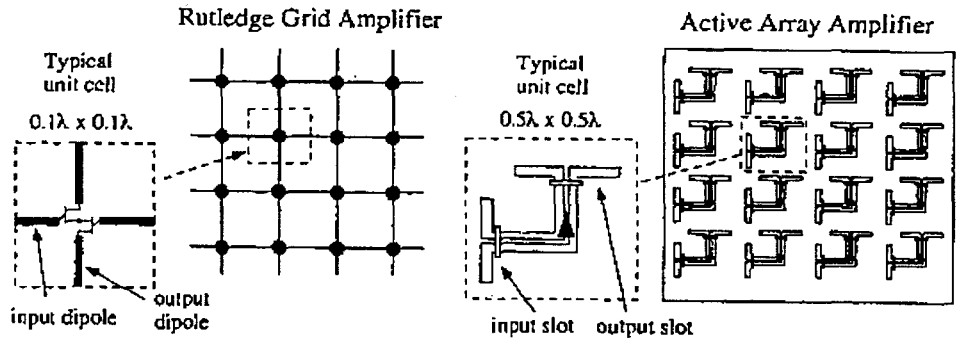

Figure 1.22: Quasi-optical grid and active array.

1.5 Conclusion.

This introductory chapter has been an attempt to highlight some of the challenging issues that currently involve research efforts worldwide in the millimeter and submillimeter wave spectrum. We have reviewed critical aspects of systems aimed at operating at these frequencies, beginning with basic concepts developed for receivers and analyzing every subsystem in a complete reception front end. For applications like radioastronomy, environment control or emerging industrial and commercial activities, the need for these systems is strongly increasing. Different aspects of these technologies have been reported through state-of-the-art results published in the literature.

In particular, we have seen the effort to integrate as many functions as possible in the same chip, by combining active devices with passive elements. Another central issue is the generation of local oscillator power for receiver applications. At increasing frequencies, power levels become extremely weak, and every element in a receiver chain has to be carefully optimized. We have reviewed solid-state sources and their applications to mixing and frequency multiplying, transmission lines that can be integrated with these active devices, and radiating elements.

In this context of space applications, our main contribution will concern the electromagnetic analysis of both active and passive devices. With this scope we have divided our study in three main subjects.

The second chapter analyzes a direct application of the HBV devices fabricated at the IEMN for a frequency tripler from 83 to 250 GHz. We have analyzed the electromagnetic behavior of a multiplier chip including an active device, which is included in a crossed waveguide mount. Full wave analysis is applied to study this complex structure including the environment of the active device, this analysis tries to get an insight into the influence of the integration techniques, notably the parasitics generated by the airbridge, as well as into the multiplier cell itself. Part of this work was performed in the framework of a European Space Agency contract #9777 for Millimeter Wave Critical Sounder Technologies.

The third chapter studies electromagnetic characteristics of micromachined technologies developed at the IEMN. In particular, we have analyzed transmission lines on dielectric membranes in terms of their electromagnetic behavior. The application of this technology to filter structures is also developed for frequencies in the millimeter wave spectrum. Mechanical structures fabricated by micromachining techniques are also investigated, with the aim of designing frequency switches with different topologies.

Finally, the fourth chapter deals with emerging technologies applied to the millimeter wave frequencies, with the study of photonic band gaps. This study concentrates mainly on the understanding of the influence of finite dimensions structures, altogether with some applications of these structures as microresonators and reflectors for dipole antennas.

REFERENCES CHAPTER 1:

[Ahmad91] W.Y.A. Ahmad, G.V. Eleftheriades, L.P.B. Katehi and G.M. Rebeiz, *Millimeter wave integrated-horn antennas, Part II experiment*, IEEE Transactions on Antennas and Propagation, Vol. 39, No. 11, pp. 1582-1586, November 1991.

[Alexopoulos83] N.G. Alexopoulos, P.B. Katehi and D.B. Rutledge, *Substrate optimization for integrated circuit antennas*, IEEE Transactions on Microwave Theory and Techniques, Vol. 31, No. 7, pp. 550-557, July 1983.

[Balanis82] C.A. Balanis, *Antenna theory. Analysis and design*, John Wiley & Sons Ed., 1982.

[Beaudin97] G. Beaudin and P.J. Encrenaz, *Fundamentals of receivers for Terahertz systems*, in New Directions in Terahertz Technology, NATO ASI Series E, Vol. 334, pp. 53-62, 1997.

[Bishop87] W.L. Bishop, K. McKinney, R.J. Mattauch, T.W. Crowe and G. Green, *A novel whiskerless diode for millimeter and submillimeter wave application*, IEEE MTT-S, pp. 607-610, 1987.

[Bradley92] R.F. Bradley, *The application of planar monolithic technology to Schottky varactor millimeter-wave frequency multipliers*, University of Virginia, PhD Thesis, May 1992.

[Brown93] E.R. Brown, C.D. Parker and O.B. McMahon, *Radiation properties of a planar antenna on a photonic crystal substrate*, J. Opt. Soc. Amer. B, Vol. 10, No. 2, pp. 404-407, February 1993.

[Chamberlain97] J.M. Chamberlain, R.E. Miles, C.E. Collins and D.P. Steenson, *Introduction to terahertz solid state devices*, in New Directions in Terahertz Technology, NATO ASI Series E, Vol. 334, pp. 3-27, 1997.

[Cheng95] S.D. Cheng, R. Biswas, E. Ozbay, S. McCalmont, G. Tuttle and K.M. Ho, *Optimized dipole antennas on photonic band gap crystals*, Applied Physics Letters, Vol. 67, No. 23, pp. 3399-3401, December 1995.

[Colllin92] R.E. Collin, *Foundations for microwave engineering*, McGraw Hill Ed., 2nd Edition, 1992.

[Crowe96] T.W. Crowe, T.C. Grein, R. Zimmermann and P. Zimmermann, *Progress toward solid-state local oscillators at 1 THz*, , IEEE Microwave and Guided Wave Letters, Vol. 6, No. 5, pp. 208-208, May 1996.

[deLange96] G. de Lange, B.R. Jacobson and Q. Hu, *A low noise millimeter-wave heterodyne mixer using Nb superconducting tunnel junctions*, Applied Physics Letters, Vol. 68, No. 13, pp. 1862-1864, March 1996.

[Dib91] N. I. Dib, W.P. Harokopous, L.P.B. Katehi, C.C. Ling and G.M. Rebeiz, *Study of a novel planar transmission line*, Proceedings of 1991 IEEE MTT-S International Symposium, Boston, June 1991.

[Eisele95] H. Eisele and G.I. Haddad, *High performance InP Gunn devices for fundamental frequency operation mode at D band*, IEEE Microwave and Guided Wave Letters, Vol. 5, No. 11, pp. 385-387, November 1995.

[Faber95] M.T. Faber, J. Chramiec and M.E. Adamski, *Microwave and millimeter wave diode frequency multipliers*, Artech House Ed., 1995.

[Gao96] J.R. Gao, S. Kovtonyuk, J. Jegers, T.M. Klapwijk and H. van de Stadt, *Fabrication of Nb SIS mixers with UHV evaporated Al striplines*, Conference Proceedings 7th International Symposium Space Terahertz Technology, Charlottesville, 12-14 March 1996.

[Garfield91] D.G. Garfield, R.J. Mattauch and S. Weinreb, *RF performance of a novel planar milimeter-wave diode incorporating an etched surface channel*, IEEE Transactions on Microwave Theory and Techniques, Vol. 39, No. 1, January 1991.

[Gearhart94] S.S. Gearhart and G.M. Rebeiz, *A monolithic 250 GHz Schottky diode receiver*, IEEE Transactions on Microwave Theory and Techniques, Vol. 42, No. 12, pp. 2504, 1994.

[Gopinath82] A. Gopinath, *Losses in coplanar waveguides*, IEEE Transactions on Microwave Theory and Techniques, Vol. 30, No. 7, pp. 11011104, July 1982.

[Gupta79] K.C. Gupta, R. Garg and I.J. Bahl, *Microstrip lines and slotlines*, Artech House Ed., 1979.

[Hacker92] J.B. Hacker, R.M. Weikle, M. Kim, M.P. De Lisio and D.B. Rutledge, *A 100-element planar Schottky diode grid mixer*, , IEEE Transactions on Microwave Theory and Techniques, Vol. 40, No. 3, pp. 557-562, March 1992.

[Hesler95] J.L. Hesler, W.R. Hall, T.W. Crowe, R.M. Weikle, S.D. Deaver, R.F. Bradley and S.K. Pan, *Submillimeter wavelength waveguide mixers using planar Schottky barrier diodes*, Conference Proceedings 7th International Symposium Space Terahertz Technology, Charlottesville, pp. 462-473, 12-14 March 1996.

[HFSS95] HP 85180A *High Frequency Structure Simulator A 4.01*, Hewlett Packard Company, Network Measurements Division, 1400 Fountaingrove Parkway, Santa Rosa, CA 95043, USA.

[Horikoshi85] Y. Horikoshi, *Semiconductor lasers with wavelengths exceeding 2 μm*, in Semiconductors and Semimetals, Vol. 22C, Academic Press, New York, pp. 93-151, 1985.

[Hübers92] H.W. Hübers, G.W. Schwaab and H.P. Röser, *Video detection and mixing performance of GaAs Schottky barrier diodes with femtofarad capacitance*, Journal of Applied Physics, Vol. 72, pp. 3194-3197, 1994.

[Itoh89] T. Itoh, *Overview of quasi-planar transmission lines*, IEEE Transactions on Microwave Theory and Techniques, Vol. 37, No. 2, pp. 175-280, February 1989.

[Jackson86] R.W. Jackson, *Considerations in the use of coplanar waveguide for millimeter-wave integrated circuits*, IEEE Transactions on Microwave Theory and Techniques, Vol. 34, No. 12, pp. 1450-1456, December 1986.

[Jackson89] R.W. Jackson, *Mode conversion at discontinuities in finite-width conductor backed coplanar waveguide*, IEEE Transactions on Microwave Theory and Techniques, Vol. 37, No. 10, pp. 1582-1589, October 1989.

[Jones96] J.R. Jones, *CAD of millimeter wave frequency multipliers: an investigation of the heterostructure barrier varactor*, University of Virginia, PhD Thesis, January 1996.

[Jones97] J.R. Jones, W.L. Bishop, S.H. Jones and G.T. Hait, *Planar multibarrier 80/240 GHz heterostructure barrier varactor triplers*, IEEE Transactions on Microwave Theory and Techniques, Vol. 45, No. 4, pp. 512-518, April 1997.

[Katehi93] L.P.B. Katehi, G.M. Rebeiz and T.M. Wheeler, *Micromachined circuits for Millimeter- and Sub-Millimeter-wave applications*, IEEE Antennas & Propagation Magazine, Vol. 35, No. 5, pp.2-17, October 1993.

[Kobayshi88] M. Kobayshi, *A dispersion formula satisfying recent requirements in microstrip CAD*, IEEE Transactions on Microwave Theory and Techniques, Vol. 36, No. 8, pp. 1246-1250, August 1988.

[Kollberg89] E.L. Kollberg and A. Rydberg, *Quantum barrier varactor diodes for high efficiency millimeter wave multipliers*, Electronics Letters, Vol. 25, No. 25, pp. 1696-1698, December 1989.

[Kollberg97] E.L. Kollberg, *Superconducting mixers for submillimeter wavelengths*, in New Directions in Terahertz Technology, NATO ASI Series E, Vol. 334, pp. 97-117, 1997.

[Kompa75] G. Kompa and R. Mehran, *Planar waveguide model for calculating microstrip components*, Electronics Letters, Vol. 11, No. 19, pp. 459-460, September 1975.

[Kooi96] J.W. Kooi, M.S. Chan, H.G. Leduc and T.G. Phillips, *A waveguide receiver for the 590-720 GHz atmospheric window using a tuned 0.5 μm^2 Nb/AlO$_x$Nb SIS tunnel junction*, , Conference Proceedings 7th International Symposium Space Terahertz Technology, Charlottesville, 12-14 March 1996.

[Krishnamurthi96] K. Krishnamurthi and R.G. Harrison, *Millimetre-wave frequency tripling using stacked heterostructure barrier varactors on InP*, IEE Proceedings on Microwaves, Antennas and Propagation, Vol. 143, No. 4, pp. 272-276, August 1996.

[Lheurette96] E. Lheurette, P. Mounaix, P. Salzenstein, F. Mollot and D. Lippens, *High performance InP-based heterostructure barrier varactors in single and stack configuration*, Electronics Letters, Vol. 32, No. 15, pp. 1417-1418, July 1996.

[Maas93] S.A. Maas, *Microwave Mixers* (2nd edition), Artech House Ed., 1993.

[Manley56] J.M. Manley and H.E. Rowe, *Some general properties of non linear elements. Part I General energy relations*, Proceedings of the IRE, pp. 904, July 1956.

[Momentum95] HP 85185A, *Momentum A 2.52*, Hewlett Packard Company, Network Measurements Division, 1400 Fountaingrove Parkway, Santa Rosa, CA 95043, USA.

[Page56] C.H. Page, *Frequency conversion with positive non linear resistor*, Journal of Research of the National Bureau of Standards, Vol. 56, No. 4, April 1956.

[Rahman96] A. Rahman, G. de Lange and Q. Hu, *Micromachined room temperature microbolometers for millimeter-wave detection*, Applied Physics Letters, Vol. 68, No. 4, pp. 2020-2022, April 1996.

[Rausch93] K. Rausch, *Planar millimeter wave varactor multipliers*, University of Virginia MSc. Thesis, August 1993.

[Rebeiz92] G.M. Rebeiz, *Millimeter wave and terahertz integrated circuit antennas*, Proceedings of the IEEE, Vol. 80, No. 11, pp. 1748-1770, November 1992.

[Riaziat96]M. Riaziat, R. Majidi-Ahy and I. Feng, *Propagation modes and dispersion characteristics of coplanar waveguides*, IEEE Transactions on Microwave Theory and Techniques, Vol. 38, No. 3, pp. 245-250, March 1990.

[Salzenstein96] P. Salzenstein, O. Dupuis, M. Hélal, E. Lheurette, O. Vanbésien, P. Mounaix and D. Lippens, *Coplanar waveguide membranes micromachined on a GaAs substrate*, Electronics Letters, Vol. 32, No. 9, pp. 821-822, April 1996.

[Shaalan97b] M. Shaalan, M. Bozzi, K. Beilenhoff, J. Weinzierl, D. Steup, G. Rehm, G. Conciauro, W. Menzel, H. Brand and H.L. Hartnagel, *An antenna array for quasi-optical frequency multiplier applications*, Conference Proceedings of the 20th ESTEC Antenna Workshop on Millimetre wave antenna Technology and Antenna Measurement, 18-20 June 1997, ESTEC, Noordwijk, The Netherlands.

[Shalaan97a] M. Shalaan, M. Bozzi, A. Vogt, J. Weber, H.L. Hartnagel and G. Conciauro, *First design of a 430 GHz quasi-optical tripler*, Proceedings of the 5th International Workshop on Terahertz Technologies, Grenoble, France, 15-18 September 1997.

[Siegel92] P.H. Siegel, R.J. Dengler, I. Mehdi, W.L. Bishop and T.W. Crowe, *A 200 GHz planar diode subharmonically pumped waveguide mixer with state of the art performance*, IEEE MTT-S Digest, pp. 595, 1992.

[Sigalas96] M.M. Sigalas, R. Biswas and K.M. Ho, *Theoretical study of dipole antennas on photonic band-gap materials*, Microwave and Optical Technology Letters, Vol. 13, No. 4, pp. 205-209, November 1996.

[Wen69] C.P. Wen, *Coplanar waveguide: A surface strip transmission line suitable for nonreciprocal gyromagnetic device applications*, IEEE Transactions on Microwave Theory and Techniques, Vol. 17, No. 12, pp. 1087-1090, December 1969.

[Yablanovitch93] E. Yablanovitch, *Photonic Band Gap structures*, J. Opt. Soc. Amer. B, Vol. 10, No. 2, pp. 283-294, February 1993.

[Yang97] H.Y.D. Yang, N.G. Alexopoulos and E. Yablanovitch, *Photonic Band Gap materials for high gain printed circuit antennas*, IEEE Transactions on Antennas and Propagation, Vol. 45, No. 1, pp. 185187, January 1997.

[York97] R.A. York and A. Alexian, *Spatial and quasi-optical arrays for power combining*, Conference Proceedings of the 20th ESTEC Antenna Workshop on Millimetre wave antenna Technology and Antenna Measurement, 18-20 June 1997, ESTEC, Noordwijk, The Netherlands.

CHAPTER II:

FREQUENCY MULTIPLIERS BASED ON THE HETEROSTRUCTURE BARRIER VARACTOR

CHAPTER 2: FREQUENCY MULTIPLIERS BASED ON THE HETEROSTRUCTURE BARRIER VARACTOR.

In this chapter, we analyze a Heterostructure Barrier Varactor (HBV) diode tripler from 83 to 250 GHz from the electromagnetic side. This work is part of a European Space Agency contract (9777/92/nl/pb-W.O.18), namely Millimeter Wave Critical Sounders Technologies, with the aim of developing reliable local oscillator sources for environmental research projects. In collaboration with Ecole Normale Supérieure (Paris), Chalmers University of Technology (Gothenburg) and Matra Marconi Space (Toulouse), IEMN has fabricated the active device planar chip, which will be integrated in a crossed waveguide mount. We report on key results obtained with HFSS and Momentum software packages concerning the analysis of parasitic elements and their influence on the tripler operation. The novelty of the analysis stems from the fact of considering the tripler as a whole, by combining different approaches.

We will start by a brief description of the characteristics of the HBVs fabricated and the different technological mask sets. As mentioned previously, the full-wave analysis of air-bridged devices is of major concern and will be explained in detail in a second stage. In addition, harmonic balance results of the HBV in frequency multiplication are supplied to effectively predict the performance of the tripler mount.

2.1 Device physics and operation of the HBV.

2.1.1 Growth of epitaxial structures.

We listed in the first chapter several types of diodes employed as non-linear devices in a receiver front-end. When the targeted application is a frequency multiplier, the HBV is inherently a promising candidate for practical situations. Indeed, by using a device with a symmetrical capacitance_voltage characteristic, only odd harmonics are generated. Thus, with the use of a HBV in a quintupler, there is only one idler at the third harmonic to consider be (compared to the three idlers needed in a Schottky varactor quintupler) and in the case of a tripler, no idler is required.

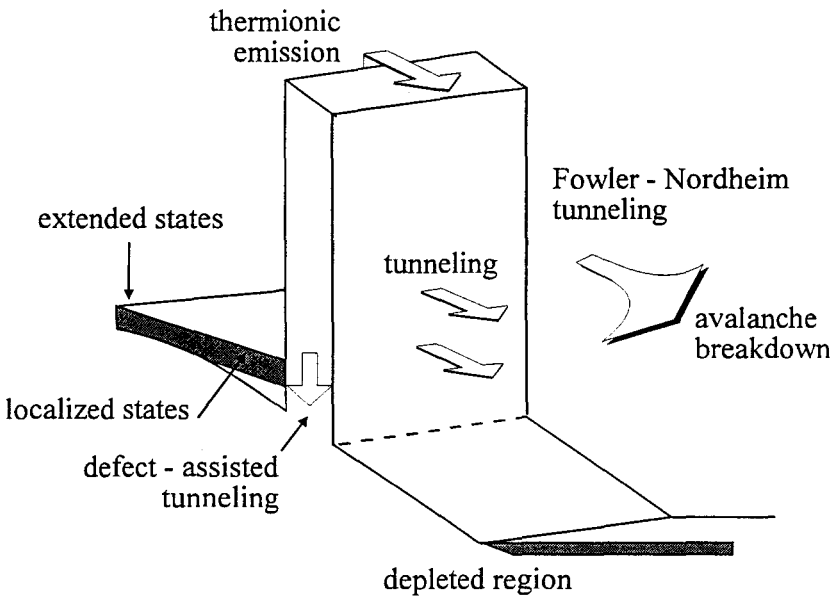

Figure 2.1: Schematic of the conduction band profile and related conduction phenomena.

The symmetrical C_V and antisymmetrical I_V characteristics are a direct consequence of the epitaxial structure of the device, which does not require any rectification contact. A single HBV consists of a wide bandgap semiconductor sandwiched between two n-type smaller bandgap cladding layers. The potential barrier thus formed in the conduction band prevents conduction through the structure, so that each cladding layer can be depleted according to bias conditions. The conduction band profile for a basic structure with the blocking barrier is schematically depicted in Figure 2.1, along with an illustration of different conduction mechanisms. Besides the symmetry properties, several remarks can be made, [Lheurette96]. The design of the epilayer and the band gap engineering aimed at improving the power handling of the devices are beyond the scope of this thesis. In short, however several guidelines in the design can be established on the basis of parasitic conduction mechanisms. At moderate voltages, it can be shown that a Fowhler Nordheim emission (tunneling through the triangular shaped barrier under bias) is responsible for the leakage current. At higher voltages, impact ionization in the cladding layer could take place yielding to a breakdown process as for conventional Schottky varactor. Therefore, the parameters of the barrier and of the cladding layers, notably for the latter the doping concentration, have to be optimized .

Over the past, most of the HBV's structures were fabricated in a GaAs technology. Relatively poor performance in terms of voltage handling has been observed as a result of complex mixing effects between X and Γ conduction paths in the barrier. Further details on these physics will be reported elsewhere. As a consequence we decided to use InP-based materials with the growth sequence depicted in Figure 2.2.

Poor blocking of the barrier is alleviated by using a stair like AlInAs/AlAs single discontinuity for a Single Heterostructure Barrier Varactor (SHBV) or a double scheme in the case of the Dual Heterostructure Barrier Varactor (DHBV). In both cases, the barrier is formed by a 3 nm thick AlAs layer surrounded by two AlInAs, 5 nm thick layers. The use of pseudomorphic AlAs/$In_{0.53}Ga_{0.47}As$ epilayers grown on an InP substrate prevents leakage currents up to high bias voltages, [Reddy93, Mounaix95]. The 5-nm thick spacer layers sandwiched between the cladding layers, which are typically 300 nm thick, and the barrier prevents the diffusion of dopant species into the barrier. At last, two contact layers, 500 nm thick, with high doping concentrations form the contact regions. All the epilayers were grown in a Gas Source Molecular Beam Epitaxy Riber Machine (GS-MBE), in the epitaxy group. The growth was performed without interruption, both for binary and ternary alloys, at 520 °C on InP substrate, typically 400 μm thick.

	InGaAs	$5x10^{18}$ cm^{-3}	500nm
	InGaAs	$1x10^{17}$ cm^{-3}	300nm
X 2	InGaAs	Undoped	5nm
	InAlAs	Undoped	5nm
	AlAs	Undoped	3nm
	InAlAs	Undoped	5nm
	InGaAs	Undoped	5nm
	InGaAs	$1x10^{17}$ cm^{-3}	300nm
	InGaAs	$5x10^{18}$ cm^{-3}	500nm
	InP Substrate		

Figure 2.2: Growth parameters for a SHBV and for a DHBV.

2.1.2 C_V and I_V characteristics.

Figure 2.3 shows the measured I_V characteristics of a SHBV and a DHBV samples with the same area (S = 1256 μm^2) at 300 K. Both are centered about 0 bias, as expected. The threshold conduction voltage, estimated for a current density of 10 A/cm^2, is obtained at 6 V (SHBV) and 12 V (DHBV). Hence, the voltage handling for the DHBV is twice the value of SHBV, which proves a scaling rule with complexity. The results are in good agreement with calculated data [Lheurette96b]. Leakage current in the device is preferentially due to pure tunneling current at low voltages and thermally assisted emission with a triangular-shaped barrier at moderated voltage. At the same time, avalanche breakdown voltage can be theoretically estimated, from simple formulas [Sze], around 6 V, thus avoiding to further increase the bias voltage.

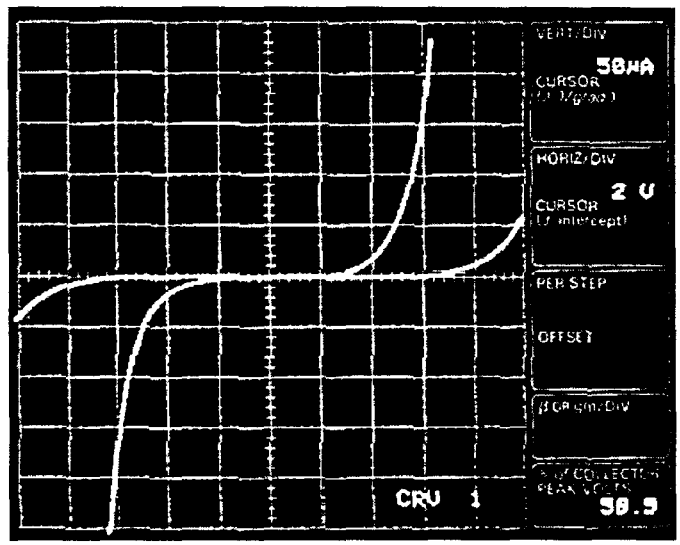

Figure 2.3: I_V characteristics for a SHBV and a DHBV with same areas (S = 1256 μm^2).

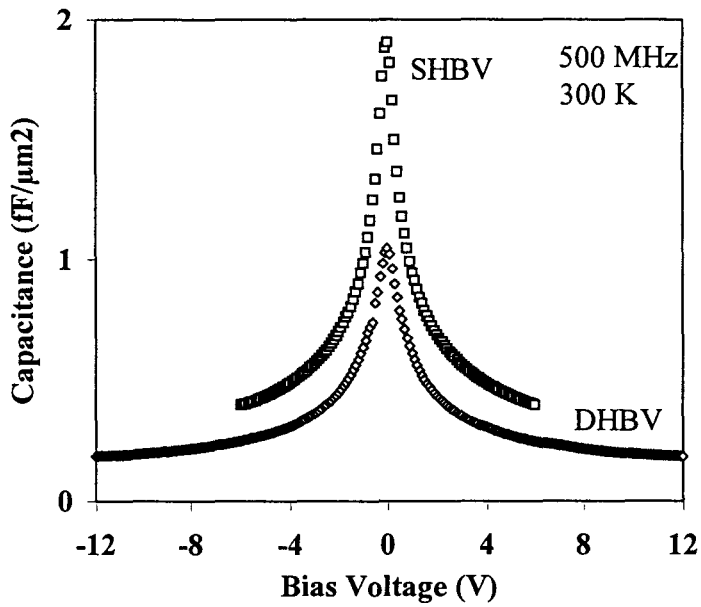

Figure 2.4: Normalized C_V characteristics for a SHBV and a DHBV.

For the same devices, measurement data, at 500 MHz, of the C_V characteristics are reported in Figure 2.4, normalized with respect to the sample area. We can note here too, a perfect symmetry with biasing, along with a high capacitance ratio, C_{max}/C_{min} = 5:1 obtained for both devices. Also, there is scaling with complexity, for any voltage we have, $C_{DHBV} = C_{SHBV} / 2$. Finally, normalized capacitance values with respect to the device area as low as 1 $fF/\mu m^2$ have been measured for the dual barrier case [Carbonell96]. Numerical simulations of the bias-dependence of the capacity can be carried out on the basis of the sheet carrier density variation versus bias voltage ($C = q\,\delta n_s / \delta V$). A comparison between experimental and theoretical data is shown in Figure 2.5. It can be seen that the agreement is overall good, enabling us to derive some design rules.

In fact, in a first analysis, the maximum value of the capacitance C_{max} can be estimated with a parallel plate capacitor formula as:

$$C_{max} = \frac{\varepsilon S}{L_b + 2L_s}$$

where L_b is the barrier thickness and L_s is the screening length. On the other hand, the minimum value C_{min} can be roughly estimated from:

$$C_{min} = \frac{\varepsilon S}{L_c}$$

where L_c is the cladding layer thickness, and under the assumption that the barrier thickness is negligible with respect to L_c.

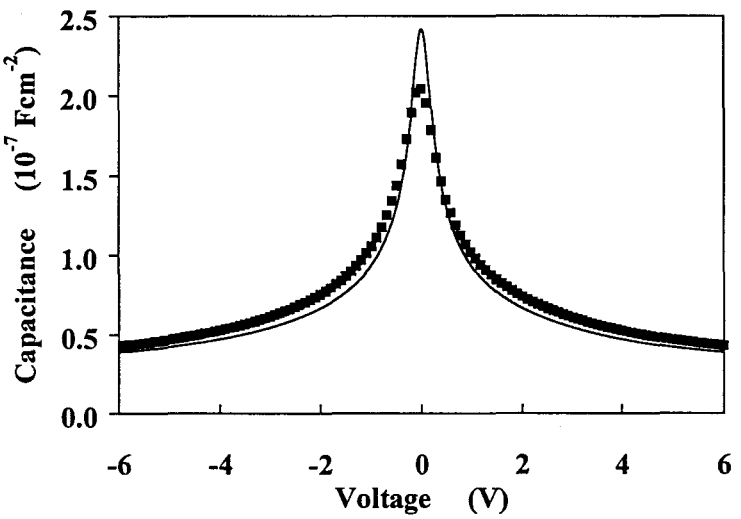

Figure 2.5: Comparison between measured and calculated C_V characteristics (SHBV).

These characteristics remain unchanged with frequency at least up to the pump frequency of the tripler under consideration. Figure 2.6 gives a comparison of measured C_V characteristics at 500 MHz and 85 GHz demonstrating the invariance up to high frequencies. This does not presume on the ability of the device to respond to the pump signal under large signal excitation. Indeed it was shown over the past that we can expect a saturation current limitation [Kollberg92], this issue was recently revisited by E. Kollberg.

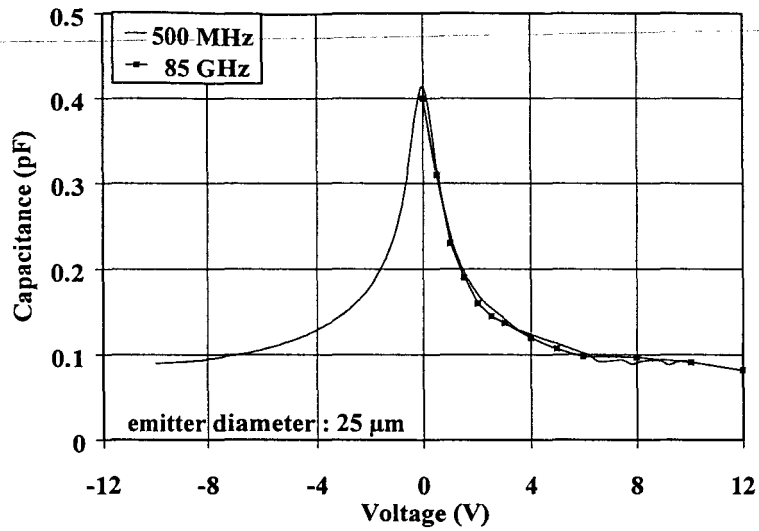

Figure 2.6: Comparison of C_V characteristics for a SHBV at 500 MHz and 85 GHz.

If we move now from current and capacitance characteristics to power considerations, the advantage of epitaxially stacking different individual devices on the same epitaxy is clearly demonstrated. We learned that the normalized capacitance for a stacked device scales with the number of barriers. However, the number of barriers will be limited by the technological complexity, but in general, and with respect to a basic varactor, we have:

$$C_n = \frac{C_b}{n}$$

for the normalized capacitance per unit area. Then, if we maintain a constant impedance level when stacking a number of barriers,

$$Z_n \propto \frac{1}{C_n \omega}$$

we will have to increase the area of the device n-times. As a consequence of this assumption, in terms of current handling, we will have,

$$I_n = J A_n = J n A_b = n I_b$$

with J being the current density and A the area of the device. In terms of voltage handling, the fact of having n stacked devices makes that the overall voltage is distributed along the different diodes with,

$$V_n = n V_b$$

If we summarize these arguments in terms of power handling we have,

$$P_n = n^2 P_b$$

for n devices epitaxially stacked. This clearly demonstrates the advantage of vertical integration of the active devices by epitaxially stacking them. Furthermore, one can expect even

better performances if we planar integrate various stacked varactors in series on the same wafer. These concepts will be detailed in the following sections.

2.2 Fabrication and characterization techniques.

In this section, we will briefly describe the technological procedures to fabricate the HBV devices, with a first attempt to make a distinction between extrinsic elements and intrinsic elements. To this aim, three technology mask sets have been designed. The first one permits direct measurement of the intrinsic elements without deembedding techniques. The second integrates the diode in a CPW access line by means of an airbridge technology. Finally, the third mask set was specially designed for a tripling application, taking into account for the first time in our group the electromagnetic aspects. We are going to present these realizations and discuss about the frequency capabilities.

2.2.1 Mask set for probing the intrinsic elements.

To assess the quality of an epitaxial growth sequence, a fast fabrication technique has been employed, which can be compared to the procedure proposed in [Stake96]. The schematic cross section of the structure is depicted in Figure 2.7. With a coaxial-type ring shaped structure, we have a direct access to the intrinsic characteristics of the device by directly probing the samples with RF coplanar Picoprobes. The 'hot' probe is positioned directly on the top of the Ω contact, whereas the 'ground' probes contact the outer ring. These measurements have been carried out from dc up to 110 GHz, with two Hewlett Packard (HP8510C) network analyzers.

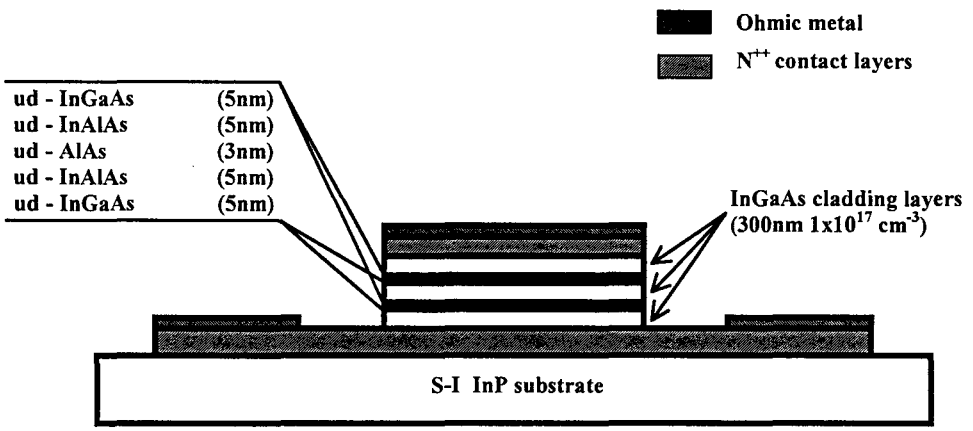

Figure 2.7: Schematic cross section of a ring shaped DHBV.

This configuration includes concentric pads with four different anode diameters (10, 20, 30 and 40 μm). The patterning of the devices requires three photolithography masks. For etching the mesas an $H_3PO_4/H_2O_2/H_2O$ solution is used, and to form the ohmic contacts we used a sequential Ni/Ge/Au/Ti/Au metallization, followed by a rapid thermal annealing (RTA). The second ohmic contact lies on the buried n^+ layer.

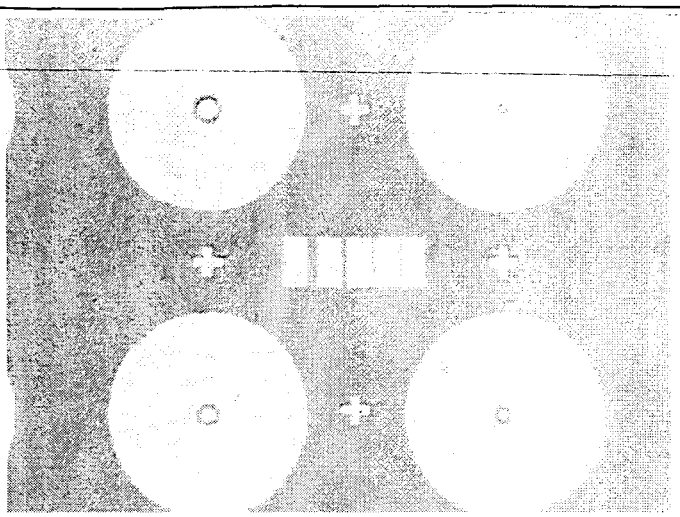

Figure 2.8: Optical view of the fabricated devices along with a TLM pattern.

An optical view of the fabricated diodes is given in Figure 2.8. Different anode areas are illustrated, along with a TLM pattern, located in the center, to measure the ohmic contact resistance. The series resistance of the device has three important contributions, as depicted in Figure 2.9. Namely, they are the ohmic contact resistance, the epilayer resistance and the spreading resistance.

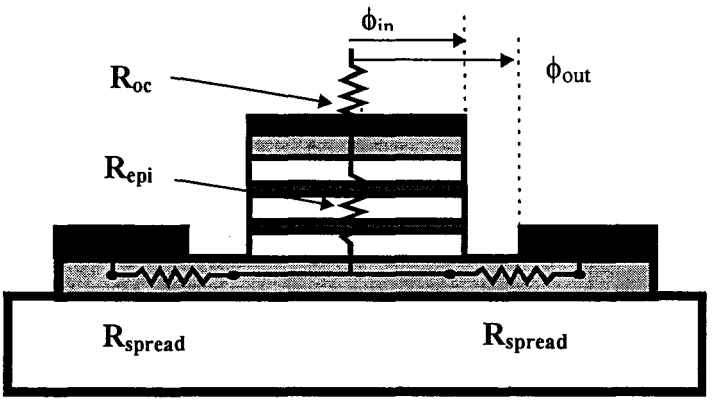

Figure 2.9: Contributions to the series resistance.

The ohmic contact resistance can be assessed experimentally from TLM measurements [ESApr97]. Its value can be found can be found in the 1 - 2 10^{-7} $\Omega.cm^2$ range. This resistance usually scales to the area of the ohmic contact, whatever its shape is. A very comprehensive theoretical study of this contribution is reported in [Bhaumik92].

The epilayer resistance depends on the epitaxial structure and on the operation conditions. In a first analysis, it can be simply deduced from:

$$R_{epi} = \frac{\rho_{epi}\, t_{epi}}{S_{anode}}$$

where ρ_{epi} is the average resistivity of the active region, S_{anode} is the area of the device and t_{epi} is the thickness of the epitaxial structure.

At last, the spreading resistance is the most important contribution to the series resistance. Moreover, it is the most difficult term to evaluate because it strongly depends on the geometry of the device. R_{spread} has been studied by Dickens, [Dickens67], by means of a field analysis of potential and current in the semiconductor volume which leads to an integral that cannot be solved

analytically. Nevertheless, under certain assumptions the bulk spreading resistance can be estimated for cylindrical planar diodes from the following expression:

$$Z_{spread} = \frac{1}{2\pi\sigma_{n^+}\phi_{in}}\tan^{-1}\left\{\frac{\phi_{out}}{\phi_{in}}\right\} + \frac{1+j}{2\pi\sigma_{n^+}\delta_s}\ln\left\{\frac{\phi_{out}}{\phi_{in}}\right\}$$

This expression takes into account the skin effect, δ_s, which becomes dominant at very high frequencies. A concise definition is given in [Dickens67] by Holm who states that "the skin effect consists of an induction by the current's own magnetic field pressing the lines of flow toward the exterior of the conductor, thus diminishing the effective conductive cross section and increasing the resistance". As a general rule, the thickness of the n^+ buried layer is of great importance because it has to be larger than δ_s. The magnitude of the skin depth can be calculated through:

$$\delta_s = \sqrt{\frac{2}{\omega\mu_0\sigma_{n^+}}}$$

Applying the typical value of the conductivity in the n^+ layer for the fabricated structures, $\sigma_{n+} = 3200\ \Omega^{-1}cm^{-1}$, at 100 GHz gives a skin depth of $\delta_s = 3\ \mu m$. In practice, the n^+ buried layer is 1 μm thick, so the effect of δ_s, under these assumptions, will be hidden by the fact of having a very thin doped layer. However, at much higher frequencies, its influence can be significant, even if at 250 GHz its value can still be greater than the n^+ layer thickness with, in this case, $\delta_s = 1.8\ \mu m$.

2.2.2 Mask set for probing the access elements.

A second mask set has been used for probing the access elements of a CPW with an airbridge technology. Figure 2.10 shows an optical view of a complete test structure (diode + airbridge + CPW access line) together with a Scanning Electron Microscope close up of a diode contacted with an airbridge. With this technique, small area devices can be contacted because Reactive Ion Etching (RIE) techniques were employed, in contrast to the previous process where a chemical etch was used to define the anode areas. In our group, up to 1 x 1 μm^2 diodes have been contacted, but the present run had varied section devices ranging from 4 x 4, 3 x 10, 6 x 10 to 11 x 11 μm^2.

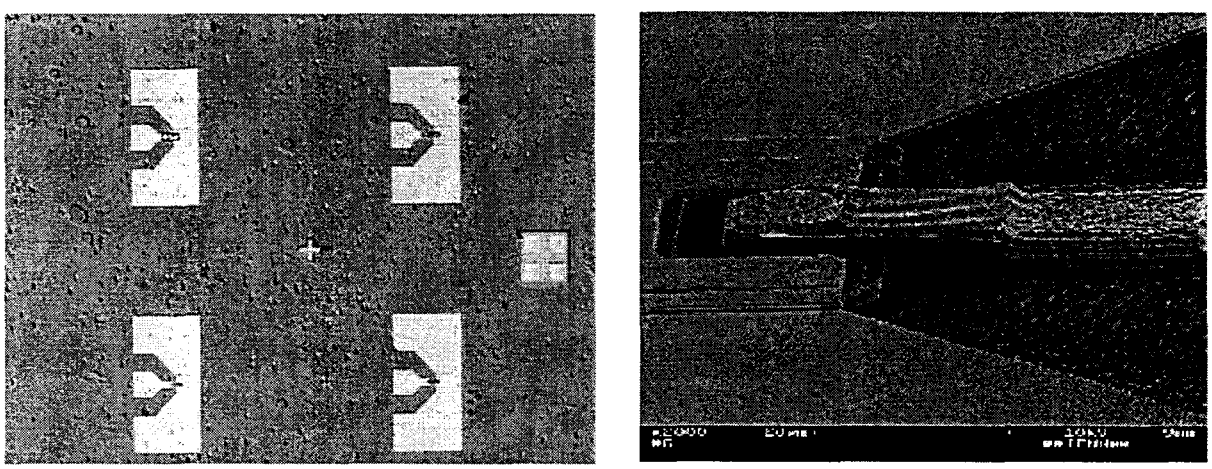

Figure 2.10: Optical and SEM views of the test structure for probing the access elements, a.), and a 11 x 11 μm^2 airbridge contacted diode, b.).

The mask set had 6 levels which correspond to the following technological steps:

- level 1: top ohmic contact definition.
- level 2: mesa definition (top Ω contact was used for the first mesa).
- level 3: second ohmic contact (U-shaped contact).
- level 4: CPW access pads deposition.
- level 5: formation of pillars of the airbridge.
- level 6: deck of the airbridge formation.

A detailed procedure to run this process can be found elsewhere [Lheurette96b], with in particular the airbridge formation which is the most critical step of the six. Let us note that the fabricated devices do not have circular patterns for the anodes, they are rather square or rectangular. This is due to the fact that spreading resistance can be reduced, keeping the area constant, if the perimeter of the active device cross section is increased. This is particularly true for rectangular shaped structures, as it has been widely exploited at JPL [Mehdi96]. This technology has the drawback of complexity, even if resistance can be reduced by a factor of two, in counterpart, the yield of the process can be strongly reduced.

Measurements have been performed on these samples by means of RF coplanar Picoprobes and HP network analyzers, from dc up to 110 GHz. Prior to measurement, a Through Reflect Line (TRL) standard calibration was carried out. Only one set of probes is used, because only reflection loss, and thus the diode impedance, has to be measured. The access coplanar pads have been designed in order to have a characteristic impedance in the order of $Z_0 = 50\ \Omega$, nevertheless the spacing between the hot line and the ground lines is not optimized to preclude dispersion and high order modes in the thick semi insulating substrate might be generated. This can be easily verified with simple analytical formulas [Gupta79], as well as with full-wave analysis, as we will see later.

The reference plane for the S_{11} measurements is, in principle, on the edge of the CPW access line. In practice, RF probes are always shifted a few microns on the line towards the device, and this is intentionally done, but it can lead to changes in the measured S parameters in the order of a few degrees (phase of S_{11}) at 100 GHz. Anyway, it is not easy to overcome this type of problem. Indeed, by moving the probes to a reference plane closer to the airbridge and the diode location, believing that the measurement would represent only the contribution of the airbridge portion, would cause an open stub effect as it is illustrated in Figure 2.11.

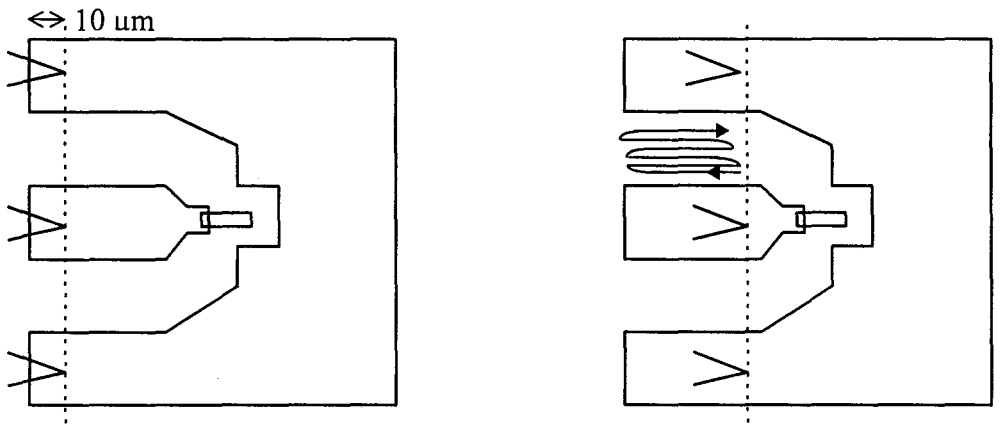

Figure 2.11: Practical shifted location of the probes in a measurement, a.), and open stub effect due to displacement of the reference plane, b.).

The key issue is to clearly differentiate between the environment of the device, notably the effect due to the airbridge, and the access CPW line. Figure 2.12 presents a schematic of the different parasitics coming from the integration of the device by means of an airbridge. Namely they are,

L_f: finger inductance
C_{pp}: pad to pad capacitance
C_{fp}: finger to pad capacitance

These parameters represent extrinsic elements that modify the reactive part of the diode impedance. Also, one can think of resistive contributions such as the airbridge resistance which can be non negligible for finger-shaped thin gold films. In the following we will discuss on the validity of such an assumption, but in this first analysis, only reactive terms will be considered. On these basis, systematic fits between impedances from a lumped element circuit according to Figure 2.12 and the one measured by means of spectrum analyzers have been performed. The measured S_{11} integrates various effects at the same time: access lines as well as airbridge, but it was found that the overall self inductance, L_f , was typically in the 50 - 60 pH range, whereas the global parasitic capacitance C_p was 17 fF.

This effect is more pronounced at low frequencies where no realistic propagation can occur in a 50 μm long coplanar access. This point will be revisited in the next section.

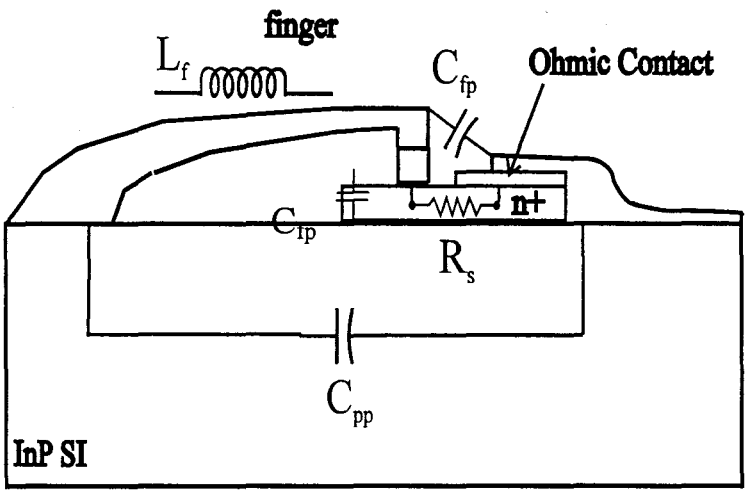

Figure 2.12: Schematic of the parasitic elements in an airbridge technology.

2.2.3 Mask set for a frequency tripler application.

On the basis of the work presented in the previous sections a new mask set was designed and manufactured (e-beam technology) to provide a HBV chip to be introduced in a crossed waveguide mount. Diodes with different sections in the 10 -100 μm^2 range have been designed, some of them in planar series configuration. This configuration is convenient because two connected diodes (≡ 4 barriers with DHBV devices) offer power handling advantages. At the same time, the chip dimensions and the device configuration have to be chosen on the basis of the design of the multiplier cell, on electromagnetic criteria and on the compatibility with a flip chip technology. The microstrip circuit is fabricated on a quartz substrate. The chip is solded to the strip line in a flip chip technology, therefore at the device level, two pads facing each other are preferable to a CPW scheme. This procedure imposes some restrictions for the chip height and width. Moreover, it is imperative to avoid any spurious substrate mode, by choosing transverse dimensions of the chip in such a way that substrate modes for this equivalent dielectric waveguide are under cut-off. In our case width and height are chosen equal to 100 μm. The length is fixed to 220 μm.

The mask set has 7 levels, the first 6 are equivalent to those of the previous mask. In fact, a seventh level has been added to pre-etch the wafer before dicing the chips. Single and double (series) configurations are depicted in Figure 2.13, in a.) a 12 x 4 μm^2 anode, and in b.) 24 x 4 μm^2 anodes. In the latter case, coupling between both devices is achieved by their lateral dimension, thus reducing resistance. In the case of series connected devices, the side ohmic contact (level 3) is not necessary since this scheme integrates the two epitaxial structures through the n^+ InGaAs buried layer. For a single device, level 3 remains unchanged with respect to the previous process. The following diode areas were available:

- finger shaped (width x length): 4 x 3, 4 x 6, 4 x 12, 4 x 15 and 4 x 24 μm^2
- circular shaped (diameter in μm): 4, 6, 8, 9 and 11 μm.

The airbridge dimensions are in all cases about 4 μm in width and 25 μm in length. From the electromagnetic side, the reduced length has a direct consequence on the inductance and pad to pad capacitance values, decreasing the former and increasing the latter. With respect to the technology issue, the most critical parameter in the airbridge formation is the difference in height between the two pillars. This is not the case for the technology from the University of Virginia, UVA, where the airbridge is totally planar, [Jones97]. For a DHBV, this height difference can reach up to 2 μm, so that secure and successful fabrication requires a short length airbridge.

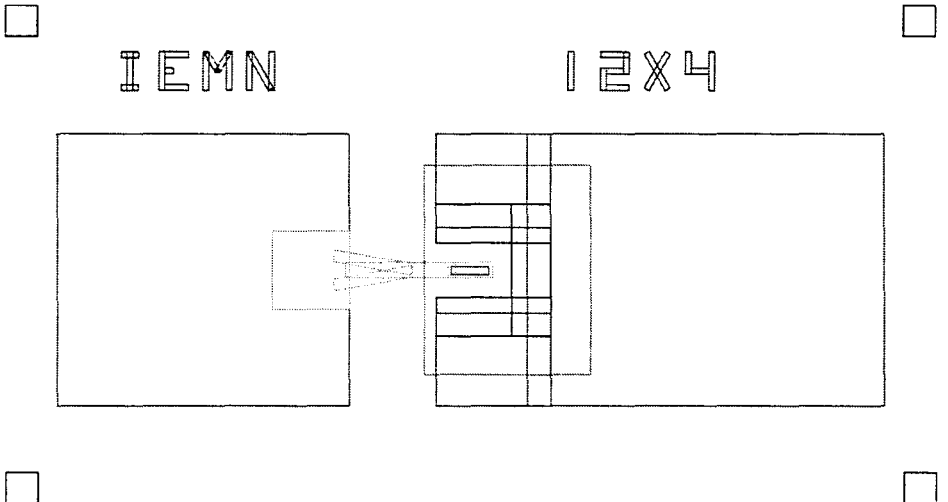

Figure 2.13a: Close-up on the design of a single device configuration (12 x 4 μm^2 anode),

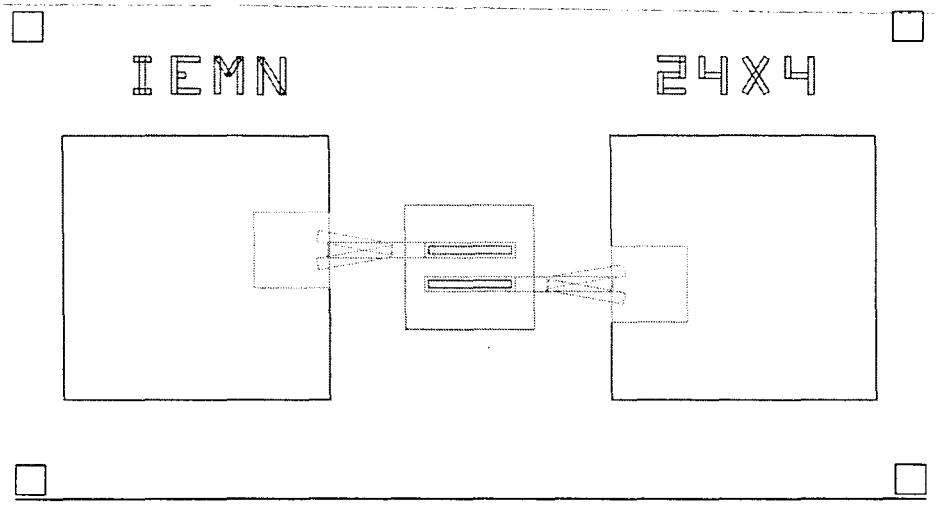

Figure 2.13b: Close-up on the design of a series device configuration (24 x 4 μm^2).

Scanning Electron Micrographs of the devices presented above are shown in Figure 2.14 for single and series configurations, before the dicing procedure. This last step is really tricky in the sense that the extremely reduced dimensions of the chips make them very difficult to handle. In any case, these devices can only be fully characterized when mounted in a crossed waveguide system. This kind of equipment is available at Matra Marconi and Observatoire de Meudon. At the IEMN, a global EM simulation of the multiplier block has been carried out.

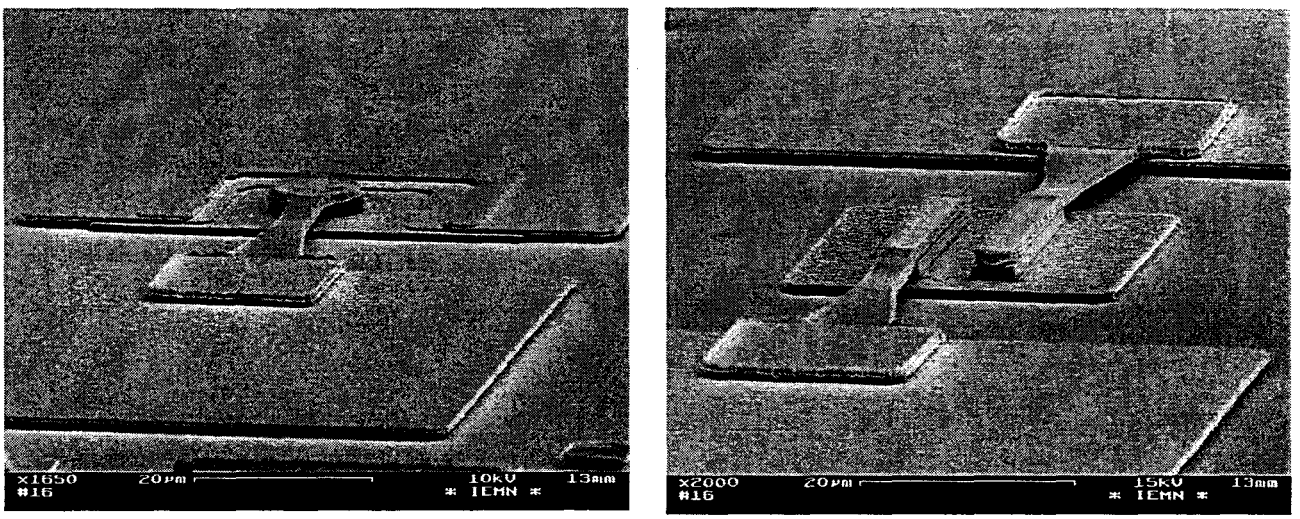

Figure 2.14: SEM views of single (a.) and series connected DHBVs (b.) for a tripler application.

Before reporting the results in connection with EM analysis, it seems interesting to give some informations about the optimum source and load impedances based on Harmonic Balance simulations.

2.3 Harmonic Balance simulation of HBVs for a tripler to 250 GHz.

Harmonic Balance calculations based on MDS code have been carried out in our group by R. Havart, in order to optimize impedances and efficiency of the tripler, and on the basis of the circuit presented in Figure 2.15. Parametric studies were conducted as a function of area and systematically

compared to the results computed at the same time in the University of Chalmers with a home made code [Havart97,Dillner97].

The main requirement concerns the target output power of 5 mW with a 5 % efficiency. Besides this, the available power delivered by solid state source has to be considered. In this sense, an order of magnitude of 100 mW can be reasonable for Gunn devices, the preferred option so far. In this context, and with the goal of taking benefit of the device voltage handling, it appears that a 50 μm^2 device satisfies these criteria.

Another important issue is the role played by the pad to pad capacitance, whose values can become comparable to those of the intrinsic capacitance. An intuitive reaction is to think that as a consequence of this high value, the overall capacitance modulation is degraded and so is the performance. In order to demonstrate that this is not the case, and provided that the extrinsic elements are only reactive, we have compared the HB simulation results in two cases. The results are given in Table 2.1 and present output power, efficiency and optimum source and load impedances for a DHBV with a 50 μm^2 section, in a single diode configuration The extrinsic elements chosen in these simulations were measured in a CPW configuration and hence do not reflect exactly the airbridge and pad contributions. Nevertheless, these values are representative of what could be expected in a planar technology.

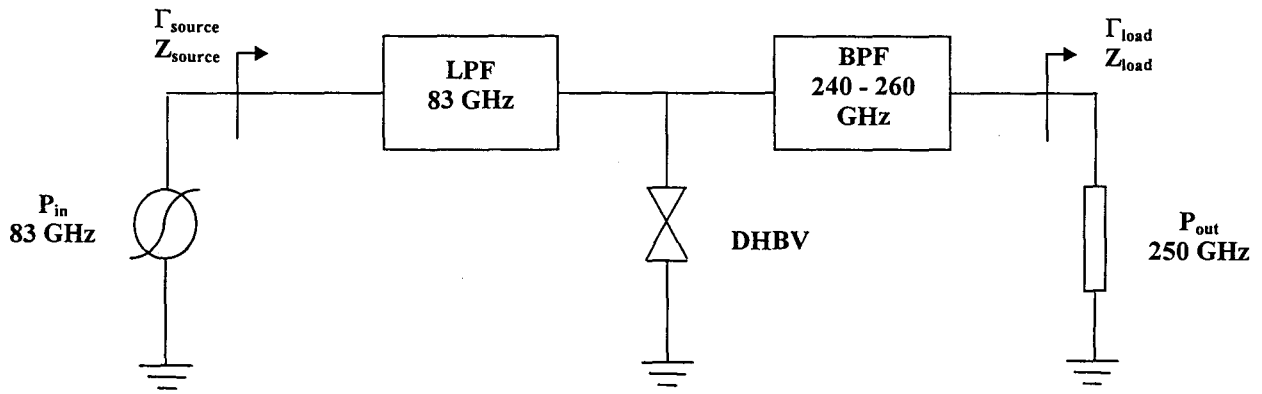

Figure 2.15: HB model for simulating the tripler performance of a DHBV.

$S = 50\ \mu m^2$ $R_s = 10\ \Omega$	P_{in} (mW)	η (%)	P_{out} (mW)	Z_{load} (Ω)	Z_{source} (Ω)
only intrinsic elements	87.8	**22.2**	**19.5**	19 + j 38	15.1 - j 90.6
with extrinsic elements (L_f = 75 pH, C_p= 17 fF)	85.6	**21.9**	**18.7**	19 + j 72	7 - j 36.9

$S = 50\ \mu m^2$ $R_s = 3\ \Omega$	P_{in} (mW)	η (%)	P_{out} (mW)	Z_{load} (Ω)	Z_{source} (Ω)
only intrinsic elements	51.9	**58.6**	**30.4**	16 + j 38	9.85 - j 88.5

Table 2.1: Harmonic Balance results for a 50 μm^2 DHBV.

These results are optimized in order to obtain a maximum efficiency with a voltage sweep across the non-linear capacitance of 12 V. In the first line, results for the intrinsic device (R_s = 10 Ω plus C_d) are given, while the second line displays results when parasitic elements are included. As a

first remark, for the $R_s = 10\ \Omega$ case, output power P_{out} is in the order of 19 mW, with an efficiency η in excess of 20%. It is to remember that these results are calculated for optimum matching at the input as well as at the output. Power levels and efficiency do not differ dramatically from one configuration to the other, but optimum impedances do change if extrinsic elements are included in the simulation or not. Therefore, it seems more useful to focus on the intrinsic elements and to incorporate the interconnecting and access elements in the environment of the diode.

Also, results for a 3 Ω series resistance intrinsic device are displayed, showing a much higher efficiency, close to 60% and an output power of about 30 mW. This comparison between 10 and 3 Ω is a striking demonstration of the dramatic influence of the series resistance.

These results do not take into account the environment losses, and in particular losses due to metallic pads and microstrip sections or the backshorts employed to match these calculated optimum impedances, but we will come back in the following about these questions.

2.4 EM simulation of the extrinsic elements.

2.4.1 General considerations on active devices modeling.

When one tries to simulate the performance in terms of harmonic power generation for a varactor diode in a waveguide, it appears necessary to carry out electromagnetic simulations of the whole structure because of the complexity of the system and the number of relevant parameters. Analytical methods suffer from a lack of versatility to really take into account every element in the real mount. An elegant approach to model the impedance seen by a diode inserted in a waveguide on top of a post was yet published in the seventies by Eisenhart and Khan, [Eisenhart71]. The diode and the connecting elements, in this case a whisker/post contact, are described by means of lumped inductive and capacitive elements, with a global impedance determined by the backshort position. Such a simplified environment can be considered in a first approximation. However in our case, the GaAs diode chip is soldered to the part of microstrip filter structure extending into the output waveguide. By this means isolation between input and output waveguides is achieved, besides mechanical robustness of the structure as it would be required for space borne systems.

We thus have to analyze the problem of a diode chip within the multiplier block focusing on the electromagnetic aspects, in the context of technological restrictions and harmonic balance results, previously outlined. This research was carried out through the use of HP HFSS™ (High Frequency Structure Simulator) a powerful software package from Hewlett-Packard. HFSS performs a Finite Element Method (FEM) full-wave analysis for calculating the field distribution and the S-parameters of passive, high frequency 3-dimensional structures. It has been the basic simulation tool of this work (please refer to appendix A for further details on the software package).

Ideally, we have to simulate the device in its three dimensional environment with a self-consistent treatment of electromagnetic couplings (EM analysis) and voltage waveforms across the device under large signal conditions (HB analysis). To our knowledge, each issue was addressed separately up to now and it seems difficult to consider such a global problem. Our contribution is based on the combination of EM analysis and network analysis with the link between both being the S-matrix of each element. As noted before, HFSS cannot take into account active devices, hence the first stage is to succeed to locally introduce the influence of the device. For this purpose, we will compare with measurements, from coaxial-like and CPW-type configurations, whenever it will be possible.

With the tools available so far, and based on the work of Tuovinen, [Tuovinen95], two solutions have been analyzed to simulate an active device within its environment:

1.- Introduce a small coaxial probe at the diode location, in a similar way to that which would be done in scale model measurements.

2.- Consider the non-linear diode as a quasi-lumped lossy capacitor, having a resistance and a reactance equivalent to the diode impedance at the frequency of the analysis.

In both cases, a model for the diode itself has to be developed in parallel to the EM analysis. In our case, the intrinsic parameters of the diode have been obtained from measurements carried out on the devices of the first mask set and, for the optimum source and load impedances, HB analysis is used. For the first alternative, the coaxial probe approach is based on scale model measurements, in which impedance is assessed with the use of a scaled prototype of the multiplier block. This is a widespread technique able to predict the performance of complex high frequency systems, and it has been employed at the Ecole Normale Supérieure on a 51:1 model of a tripler mount. In this case, all the geometric dimensions of the model are increased by a factor 51, while the measurement frequency is reduced according to the same ratio. The impedance seen by the device can be assessed by this means, with complementary information from HB (source and load optimum impedances) to improve the circuit performance. The fact of using coaxial transmission lines in the simulation to probe the impedance at the diode location is based on the same idea, except that no scaling of the geometry is done. Figure 2.16 shows the location of the probe in an airbridge structure. The inner conductor of the probe extends to the airbridge section on top of the cap ohmic contact and the outer conductor lies on the side ohmic contact. A port is considered at the coaxial flange to obtain a generalized scattering matrix, normalized to the coaxial impedance.

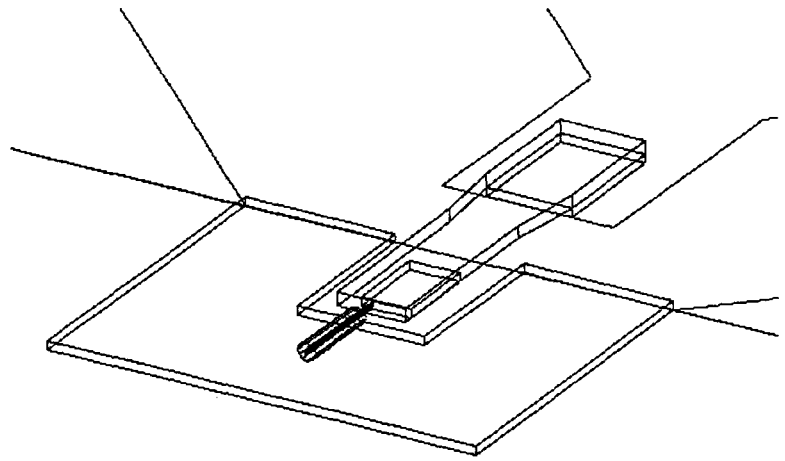

Figure 2.16: Small coaxial transmission line to probe the impedance at the diode location.

Instead of leading small probes to the diode locations, the impedance of the intrinsic diode might be considered at the diode location by means of a lossy capacitor. This can be realized in the full-wave analysis by considering a lossy dielectric, i.e. with a complex permittivity, in the volume occupied by the active epilayer:

$$\hat{\varepsilon} = (\varepsilon_r + j\varepsilon_i)\varepsilon_0$$

The series resistance and the capacitance of the active device can be modeled by using an equivalent RC circuit for the lossy capacitor with:

$$C_s = C_0 \frac{\varepsilon_r^{\,2} + \varepsilon_i^{\,2}}{\hat{\varepsilon}}$$

$$r_s = \frac{\varepsilon_i}{\omega C_0 (\varepsilon_r^{\,2} + \varepsilon_i^{\,2})}$$

where $C_0 = \varepsilon_0 A/d$, A is the area of the capacitor plates, d is the separation between the plates, and ω is the angular frequency. In our case, the area is that of the varactor diode and the separation is the thickness of the epitaxial layer.

Prior to choose one or the other solution, a number of important aspects have to be considered. The advantage of using lossy capacitors over the small probes is that physically the model corresponds better to a real diode. The fringing fields around the airbridge are supposed to be less perturbed than in the presence of a coaxial probe. Figure 2.17 shows a schematic of this configuration. However, the disadvantages of the lossy capacitor are two. First, the parameters for the complex permittivity of the dielectric material include frequency, which means that at every frequency the model has to be changed according to this dependence, hence there is a lack of flexibility in performing frequency sweeps. Second, as we pointed in previous sections, the most important term in the series resistance of the device is the spreading resistance, which corresponds to the contribution of the n^+ buried layer. The lossy capacitor model considers the resistance of the device included in the lossy dielectric, while the spreading resistance is the major contribution. In [Tuovinen95], this problem is alleviated by considering the thickness of the epitaxial layer twice the real value, and this modifies too the geometry in the close vicinity of the device.

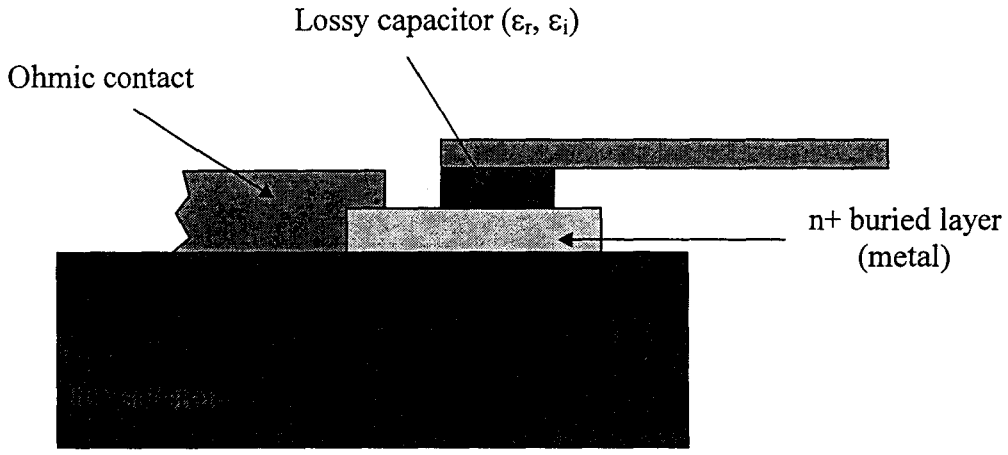

Figure 2.17: Cross section of the structure modeled as a lossy capacitor.

The preferred approach has been the use of a small coaxial probe at the diode location, owing to the flexibility in performing frequency dependent analysis and the possibility of directly transferring the results from EM simulations to a circuit solver, where the diode can be modeled with a non linear behavior. The results are the S-parameters measured with the small probe at the diode location, and normalized to the coaxial line impedance. By this means, a model for the diode,

as well as for the tunable backshorts can be added in a later stage, and thus evaluated in the circuit environment, with the consequent benefit in time saving for the simulations.

2.4.2 Simulation of the CPW mask set and validation of the method.

We pointed out in section 2.2.2, when detailing the CPW access mask set, that the measurements done with this type of structure integrate different effects, notably the influence of the access pads length. The first effort in modeling the structure was to determine the influence of these pads prior to model the whole structure, with the device contacted through an airbridge.

A first approach to this problem has been done taking advantage of several test samples of the second mask set prior to the airbridge formation, with a process including only levels 1 to 4. This structure is designed on a 400 μm thick InP (ε_r = 13) substrate. A schematic of this geometry is given in Figure 2.18, together with a comparison of the measured and calculated reflection losses of the structure.

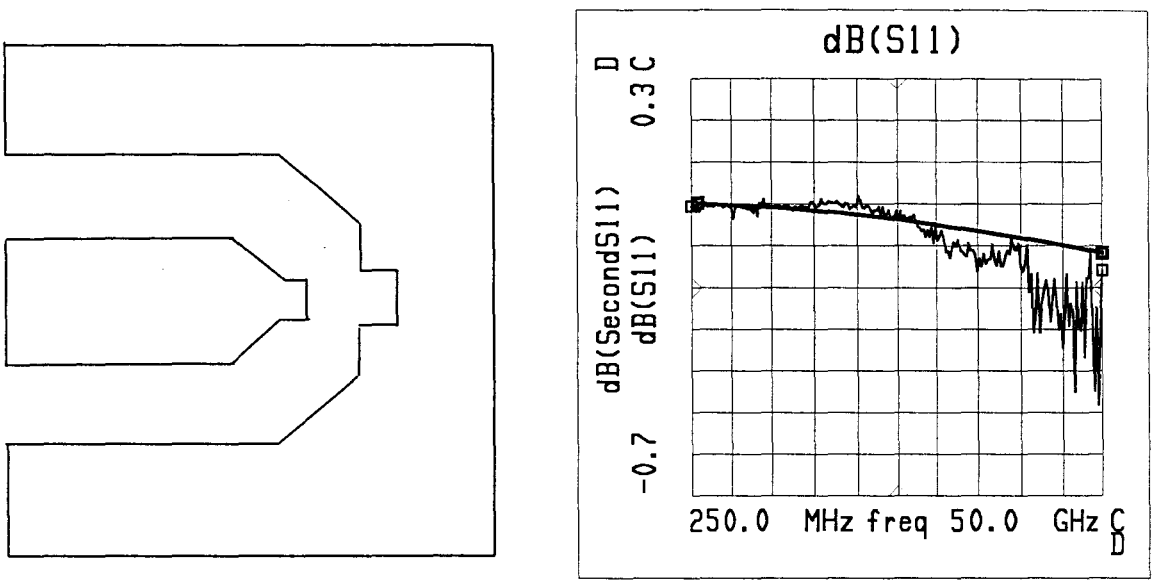

Figure 2.18: Second mask set access pads, schematics and comparison of the simulated and measured reflection loss.

Comparison between measured and simulated characteristics shows good agreement, from dc to 50 GHz. Let us note the reduced scale of 1 dB in the vertical axis. In fact, we are measuring almost an open circuit, with very high reflection loss, but at the same time, there is also a capacitance term that shunts the access pads, and subsequently will shunt the active device, after the airbridge formation. The importance of this effect will, in principle, increase with frequency. To confirm this behavior a study of the shunt capacitance has been done showing that, in this frequency range, an increase the length of the pads, tends to increase the capacitance between them. This has been checked by performing simulations on the structures of Figure 2.18, varying the access length L (see Figure 2.19).

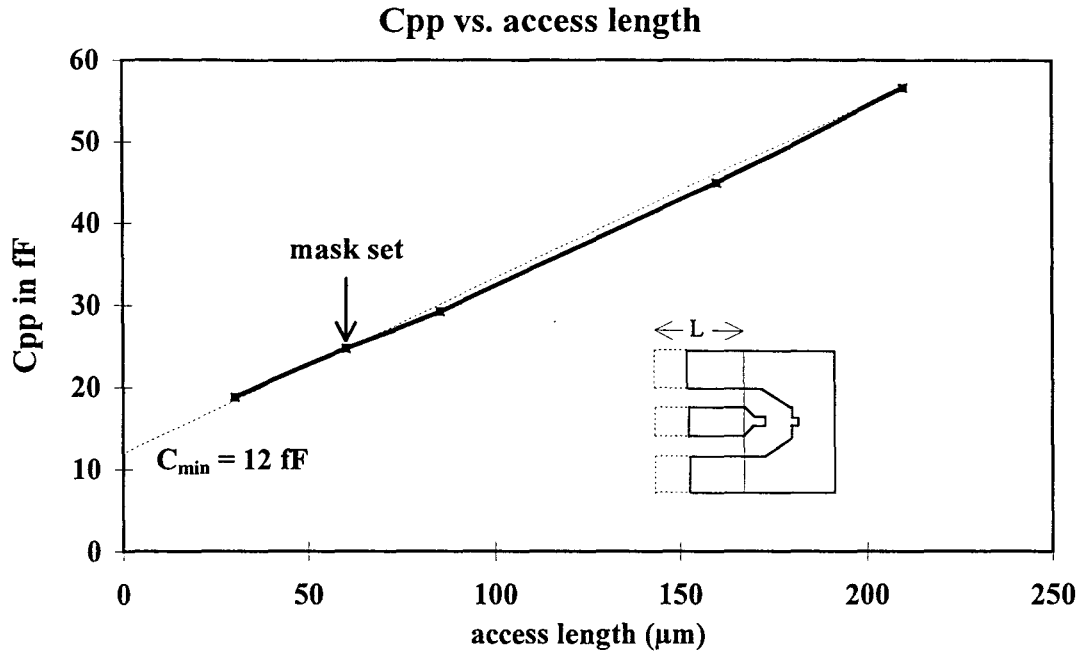

Figure 2.19: Evolution of the shunt capacitance of a CPW access line as a function of the pad length.

Figure 2.19 shows that the evolution of the pad to pad capacitance as a function of the pad length is almost linear. If length L tends towards zero, the limit value for the capacitance would be C_{pp} = 12 fF, thus only considering the tapered transition on which the airbridge pillar would be formed. It is demonstrated that this value compares to the intrinsic capacitance of the device, because for a DHBV with a surface S = 50 µm^2, we have C_d = 50 fF (C_{norm} = 1 fF/µm^2). According to Figure 2.19, an increase of 25 µm in the pads length gives an increase of the capacitance of C_{eq} = 5 fF. The high limit value calculated for the 'zero' access line, has to be put back in context after the airbridge formation. The EM problem is qualitatively different, because the RF signal will tend to reach to ground plane, in this instance, through the airbridge. The E-field will be much concentrated in the vicinity of the airbridge than around the edge of the hot line, creating a problem conceptually different.

Also, a complementary study has been undertaken for a strip configuration, with two microstrip pads facing each other. This configuration is closer to the third mask set structures, but with the difference of a ground plane on the bottom of the substrate. Figure 2.20 shows the equivalent circuit obtained for the simulated pads. Here, the substrate thickness is 100 µm, close to the aimed thickness for the chip inserted in the cross waveguide system. The length separating the pads is varying and, for example, we obtain a parasitic capacitance of C_{pp} = 1.5 fF, for a separation of L = 50 µm (corresponding to the mask set separation for series connected diodes). Even if this configuration of the pads is not directly comparable to that of the final mount, because of the ground plane, we can observe a great decrease of this parasitic element with respect to the CPW configuration. This comparison points out that the equivalent circuit of any discontinuity is strongly dependent on the exact parameters used in the analysis. In other words, results for one type of technology cannot be extrapolated to another.

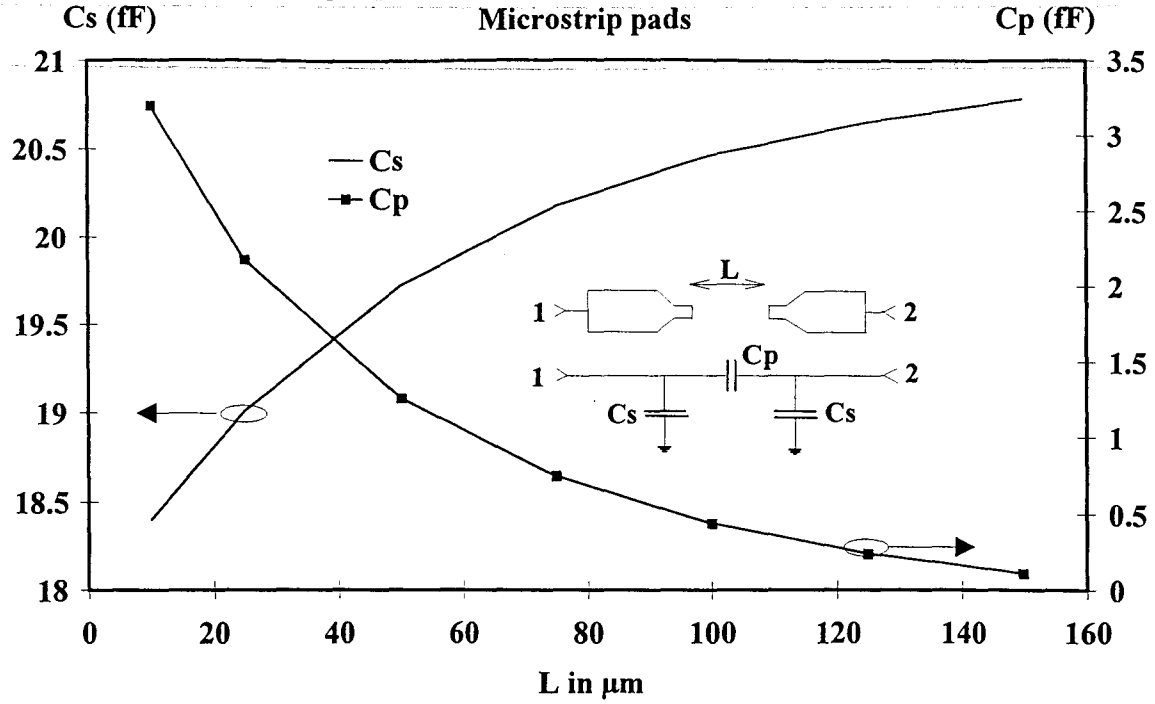

Figure 2.20: Evolution of the equivalent circuit capacitances versus separation for microstrip pads.

Several devices on CPW configuration have been analyzed combining results from full-wave analysis and from circuit analysis. The RF characteristics of these devices have been measured from dc up to 110 GHz, for different active areas and bias voltages. The schematic of the simulated design is illustrated in Figure 2.21. The primary goal of this analysis is to describe the environment of the device, and in particular the extrinsic elements of the device. The intrinsic elements of the varactor (series resistance R_s and junction capacitance C_d), were already known from measurements performed on the first mask set batch (coaxial-type). The CPW access has been simulated for different diode areas (4 x 4, 6 x 10 and 11 x 11 μm^2) and for the rest of the embedding regions, exact geometrical mask set specifications are used. The contact pads, as well as the airbridge or the ohmic contact, are simulated as lossy conductors (σ = 4.1 10^7 $S.m^{-1}$). The volume occupied by the diode itself is assigned to be a lossless GaAs dielectric (ε_r = 12.9). Figure 2.21 shows the simulated structure, together with a close up on the diode region.

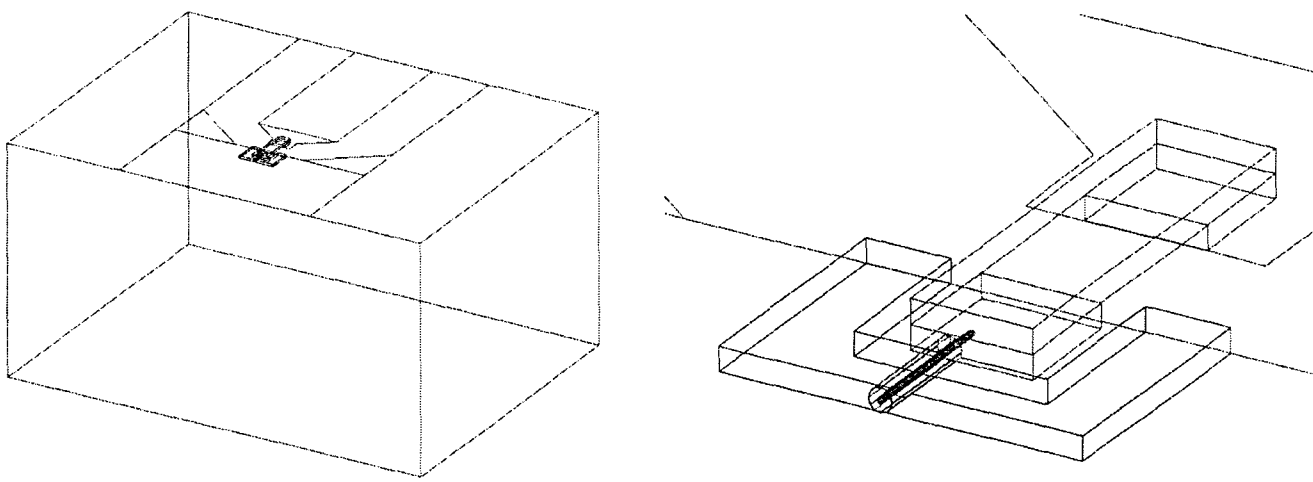

Figure 2.21: CPW simulated structure and vicinity of the active device.

The goal of this simulation procedure is to obtain the frequency dependent behavior of the environment to be able, in a later stage, to couple the non-linear behavior of the active device. This has been accomplished by creating an artificial port inside the structure at the diode plane, by means of the coaxial probe. The simulation domain has then two ports. The first one corresponds to the coplanar access line where the RF probes are directly laying, and the second port giving the impedance seen at the diode location. The result of the simulation is a 2 x 2 S-matrix. Figure 2.22 illustrates the circuit employed in MDS to implement impedance calculations of the complete structure.

The active device is here modeled as a RC circuit, in which a biasing dependence is applied to the capacitance C_d. For a sake of simplicity, C_d is has been defined with the following expression:

$$C(V) = C_{sat} + (k-1)\frac{hC_{sat}}{h+V^2}$$

where V is the bias voltage, C_{sat}, the minimum capacitance, k the capacitance ratio and h a fitting parameter depending on the area of the device. The parallel conductance, reflecting the parasitic conduction through the device, was neglected owing to the extremely low leakage current of the fabricated HBVs. A more accurate expression could have been chosen in order to model this $C_d(V)$ dependence, but comparison with measurements demonstrates good agreement, at least at low voltages (up to 4 V). For this run, the maximum value of the capacitance has been obtained from measurements of the first mask set devices to be C_{max} = 1.4 fF/μm^2 (normalized with respect to the area). The value of the series resistance has been chosen to be R_s = 2.5 Ω, according to spreading resistance measurements [Melique98].

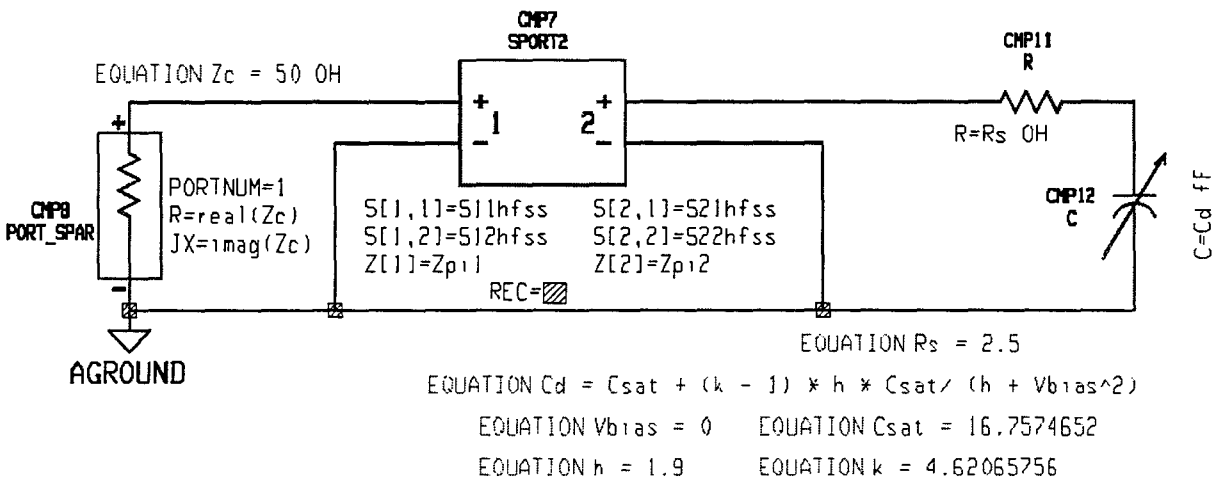

Figure 2.22: Circuit model in MDS modeling the impedance of a CPW structure.

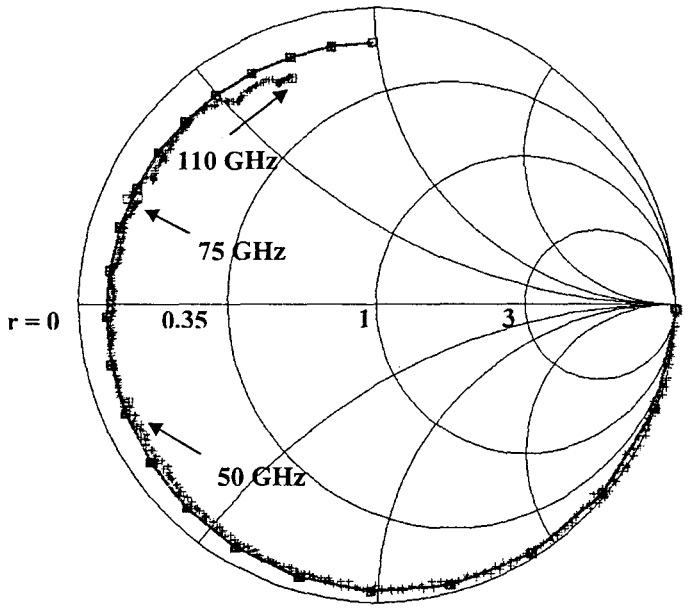

Figure 2.23: Comparison simulation/measurements for a 6 x 10 μm^2 DHBV, dc-110 GHz.

A device with a typical area of 6 x 10 μm^2 has been simulated and compared to the measurements obtained from dc to 110 GHz, see Figure 2.23. The Smith chart plot shows, overall, a good agreement, and in particular for the resonance frequency 65 GHz. The slight discrepancy at the higher frequencies might be explained on one hand from the fact that HFSS model simplifies the geometry of the structure and, on the other hand, because the measured resistance level changes (the locus of S_{11} no more describes a constant resistance circle). This can be due to the increasing importance of skin effect with frequency. If we plot, for the same device, the susceptance characteristics as a function of the bias voltage, see Figure 2.24, we can as well observe a good agreement, at least at low voltages.

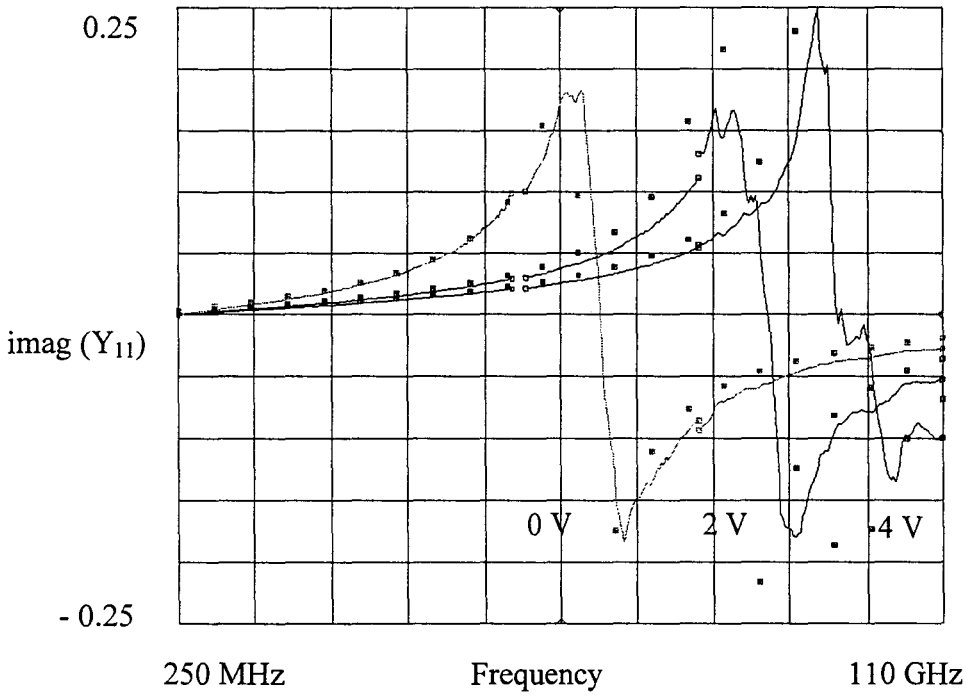

Figure 2.24: Comparison between simulated (□) and measured (-) susceptances as a function of frequency for different voltages.

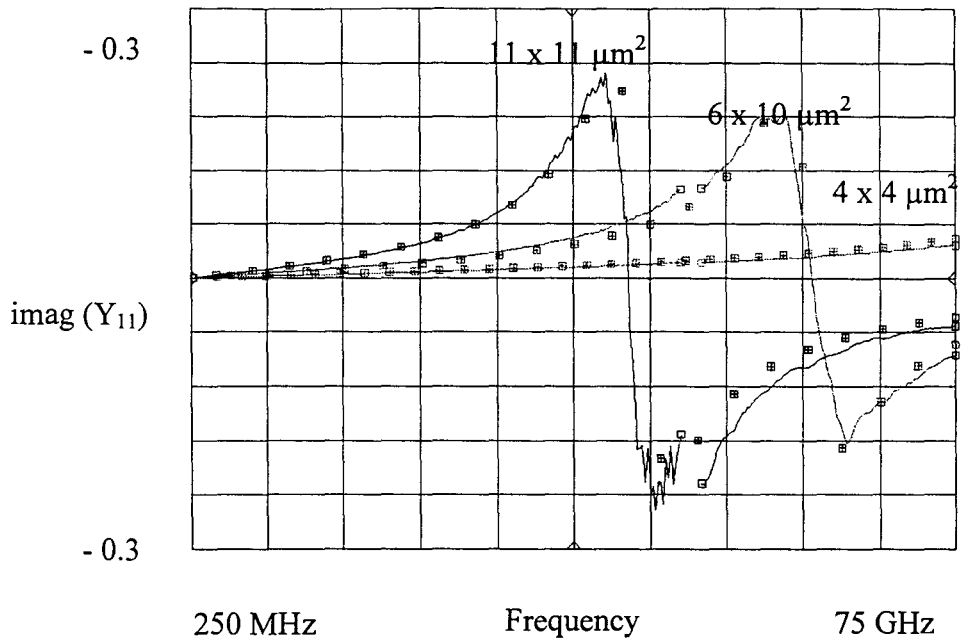

Figure 2.25: Comparison between simulated (□) and measured (-) as a function of frequency for different area devices.

Figure 2.25 shows the comparison between the measurements and simulation for devices with 4 x 4, 6 x 10 and 11 x 11 μm^2 sections. In general, the agreement is good up to 75 GHz, and only for the small area devices, simulations show less accuracy at frequencies above this range. This might be explained by the fact that for smaller the area of the device, the more complicated technology, and thus less accuracy in the process control. In any case, the area of the varactor does not have to be too small in a multiplier application, as we discussed in the previous sections, according to power handling and thermal considerations. Typically, the optimum area would be in the 50 - 60 μm^2 range.

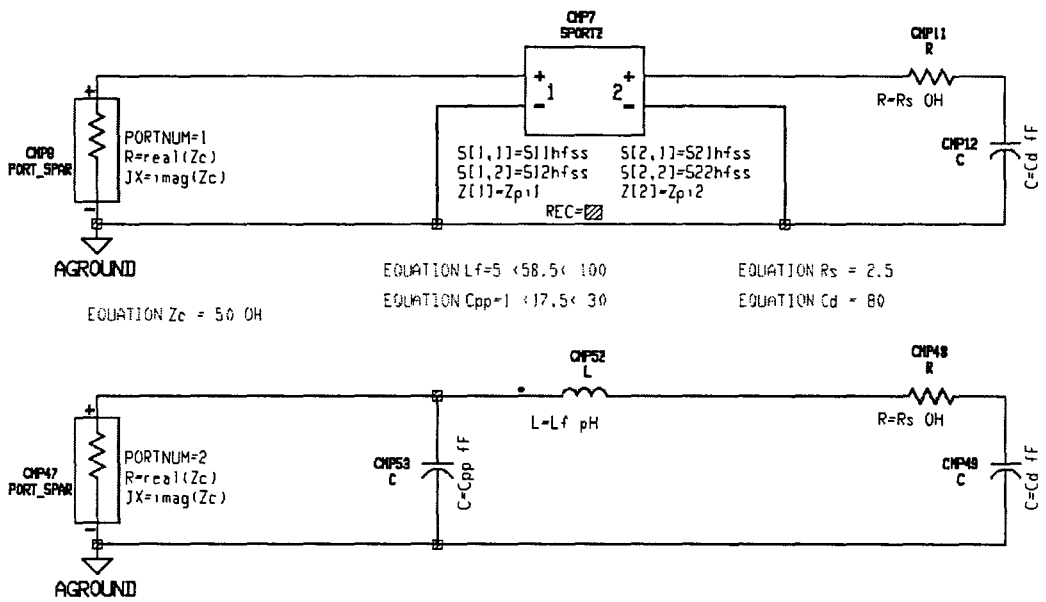

Figure 2.26: Circuit analysis comparing lumped elements versus full-wave analysis.

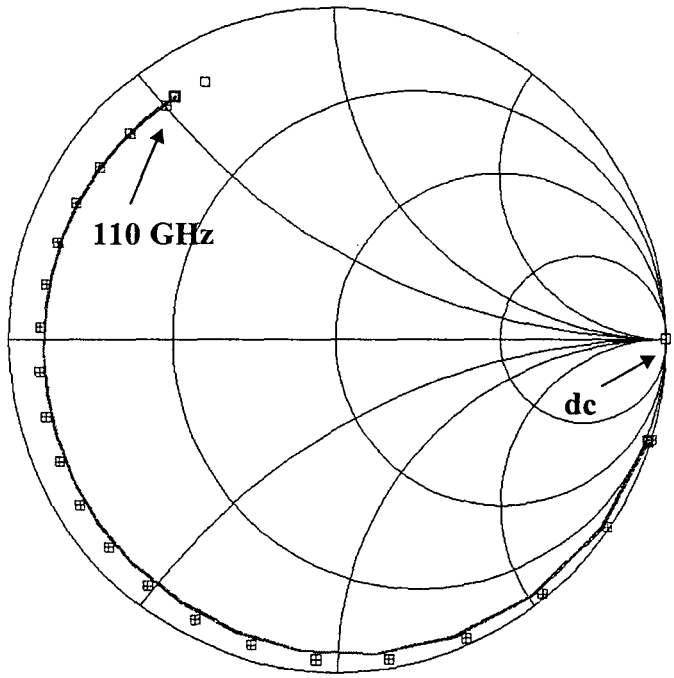

Figure 2.27: Comparison between lumped element equivalent circuit (□) and full -wave analysis results (-), as a function of frequency (6 x 10 μm^2).

As a final step in this analysis, a deembedding of the S-parameters has been done to obtain impedance information of the structure at a reference plane located close to the airbridge position. These S-parameters are obtained from the same simulation previously compared to the measurements applying simple deembedding transformation formulas based on the propagation constant of the CPW access line. This type of procedure, should give us the behavior of the free-standing structure and of the intrinsic diode, but free of any access transmission line effect. Figure 2.26 presents the compared circuits, with deembedded S-parameters for the top one, and equivalent lumped elements, which are to be determined, for the bottom one. These circuits represent a 6 x 10 μm^2 diode within its environment. Figure 2.27 shows the compared impedance locus on a Smith chart, with a slower variation, from dc to 110 GHz, due to the lack of the CPW lines. The values of L_f and C_{pp} are optimized in order to obtain the same input impedance for both circuits, and thus give L_f = 58.5 pH and C_{pp} = 17.5 fF. These values are very close to those fitted with a 'only lumped elements' equivalent circuit reported in [ESApr97], showing that for this simple configuration lumped equivalent circuits give a good approximation to the millimeter wave behavior of the structure. Nevertheless, a more complex structure like a crossed waveguide multiplier block cannot be analyzed with simple lumped elements at very high frequencies, where even a structure like the airbridge can be compared to a propagation line. In the following, and owing to the fact that a validation of this procedure has been done for a simple structure, EM full-wave analysis is applied to a multiplier cell.

2.4.3 Simulation of the multiplier mount.

As we stated above, the multiplier circuit analysis cannot be treated in a global approach. However, this problem can be overcome by dividing it into three separate tasks. These include EM simulations, (i) at 83 GHz, (ii) at 250 GHz and (iii) Harmonic Balance simulations for the non linear device. The input and output circuits are analyzed, at the input and output frequencies respectively, by means of HFSS simulations. The results in terms of impedance matching can be obtained adjusting the positions of each backshort in the block (four in our case). The simulated mount is adapted from an original design from Matra Marconi Space (Toulouse) in which two adjustable backshorts have been simulated at the input and output frequencies. This enables us to correctly match the impedances resulting from EM simulations to those obtained with HB as the optimum source and load impedances, with the expected drawback of the loss added by each one these backshorts. This is particularly critical at the output frequency, where an estimate of 1 dB loss can be predicted for each tuner.

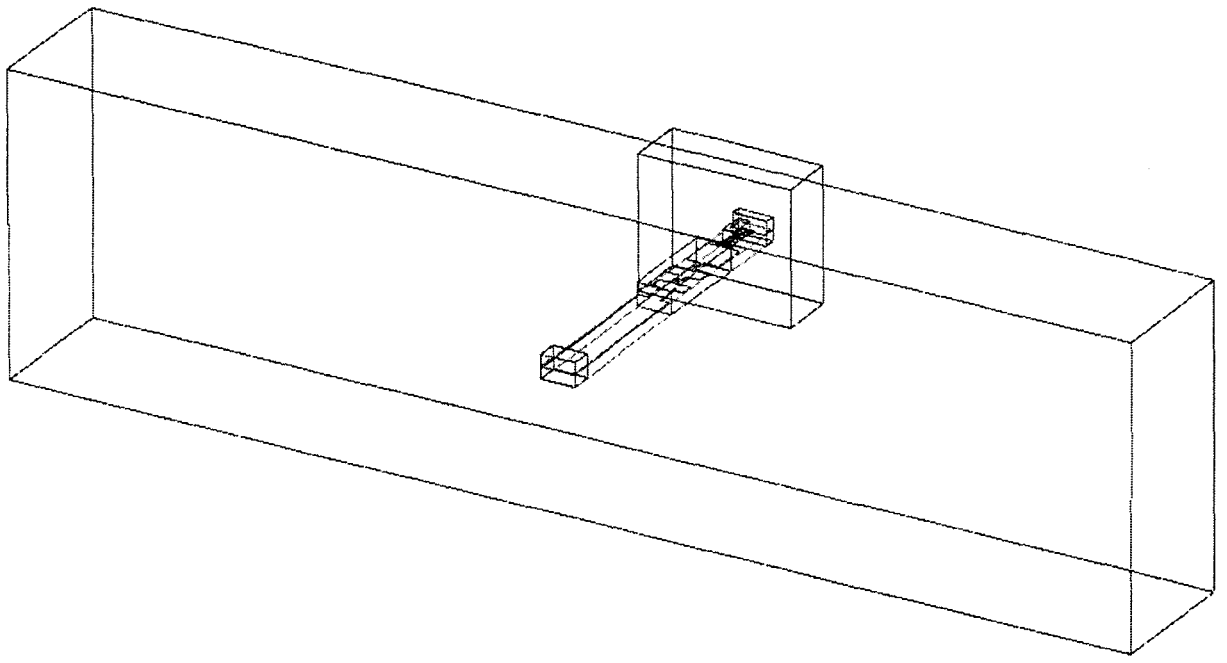

Figure 2.28: Schematic of the simulated multiplier block.

A schematic of the multiplier block is presented in Figure 2.28, with a typical crossed waveguide structure. The input waveguide (from left to right) is a WR 10, designed for W band, 75 - 110 GHz, with dimensions 2.54 x 1.27 mm^2. The output waveguide is a WR 4, for band 170 - 260 GHz, with dimensions, 1.3 x 0.51 mm^2, at the back of the graph. To connect both waveguides, an E-plane transition on quartz substrate is employed ($\varepsilon_r = 4$, thickness t = 100 μm). The design of this transition was provided by Matra Marconi.

The chip is mounted in a flip-chip configuration on the quartz substrate and inside the output waveguide. The third harmonic thus generated by the varactor will then be radiated directly to the output port, hence reducing losses. The chip is supposed to be soldered to the pads on quartz by means of two pads 10 μm thick and having the same area of the metallic pads on quartz.

2.4.3.1 Input circuit at 83 GHz.

At 83 GHz, the simulated structure corresponds exactly to the schematic of Figure 2.28, with the specifications reported on Figure 2.29, where the ports of the simulation are displayed. The simulated structure has three ports, the first two refer to waveguide ports and the third to the impedance probing at the diode location. Only a portion of the input waveguide is simulated extending far enough from the discontinuity created by the E-plane transition. At each end, there is a port located to obtain the S-parameters and then, in a later stage in MDS, connect circuit models for the stubs, which are clearly simpler and faster to optimize in a circuit environment [Jain97]. The output waveguide is under cut-off at the input frequency and acts as a filter for the fundamental frequency, so only a short and closed guide is simulated.

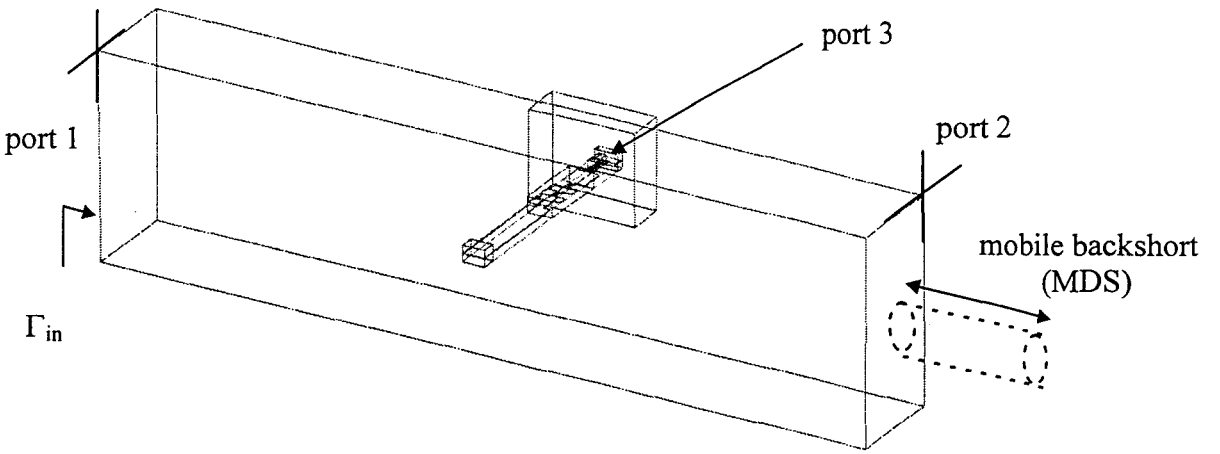

Figure 2.29: Multiplier mount simulated at the input frequency.

At first, we have analyzed the E-plane transition and the microstrip low-pass filter, to determine their characteristics in terms of equivalent impedance and insertion loss respectively. For the waveguide-to-microstrip transition, we analyzed the antenna portion loading the microstrip port with a matched impedance. The schematic of the simulated structure is depicted in Figure 2.30

.

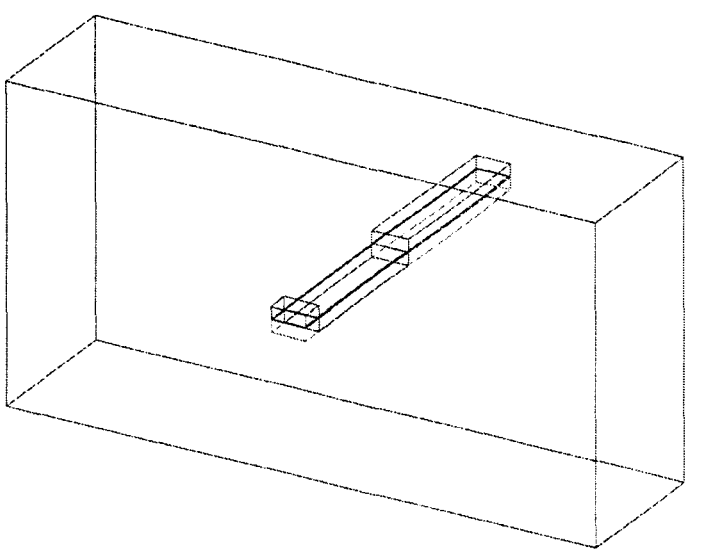

Figure 2.30: Simulated E-plane waveguide-to-microstrip transition.

Figure 2.31 shows the E-field pattern at the transition plane at 83 GHz in the doubly matched case, that is to say when ports 2 and 3 are matched respectively to the waveguide and microstrip characteristic impedances, and with the signal partly flowing to the microstrip port. When a backshort is located at port 2 an impedance matching might be achieved, to increase the coupling to the microstrip line.

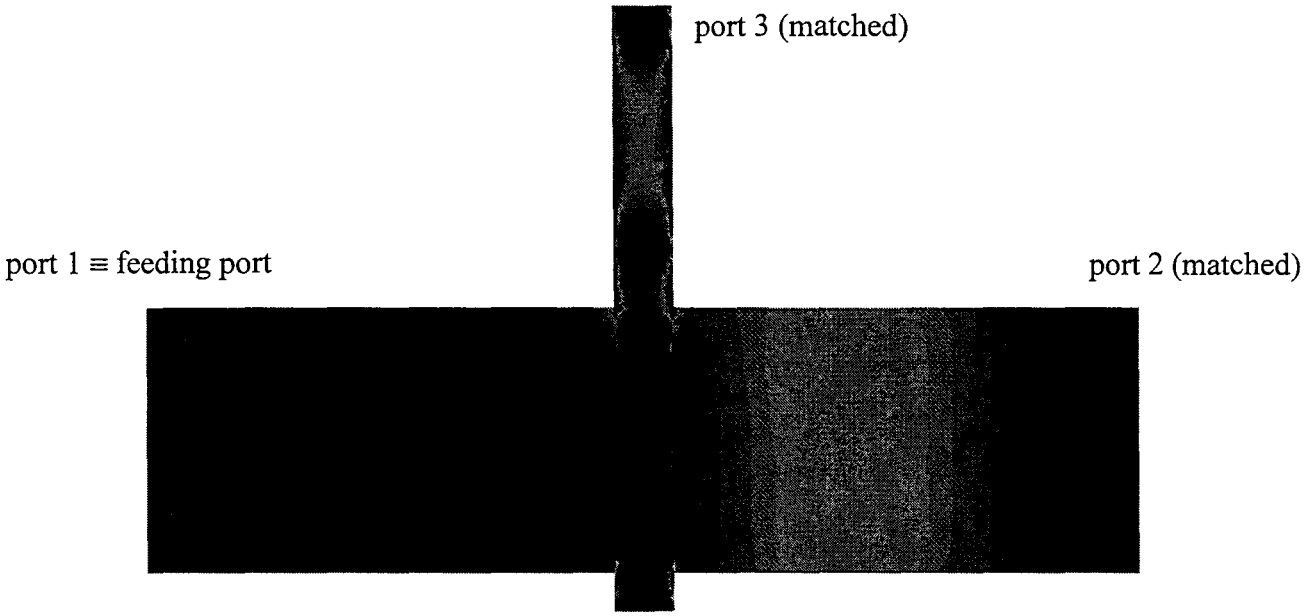

Figure 2.31: E-field pattern at the transition plane at 83 GHz in the doubly matched case.

The impedance of the E-plane transition as a function frequency in the doubly matched case is given in Figure 2.32, showing that near the pump frequency, it is close to the 50 Ω impedance of the microstrip circuit [Yassin96]. Figure 2.33 presents the evolution of the input impedance as a function of frequency, for the backshort at a $\lambda_g/4$ distance at 83 GHz. Finally the impedance dependence as function of the backshort length is given in Figure 2.34, for the input frequency 83 GHz.

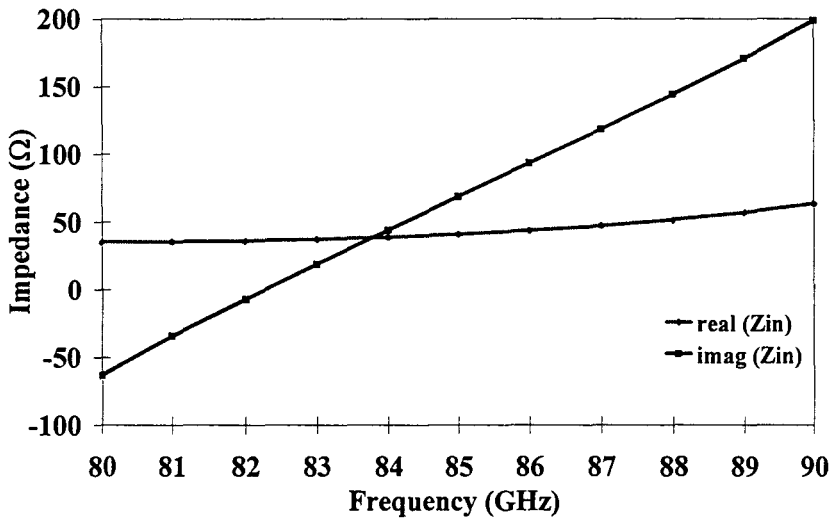

Figure 2.32: Impedance of the E-plane transition as a function of frequency in the doubly-matched case.

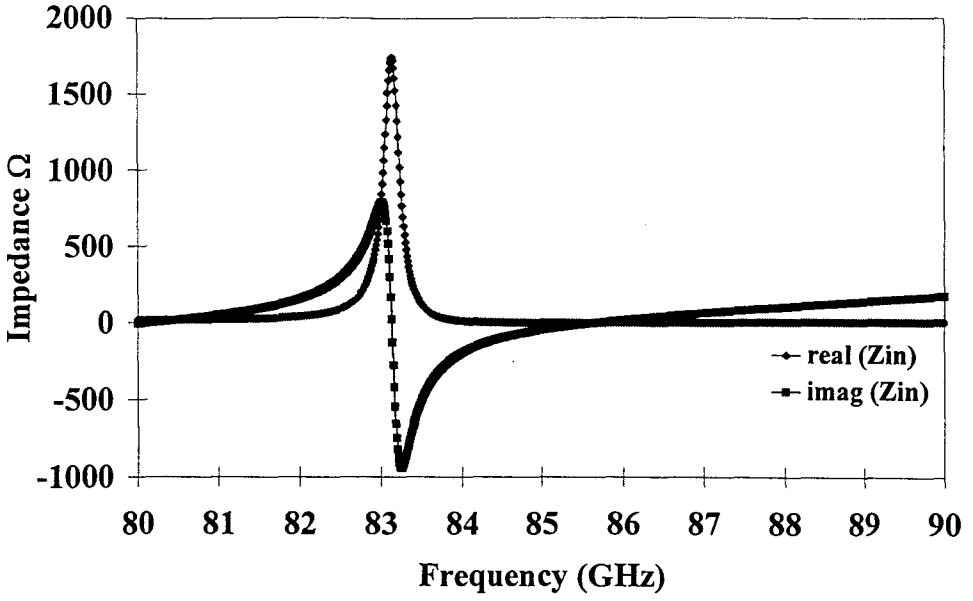

Figure 2.33: Impedance of the E-plane transition as a function of frequency in the presence of a backshort in port 2.

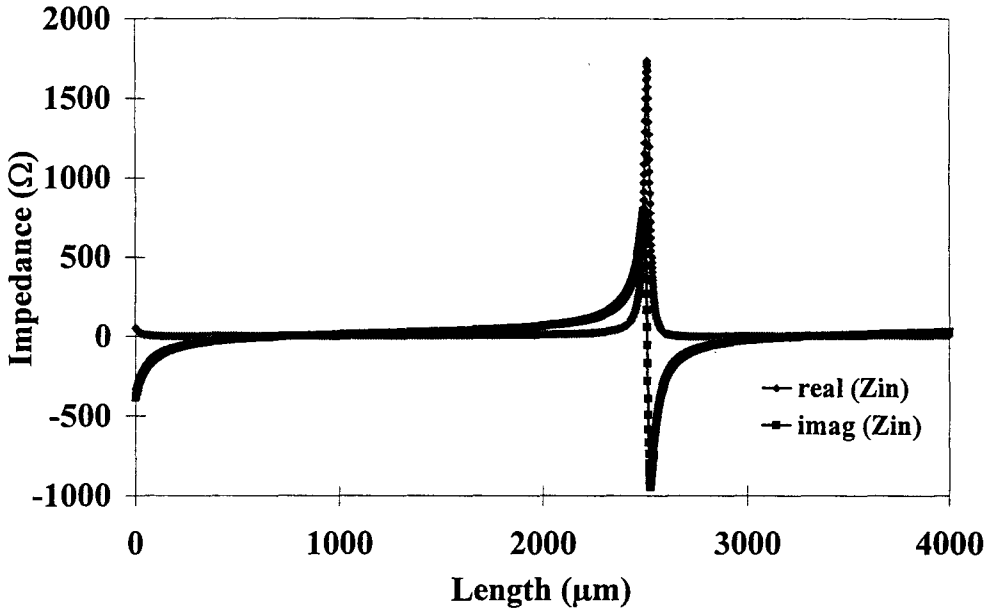

Figure 2.34: Impedance of the E-plane transition as a function of the backshort position at the input frequency.

The microstrip low pass filter is designed to prevent the generated harmonics to flow back into the input circuit. To check out this issue, a simulation of the filter portion has been carried out from 5 to 250 GHz. The results, given in Figure 2.35, show that, at the input frequency, an insertion loss of 1.4 dB can be estimated due to the ripple in the pass-band and to metallic losses. Also, it can be observed that the reflection loss at the output frequency is about 30 dB. From all this, we will consider in the following section, that for the output frequency no signal is reflected back to the input circuit, and thus the output circuit might be simplified to the output waveguide section with the chip mounted on the quartz support extending into it.

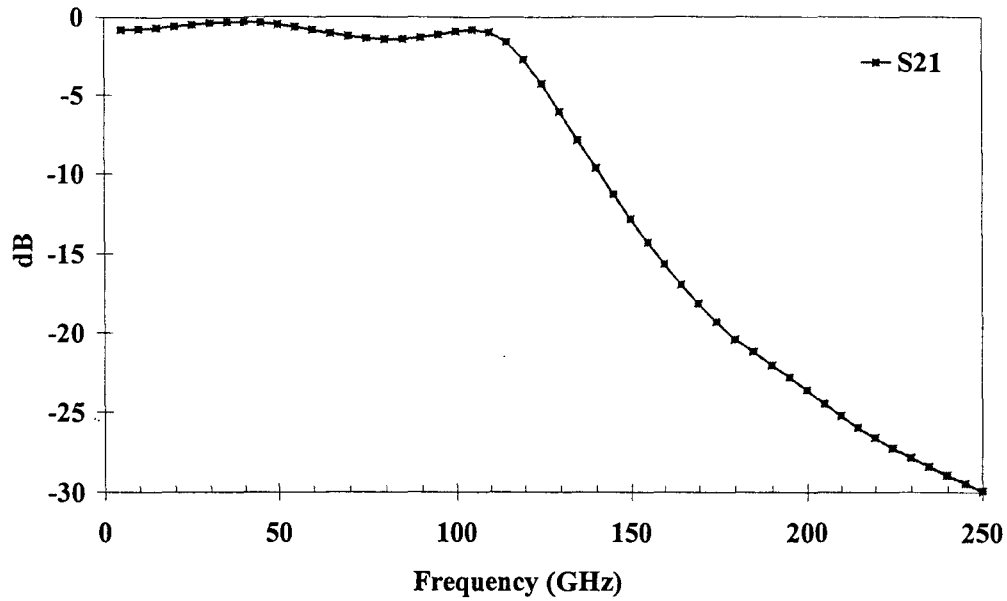

Figure 2.35: Insertion loss for the microstrip input filter.

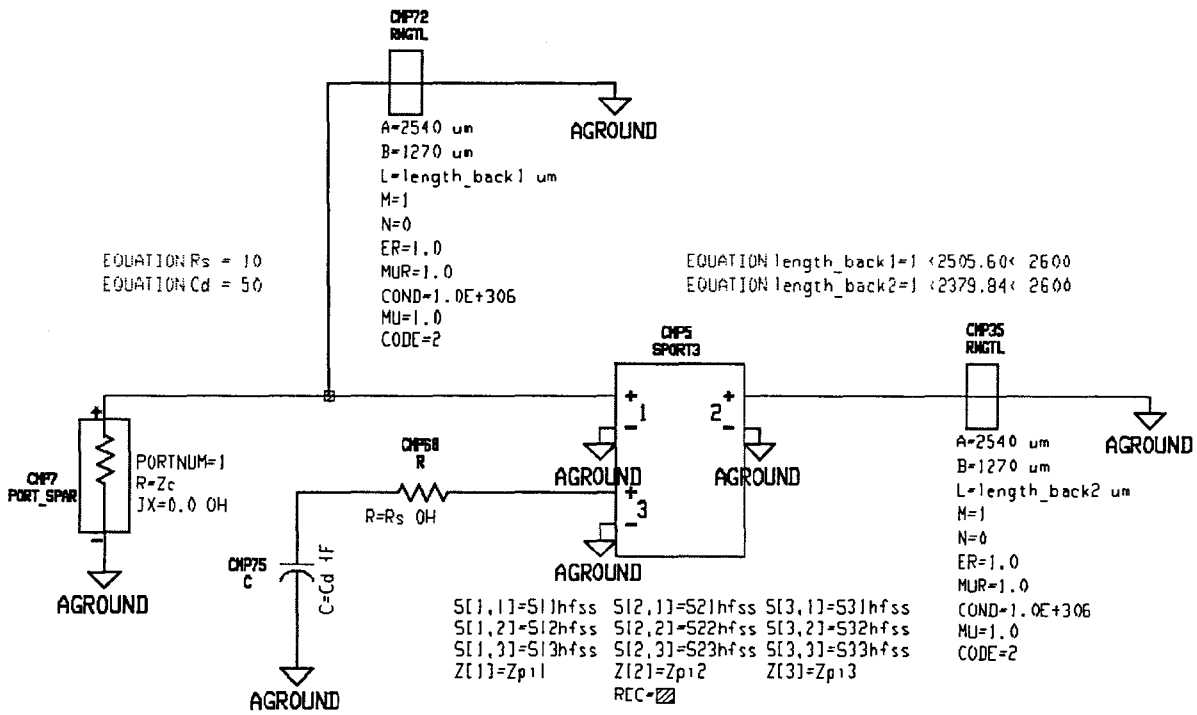

Figure 2.36: Input circuit model for impedance matching.

EM simulation results of the mount at the input frequency are now used to effectively match the input impedance to the optimum source impedance found with HB simulations. The S-parameters from full wave analysis are transferred through the use of a generalized scattering matrix with three ports. Ports 1 and 2 correspond to waveguide ports, whereas port 3 corresponds to the impedance seen at the diode location. The waveguide ports are loaded each with a short circuit in the circuit analysis, so that a double stub matching can be achieved. In a first analysis, they are considered ideal with no losses added at the input frequency, but this cannot be applied to the output circuit where each backshort may add significant loss. The third port is loaded with a simple model for the intrinsic device. In this case, and for a 4 x 12 μm^2 diode, values for R_s and C_d are 10 Ω and

50 fF, respectively. The described circuit is depicted in Figure 2.36, using the input waveguide impedance which was obtained from HFSS, as the reference impedance for the analysis.

The target of the analysis is to minimize the reflection loss from the analysis port of Figure 2.36. There is a couple of distances for the stubs that give, at the input reference plane the waveguide characteristic impedance, thus matching the circuit. This is demonstrated in Figure 2.37, where Z_{in} from the analysis is plotted as the impedance circles described by the reflection coefficient if one of the input stubs varies a half wavelength, while the length for the second stub is parametrized to three values, each separated with a 20 μm step. Half a wavelength in a stub describes a complete circle on the Smith Chart, and we can see that the trace of the intermediate circle goes over the center of the Smith Chart, hence achieving optimum matching, [Carbonell98].

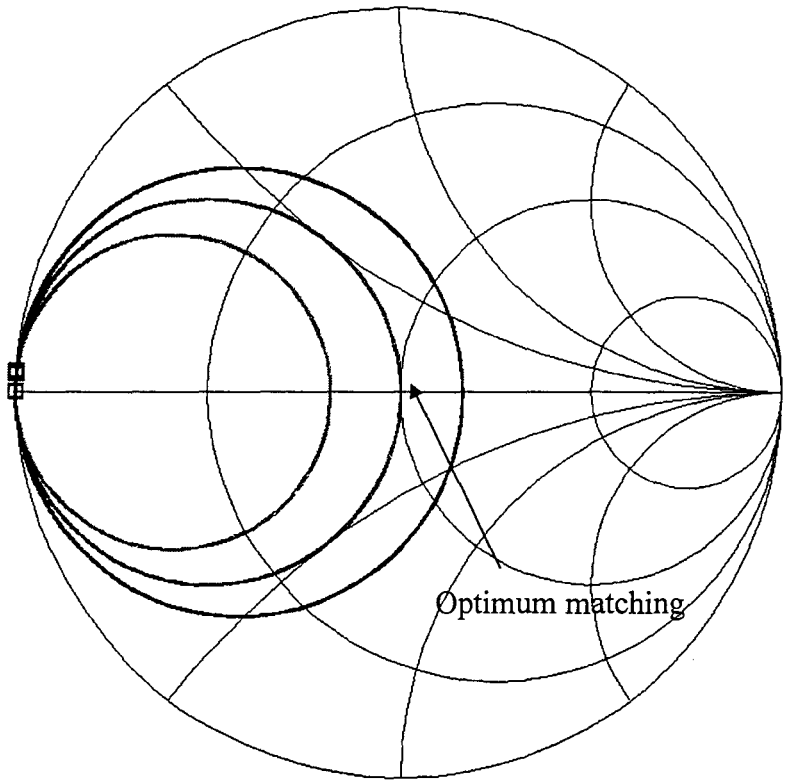

Figure 2.37: Impedance locus for Z_{source} with a double stub matching.

2.4.3.2 Output circuit at 250 GHz.

The simulation procedure to analyze the output circuit is similar to that employed in the previous section. Only a section of the block is simulated assuming that the microstrip filter isolates the input waveguide from the output signal. Figure 2.38 shows the analyzed structure.

At 250 GHz, the active device generates power through the harmonic conversion of the input signal. This generation is based on the non-linear behavior of the diode, and hence it cannot be treated with the FEM. Nevertheless, the use of full-wave analysis can be able to predict how this generated harmonic would propagate into the output waveguide and how the different elements in the mount can influence the generated output signal, with in particular the output matching issue. The 250 GHz signal is locally generated by the HBV, but it would rapidly propagate through the whole structure, metallic pads, airbridge, substrate, etc.

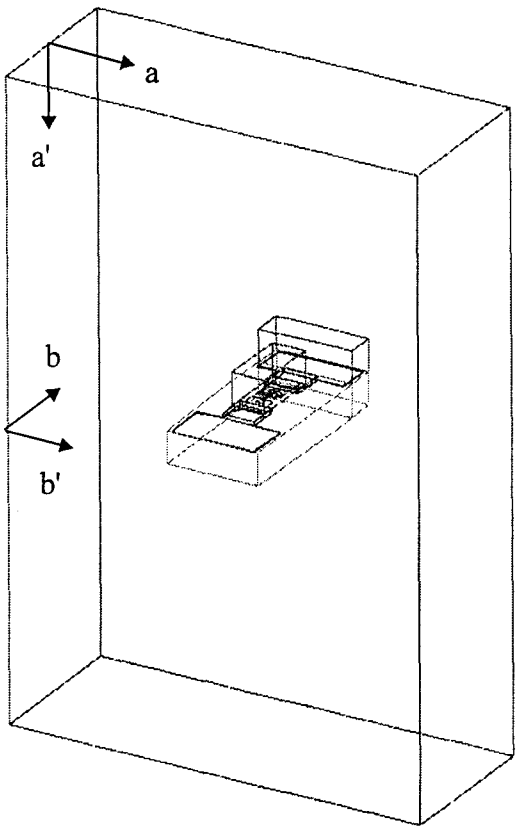

An evidence from EM analysis of the vicinity of the device is that every element in the simulation interacts with the signal and modifies E-field patterns. This is particularly true for access and metallic pads, which act as antennas inside the waveguide. It is also verified for the substrate, because at the air/substrate interfaces there are strong reflection/radiation mechanisms. The substrate thinning process is critical in this sense to avoid trapped waves resulting in a poor performance of the system. As it was mentioned in [Eisenhart71], the relative position of the device inside the waveguide changes the impedance presented to its terminals. Moreover, the interaction of the E-field TE_{10} mode with every element in the waveguide generates high order modes that are evanescent in the close environment of the chip. These modes can store reactive energy that would not flow to the output load. These effects are illustrated in Figures 2.39 and 2.40, showing on one hand how the TE_{10} mode is formed near the chip mount (aa' plane) and also, the complex E-field pattern on a transverse plane (bb') including the active device.

Figure 2.38: Simplified output structure for EM analysis.

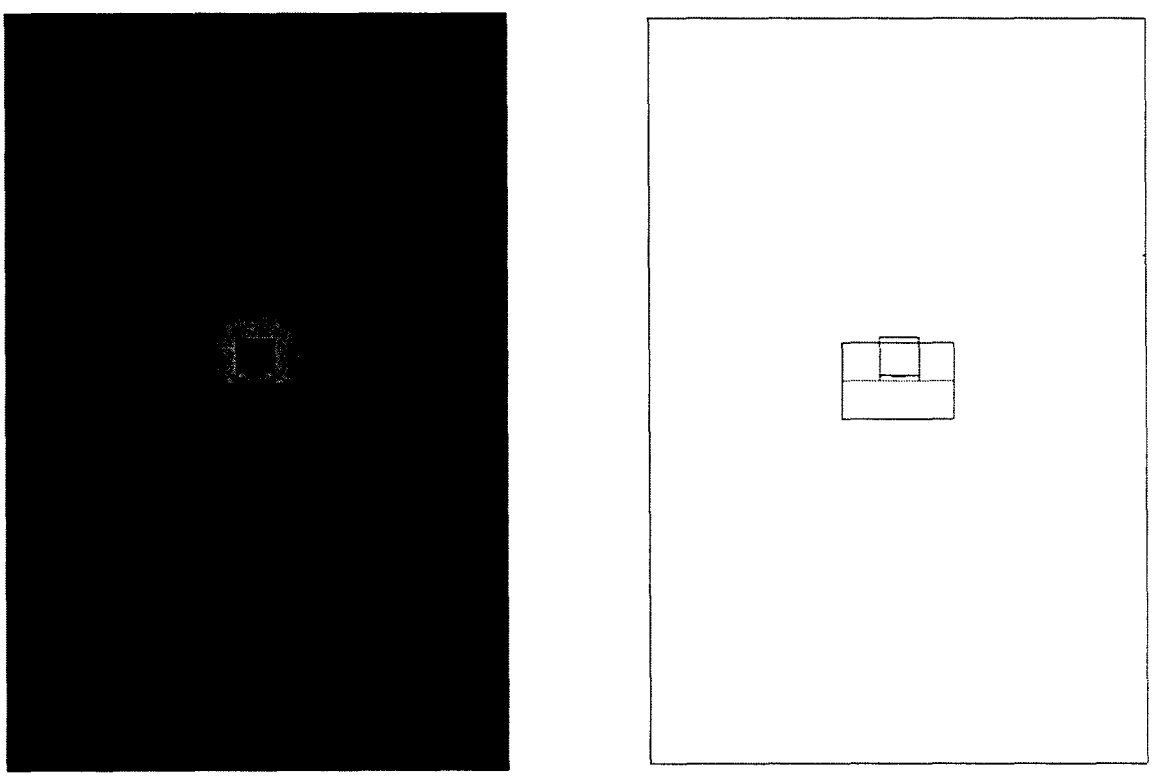

Figure 2.35: TE_{10} mode generated in the output waveguide (aa' plane).

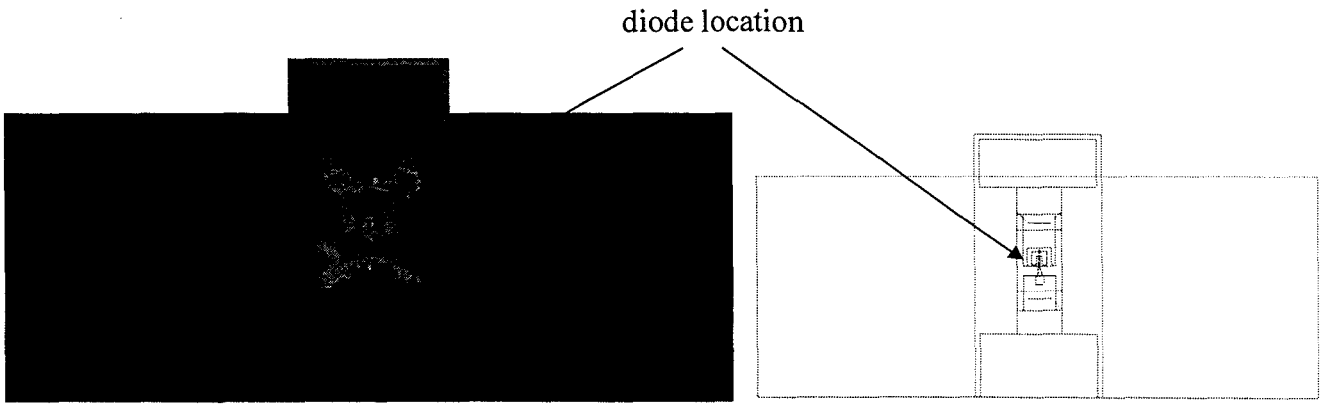

Figure 2.40: E-field pattern on a horizontal transverse plane (bb').

In Figure 2.40, the diode location is clearly seen at the plot center as well as the contours of the metallic pads. These concentrate great E-field values, and thus act as antennas in the waveguide.

The S matrix obtained from full-wave analysis has three ports corresponding to waveguide ports (for the first two) and to the diode generating the harmonics (for the third). These results are now transferred to the circuit simulator to optimally match the circuit according to the value calculated for Z_{load} with HB simulations (Figure 2.41). We had $Z_{load} = 19 + j\,38$. Now, this optimum impedance has to be presented to the diode terminals to achieve matching, so the analysis is carried out from the reference plane of the device (which is actually the generator of the 250 GHz signal), here assessed by the use of the small probe. The circuit is similar to that of the input except for this last aspect (see Figure 2.36). Again the results on Smith Chart show that there is a couple of stub distances for which the optimum impedance can be obtained, Figure 2.42.

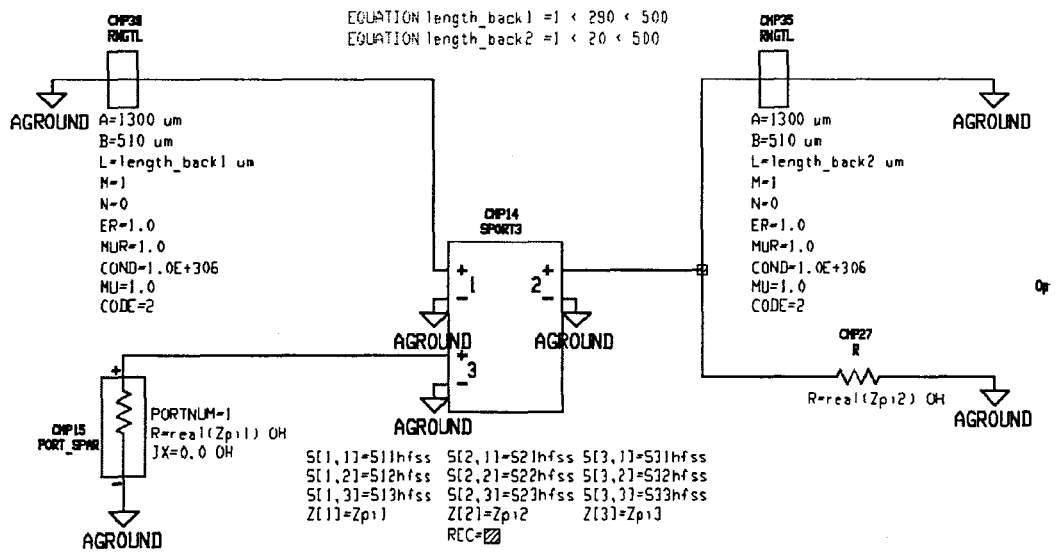

Figure 2.41: Impedance matching circuit for Z_{load} with double stub technique.

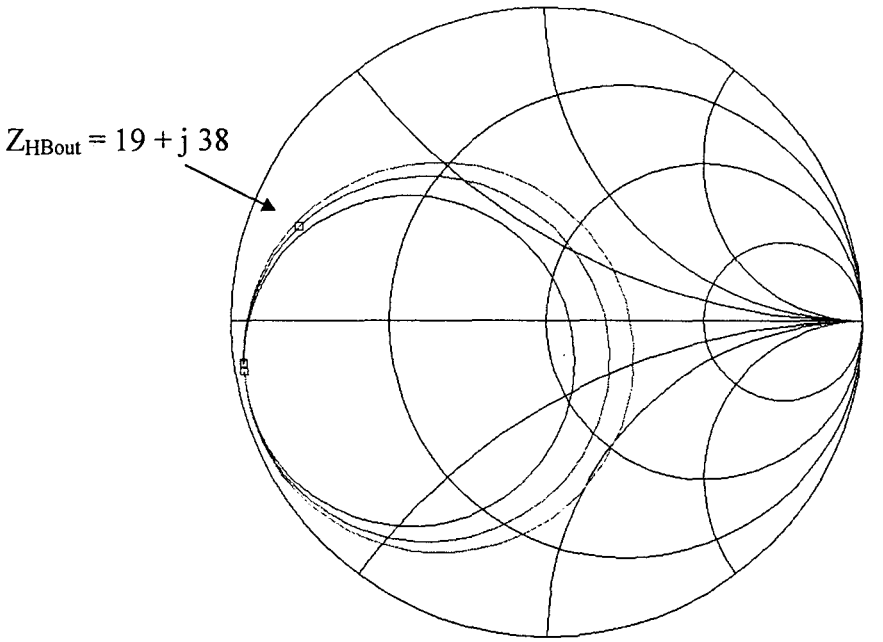

Figure 2.42: Impedance locus for Z_{load} with double stub matching.

The circles describe the length sweep of one of the output backshorts parametrized to three distances for the second output backshort. Nevertheless, it is a common option to use only one output backshort. This makes that the mount itself has to be re-designed (position of the chip in the waveguide, geometry, separation and width of the metallic pads, etc.) to achieve a reasonable matching. The tradeoff between matching losses or backshort losses makes that the use of two backshorts will provide a better matching, but with the drawback of twice the losses with respect to the single stub case. The previous analysis considered ideal backshorts synthesized with a length of waveguide terminated with an ideal short circuit. This model can be refined to take into account the losses present in a real block.

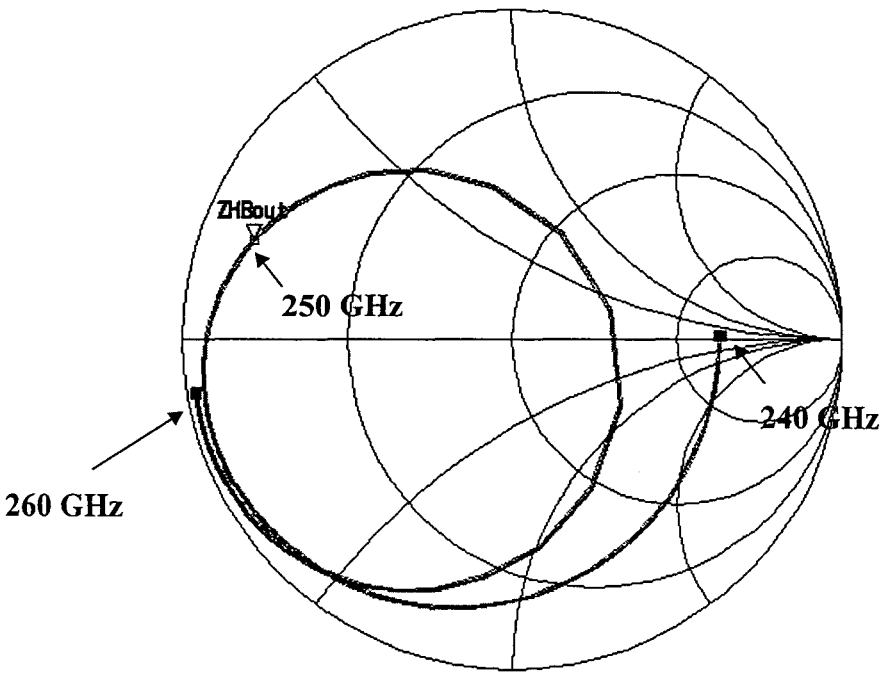

Figure 2.43: Output frequency dependence of Z_{load}.

As an example of the frequency dependence of the impedance matching, Figure 2.43 shows a Smith Chart plot with the Z_{load} variation with respect to the output frequency for fixed tuner positions. This extremely changing locus demonstrates that the bandwidth achieved with this procedure is quite narrow, and every selected pair of pump and harmonic frequencies requires different positions for the stubs.

2.5 Conclusion.

In this chapter, we have analyzed the Heterostructure Barrier Varactor and its applications in frequency multiplier circuits. Basic physics of the device has been reviewed outlining the main advantages afforded by this kind of device. The epitaxial structure, specially because of the possibility of stacking several devices, and the electrical characteristics, in terms of I_V and C_V make that the HBV has a strong non-linearity (a state of the art capacitance ratio 5:1 is reported) with a very low normalized capacitance, C_{norm} = 1 fF/μm^2 for the DHBV, and can also handle large amounts of power, with a breakdown voltage around 12 V for stacked varactors.

The devices have been fabricated, measured and simulated at the IEMN in different configurations, thus allowing a deep knowledge of all the relevant features to operate a frequency multiplier. Three technology mask sets have been developed with the aim of differentiating between the intrinsic behavior of the device and the technological parasitics or other elements in a large multiplier system. A procedure has been employed to characterize all these components by comparing simulated results with on-wafer measurements. Then an extension of the full wave analysis to a crossed waveguide mount has been proposed. Comparisons of simulated and measured S parameters show good agreement for a broad frequency range (dc up to 110 GHz) in the CPW case, and also for different biasing conditions. The analysis of the multiplier cell showed that two adjustable backshorts can provide optimum matching impedances both at the input and at the output circuits.

The coupling between different EM simulations to the non-linear behavior of the intrinsic device has been done through Harmonic Balance analysis, showing that great performance in terms of efficiency or output power should be obtained in practice for a tripler to 250 GHz.

The prospects for this work are the comparison of the simulated results to experiment in terms of efficiency and output power for the test structure. In particular, losses due to the tuning elements seem to be responsible for efficiency and output power degradation, as well as geometrical tolerances in the chip fabrication, the soldering procedure or the mount geometry.

REFERENCES CHAPTER 2:

[Bhaumik92] K. Bhaumik, B. Gelmont, R.J. Mattauch and M. Shur, *Series impedance of GaAs planar Schottky diodes operated to 500 GHz*, IEEE Transactions on Microwave Theory and Techniques, Vol. 40, No. 5, pp.880-885, May 1992.

[Carbonell96] J.Carbonell, E. Lheurette, P. Mounaix, R. Havart, F. Mollot and D. Lippens, *High power heterostructure barrier varactor for terahertz applications*, 6th European Heterostructure Technology Workshop, Lille (France), 16-17 September 1996.

[Carbonell98] J. Carbonell, R. Havart, P. Mounaix, O. Vanbésien, J.M. Goutoule and D. Lippens, *RF characterization and computer aided design of Heterostructure Barrier Varactors*, ESA Workshop on Millimeter Wave Technology and Applications, May 27-29, 1998,Espoo, Finland.

[Dickens67] L.E. Dickens, *Spreading resistance as a function of frequency*, IEEE Transactions on Microwave Theory and Techniques, Vol. 15, No. 2, pp.101-109, February 1967.

[Dillner97] L. Dillner, *Heterostructure barrier varactors*, Chalmers University of Technology, Technical Report No. 277L, 1997.

[Eisenhart71] R.L. Eisenhart and P.J. Khan, *Theoretical and experimental analysis of a waveguide mounting structure*, IEEE Transactions on Microwave Theory and Techniques, Vol. 19, No. 8, pp.706-719, August 1971.

[ESApr97] *Millimeter Wave Sounders Critical Technologies*, contract #9777 European Space Agency Progress Report, October 1997.

[Gupta79] K.C. Gupta, R. Garg and I.J. Bahl, *Microstrip lines and slotlines*, Artech House Ed., 1979.

[Havart97] R. Havart, J.Carbonell and D. Lippens, *Harmonic multiplication with heterostructure barrier varactor at 250 GHz*, 5th Int. Workshop on Terahertz Electronics, Grenoble (France), 18-19 September 1997.

[Jain97] N. Jain and P. Onno, *Methods of using commertial simulators for microwave and millimeter-wave circuit design and optimization*, IEEE Transactions on Microwave Theory and Techniques, Vol. 45, No. 5, pp.724-746, May 1997.

[Jones97] J.R. Jones, W.L. Bishop, S.H. Jones and G.T. Hait, *Planar multibarrier 80/240 GHz heterostructure barrier varactor triplers*, IEEE Transactions on Microwave Theory and Techniques, Vol. 45, No. 4, pp. 512-518, April 1997.

[Kollberg92] E.L. Kollberg, T. J. Tolmunen, M.A. Frerking and J.R. East, Current saturation in submillimeter wave varactors, IEEE Transactions on Microwave Theory and Techniques, Vol. 40, No. 5, pp.831-838, May 1992

[Lheurette96] E. Lheurette, P. Mounaix, P. Salzenstein, F. Mollot and D. Lippens, *High performance InP-based heterostructure barrier varactors in single and stack configuration*, Electronics Letters, Vol. 32, No. 15, pp. 1417-1418, July 1996.

[Lheurette96b] E. Lheurette, *Fabrication de composants non linéaires à hétérostructures pour les longueurs d'ondes millimétriques et submillimétriques*, Université des Sciences et Technologies de Lille, PhD Thesis, December 1996.

[Mehdi96] I. Mehdi, S.C. Martin, R.J. Dengler, R.P. Smith and P.H. Siegel, *Fabrication and performance of planar Schottky diodes with T-gate like anodes in 200 GHz subharmonically pumped mixers*, IEEE Microwave and Guided Wave Letters, Vol. 6, No. 1, pp. 49-51, January 1996.

[Melique98] X. Mélique, J. Carbonell, R. Havart, P. Mounaix, O. Vanbésien and D. Lippens, *InGaAs/InAlAs/AlAs Heterostructure barrier varactors for harmonic multiplication*, accepted for publication in IEEE Microwave and Guided Wave Letters, 1998.

[Mounaix95] P. Mounaix, E. Lheurette, F. Mollot and D. Lippens, *Frequency capability of strained AlAs/InGaAs resonant tunneling diodes*, Electronics Letters, Vol. 31, No. 17, pp. 1508-1510, 1995.

[Reddy93] V.K. Reddy and D.P. Neikirk, *High breakdown voltageAlAs/InGaAs quantum barrier varactor diodes*, Electronics Letters, Vol. 29, No. 5, pp. 464-466, 1993.

[Stake96] J. Stake and H. Grönqvist, *An on-wafer method for C-V characterization of heterostructure diodes*, Microwave and Optical Technology Letters, Vol. 9, No. 2, pp. 63-66, 5 June 1995.

[Sze66] S.M. Sze and G. Gibbons, *Avalanche breakdown voltages of abrupt and linearly graded p-n junctions in Ge, Si, GaAs and GaP*, Applied Physics Letters, Vol. 8, No. 5, pp. 111-113, 1966.

[Tuovinen95] J. Tuovinen and N.R. Erickson, *Analysis of a 170 GHz frequency doubler with an array of planar diodes*, IEEE Transactions on Microwave Theory and Techniques, Vol. 45, No. 5, pp.724-746

[Yassin96] G. Yassin and S. Withington, *Analytical expression for the input impedance of a microstrip probe in waveguide*, Int. J. of Infrared and Millimeter Waves, Vol. 17, No. 10, pp. 1685-1705, October 1996.

CHAPTER III:

MICROMACHINED STRUCTURES AT MILLIMETER WAVELENGTHS

CHAPTER 3: MICROMACHINED STRUCTURES AT MILLIMETER WAVELENGTHS.

As we saw along the first chapter, and in addition to active devices, several passive elements are also typically included in a millimeter wave receiver front end. This third chapter deals with different types of structures fabricated by means of micromachining techniques with, on one hand, membrane technologies applied to transmission lines and filtering structures and, on the other hand, RF micromechanical switches. Despite the fact that both issues appear different in the sense that they are designed for distinct application fields, the problems that face us in the simulations are closely related. Indeed, we start from the same technological background of GaAs micromachining applied to free-standing structures. Since most solid state devices are now fabricated in the GaAs material system, it is believed that such a scheme will provide greater opportunities for integration. With increasing frequency capability, achieved by further decreasing the geometrical dimensions, it does become imperative to determine accurately the electrical properties of these elements by means of a ground electromagnetic approach. Parasitic couplings or losses in passive devices become a critical factor to operate any system at millimeter wavelengths, so a deep understanding of the EM behavior of such structures is necessary.

3.1 Membrane transmission lines and filtering structures.

3.1.1 Interest of membrane transmission lines.

During the past few years, a tremendous effort has been brought concerning zero-dispersion and low-loss transmission lines. To this purpose, several techniques have shown promise, notably dielectric membranes [Dib91]. To understand the dispersion phenomena associated with thick substrate propagation structures, Figure 3.1 gives the evolution of impedance and propagation constants as a function of frequency, for a 50 Ω conductor backed CPW on GaAs substrate (ε_r = 13, H = 400 μm).

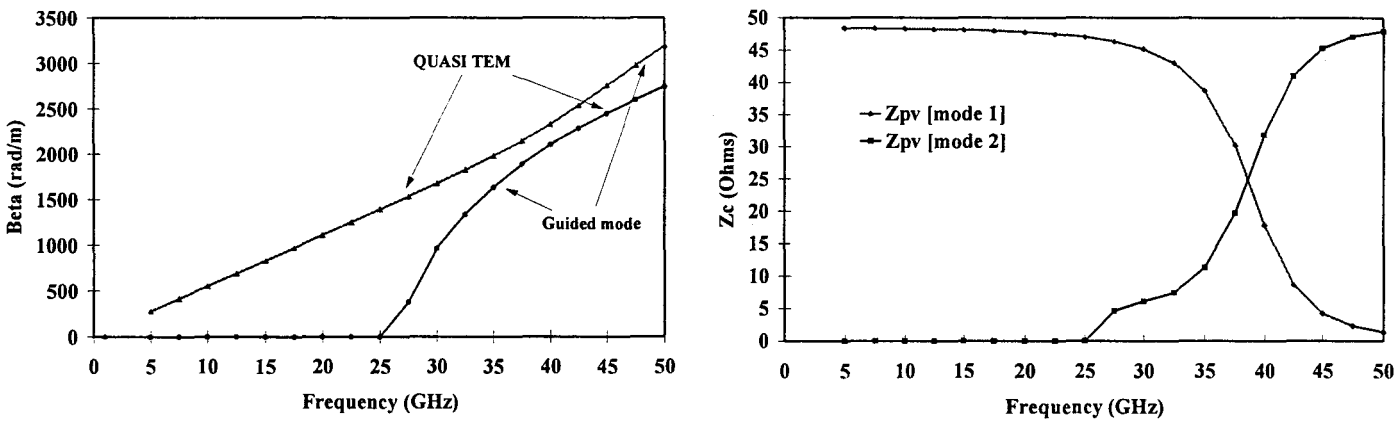

Figure 3.1: Impedance and propagation constant as a function of frequency for a 50 Ω CPW on a GaAs (ε_r = 13, h = 400 μm) substrate.

The presence of high order propagation modes dramatically changes the electrical characteristic figures of this transmission line. As we can observe, at the cut-off frequency of the parallel-plate substrate mode (around 25 GHz), the characteristic impedance decreases rapidly and at higher frequencies, dispersion causes the propagation constants of the dominant and second mode

to cross each other. This is obviously unacceptable for practical purposes, and the trends towards zero-dispersion lines have lead to the development of transmission lines deposited on a membrane.

The advantages of this type of lines stem from the fact that the thick dielectric substrate has been removed and the conducting strips are suspended in an almost homogeneous air-like medium. Figure 3.2 illustrates a schematic longitudinal section of a CPW on membrane, with the membrane-suspended metallic strips, the tapered transmission lines from thick to thin substrates and standard CPW access lines for RF probing. The first advantage is the possibility of propagating a pure TEM mode together with a lack of dispersion up to very high frequencies. For a conventional CPW on thick substrate, dispersion phenomena occur, in general, at the beginning of the millimeter wave range. For membrane lines, the lack of dispersion has been demonstrated up to the submillimeter wave range, making this technology suitable for very high-speed circuits. In digital communications, pulsed signals will be less affected by inter-symbol-interference (ISI), because of the broad band characteristics of these lines. At the same time, the phase constant, in contrast with high permittivity dielectrics, will not be reduced by the fact of working with an inhomogeneous medium usually modeled by an effective dielectric constant (ε_{eff}). As we pointed out previously, an effective dielectric permittivity of $\varepsilon_{eff} = 1.08$ and a phase velocity $v_\phi = 2.9\ 10^8\ m.s^{-1}$ make them very attractive with quasi free-space propagation conditions.

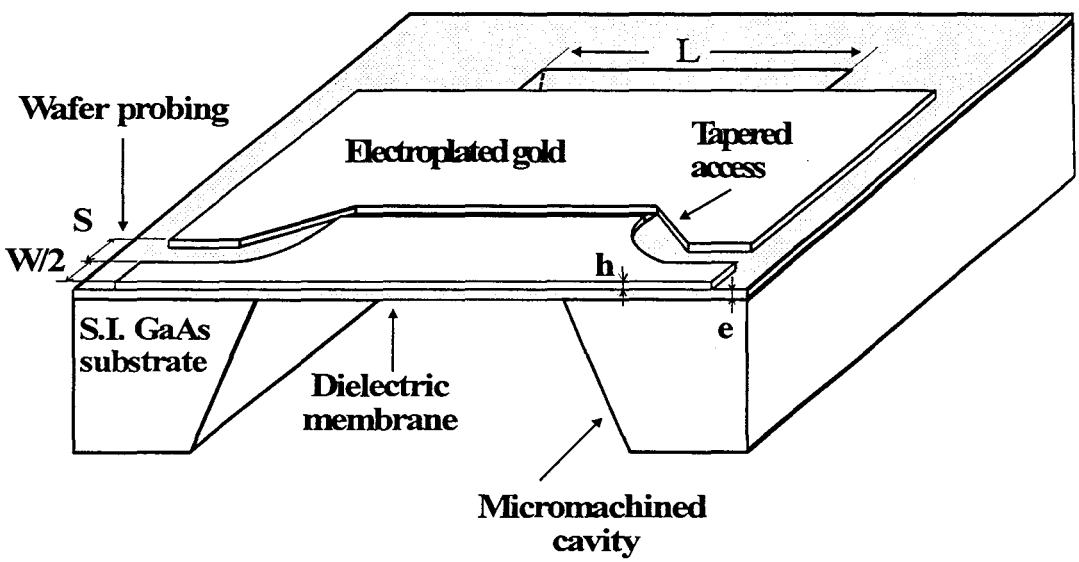

Figure 3.2: Schematic longitudinal section of a CPW on membrane.

Another advantage is related to the loss issue, it might be wise to remove the high permittivity substrate and hence avoid parasitic trapped waves in the substrate. Nevertheless, the importance of the dielectric loss term becomes serious at frequencies above 100 GHz. Also, concerning discontinuities, and owing to the fact that the transmission medium is comparable to air, all the problems associated with them will be, in principle, alleviated, in particular those related to unwanted radiation into the substrate.

The disadvantages of this type of technology with respect to thick substrates can also be mentioned. First, there is a transition from the thick substrate to the dielectric membrane to be designed if one wishes to characterize the S-parameters of a line with RF probes. The membrane may be damaged by the probes if they are directly positioned on it. The transition has to be optimized in order to correctly match the impedances of both transmission media. This is a tricky issue to solve, strongly dependent on the etching profiles achieved and on the correct back-side

alignment procedure. A second disadvantage, just partially outlined is the inherent fragility of this type of structure. Nevertheless, mechanical vibration and deformability studies have shown that membrane lines can stand quite adverse conditions without dramatic degradations. The results of these analysis will be reported elsewhere.

Early works on membrane technologies were carried out at the University of Michigan, for fabrication procedures, [Weeler95], as well as for EM simulations, [Katehi93, Drayton93], with the focus on transmission lines, filtering structures and antennas. Later on, more advanced applications have been studied in the micromechanical devices field, taking advantage of their elastic properties, as micro-switches. We will outline some of these properties in the second part of this chapter.

3.1.2 Membrane transmission lines.

3.1.2.1 Technological fabrication and measurements.

Even if a detailed fabrication description is out of the scope of this thesis, it is worth mentioning some of the basic features of the process, [Salzenstein96].

If we consider, in a first stage, the geometrical dimensions of the membrane, they are fixed according to different aspects. The thickness has to be reduced with respect to the field distribution around the conducting strips. This is an intuitive statement if the substrate influence has to be minimized. In a CPW configuration, the E-field is concentrated in the air gaps between the central conductor and the ground planes (see Figure 1.14c). Therefore, the objective would be to make the membrane as thin as possible in order to have a low perturbation of these gap fields. Technological constraints precluded thicknesses below 1 μm, mainly due to fragility in the processing and to large aspect ratios with respect to the lateral dimensions. Consequently, membranes are typically in the 1.5 - 2.5 μm thick range. Lateral dimensions are fixed from the transmission line design. To obtain a 'suspended' - 50 Ω CPW, the width of the line (central conductor + ground planes) has to be around 500 μm [Dupuis95], and in practice the width of the membrane, exceeding that of the strips, was chosen several millimeters. CPW lines with different lengths in the 3.5 - 13 mm range have been designed, hence allowing to assess attenuation and propagation constants by de-embedding techniques. The length of the membrane, closely fits the line dimensions in each case.

First realizations were based on a tri-layer $SiO_2/Si_3N_4/SiO_2$ [Weeler95]. The main motivation for using this structure is technological, with a compensation between the strains from SiO_2 and Si_3N_4. Deposition of the Si_3N_4 material is realized with a LPCVD procedure (Low Pressure Chemical Vapor Deposition). Very high temperatures are required, this fact being a drawback when working with thermally-sensible heterostructure devices.

In practice, at the IEMN, the process flow is divided into two steps involving a front-side processing (dielectric and metal deposition) and a back-side processing (bulk machining of a cavity) which is performed in a last stage reducing hence the risk of deterioration of the samples. The complete technological procedure is summarized in Figure 3.3. Two material systems have been proposed to fabricate thin dielectric membranes, they are based respectively on Si_3N_4 and polyimide films. On a semi-insulating 400 μm thick GaAs substrate, a Si_3N_4 layer is deposited by Plasma Enhanced Chemical Vapor Deposition (PECVD) or a polyimide deposition is done by a spin coating technique. The latter is technologically simpler than the former, and thicker and more uniform layers of polyimide can be deposited by spin coating.

Once the dielectric layer is formed on top of the GaAs substrate, the coplanar conducting strips can be deposited either by etch-masking or lift-off processes. The latter option was chosen according to aspect ratio considerations, between the length of the lines (several millimeters) and the width of the slots (several tens of microns). Therefore, we deposited a Ti/Au film by evaporation, followed by electroplating of a thick gold layer ($h \sim 2$ μm). The metal layer uniformly deposited was afterwards patterned and etched using gold and titanium etchants.

Finally, after the metallization, the wafer was patterned on the back-side in order to completely remove the GaAs substrate underneath the area defining the membrane. The etch for micromachining this cavity was made by wet chemical etching using a H_2SO_4:1/H_2O_2:8/H_2O:1 and a photoresist as a mask. These concentrations offer the advantage of a high etching rate (typically 15 $\mu m.min^{-1}$) and a high selectivity against photoresists and dielectric layers. However the etching was found highly anisotropic with a pronounced tilted profile along the (011) direction. As a consequence, it was decided to take advantage of such an etching profile to provide a tapered transition between the probing region on semi-insulating substrate and the substrate-free region of the membrane. Of course, this objective involves a careful opening on the back-side, accurately aligned with respect to the transmission lines. This step was found the most critical in the whole procedure, requiring a double-side photolithography equipment.

Si_3N_4 or polyimide deposition by PECVD or spin coating respectively.

deposition of a Ti/Au film by evaporation, followed by electroplating of a thick gold layer.

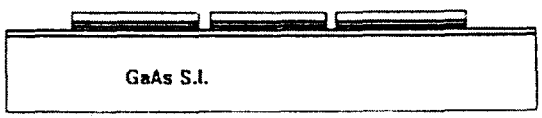

chemical etch of the gold layer

backside bulk micromachining of a cavity under the membrane

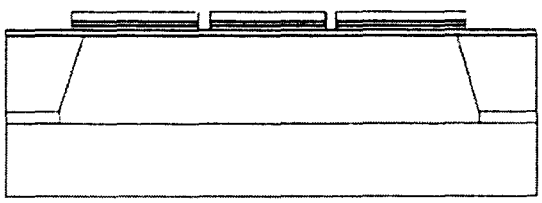

the suspended structure is fixed on a Si substrate for RF characterization

Figure 3.3: Schematic technological fabrication process for CPW on membrane.

Technological realizations of membrane transmission lines are illustrated in Figure 3.4, showing back- and front-sides. The lengths of the lines are 3.5, 7 and 13 mm, and three impedances have been selected for the test structures summarized in Table 3.1, together with the design of the standard CPW access lines.

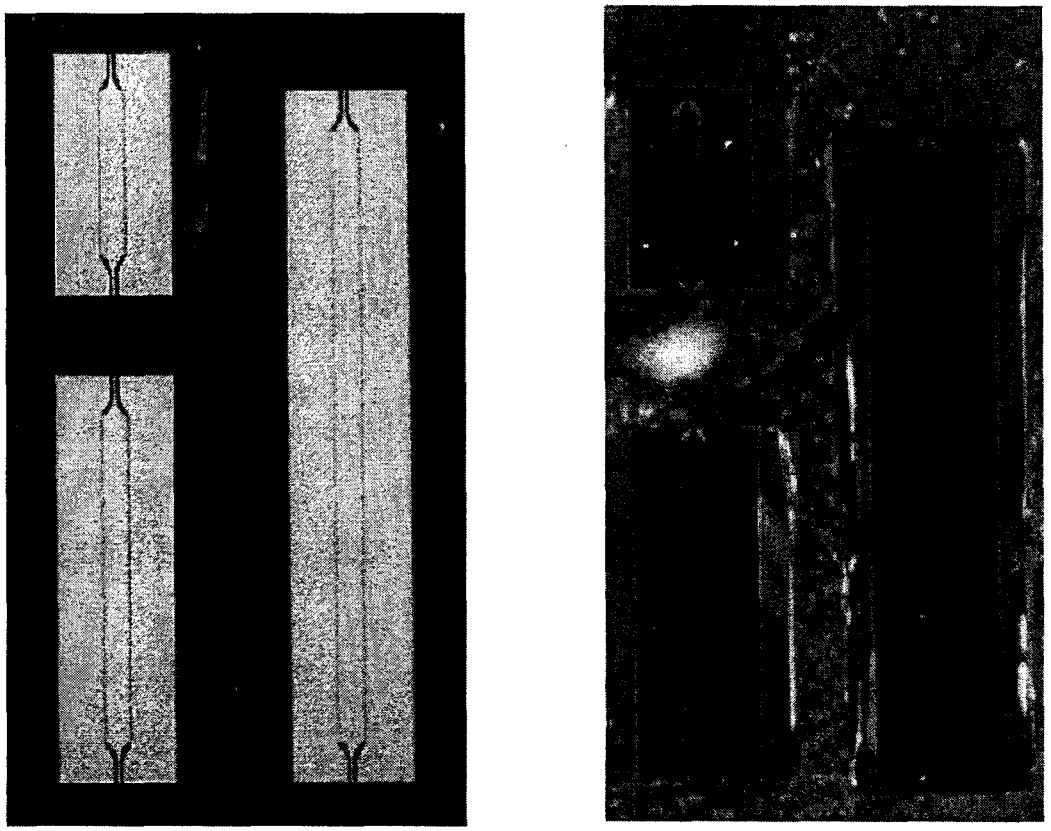

a.) b.)

Figure 3.4: Technological realizations of CPW on membrane, front-side in a.), back-side in b.).

Z_c (on membrane)	*central strip width (w)*	*slot width (s)*
50 Ω	550 μm	10 μm
75 Ω	300 μm	27 μm
100 Ω	300 μm	75 μm
Z_c (access line)	*central strip width (w)*	*slot width (s)*
50 Ω	70 μm	50 μm

Table 3.1: Characteristic impedance (Z_c), design of the fabricated CPWs.

In practice, the line characteristic impedance can be adjusted by varying the slot and line widths. These designs are based on analytical models [Gupta79], but have been also verified with full-wave analysis [Hélal94]. By analyzing different lengths, the propagation on the substrate-less medium can be fully characterized while the study of Z_c gives an insight into the matching

conditions and the field patterns. The relevant dimensions are chosen in order to keep a reasonable overall lateral size (around 2.5 mm).

The problem of connecting an access line on thick substrate to a membrane supported transmission line leads to the design of an optimal transition between both media. In principle, this transition should match the characteristic impedances, Z_c, with a minimum discontinuity step. This type of problem has been widely analyzed in the past for different line topologies, and starting from classic transition designs [Klopfenstein56]. An optimum transition has been proposed here in order to keep a constant impedance level of 50 Ω, taking at the same time advantage of the etch profile of the micromachined cavity underneath the membrane. Figure 3.5 shows the schematics of different transitions in CPW technology.

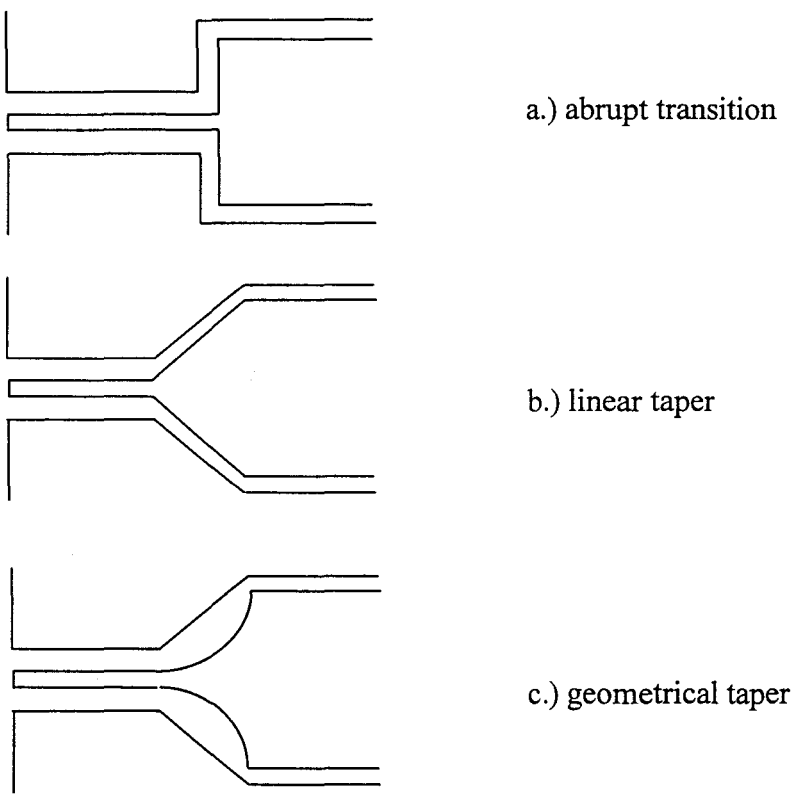

Figure 3.5: Different transitions in CPW technology.

Figure 3.5 a.) illustrates an abrupt transition from narrow line - thick substrate access line to wide line - membrane supported 50 Ω transmission lines, which is usually considered capacitive [Gupta79]. Case b.) considers a linear transition for the line and slot dimensions of the CPW, thus providing a gradual variation of the geometry of the taper. By extending the length of the taper a reduced capacitance level can be achieved [Yu93]. In contrast, case c.) illustrates a geometrical design for the taper providing a constant impedance level of 50 Ω all along the taper length. This feature is achieved through the use of a linear transition for the ground planes and a geometrical variation of the line width taking into account the etching profile of the GaAs substrate. For a given substrate height, the central conductor width is calculated in order to obtain a constant impedance of 50 Ω all along the length of the taper. In practice, this was the preferred option. A 3-dimensional view of this type of taper can be seen in Figure 3.6, together with the analytical model used to describe the characteristic impedance of a CPW [Hoffman87].

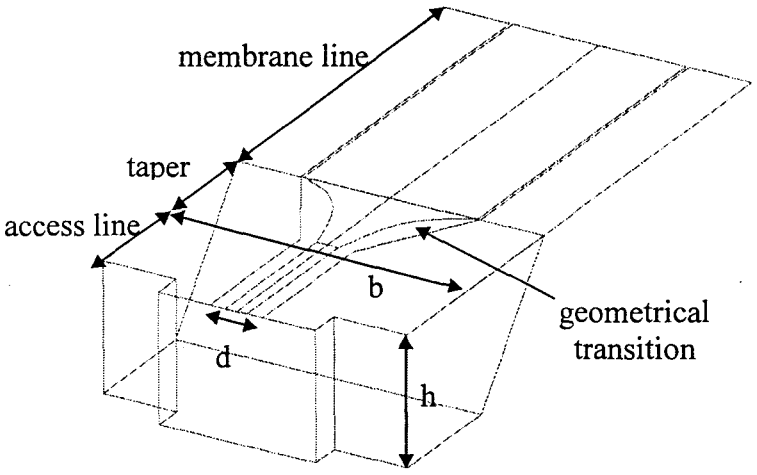

for $0 < k < 0.173$

$$Z_c = \frac{\pi \eta_0}{16\sqrt{\varepsilon_{eff}}\ln(2/\sqrt{k})}$$

for $0.173 < k < 1$

$$Z_c = \frac{\eta_0}{4\pi\sqrt{\varepsilon_{eff}}}\left\{\ln(2) + 2\,\mathrm{arcth}(\sqrt{k})\right\}$$

$k = ((1\text{-}w/d)^2/(1\text{-}w/b)^2)^{1/2}$ $\quad (d = w + 2s)$

ε_{eff}: effective permittivity

η_0: vacuum impedance (377 Ω)

Figure 3.6: Geometrical taper in CPW technology and analytic model for Z_c.

Access lengths are 500 μm long and tapered sections are 350 μm long. A detailed derivation of tapered transmission line theory can be found in [Collin92]. The 350 μm value is fixed by the substrate thickness and the etching profile angle (45°) of the micromachined cavity.

With respect to RF measurements, the frequency characteristics of the coplanar waveguides have been measured over the bands [0.4; 40] GHz, [50; 75] GHz and [75; 110] GHz. At the time of these measurements, for the frequency window from 40 to 50 GHz was out of the range of the network analyzers available in the laboratory. Figures 3.6 and 3.7 illustrate, for a 13 mm long line (Z_c = 100 Ω), the frequency dependence of the scattering parameters magnitude and phase in linear and degree scales respectively. The S-parameters measured with RF probes positioned on the access lines are compared to simplified theoretical results. The latter were obtained using a set of matrixes, describing in terms of a complex propagation constant (including losses) and a characteristic impedance, the transmission line behavior. This simple analytic model fits the S parameters of the structure with a good agreement up to 40 GHz, or even higher frequencies because resonances and attenuation show a monotonous behavior up to 110 GHz. The evolutions of S_{11} (S_{11}=S_{22}) and S_{12} (S_{12}=S_{21}) exhibit pronounced resonances at frequencies which follow the condition:

$$f_r = n\, v_\phi / 2L$$

where n is the resonance index, v_ϕ is the phase velocity and L is the line length. Thus, the membrane line section behaves as a micro-resonator and each resonance corresponds to the matching of a multiple of a half-wavelength to the physical length of the line. A first estimate of the phase velocity can be calculated from resonance conditions. The decrease of the magnitude of the S_{ij} parameters is due to increasing losses with frequency. However, to have further insight into the loss and dispersion issues, we analyzed the above experimental data by using the de-embedding technique from Bianco and Parodi [Bianco76], applied to two different length lines.

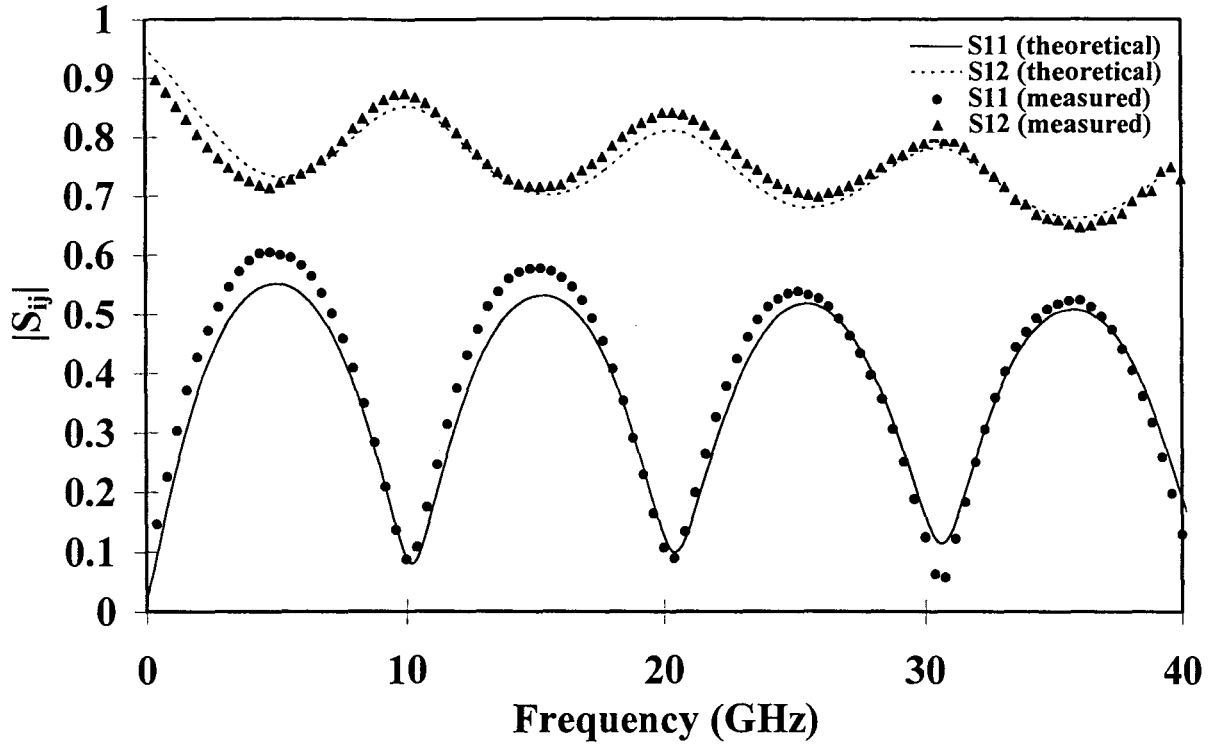

Figure 3.7: Comparison theory-experiment for the magnitude of S_{ij} versus frequency for a 13 mm long line (Z_c = 100 Ω).

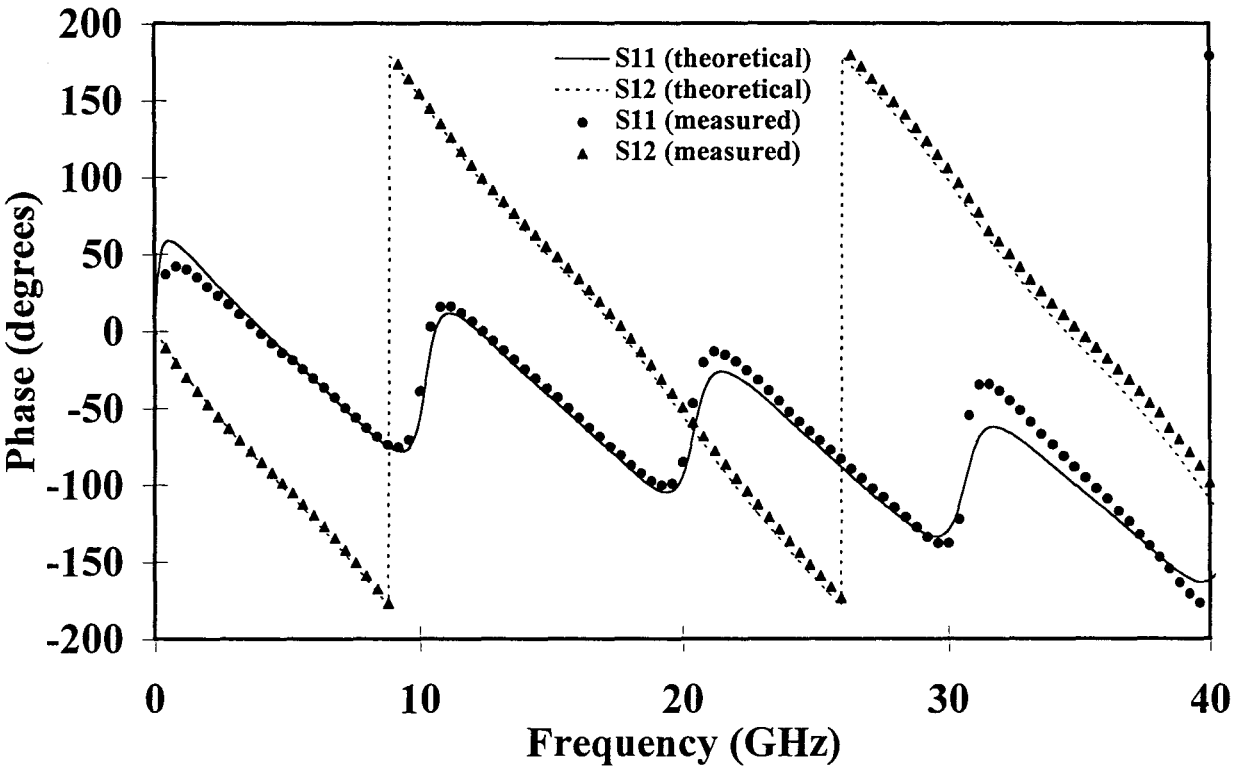

Figure 3.8: Comparison theory-experiment for the phase of S_{ij} versus frequency for a 13 mm long line (Z_c = 100 Ω).

Figure 3.9 shows the frequency dependence of the attenuation constant (plotted in log-log scales) for different values of Z_c (50, 75 and 100 Ω). From this behavior, we can observe that the attenuation exhibits an almost square root evolution versus frequency, which is typical of metallic losses (skin depth effect). Also, we can note that the level of attenuation is directly influenced by the dimensions of the lines. There is a pronounced shift of the curves for Z_c equal to 75 and 100 Ω. These two lines have the same central conductor width (w = 300 μm) but different slot widths (27 and 75 μm respectively). In terms of aspect ratio, the attenuation is clearly proportional to the ratio w/(w+2s) = w/d. Concerning the 50 Ω line, despite a greater aspect ratio between w and s (w = 550 μm and s = 10 μm), the attenuation is found comparable to the 75 Ω line demonstrating the effect of a larger ground plane separation d = w +2s on the attenuation. With the derivation of the complex propagation constant, we also assess the phase constant β and then, from the slope of this curve, the effective dielectric permittivity:

$$\varepsilon_{eff} = \left(\frac{c\ \Delta\beta}{2\pi\ \Delta f} \right)^2$$

with c being the light velocity. Its frequency dependence, also for different values of Z_c is plotted in Figure 3.10. The increase in the ε_{eff} with the reduction of the slot width is a direct consequence of the stronger field confinement in the slot region, and thus in the membrane. The linear behavior of β versus frequency is also reported in inset, demonstrating the ability to maintain a quasi TEM propagation without dispersion far inside the millimeter wave spectrum.

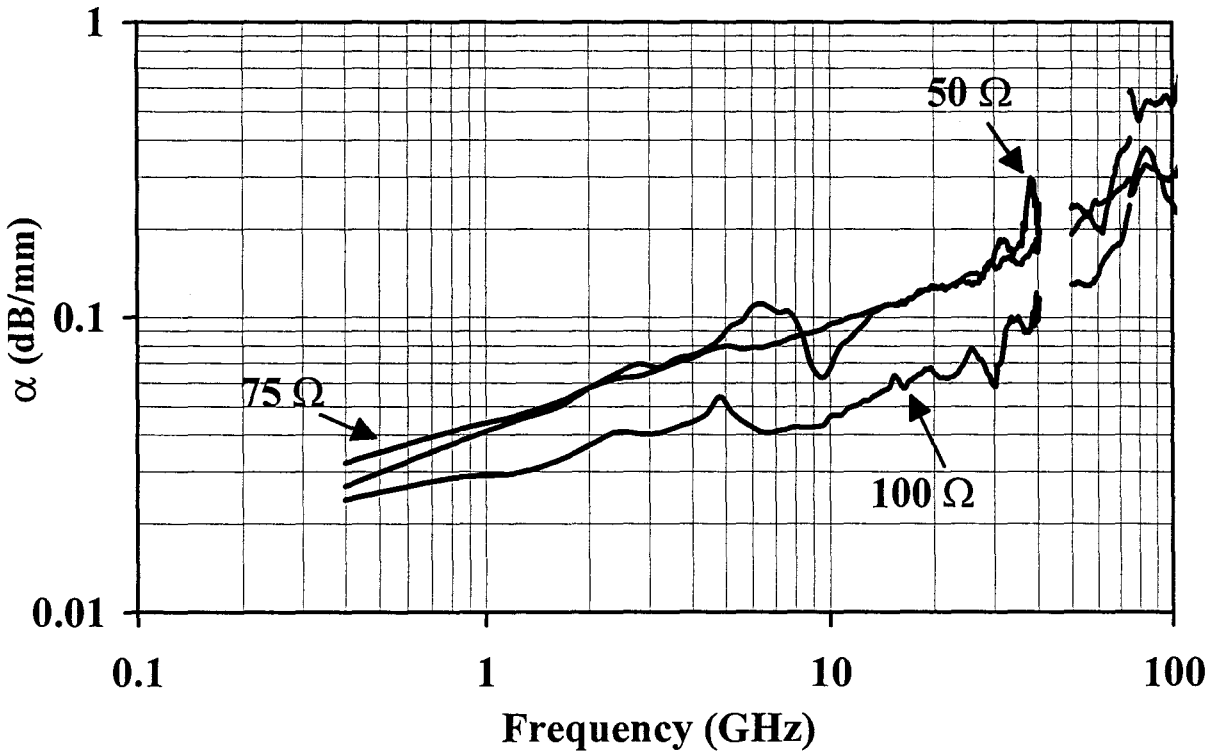

Figure 3.9: Attenuation constant versus frequency for different values of Z_c.

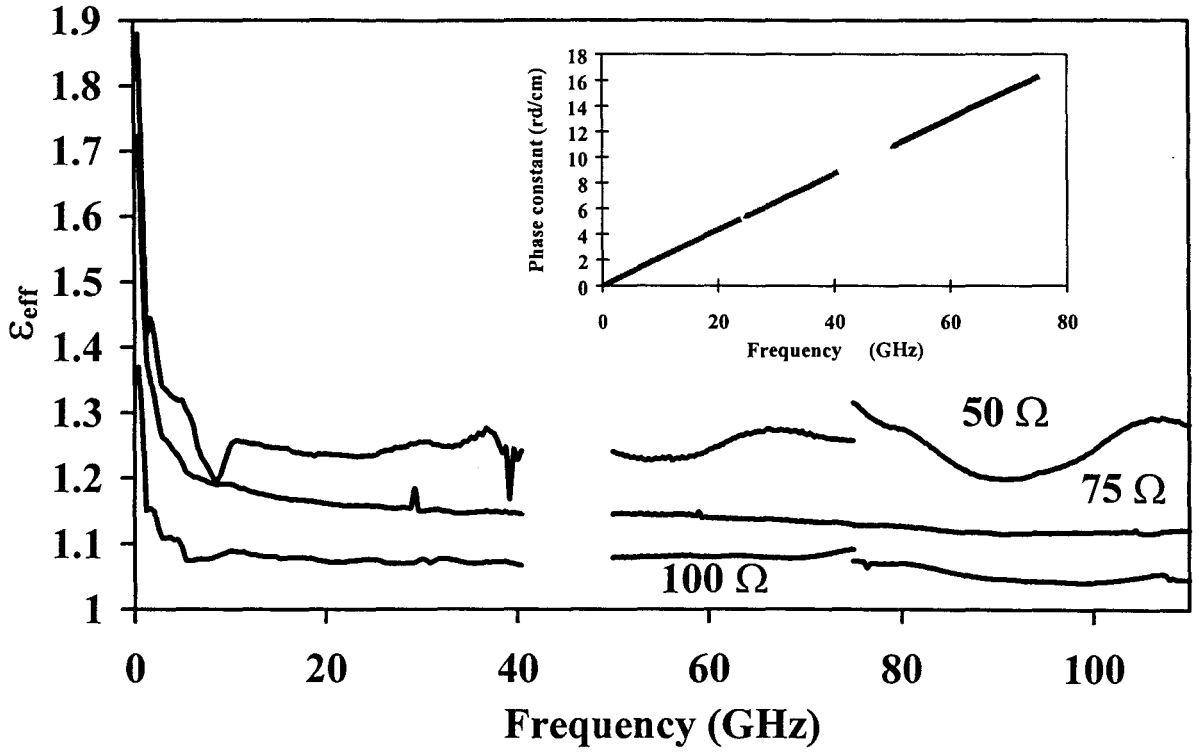

Figure 3.10: Effective dielectric permittivity and phase constant versus frequency.

3.1.2.2 EM simulation of membrane transmission lines.

In this section, we will give and analyze the results obtained by applying a full-wave EM analysis to the transmission lines fabricated and characterized, and previously reviewed. This type of structure has particular characteristics to be considered prior to model its electromagnetic behavior. In fact, the geometry of the structure, notably because of the large aspect ratio between the membrane lateral and thickness dimensions, and also because of the fact of working with thick and very thin substrates at the same time, limits in a certain way the procedure able to correctly analyze its EM features. In general, the Finite Element Method (FEM) is not suited to treat problems with large aspect ratios like in this case: a membrane several millimeters long but only 1 or 2 μm thick and also combined with a thick GaAs substrate (410 μm). On the other hand, the Method of Moments (MoM) is suitable to solve planar 2-dimensional structures.

Our solution has been then to divide the problem into two parts and then couple the solutions through matrix calculations. Figure 3.11 summarizes the procedure employed, solving different media with different solvers, [Jain97]. In a first stage, the 3D problem of the transition is analyzed with HFSS in order to characterize through its S matrix the taper section including the etched profile in the GaAs wafer. This is clearly a 3-dimensional problem, so our MoM code is not able to solve it. The membrane line is not simulated, only a section of the metallic strips is considered, although a de-embedding of the reference plane in the 'membrane-side' is done to assess the S parameters exactly at the end of the transition. In a second stage, the membrane coplanar line portion is simulated through the use of the MoM, which appears as a powerful tool to model multilayered dielectric medium. In this case, the membrane is simulated with a finite thickness, a real permittivity and the conducting strips also have finite thickness and conductivity. These parameters can be easily varied to analyze different configurations with an important time saving with respect to the FEM. A summary of all the simulation parameters is given in Tables 3.2 and 3.3 for further information.

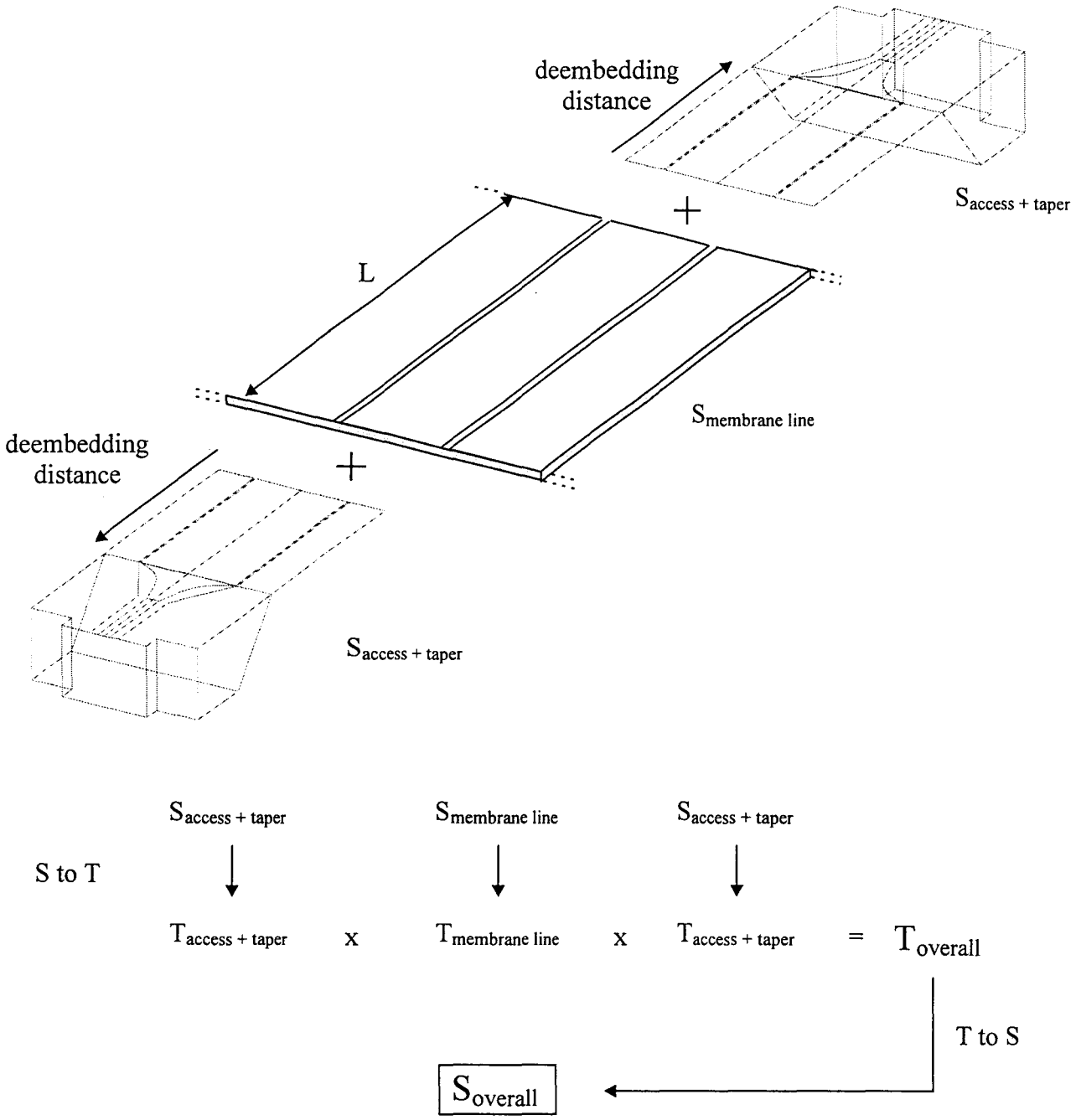

Figure 3.11: Procedure to analyze a CPW transmission line on membrane.

thick GaAs substrate	thickness	400 µm
	ε_r	13
	access length	500 µm
taper	length	350 µm
	ε_r	13
conducting strips	thickness	t = 2 µm
	conductivity	$\sigma = 4.1\ 10^7\ S.m^{-1}$

Table 3.2: HFSS simulation parameters.

membrane	line length	3.5 or 7 mm
	thickness	1.5 - 2.5 μm
	ε_r	2.7 (polyimide)
conducting strips	thickness	t = 2 μm
	conductivity	$\sigma = 4.1\ 10^7\ S.m^{-1}$

Table 3.3: Momentum simulation parameters.

If we now consider the results obtained with EM simulations and compare them to measurements, we can observe, see Figure 3.12, that for a 50 Ω - 3.5 mm long line the agreement is good overall. There still exists a slight shift in the resonance frequency and a discrepancy in the reflection loss level obtained, which might be explained by numerical errors in the simulation procedure, or more likely by the fact that there is always an uncertainty in the alignment procedure during the fabrication process. A difference in the positions between the tapered line section on the membrane and the tilted profile etched in the GaAs wafer would cause an impedance mismatch, and consequently a raise in the reflection loss. Moreover, it might happen that one of the transitions is well aligned, while the other may be slightly shifted. These fabrication tolerances also apply to the slot widths, which are difficult to control considering the gold etching techniques. This can impact the final result because any deviation of a few microns may cause a significant impedance mismatch.

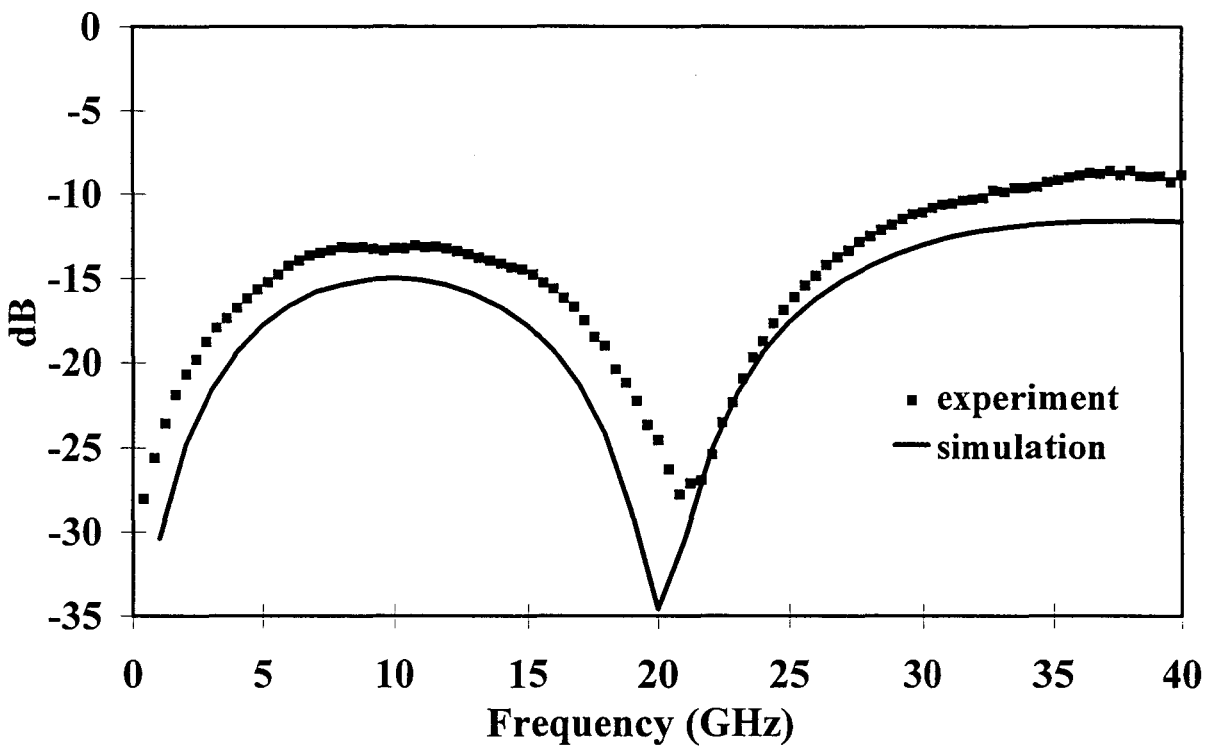

Figure 3.12: Reflection loss (S_{11}) versus frequency for a 50 Ω - 3.5 mm long line.

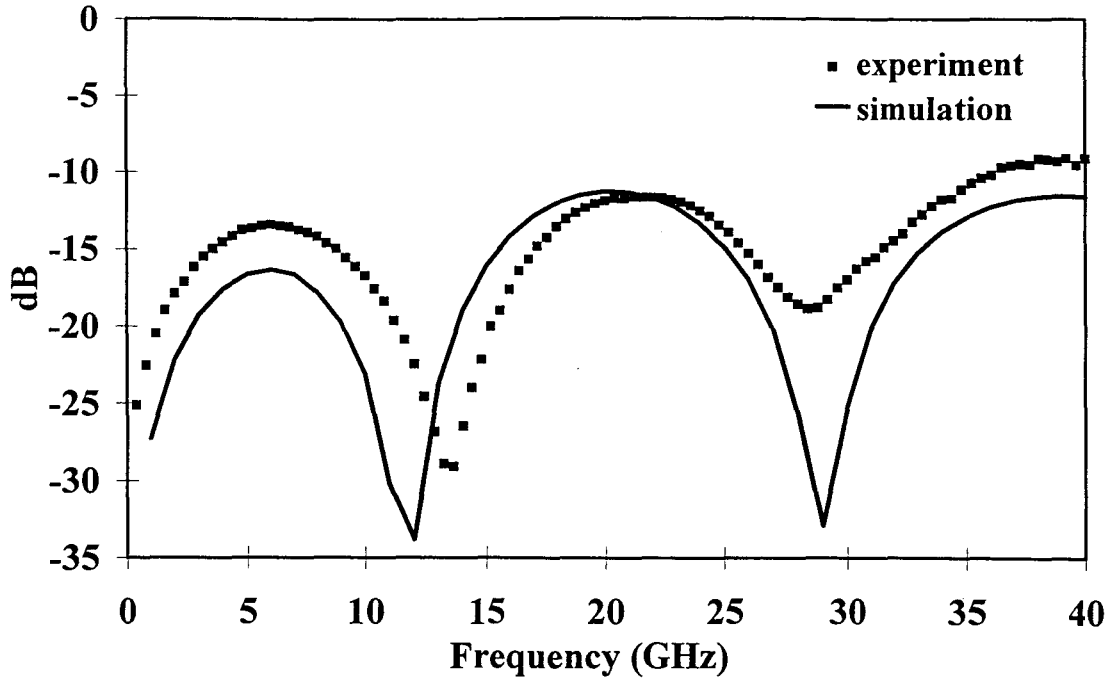

Figure 3.13: Reflection loss (S_{11}) versus frequency for a 50 Ω - 7 mm long line.

In the case of a 7 mm long line, there is the same type of discrepancies, that is to say slight changes in the resonant frequencies and differences in the reflection loss levels. As in the previous comparison (3.5 mm line) the differences are within 5%.

Nevertheless, in both curves we can observe a progressive increase in the maximums of S_{11} with frequency, as it was noticed for the measurements. Metallic losses, increasing with frequency should be, in principle, responsible for this effect.

If we now pay attention to the dispersion characteristics simulated with the MoM, we can see in Figure 3.14 a comparison of the measured ε_{eff} and the calculated value of this parameter. In this case the simulated membrane thickness is 1.5 μm. Figure 3.15 shows a comparison of the calculated values for ε_{eff} for two membrane thicknesses, 1.5 and 2.5 μm, demonstrating the importance of achieving thin membranes in order to effectively work in quasi-free-space conditions.

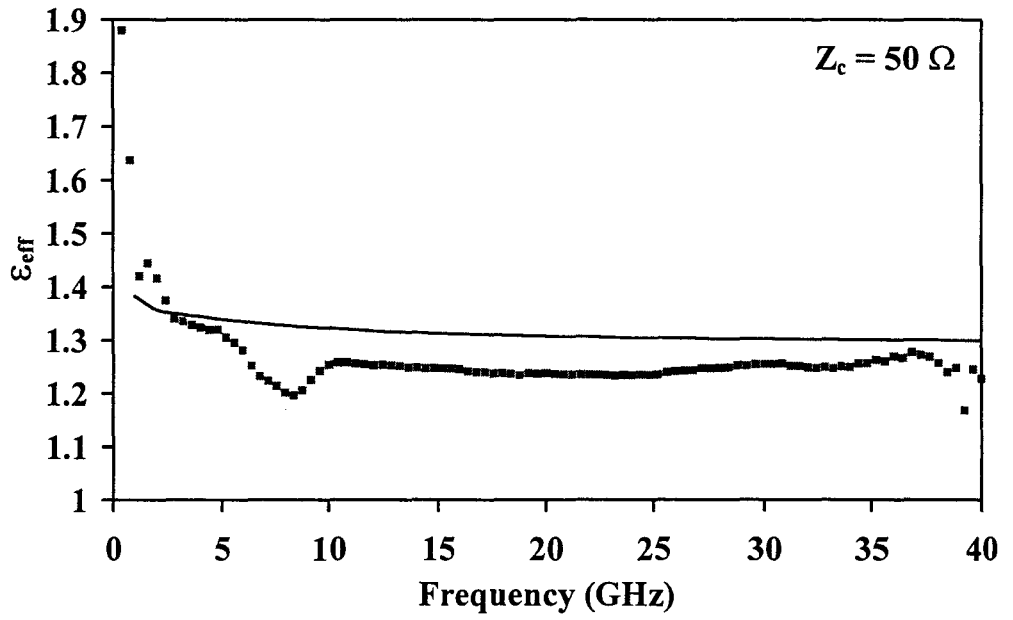

Figure 3.14: Comparison of the measured and calculated ε_{eff} for a 50 Ω line.

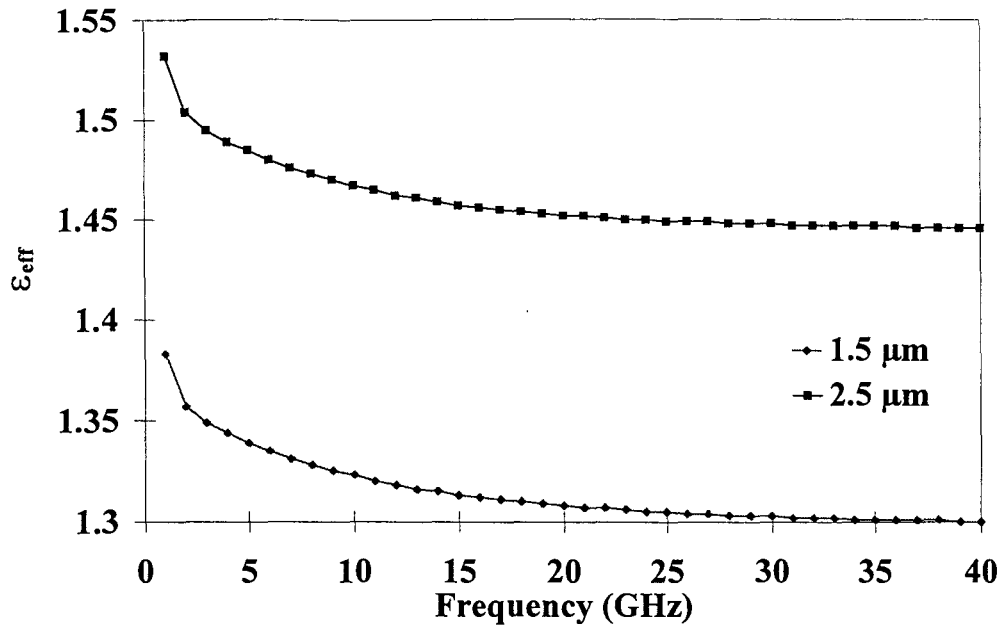

Figure 3.15: Comparison of the calculated ε_{eff} for 50 Ω lines with 1.5 and 2.5 μm thick membranes.

For illustrating the effect of an alignment offset in the reflection loss, Figure 3.16 shows the results obtained by shifting the tilted etching profile 50 μm towards the membrane position on both sides of the structure. As expected, reflection losses increase with respect to the previous configuration.

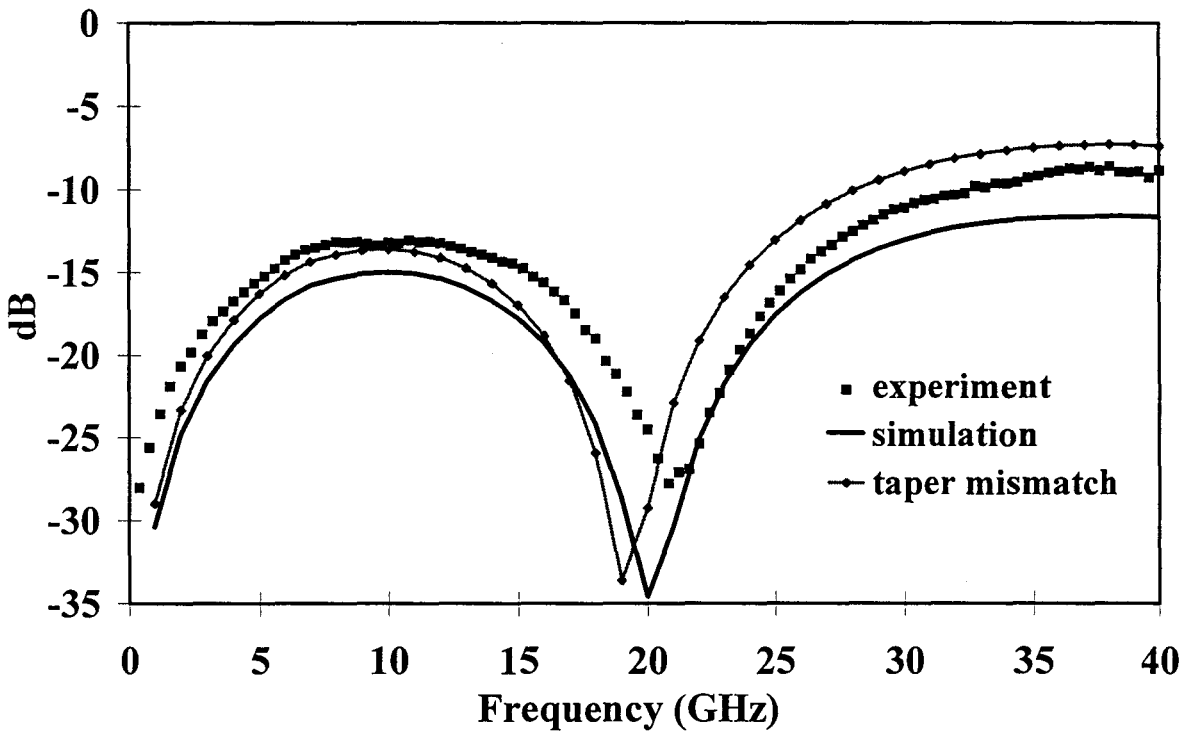

Figure 3.16: Reflection loss (S_{11}) versus frequency for a 50 μm-shifted taper transition in a 50 Ω - 3.5 mm line.

3.1.3 Filtering structures on membrane.

As a direct extension of the previous analysis concerning membrane transmission lines, it is useful to have a first insight into filtering structures based on this technology. First, we briefly review basic issues of filter design and afterwards we give the results for different filters, notably designs for K band (around 25 GHz), and also results for a 250 GHz bandpass filter.

3.1.3.1 Basic filtering topics.

The ideal filter network is a network that provides perfect transmission for all frequencies in certain passband regions and infinite attenuation in the stopband regions. Such ideal characteristics cannot be obtained in practice, and the goal of filter design is to approximate the ideal requirements to within an acceptable tolerance. Filters fall into three main categories, namely, (i) low-pass filters that transmit all signals between zero frequency and some upper limit ω_c and attenuate all frequencies above the cut-off value ω_c, (ii) high-pass filters that pass all frequencies above a lower cut-off value ω_c and reject all frequencies below ω_c, and (iii) bandpass filters that pass all frequencies in a range ω_1 to ω_2 and reject frequencies outside this range. The complement to the bandpass filter, i.e., the band-rejection filter, which attenuates frequencies in the range ω_1 to ω_2, is also of interest in certain applications. A basic theory for filter design and synthesis can be found in [Collin92], or more in detail in [Matthaei80], but our goal in this part of the work has been to understand, for filtering applications, the specific features arising from the use of a membrane technology.

A well known paper from Williams and Schwarz [Williams83], described for the first time the design principles and physical configurations of filter structures in CPW technology. Figure 3.17 depicts four patterns of basic resonant elements achieved by cutting gaps in the inner conductor of the guide or adding narrow strips. Starting from a direct transposition of microstrip resonators, case a.) shows an end-coupled resonant element acting as a capacitively coupled resonant section, and having a band pass frequency behavior. Case b.) shows an interleaved finger (edge-coupled) presenting an open circuit in the inner conductor and thus achieving higher coupling than the previous design. It is also applied to bandpass filters. Case c.) is an evolution of the previous design considering an edge-coupled section in short circuit configuration, suitable for band-stop filter applications [Dib91b]. Finally, case d.) illustrates a shunt inductively coupled section, [Everard93], also for bandpass applications, with reduced radiation losses, and based on similar designs than those employed for coaxial filters.

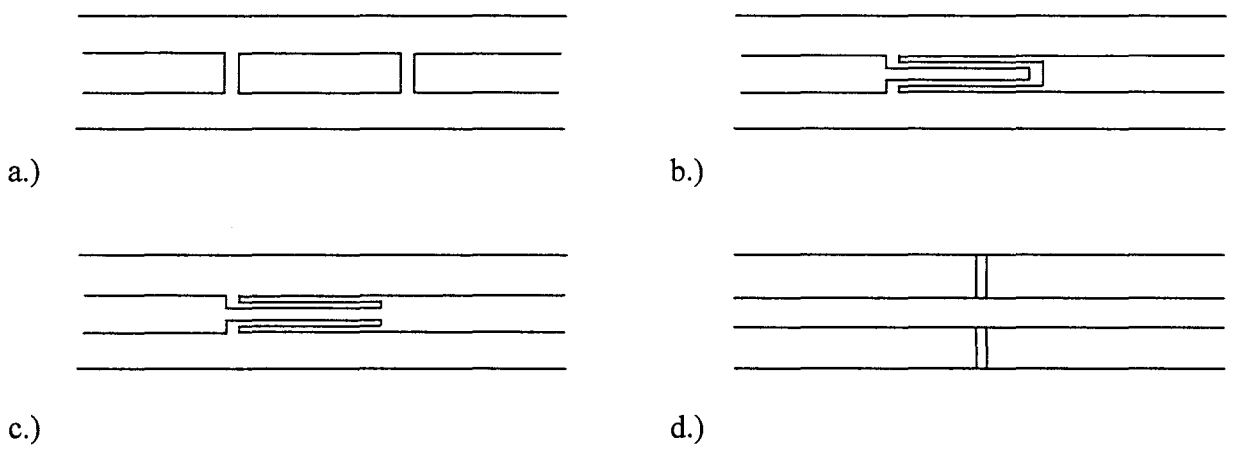

Figure 3.17: Basic resonator sections for filter applications.

Our work has focused on the study of several structures of the b.)-type at 25 and 250 GHz. A classic characteristic of any kind of filter is the connection of multiple elementary resonant sections to achieve a transmission window with tailored characteristics. As we will see in the following, out of band rejection characteristics are clearly improved by series connecting multiple sections, while maintaining a low insertion loss in the pass band.

A common characteristic when working with filters is the fact of using a characteristic impedance higher than the nominal 50 Ω value, [Robertson96]. In our study, S parameters are always referred to the characteristic impedance of the planar port on the line calculated by full-wave analysis. This type of S matrix is known as generalized S matrix.

3.1.3.2 Micromachined filters at 25 and 250 GHz.

The fist structure analyzed is an open stub in CPW technology with the dimensions displayed in Figure 3.18. This open stub design is optimized to behave as a $\lambda_g/4$ resonator at 25 GHz, with a targeted bandpass characteristic.

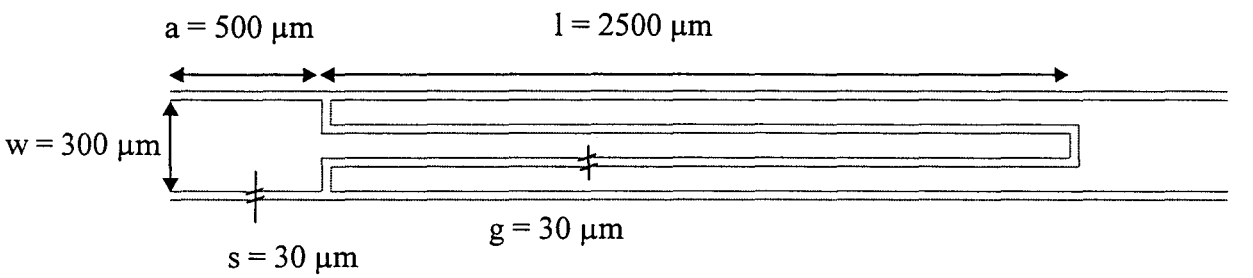

Figure 3.18: Open stub design ($\lambda_g/4$ resonator at 25 GHz).

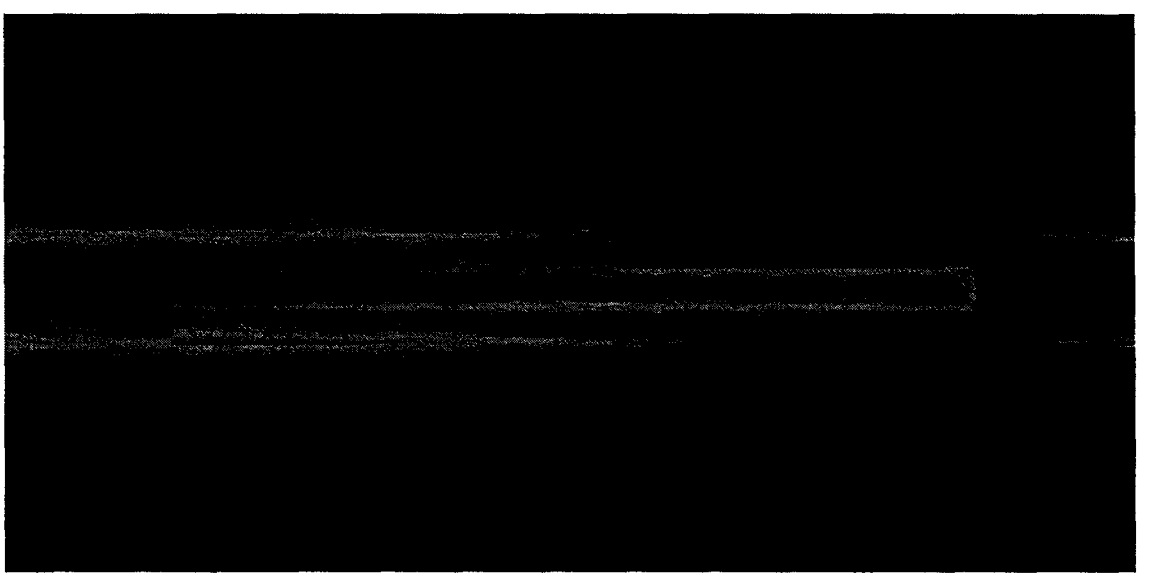

Figure 3.19: E-field pattern at 25 GHz.

Figure 3.19 illustrates the E field pattern on the conducting strips plane at 20 GHz, simulated with the FEM. At this frequency, the open stub physical length matches an electrical quarter wavelength and hence there is a resonance with a maximum of transmission. For frequencies higher or lower than this, the open stub will reflect the major part of the signal. By this means we can synthesize a multiple section (multiple pole) filter by connecting several stubs in series. However, in this frequency range (microwaves), it is often useful to work with lumped equivalent circuits and specially if the objective is filter synthesis, [Dib91b]. Hence, we have used a basic cell, depicted in Figure 3.20, to fit the S parameters obtained from full-wave analysis and foresee the transfer function of a filter designed from the connection of multiple cells.

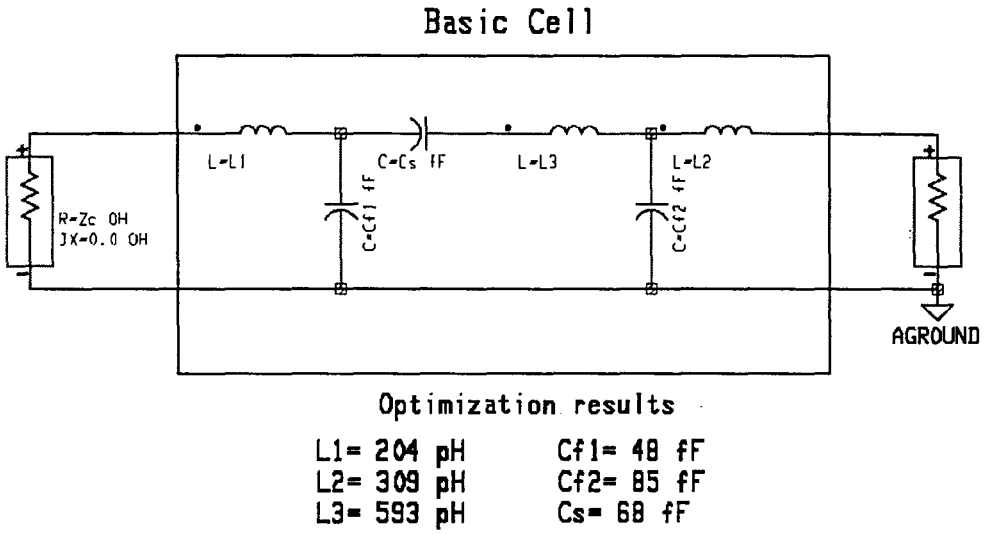

Figure 3.20: Lumped element equivalent circuit of the open stub.

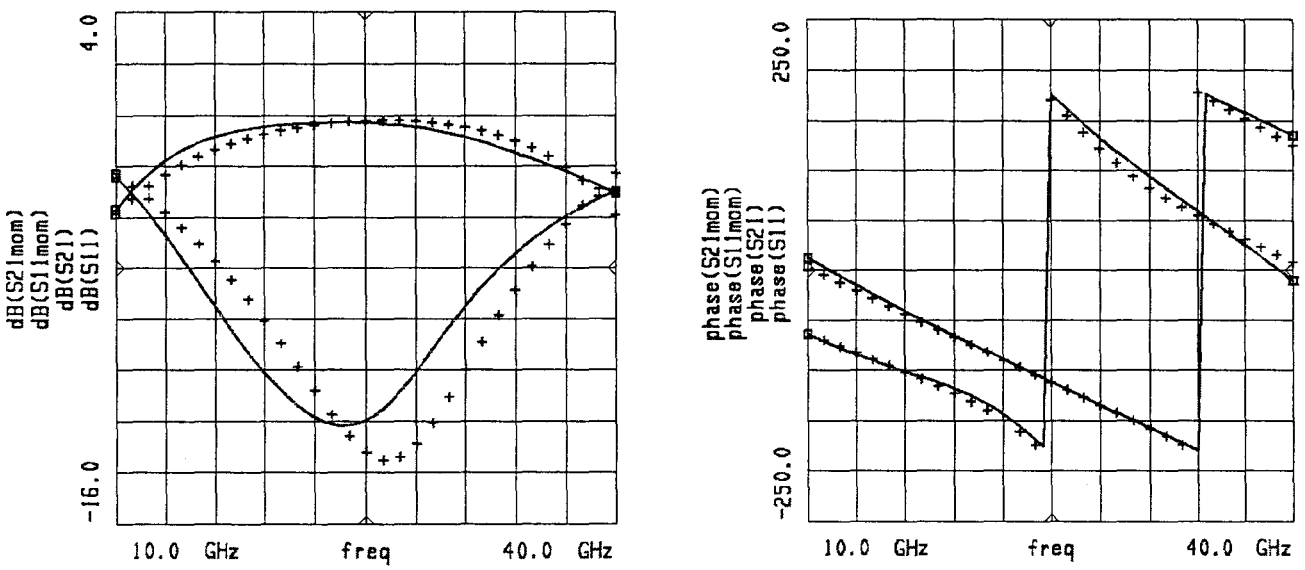

Figure 3.21: S parameter fitting of the open stub MoM simulation (+) through a lumped element equivalent circuit (-).

Figure 3.21 shows the S parameter frequency dependence (reflection loss and insertion loss) both in magnitude and phase calculated by means of EM analysis and fitted with a lumped element approach. A good agreement from 10 to 40 GHz can be observed. These set of data are then employed to predict the performance of multiple pole filters. This idea is based on the assumption of a low coupling between the connected stubs, because we are treating the overall filter as several non-coupled elements in series. It has been demonstrated in Si technology, that stub separations in the 150 μm range are enough to prevent coupling effects between the sections, [Weller95]. In our case the separation between the stubs is 500 μm. This concept is useful above all because, at these frequencies, it is much time consuming to solve the entire structure consisting of multiple stubs with full-wave analysis rather than using equivalent circuits.

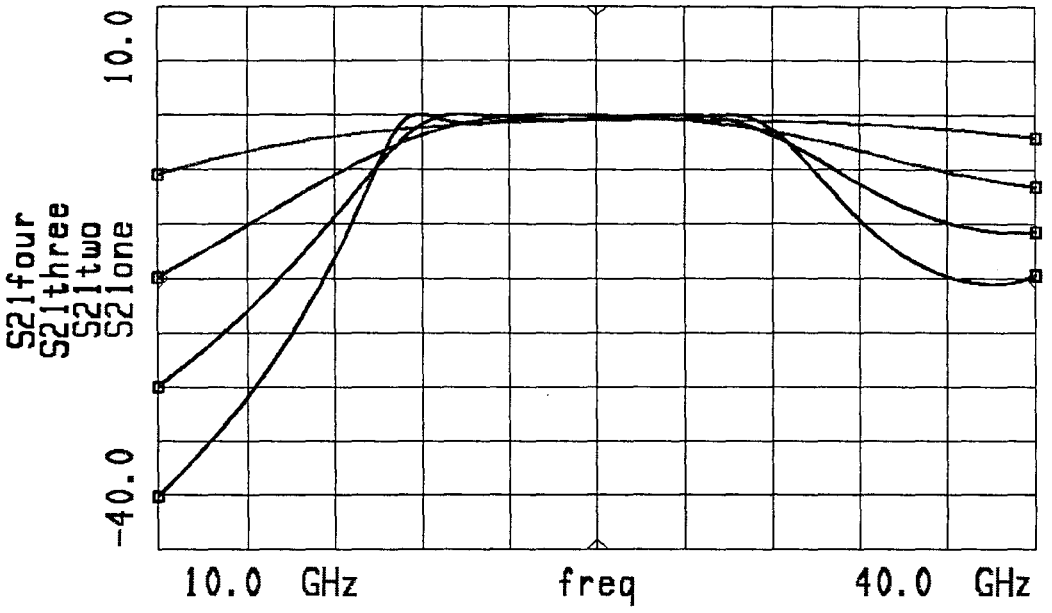

Figure 3.22: Insertion losses for filters from one to four series connected sections.

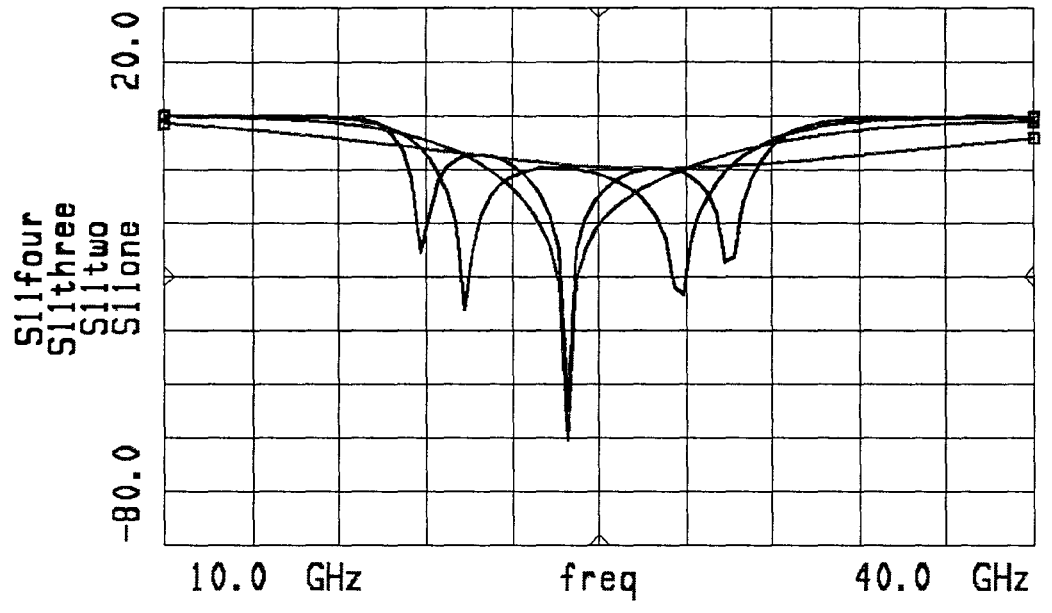

Figure 3.23: Reflection losses for filters from one to four series connected sections.

From Figure 3.21, we can observe a resonance behavior with a poor out-of-band rejection (-4 dB for 10 and 40 GHz). Now, Figures 3.22 and 3.23, show respectively insertion losses and reflection losses for filters with one up to four sections. Out of band insertion losses clearly increase with the number of sections with -40 dB at 10 GHz or -15 dB at 40 GHz, in the four section case. Also, for the latter, the relative bandwidth is 56 % (BW_{-3dB} = 14 GHz at 25 GHz). With this type of technology, broadband filters can be designed. Reflection losses in the pass band are also improved varying from -30 to -60 dB in the most favorable cases. The number of poles in the pass band is directly related with the number of sections as number of poles = number of sections -1.

This kind of study demonstrates the feasibility of filtering structures based on membrane technology at relatively low frequencies, suitable for communication systems. Nevertheless, metallic losses have not been taken into account, even if they should not be dramatic in this frequency range. At the same time, the fact of working with an almost free space wavelength makes the physical dimensions of the circuits large, and thus limits the ease of integrating them when payload volumes are a critical issue (every stub is 2.5 mm long). If multiple sections are series connected, the dimensions become rapidly non negligible. However, when working close to the submillimeter wave spectrum, this drawback may become an advantage because handling would be easier. On these basis we now analyze the simulation results of a 250 GHz micromachined bandpass filter.

The guidelines for the design and synthesis remain unchanged with the only difference in higher working frequency and hence reduced geometrical dimensions. Let us recall that the basic features of membrane technology also remain unchanged, with quasi TEM monomode propagation and losses in practice due to metallic and radiative contributions. The filter design is based on the prototype fabricated and measured at the University of Michigan, [Weller95b], with the dimensions indicated in Figure 3.24. The filter consists of four series connected open stubs.

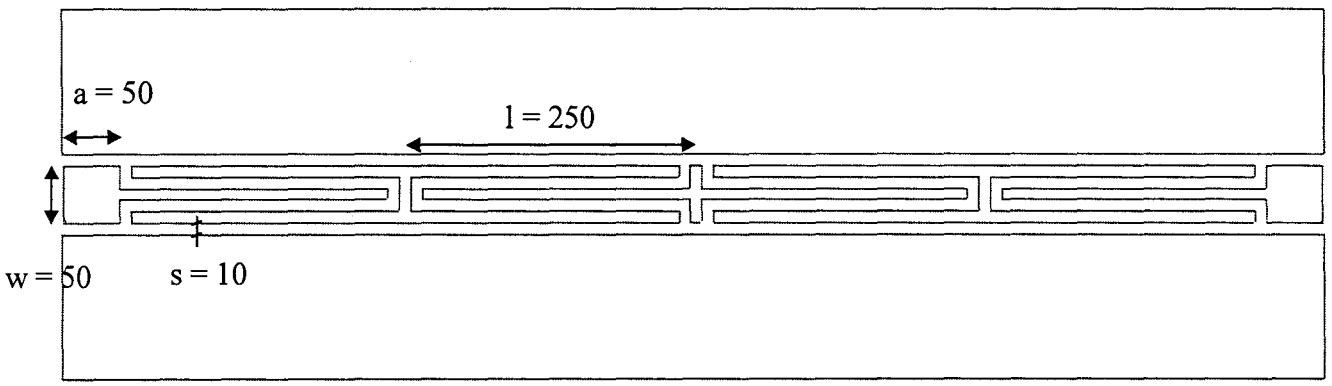

Figure 3.24: Micromachined 250 GHz bandpass filter design
(dimensions in μm).

Figure 3.25 illustrates the E field pattern at 250 GHz demonstrating the EM effect on the coplanar guided mode produced by the different stubs cut on the central conductor. At this frequency, there is a matching of a half wavelength to pair of open stubs, thus creating the same effect than in the previous structure at lower frequencies, i.e. a maximum of transmission and hence a bandpass behavior. This type of filter technology is broadband. Figure 3.26 shows the comparison for the calculated S parameters with the MoM and the measured values from the University of Michigan, reflecting a quite good agreement. There is a slight shift to higher frequencies in the simulation, that might be caused by the fact of approximating the tri-layer membrane of the real structure with a homogeneous medium with an average characteristic permittivity of ε_r = 5.2 for SiO_2. At the same time, membrane thickness is taken equal to 1.5 μm, while the exact value of this parameter may vary with fabrication tolerances.

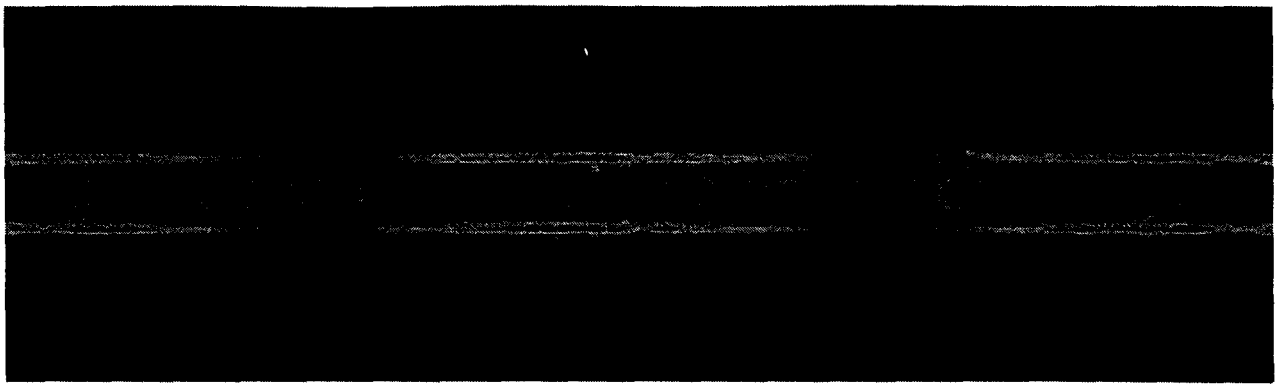

Figure 3.25: E field pattern at 250 GHz for the micromachined band pass filter.

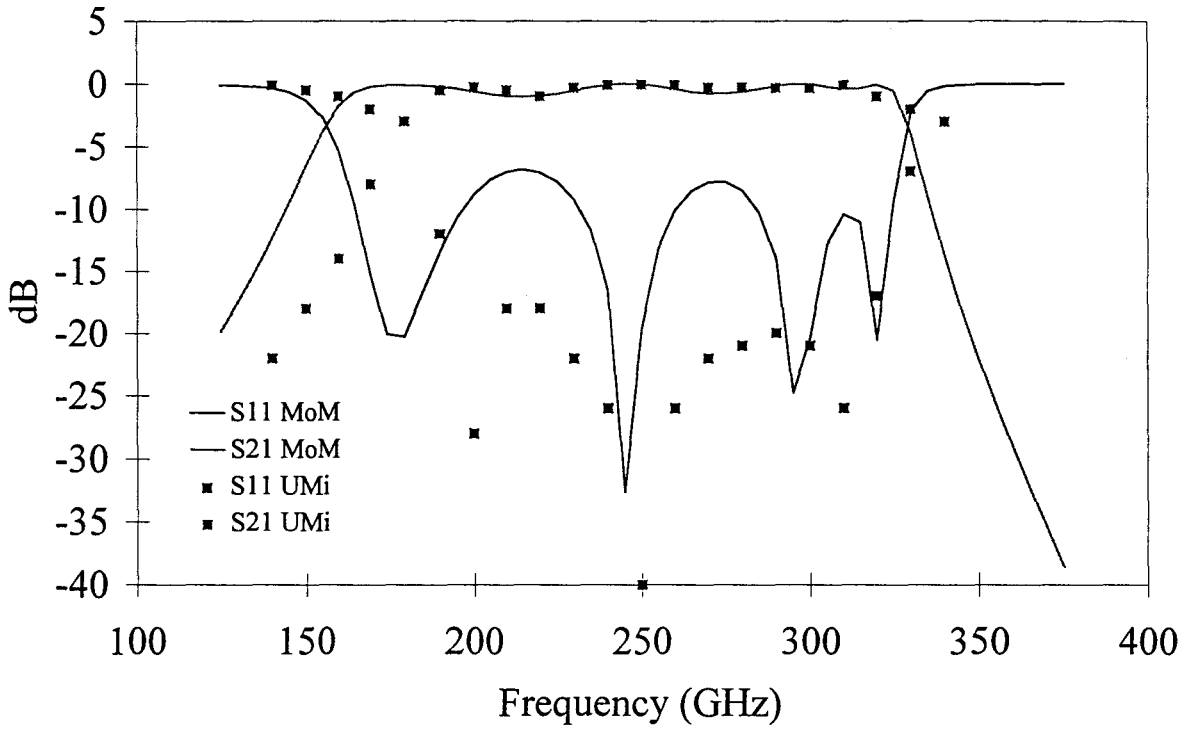

Figure 3.26: Comparison between measured (University of Michigan) and calculated (MoM) insertion and reflection losses for the 250 GHz bandpass filter.

From Figure 3.26, we can also calculate a relative bandwidth of 56 %, like in the previous low frequency structure, BW_{-3dB} = 140 GHz at 250 GHz. Scaling with frequency is consequently preserved up to these high frequencies. On the basis of this overall agreement, it is believed that HP HFSS is still accurate in the up-millimeter wave spectrum.

3.2. Micromechanical switches.

3.2.1 State of the art and motivations.

During the last few years, there has been a growing interest in microwave and millimeter wave devices able to switch RF signals. The need of tuning, switching or routing a high frequency signal has lead to great research efforts both on active and passive switches. Some of the applications involving these types of devices can be mentioned. Among them, electronically steerable antenna arrays which can be oriented through the use of a beam forming network dependent on RF switches, or frequency selective tuners that make use of a switch to achieve a determined resonant length by activating a short circuit at a precise location. Active devices are generally based on a diode or a transistor. Passive switches usually employ a moveable mechanical element, which can be alternatively in ON- or in OFF-state. The change from an open state to a closed state is often mechanically induced by an applied electrostatic force, in the case of a three terminal configuration. However, other actuation principles have been proposed.

The design criteria and features of these devices are generally based on impedance ratio between on and off states, power consumption, linearity and switching speed. The ease of integration is also a key issue in this problem, and consequently, micromachining techniques are attractive in the sense that they offer the opportunity of making different types of metallic or semiconductor structures within a complete MMIC (Monolithic Microwave/Millimeter-Wave Integrated Circuits).

3.2.1.1 Active switches.

Active switches usually employed are PIN diodes or FET transistors in GaAs technology. They are often the preferred option for example in radar systems, mainly because of their high switching speeds, which are clearly superior to those of passive devices. Also, this type of technology integrates confortably with other high frequency electronics and can achieve excellent results even at high frequencies when an InP technological system is used, [Alekseev96]. Nevertheless, they have some limitations essentially due to their 'active' nature. Power consumption or losses in the switches can be of major concern, and may even become unacceptable in particular for applications where power requirements are extremely critical. Also, active devices usually present different non-linearities like turn-on voltages (minimum voltage to switch to the ON state). Consequently, the devices do not respond linearly to the driving voltage, hence complicating the switch operation.

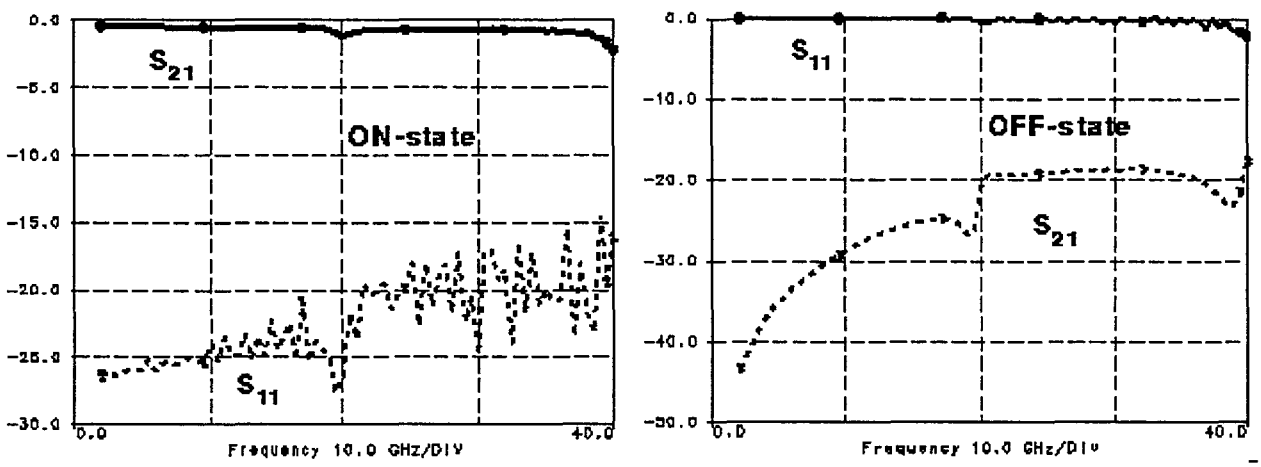

Figure 3.27: Frequency performance of an InGaAs PIN diode [Alekseev96].

Figure 3.27, illustrates the frequency performance of an InGaAs PIN diode with low insertion loss in ON state (around 1.2 dB up to 38 GHz) and high isolation in OFF (> 20 dB up to 40 GHz). These can be typical values to consider in a practical application.

3.2.1.2 Passive switches.

Micromechanical switches, a particular class of Micro-Electro-Mechanical-Systems (MEMS), have several advantages over other switch technologies for the routing of microwave and mm-wave signals. They offer low loss, low switching power, very low standby power and are extremely linear. In counterpart, the switching speeds are very slow compared to solid state switches; however, for a number of applications, their specifications appear attractive. For instance electronically steerable antenna arrays operated below 30 GHz need phase shifters for each antenna element. Micromechanical RF switches that offer lower losses can find significant applications as phase shifters for telecommunications applications, [Randall96]. Another significant feature is that a micromechanical switch has potentially a much broader operating temperature range than silicon electronic devices, so both low- and high-temperature applications may be considered.

Often, two categories of micromechanical devices can be distinguished, depending on the number of terminals, [Zavracky97]. Four terminal devices are usually referred as microrelays, with two terminals used for actuation while the other two are switched. Three terminal devices make use of an electrostatic field applied between the drive command and the input signal terminal, they are usually referred as microswitches. Switch closure shorts a beam that contacts the output terminal. The latter category is more detailed in the following.

Depending on the type of contact between the input and output terminals, two main categories of devices have been proposed: resistive or capacitive switches. The difference between both is illustrated in Figures 3.28 and 3.29. The cantilever makes use of a contact resistance to transfer the RF signal in the ON state, while the membrane diaphragm uses a coupling through a capacitance. Cantilever type devices have been widely investigated by different groups, [Larson91, Grétillat95, Zavracky97], whereas membrane devices from Texas Instruments exhibit state of the art performance, [Randall96], see Figure 3.27 (membrane up: switch off; membrane down: switch on). Resistive devices can also have a rotational motion instead of a vertical displacement, thus allowing greater isolation in OFF state, but with the drawback of higher switching times (an order of magnitude can be 1 ms versus 1 μs), [Yao95].

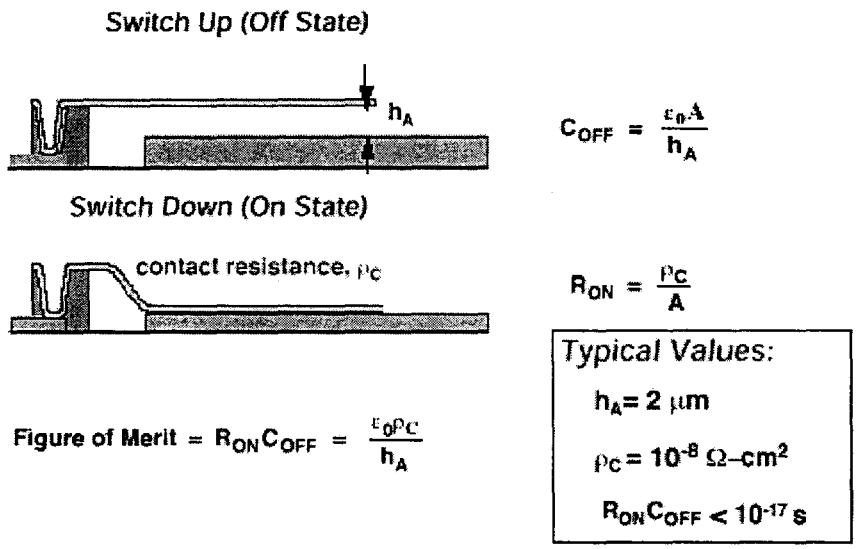

Figure 3.28: MEMS cantilevers, resistive based, switches.

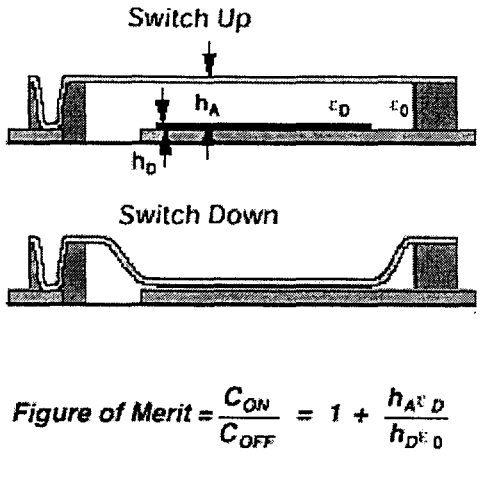

Figure 3.29: Membrane MEMS , capacitive based, switches.

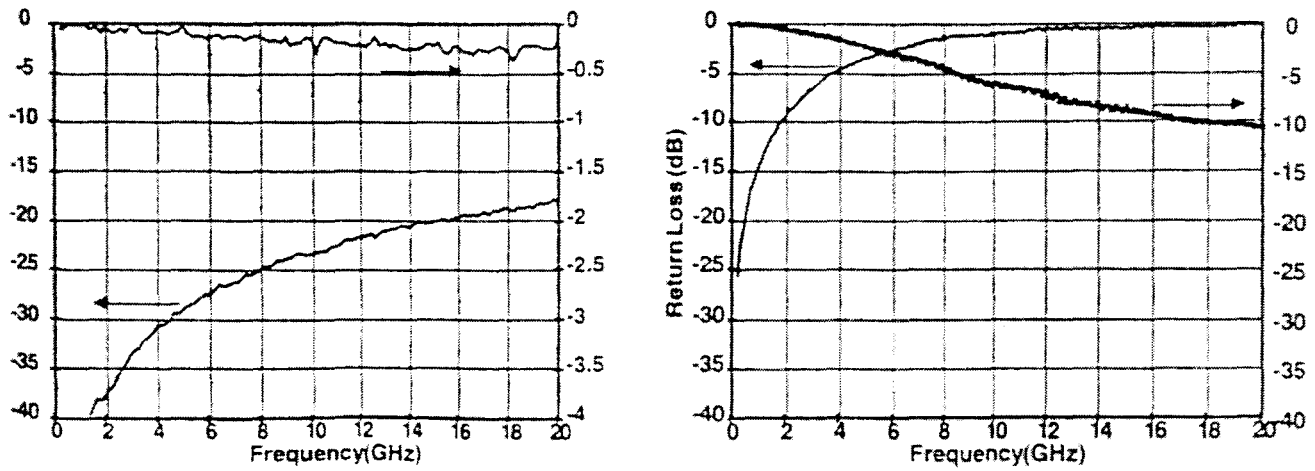

a.) b.)

Figure 3.30: Frequency performance (S_{11} on the left axis, S_{21} on the right axis) of a membrane switch, a.) membrane down, b.) membrane up.

Figure 3.30 a.) shows, for the membrane down case (switch on), a low insertion loss 0.3 dB together with a return loss of 18 dB at 20 GHz. For membrane up case (switch off, 3.28 b.)), the results are not as good, with an insertion loss of 11 dB at 20 GHz. The RF signal should 'see' an open circuit and hence a very low value of S_{21} should be obtained.

3.2.2 EM characteristics of passive switches.

The goal of the present work is to characterize the high frequency behavior of micromechanical actuators. We have simulated structures that can be described as microswitches, because a high isolation between the input and output port is expected in an off-state and very low transmission loss is also expected in an on-state.

off-state:	$S_{11} \approx 1$ $S_{21} \approx 0$	→ target parameters
on-state:	$S_{11} \approx 0$ $S_{21} \approx 1$	

The change between on and off states would be performed by electrostatic force applied to the switch in the case of a three terminal configuration. These S-parameters should also remain constant in a large frequency range. A general design of such structure is presented in Figure 3.31. The cantilever is controlled by an electrostatic force applied to the third terminal and it would be, by this means, mechanically driven from off to on-state.

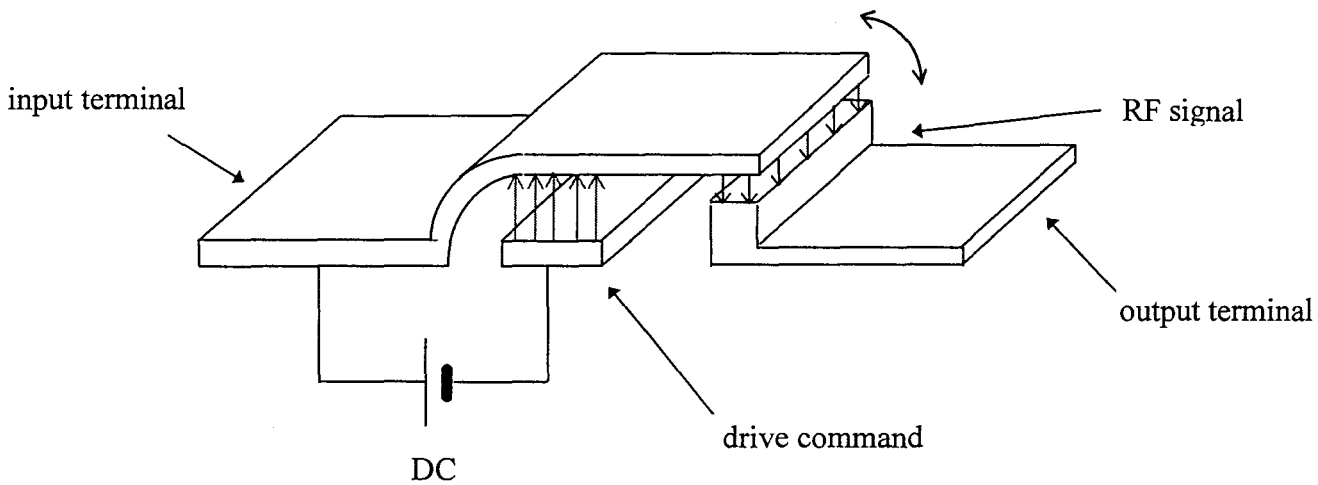

Figure 3.31: Three terminal configuration of a microswitch.

3.2.2.1 Vertical cantilever.

The goal with EM analysis of this type of structures has been the study of their electromagnetic behavior as a function of their geometry. In particular, special attention was paid to the performance of the device in terms of isolation. To this aim the influence of some of the geometrical parameters has been analyzed. We have, in a first approach, analyzed some two terminal structures. A two port configuration of the microswitch is depicted in Figure 3.32, standing for a typical cantilever.

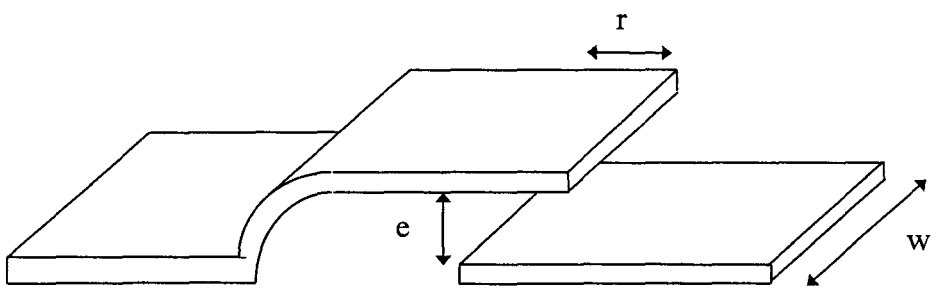

Figure 3.32: Typical configuration of a two port cantilever microswitch.

Figure 3.33 illustrates a technological realization of a microswitch manufactured in our research group. This is a SEM (Scanning Electron Microscope) view of a structure similar to those simulated in the following.

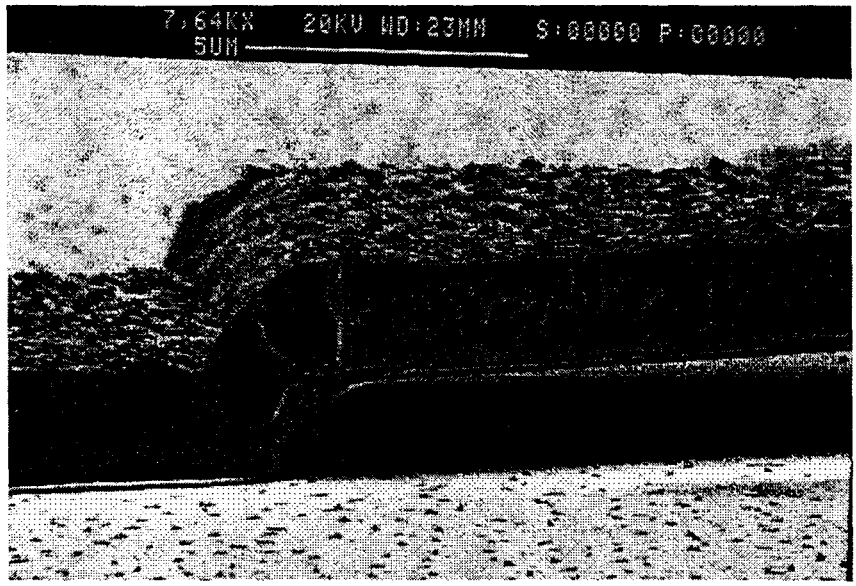

Figure 3.33: SEM view of a cantilever microswitch.

For the simulation, we have currently used a microstrip design, with technological parameters that can be, in practice, achieved in the laboratory. The substrate thickness, for all the tested configurations, is h = 100 μm; and the line width is w = 50 μm. The metal thickness employed is t = 2 μm, for all the configurations.

There are two critical design parameters, from Figure 3.30:

-overlapping between plates (r) and,
-spacing between them (e).

whereas w is chosen for a characteristic impedance close to 50 Ω. These two parameters determine the electromagnetic characteristics of the structure. Basically, it has to be seen as a series capacitance in the planar transmission line. A typical frequency behavior, described in terms of the S parameters, is displayed in Figure 3.34, for an OFF state. If it is true that the switch acts as an open circuit at low frequencies, when frequency increases, isolation between both terminals is not enough to consider the switch open. Actually, a large amount of energy will reach the output terminal as a parasitic signal. A minimum value to consider for the isolation in OFF state would be 20 dB. Below this reference threshold, the switch will be considered shunted by the parasitic signal.

The e parameter is limited because of the mechanical displacement of the switch. Since it has to be mechanically driven from off- to on-state and vice versa, this vertical dimension must not exceed a limit value. An evaluation of the mechanical characteristics has been carried out by other team members, using mechanical simulation tools. In practice, we have used $e \leq 2$ μm as a design criterion. For metallic structures, care has to be taken in order to avoid sticking between the plates, but this issue is not discussed here, since we have only evaluated the devices in the OFF state.

We have tested several models, trying to reduce the overlapping surface with every new configuration, and to obtain an optimum shape. The technological fabrication of these structures becomes more and more difficult as complexity increases. For simulation purposes, we have tested the designs in Figure 3.35. The line step in the vertical dimension has been modeled with a right

angle to decrease the complexity of the structure. In fact, simulating arcs increases notably the complexity of the mesh generation and the calculation times. The design of this clamping region is of major concern from the technological side. In contrast, the impact on the electromagnetic behavior is quite poor.

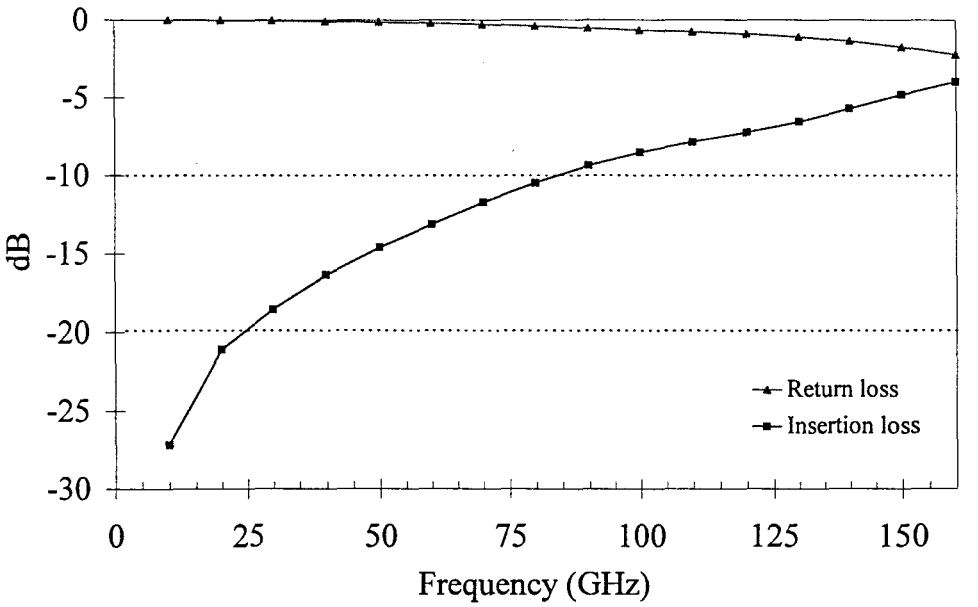

Figure 3.34: Typical frequency behavior of a switch: S_{11} and S_{12} parameters.

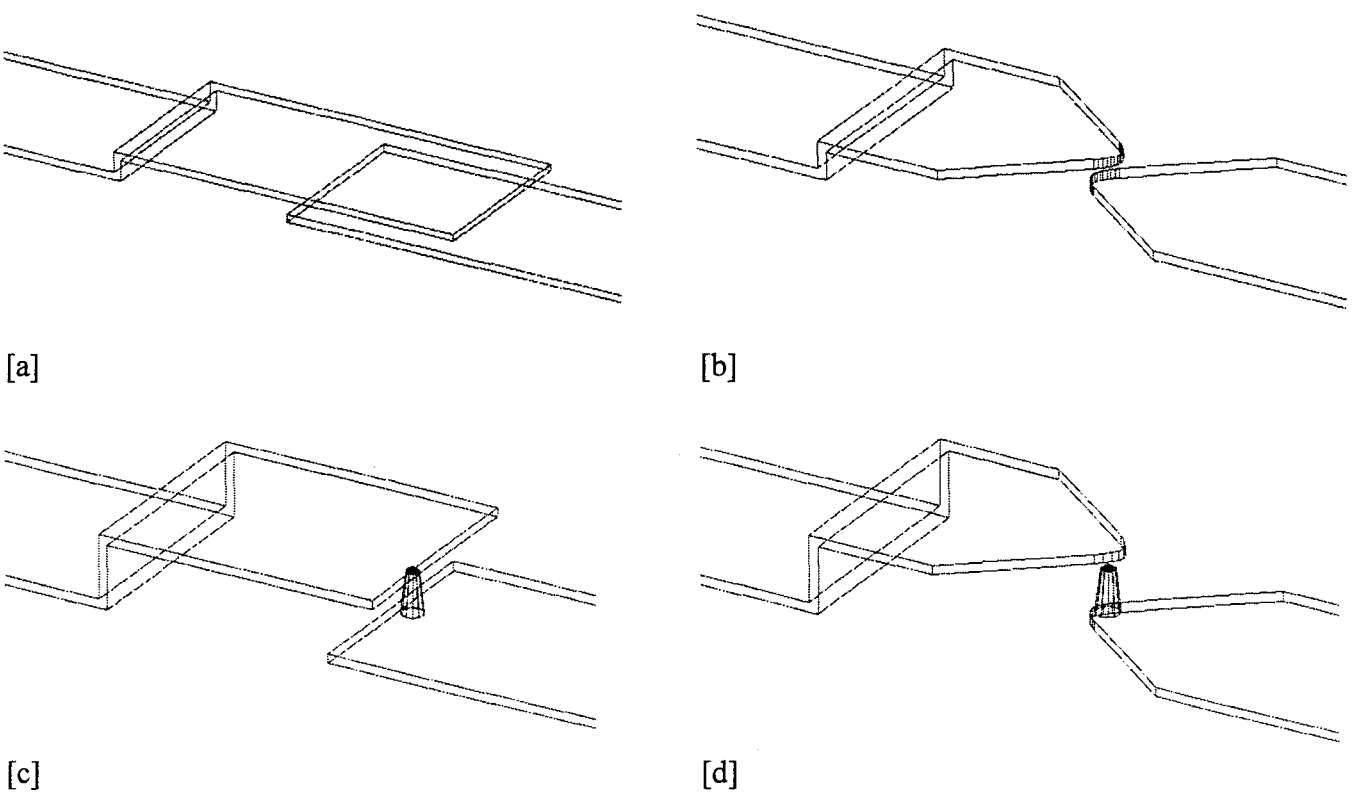

Figure 3.35: Different configurations of microswitches.

From Figure 3.35, we have tried to optimize the frequency characteristics of the cantilever structure in the OFF state. Starting with a rectangular plate switch [a], with a large overlapping surface (r = 50 μm), we have next simulated a tapered plate switch (r = 7 μm), [b], with a surface shrinking of 25 times. To improve even more the electrical characteristics of the model, and to reduce more and more the overlapping surface, we have then tested a point-contacted cantilever, [c], with a surface reduction of more than 10 times, with respect to design [b]. The metallic point structure is 10 μm high, it has a base diameter of 5 μm and a top diameter of 3 μm. The overlapping between the plates is 10 μm, but only the region near the top of the point will contribute to the E-field coupling. The e parameter, spacing between the top of the point structure and the top plate, was e = 2 μm, to permit the mechanical contact. The overlapping surface is clearly reduced but there still is some influence between the top and bottom plates. This influence is not negligible when increasing frequency, because separation between the plates is only 12 μm. Finally, in this series we have tested a structure combining the effect of tapering the plates and the use of a point-contact, [d]. The geometrical dimensions for the point and for the tapered plates are the same as in the previous designs. This is the configuration that has the best frequency behavior for the S parameters, thus giving the better isolation in the OFF state. Isolation is plotted in Figure 3.36 for all the configurations from Figure 3.35, [Mounaix97].

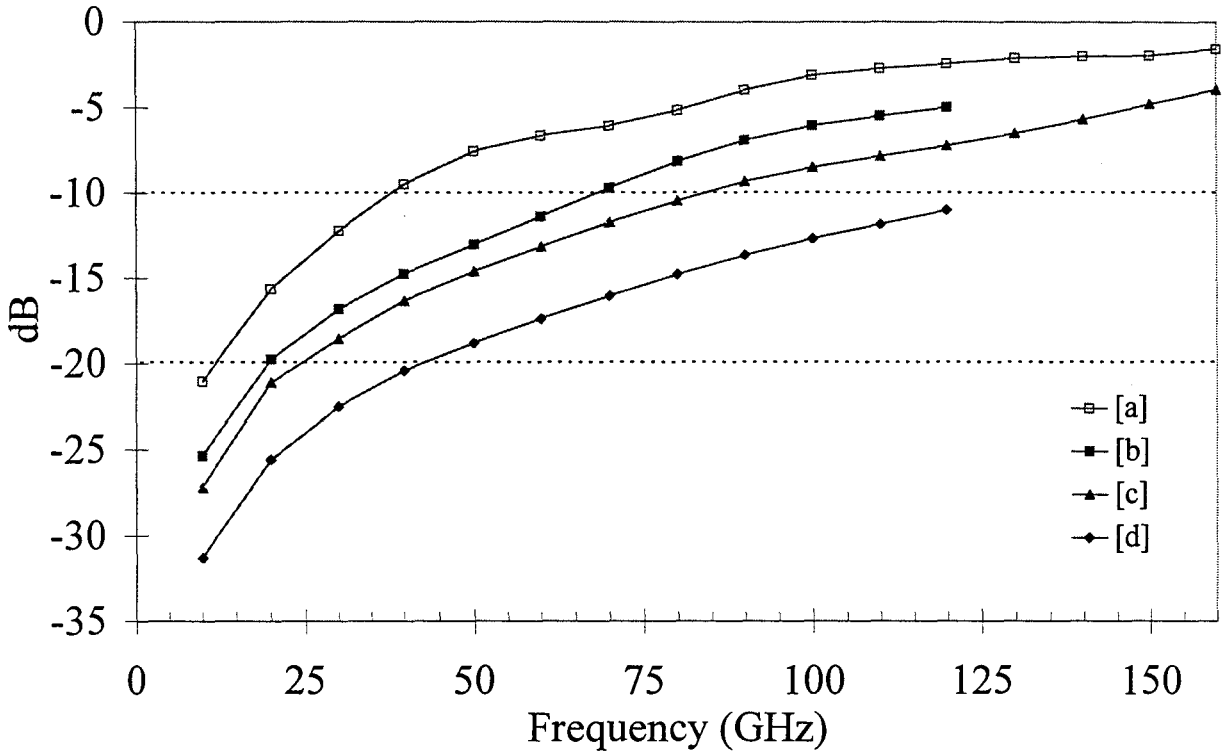

Figure 3.36: Isolation (S_{21}) in the OFF state for the different configurations of Figure 3.32.

With the shape optimization we obtain improved EM characteristics for the devices, and for example, if structure [a] had a limit operating frequency of around 10 GHz (for the insertion loss value 20 dB), structure [d] has a cut-off frequency of 40 GHz. The shapes of these curves are in close agreement with those already presented for devices fabricated with other technologies.

The most important aspect we learned from simulations is that the equivalent effective surface which has to be really taken into account for the EM parasitic coupling is much larger than the geometric surface between the two overlapping plates. This effect becomes more and more important at increasing frequencies. For a given structure, the fringing E-field becomes more and

more important and raises the transmitted energy. We can see an E-field plot in the region near the point structure [d] in Figure 3.37, for a frequency f = 120 GHz.

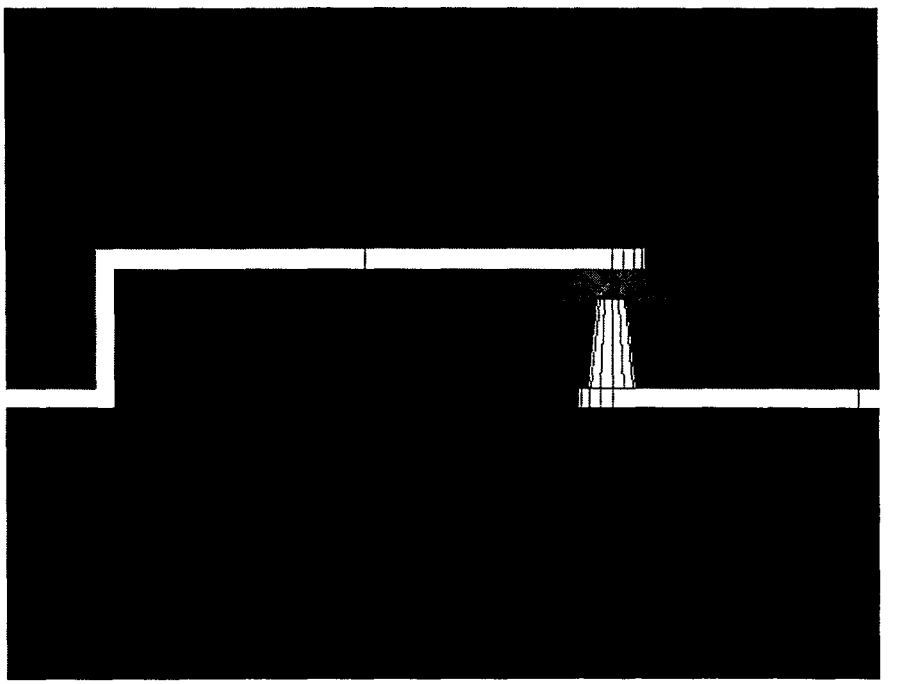

Figure 3.37: E-field magnitude plot in the region near the point contact.

It is clearly seen that the surface involved in the energy transmission is larger than the top cover of the point contact, even if the greater part of the field is confined in that region. Also, we have to say that the point contact and the line on which it is lying can present fringing effects too. A technological realization of a point contacted microswitch is displayed in Figure 3.38.

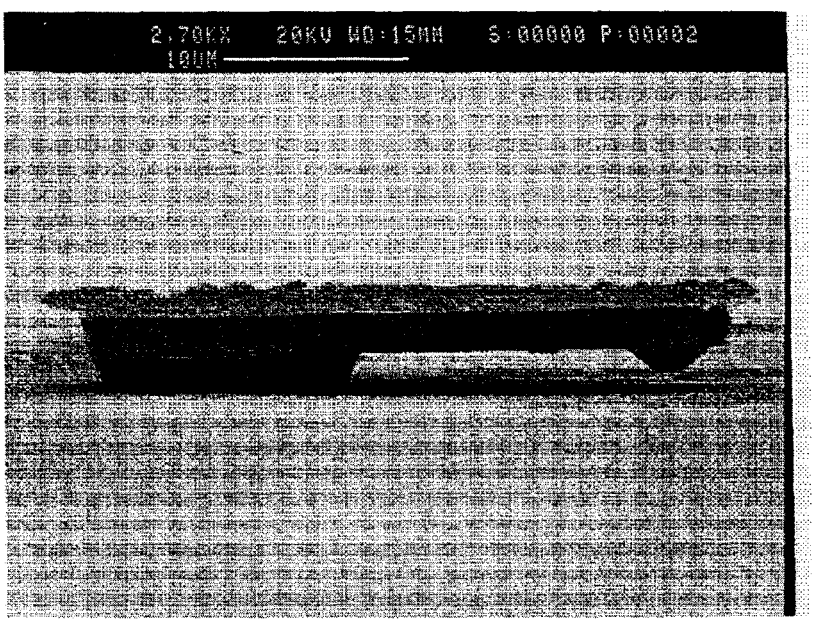

Figure 3.38: Technological realization of a point contacted microcantilever.

3.2.2.2 Planar switch.

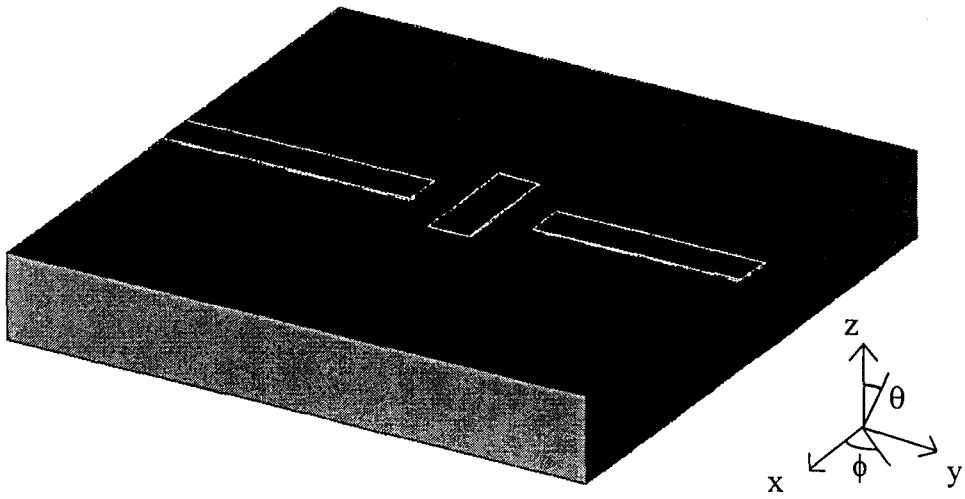

Figure 3.39: Planar rotating switch.

The next step in the switch shape optimization is what we have called a 'planar switch'. Theoretically, this kind of structure is understood to rotate along a vertical axis to allow a contact between the plates, with the transition from OFF to ON states performed using micromechanical techniques. The central plate rotates like in a configuration that we already presented before. This type of scheme increases notably the difficulty for the propagating wave to go through the discontinuity region. The port configuration of the line is the same as in the previous designs, the gap between the input and output terminals is $l = 150$ μm and the rotating plate is 50 μm wide, 150 μm long, with air gaps on both sides $g = 50$ μm. We can see such a configuration in Figure 3.39.

As we have used Absorbing Boundary Conditions (ABCs) for the side walls of this structure, we have taken into account radiation losses, which can intuitively be quite important. At the same time, we can have access to the far field plots of the structure, and hence predict the radiative behavior of this structure. The maximum radiation directions are parallel to the propagation direction and towards the substrate (more important) or the air; minima are oriented in the perpendicular directions. This behavior was already pointed out in previous sections and referred as the trapped substrate waves issue. At this frequency, substrate modes are under cut-off conditions, but there is a reactive storage of the energy in the evanescent modes. Another part of this energy is effectively radiated to the air. These phenomena are due mainly to the polarization change of the E-field in the discontinuity region. On the input side the E-field has a dominant z-component in the substrate (as it is expected for a microstrip line: from the ground plane to the line), but in the air gap region the E-field has a dominant y-direction (the propagation direction), [Carbonell95].

3.2.2.3 Equivalent capacitances.

With the purpose of quantifying the performances of each design, we have investigated the equivalent capacitance created by the switch for every configuration. To obtain a good isolation in the off-state ($S_{11} \approx 0$), we have to reach equivalent capacitances in the fF range or even less.

A first estimate of the value of this capacitance considering the approximated formula:

$$C_{geom} = \frac{\varepsilon_0 S}{e}$$

where S is the overlapping surface and e is the spacing between the plates. Calculating the geometrical surface that overlaps between the two plates is not straightforward for the point-structures because they include a 3-dimensional object, but we can have approximated values in the following table:

Structure	*r (μm)*	*e (μm)*	*S (μm²)*	*C_{geom} (fF)*
[a]	50	2	2500	11
[b]	7	2	≈100	0.44
[c]	≈4	2	≥ 7	0.03
[d]	≈3	2	≈ 7	≤0.03

Table 3.4: Overlapping surfaces and geometrical capacitance.

From EM simulations, we evaluate the electrical behavior of the simulated configurations in terms of their S parameters, with a simple equivalent circuit including the transmission line access lengths and an equivalent capacitance for the device. For these purposes we have used the following equivalent circuit:

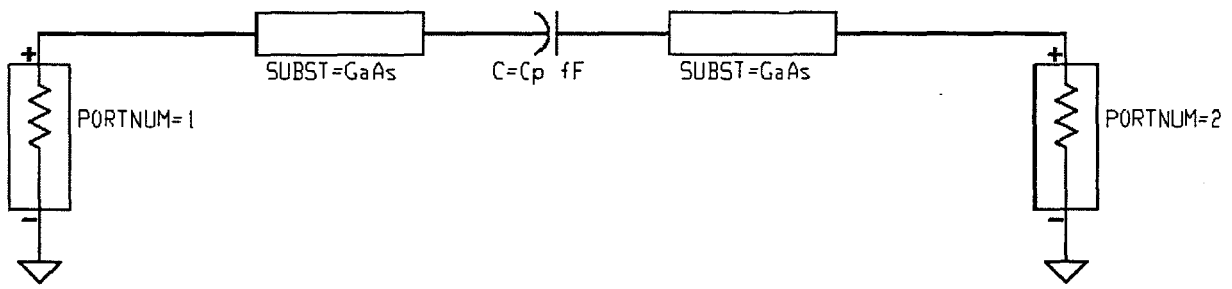

Figure 3.40: Equivalent circuit for a switch.

An example of the optimized curve for the S parameters (S_{11}, S_{21}) is given in Figure 3.41 for the planar switch, with results from EM analysis and S parameters obtained from the equivalent circuit. The agreement is good, nevertheless with the above type of circuit, radiation losses are not taken into account. The optimized values for the equivalent capacitances are listed in Table 3.5. The approximated geometrical value, calculated previously, is also displayed to take the effect of the fringing fields, and hence of the parasitic couplings, into account.

Structure	*C_{geom} (fF)*	*C_p (fF)*
[a]	11	12.38
[b]	0.44	7.24
[c]	0.03	5.24
[d]	≤ 0.03	3.26
planar	-	0.55

Table 3.5: Equivalent capacitances of the microswitches (from Figures 3.33 and 3.37).

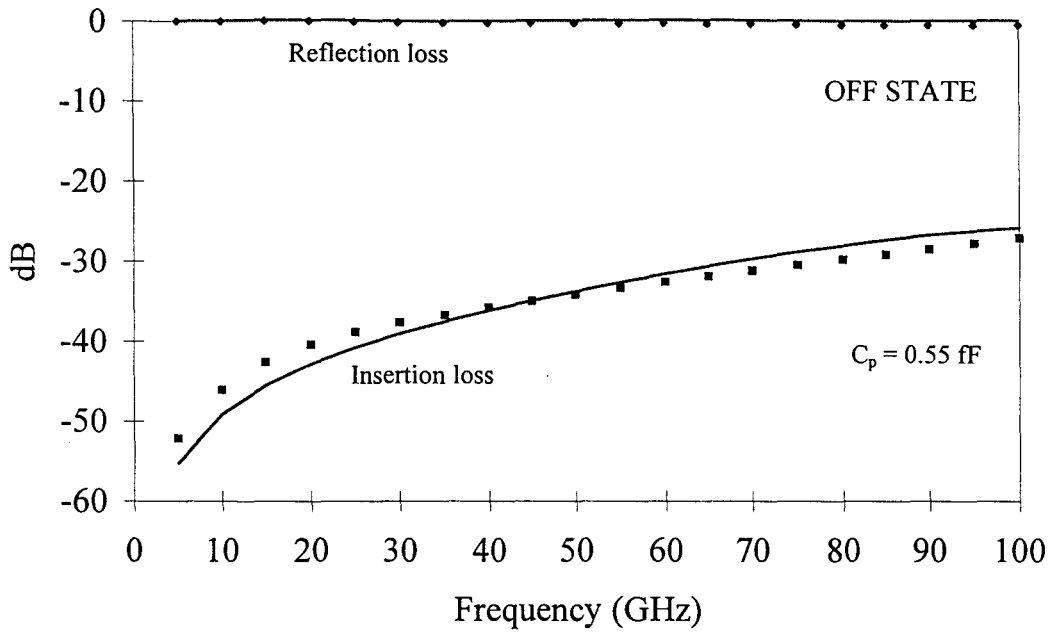

Figure 3.41: Optimized S parameters from the equivalent circuit for the planar switch.

For the rectangular plate switch both values do not differ in a significant manner. However, as expected for the other structures, the calculated values and the effective values are quite different. As a consequence, the reduction of the equivalent capacitance value is not proportional to the overlapping surface. Also, we have obtained a much lower equivalent capacitance value for the planar switch (lower than 1 fF).

3.3 Conclusion.

We have analyzed different technologies based on micromachining techniques from the electromagnetic side. Basically, two kinds of systems have been analyzed, with the common denominator of free standing structures, (i) to optimize propagation conditions in a planar transmission line at high frequencies, and (ii), to achieve switching features in microstructures.

Membrane technology has been shortly reviewed and EM analysis has demonstrated good agreement with measured characteristics of the fabricated lines. The tapered transitions from thick to thin substrate play a key role in the millimeter wave behavior. They have been analyzed separately from the membrane lines. Moreover, the lack of dispersion up to very high frequencies has permitted us to demonstrate the characteristics of this technology applied to filter structures, both for communication frequency bands (K band) and for high millimeter wave frequencies (250 GHz).

This study is completed with the analysis of different configurations of passive microswitches, a field where membrane technology can also be promising for the applications. Here again, the focus was on the EM behavior of cantilever type switches, with special attention to the isolation characteristics. This type of technology may be operated up to microwave frequencies, but parasitic couplings through fringing fields could preclude operation at millimeter waves. A possible evolution towards higher isolation concerns rotating switches, as it was demonstrated over the past, but in counterpart, the more complicated technology and higher switching times are severe drawbacks. However, cantilevers or rotating structures may be profitable for applications where switching speeds and frequencies are not stringent requirements.

When operating frequencies are in the upper region of the millimeter wave spectrum, quasi optical open structures can be of great interest considering the interference phenomena involved. Open structures presenting different pass- and stop-bands (states), as a consequence of EM interference phenomena, are the subject of the next chapter.

REFERENCES CHAPTER 3:

[Alekseev96] E. Alekseev, K. Hong, D. Pavlidis, D. Sawdai and A. Samelis, *InGaAs/InP diodes for microwave and millimeter-wave switching and limiting applications*, http://www.eecs.umich.edu/dp-group/PIN/isdrs95.html, International Semiconductor Device Research Symposium 1996.

[Bianco76] B. Bianco and M. Parodi, *Determination of the propagation constant of uniform microstrip lines*, Alta Frequenza, Vol. XLV, No. 2, pp. 107-110, February 1976.

[Carbonell95] J. Carbonell, *Electromagnetic simulation of microelectronic and micromechanical millimeter wave systems*, Training report, IEMN, Université des Sciences et Technologies de Lille, April 1995.

[Colllin92] R.E. Collin, *Foundations for microwave engineering*, McGraw Hill Ed., 2nd Edition, 1992.

[Dib91] N.I. Dib, W.P. Harokopous, L.P.B. Katehi, C.C. Ling and G.M. Rebeiz, *Study of a novel planar transmission line*, Proceedings of 1991 IEEE MTT-S International Symposium, Boston, June 1991.

[Dib91b] N.I. Dib, L.P.B. Katehi, G.E. Ponchak and R.N. Simons, *Theoretical and experimental characterization of coplanar waveguide discontinuities for filter applications*, IEEE Transactions on Microwave Theory and Techniques, Vol. 39, No. 5, pp. 873-882, May 1991.

[Drayton93] R.F. Drayton and L.P.B. Katehi, *Micromachined circuits for Mm-wave applications*, Proceedings of the 23rd European Microwave Conference, Madrid, Spain, pp. 587-588, September 1993.

[Dupuis95] O. Dupuis, *Fabrication et caractérisation de lignes coplanaires sur membranes diélectriques*, Université des Sciences et Technologies de Lille, DEA report, July 1995.

[Everard93] J.K.A. Everard and K.K.M. Cheng, *High performance direct coupled bandpass filters on coplanar waveguide*, IEEE Transactions on Microwave Theory and Techniques, Vol. 41, No. 9, pp. 1568-1572, July 1983.

[Grétillat95] M.A. Grétillat, P. Thiébaud N.F. de Rooij, *Integrated circuit compatible with electrostatic polysilicon microrelays*, Journal of micromechanics and microengineering, Vol. 5, No. 2, p. 156, June 1995.

[Gupta79] K.C. Gupta, R. Garg and I.J. Bahl, *Microstrip lines and slotlines*, Artech House Ed., 1979.

[Hélal94] M. Hélal, J.F. Légier, P. Pribetich and P. Kennis, *Analysis of coplanar transmission lines and microshield lines with arbitrary metallization cross sections using finite element methods*, IEEE MTT-S Digest, San Diego, USA, pp. 1041-1044, May 1994.

[Hoffman87] R.K. Hoffman, *Handbook of microwave integrated circuits*, Artech House Ed., 1987.

[Jain97] N. Jain and P. Onno, *Methods of using commertial simulators for microwave and millimeter-wave circuit design and optimization*, IEEE Transactions on Microwave Theory and Techniques, Vol. 45, No. 5, pp. 724-746, May 1997.

[Katehi93] L.P.B. Katehi, G.M. Rebeiz and T.M. Weeler, *Micromachined circuits for Millimeter- and Sub-Millimeter wave applications*, IEEE Antennas & Propagation Magazine, Vol. 35, No. 5, pp.2-17, October 1993.

[Klopfenstein56] R.W. Klopfenstein, *A transmission line taper of improved design*, Proceedings of the IRE, Vol. 44, pp. 31-35, January 1956.

[Matthaei80] G.L. Matthaei, L. Young and E.M.T. Jones, *Microwave filters, impedance-matching networks and coupling structures*. Artech House Ed., 1980.

[Monaix97] P. Mounaix, J. Carbonell, X. Mélique, O. Vanbésien and D. Lippens, *Micro-interrupteurs mécaniques hyperfréquences*, Proceedings of the 10es Journées Nationales Microondes, pp. 20-207, 21-23 May, 1997, Saint Malo, France.

[Randall96] J.N. Randall, C. Goldsmith, D. Denniston and T.H. Lin, *Fabrication of micromechanical switches for routing radio frequency signals*, J. Vac. Sci. Technol. B Vol. 14, No. 6, pp. 3692-3696, Nov/Dec 1996.

[Robertson96] S.V. Robertson, L.P.B. Katehi and G.M. Rebeiz, *Micromachined W band filters*, IEEE Transactions on Microwave Theory and Techniques, Vol. 44, No. 4, pp. 598-606, April 1996.

[Salzenstein96] P. Salzenstein, *Technologie des composants à hétérostructures pour les têtes de réception par satellite aux longueurs d'ondes millimétriques*, Université des Sciences et Technologies de Lille, PhD Thesis, December 1996.

[Weeler95] T.M. Weeler, L.P.B. Katehi and G.M. Rebeiz, *High performance microshield line components*, IEEE Transactions on Microwave Theory and Techniques, Vol. 43, No. 3, pp.534-543, March 1995.

[Weller95b] T.M. Weeler, L.P.B. Katehi and G.M. Rebeiz, *A 250 GHz microshield bandpass filter*, IEEE Microwave and Guided Wave Letters, Vol. 39, No. 5, pp. 153-155, May 1995.

[Williams83] D.F. Williams and S.E. Schwarz, *Design and performance of coplanar waveguide filters*, IEEE Transactions on Microwave Theory and Techniques, Vol. 31, No. 7, pp. 558-566, July 1983.

[Yu93] M. Yu, R. Vahldieck and K. Wu, *Theoretical and experimental characterization of coplanar waveguide discontinuities*, IEEE Transactions on Microwave Theory and Techniques, Vol. 41, No. 9, pp.1638-1640, September 1993.

[Zavracky97] P.M.Zavracky, S. Majumder and N.E. McGruer, *Micromechanical switches fabricated using nickel surface micromachining*, Journal of Microelectromechanical Systems, Vol. 6, No. 1, pp. 3-9, March 1997.

CHAPTER IV:

PHOTONIC BAND GAP MATERIALS

CHAPTER 4: PHOTONIC BAND GAP MATERIALS.

Photonic band gap crystals offer unique ways to tailor light and from a more general point of view the propagation of electromagnetic (EM) waves. In analogy to electrons in a crystal, or acoustic waves in a composite medium, EM waves propagating in a structure with a periodically-modulated dielectric constant are organized into photonic bands which are separated by gaps where propagating states are forbidden [Soukoulis96].

4.1 Motivations for using Photonic Band Gaps (PBGs).

During the last few years, a new class of materials called Photonic Band Gap materials has emerged. The underlying concept behind these materials stems from early notions by Yablonovitch and John [Yablonovitch87, John87]. This type of periodic artificial structures, metallic or dielectric, have recently received much interest both theoretically [Meade92, Pendry92, Winn94] and experimentally [Cheng96, Biswas96, Chen97]. Primarily designed for optical applications, more and more studies are now devoted to the lower part of the spectrum notably at centimeter and millimeter wavelengths. Therefore, PBGs have shown promise for different applications. Several examples of PBGs are illustrated in Figure 4.1. Essentially, they are designed on the basis of a periodic variation of the EM properties of the transmission medium. Figure 4.1 depicts this concept of periodic structure for one, two or three-dimensional structures. The one-dimensional case is a conventional multilayer film, studied for a long time, and here, the photonic band gap exists only for one propagation direction. By including a periodicity in the other dimensions, a complete photonic band gap can be fabricated. For the following, our research will focus on two-dimensional structures, but the concepts analyzed are applicable to the three-dimensional case.

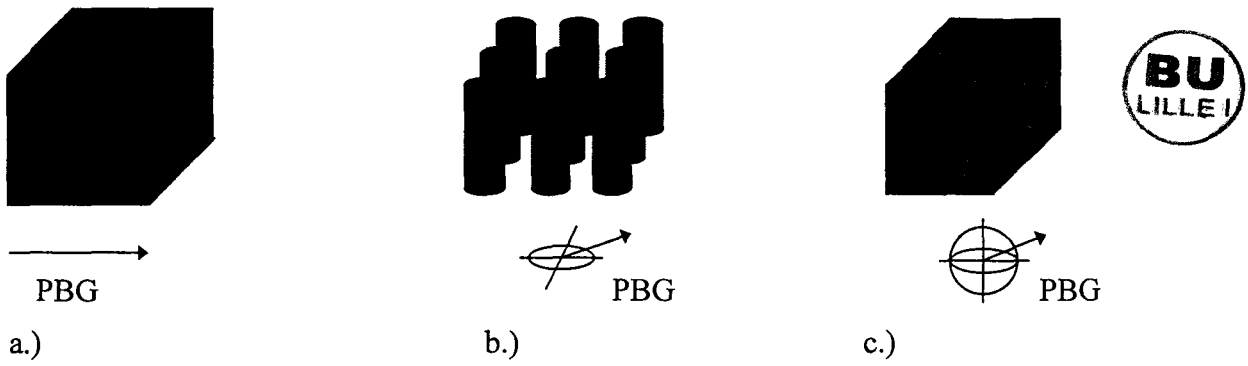

Figure 4.1: Different examples of PBG materials, a.) 1-dimensional, b.) 2-dimensional, c.) 3-dimensional.

The basic idea with these materials is that they can control the properties of EM waves in a same way solids or crystals control the properties of electrons. An analogy between the 'electronic' and the 'photonic' behaviors can be addressed through the study of the basic relationships describing the eigenstates of the system. The electron's behavior in a crystal is governed by the Schrödinger equation,

$$\left\{-\frac{\nabla^2}{2}+V(r)\right\}\Psi(r)=E\Psi(r)$$

Properties of EM waves (or photons in the optical regime) can be described through Maxwell's equations, but these can be re-written in a form analogous to the Schrödinger equation,

$$\left\{\nabla \times \frac{1}{\varepsilon(r)\mu_r} \nabla \times\right\} \vec{E}(r) = k_0^2 \vec{E}(r)$$

Both equations are linear eigenvalue problems whose solutions are determined entirely by the properties of the potential, V(r), or the dielectric function, ε(r), respectively. Therefore, if one fabricates a crystal consisting of a periodic array of macroscopic uniform dielectric "atoms", then, as in the case of electrons, the EM properties could be described in terms of a band structure. If one can have a band structure, one might be able to have a complete photonic band gap. In summary, a photonic band gap is a frequency band for which EM waves are forbidden to propagate through the "crystal" in any direction, [Joannopoulos96].

Recently, there has been a growing interest in these structures at microwave and millimeter wavelengths. Most of the research efforts were concentrated in the development of 2D and 3D PBG materials consisting of positive and frequency-independent dielectrics because, in that case, one can neglect the problems related to absorption. However, there have been some recent works on PBG materials constructed from metals [Smith95, Pendry96, Sievenpiper96], which suggest that those metallic structures may be advantageous in low-frequency regions where the metals become almost perfect reflectors. From the transmission point of view, both types of structures exhibit allowed and forbidden band gaps, but the main difference between dielectric- or metallic-type structures is, for the latter, a forbidden band extending from DC to a certain cut-off frequency, defined by Yablonovitch as a plasma-type frequency (for the incident E-field polarized parallel to the wires). Figure 4.2 shows the transmission characteristics of a structure formed of 4 rows in the propagation direction of dielectric (ε_r = 9.6) or perfect conductor cylinders (case b.) in Figure 4.1 with a triangular lattice design). The metallic structure will be analyzed in more details in the next section.

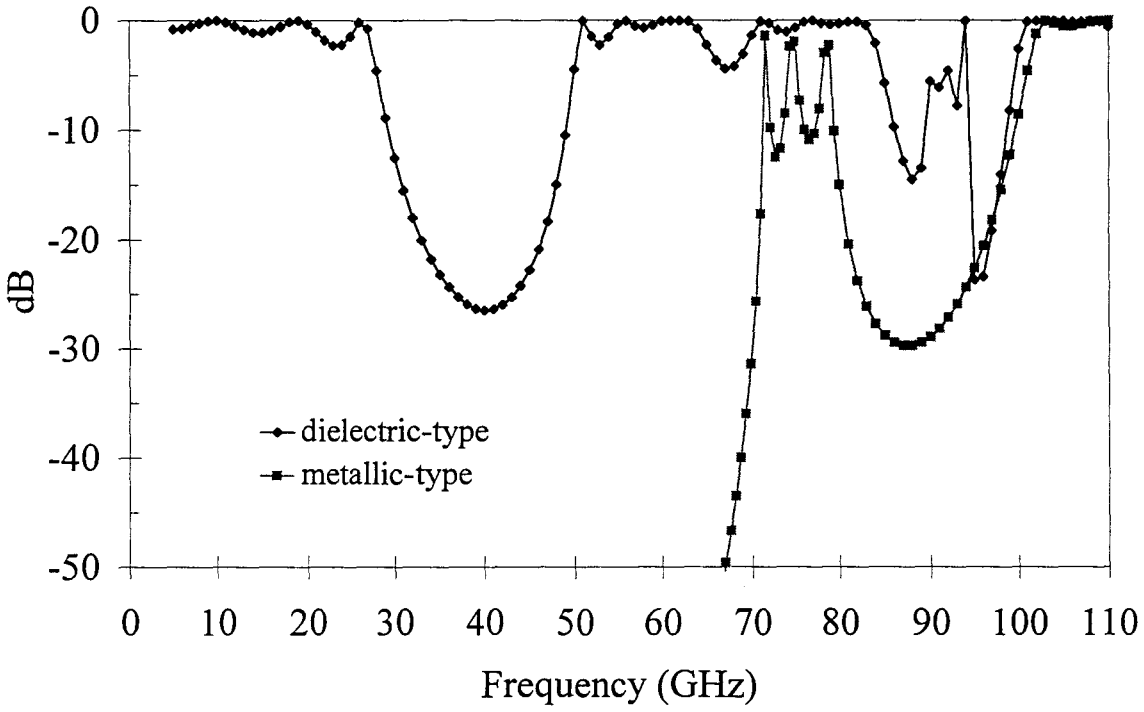

Figure 4.2: Typical transmission characteristics of dielectric- and metallic-type 2D-PBGs.

While the dielectric structure is transparent at low frequencies and shows several attenuated bands (around 40 GHz for example), the metallic structure is opaque at low frequencies (up to 70 GHz), and different pass bands can be noticed for higher frequencies.

Used as reflectors or substrates for planar antennas, PBGs have shown potential advantages over other well-known technologies [Sigalas96, Suzuki96, Ellis96, Kesler96, Poilasne97]. Indeed, radiation performances can be greatly improved in terms of directivity and/or substrate losses if the frequency band where the antenna radiates fits the forbidden gap of the artificial structure. In this context, metallic lattices appear as good candidates to go further in optimization due to the important know-how for patch antennas. An analysis of a combination of a PBG and a dipole antenna is given in the following. Also, other applications have been successfully investigated, like high-Q cavities (which are also analyzed in the present work), [Smith94], or tuning elements in broadband circuits [Radisic98].

In the next sections a detailed analysis of a metallic PBG structure is done on the basis of different concepts. First, a particular metallic lattice with geometrical dimensions on the millimeter scale is designed and analyzed, both theoretically and experimentally. EM simulations are compared to RF measurements at millimeter wave frequencies in terms of insertion loss and phase of reflection coefficient. The localization of the electric field inside the cavity formed by the periodic medium is described and an original analogy with semiconductor superlattices is established, [Carbonell97]. Three dimensional structures are then analyzed starting from a diamond-like lattice. The same metallic structure is afterwards studied when the periodicity of the structure is broken through the creation of a cavity. Finally, the combination of such a metallic structure with a dipole antenna is addressed by means of theoretical calculations of the far field radiation patterns.

4.2 Metallic PBG Structures.

Metallic PBG structures are analyzed by considering two- and three-dimensional cases. The two-dimensional case has been carried out on structures excited with a TM_z incident wave normal to the PBG surface. Three-dimensional structures exhibit the same characteristics for TE_z or TM_z polarizations. In each case the structure is assumed to be infinite in the transverse directions and finite only in the propagation direction. As we will see, this fact strongly influences the behavior of the simulated and characterized structures.

4.2.1 Two-dimensional PBG analysis.

4.2.1.1 Measurements.

Figure 4.3 gives a schematic top view of the two dimensional wire photonic lattice investigated in the following, whereas Figure 4.4 depicts the experimental set up used for the measurements. The structure consists of metallic cylinders embedded in air and arranged in a diamond-like scheme. The dimensions, on the millimeter scale, are equal to those of the structure characterized experimentally (4.96 mm and 2.69 mm for the long and short diagonals, respectively). The diameter of the wires is 1.17 mm. By analogy with solid state physics, two vectors a_1 and a_2, defining the basic cell with one wire per cell, can be chosen. In this case, the filling factor is calculated by dividing the unit cell area by the area of a wire, we then have $\rho = 16\%$.

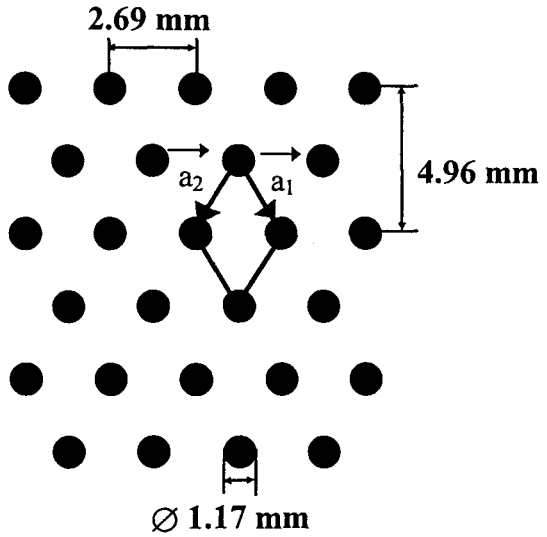

Figure 4.3: Schematic design of a 2-D PBG formed of metallic cylinders embedded in air.

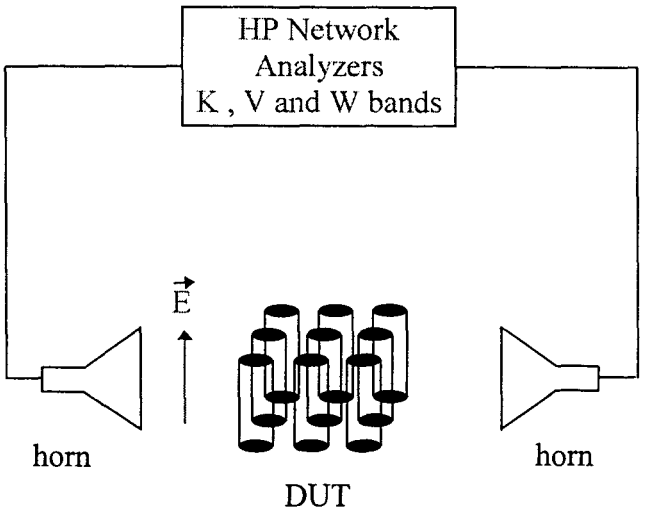

Figure 4.4: Experimental set up for the measurements.

In practice, the metallic wires were mounted between two drilled plastic plates according to the mesh design, see Figure 4.5, the distance between the two plates is around 3 cm. With this type of configuration, some parameters, such as the filling factor or the number of rows constituting the PBG can be easily modified, and several lattice schemes can be considered.

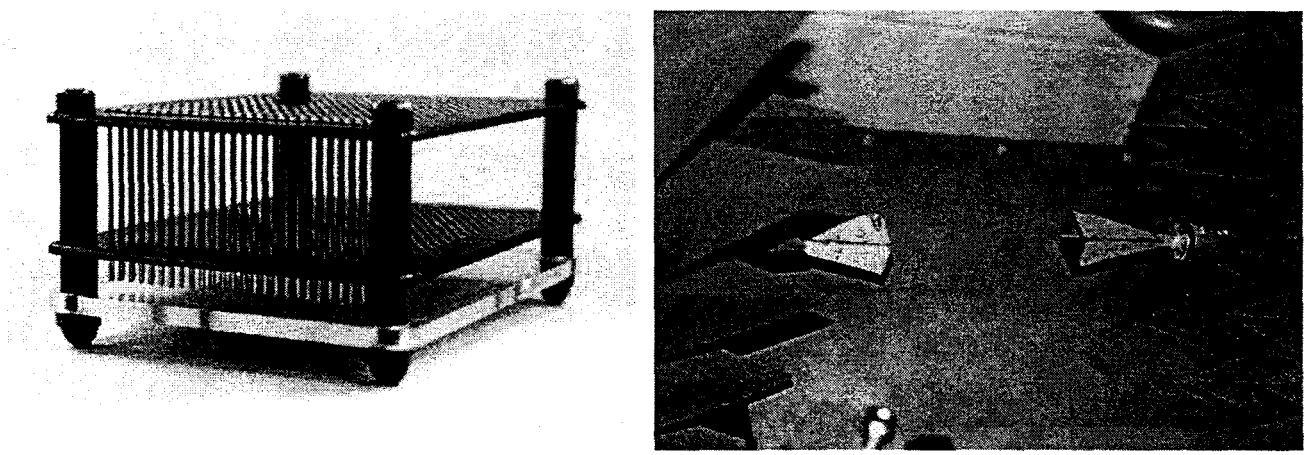

a.) b.)

Figure 4.5: Photographs of the experimental mount for the PBG structure, a.) and the 50 - 75 GHz horn antennas used for the measurements, b.).

Measurements have been carried out by means of different Hewlett-Packard network analyzers operating in the K (22 - 40 GHz), V (50 - 75 GHz) and W (75 - 110 GHz) bands. Microwave absorbers can also be seen, they are used in order to minimize parasitic reflections from the environment. In every case, a TRL calibration was performed between the input and output

waveguide flanges. Horn antennas are then used as the feeding and probing elements. Under these conditions, the electric field polarization is vertical. Furthermore, measurements were performed under normal incidence, i.e. the propagation direction is parallel to the long diagonal axis of the diamond scheme, [Carbonell97b].

In the experimental study, we have analyzed four structures to evidence the localization of the electric field inside the periodic structure; one, two and four rows of wires in the propagation direction with the lattice scheme of Figure 4.3 and five rows of wires doubling the lattice dimensions and reducing the filling factor by four (5.38 mm and 9.92 mm for the short and long diagonals, respectively, and ρ = 4%). For the insertion loss measurement, we proceeded in two steps, (i) the transmission losses of the experimental set-up between the emitting and the receiving antennas were measured without the PBG; (ii) the PBG is sandwiched between the two antennas keeping the same distance between them. The S_{21} parameter is then deduced from the difference between the first and second measurements. These structures are 42 wires wide in order to avoid any end effects in the transverse direction.

One row of wires in the propagation direction forms a typical metallic grid, which stops the polarized waves parallel to the metallic wires, but two rows already have a resonant cavity behavior which is carefully analyzed. A comparison between measured and calculated transmission coefficients is displayed in Figure 4.6, for these two structures. The resonant frequency for the two rows structure is 74.7 GHz, whereas for the one row structure, transmission increases monotonously until the half wavelength is comparable to the wire spacing in the transverse direction. When the second row is added, there is a cavity created, and hence a resonant behavior, due to the matching of a half wavelength to the lattice dimension in the propagation direction. In this case, the second pass band has the same origin as for the single row structure.

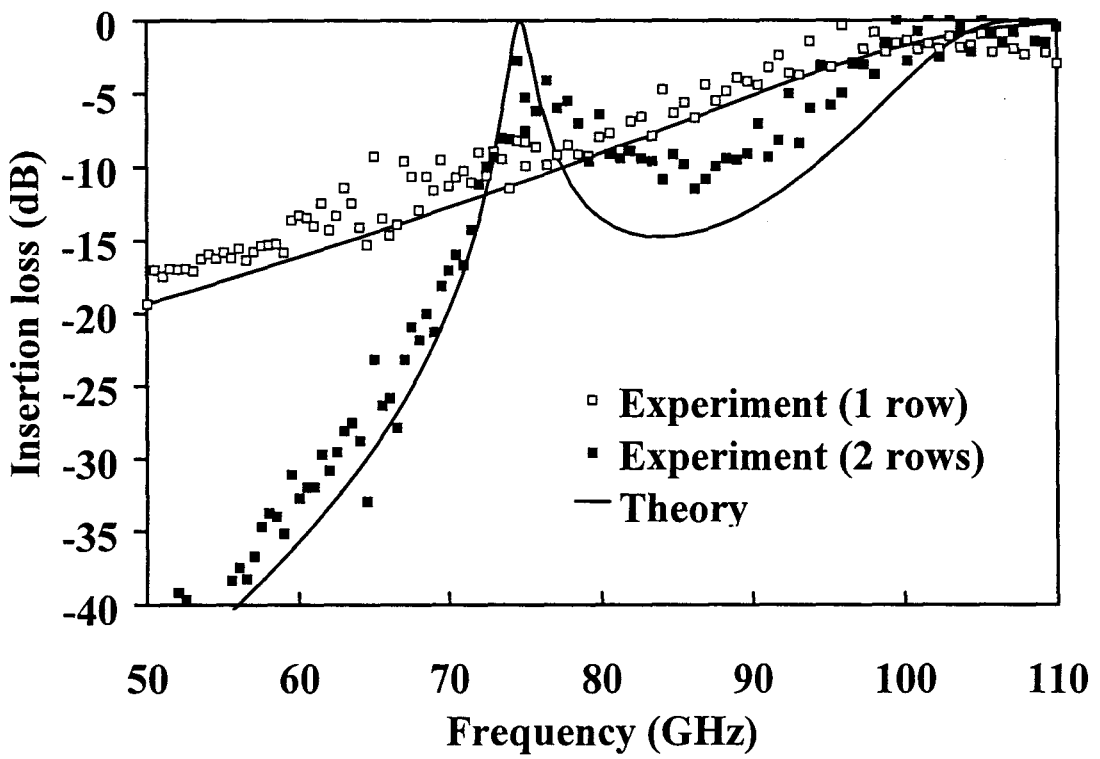

Figure 4.6: Transmission coefficients calculated (full lines) and measured through one row (open square) and through two rows (full square).

Now, Figures 4.7 and 4.8 show the transmission spectra for a four rows structure in the 50 - 110 GHz band and for a five rows double structure (doubled dimensions) in the 22 - 40 GHz band. In all cases, the agreement between measured and calculated characteristics is good, in particular for the resonant peaks and the pass bands.

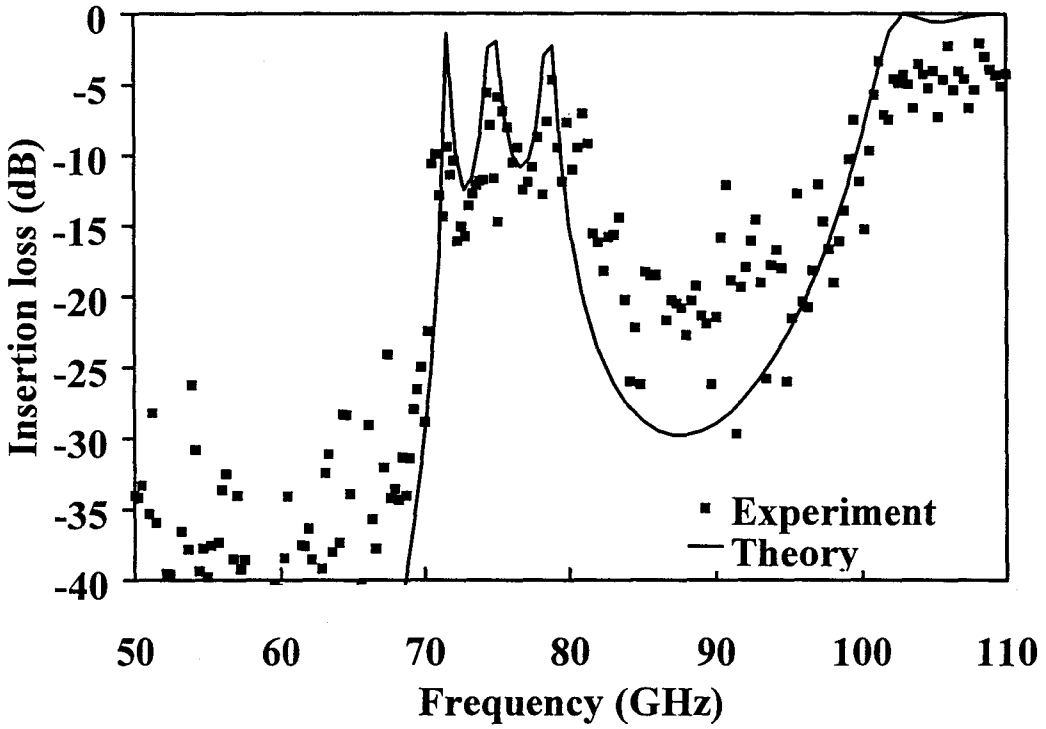

Figure 4.7: Experimental and calculated magnitudes for S_{21} for a four rows structure between 50 and 110 GHz.

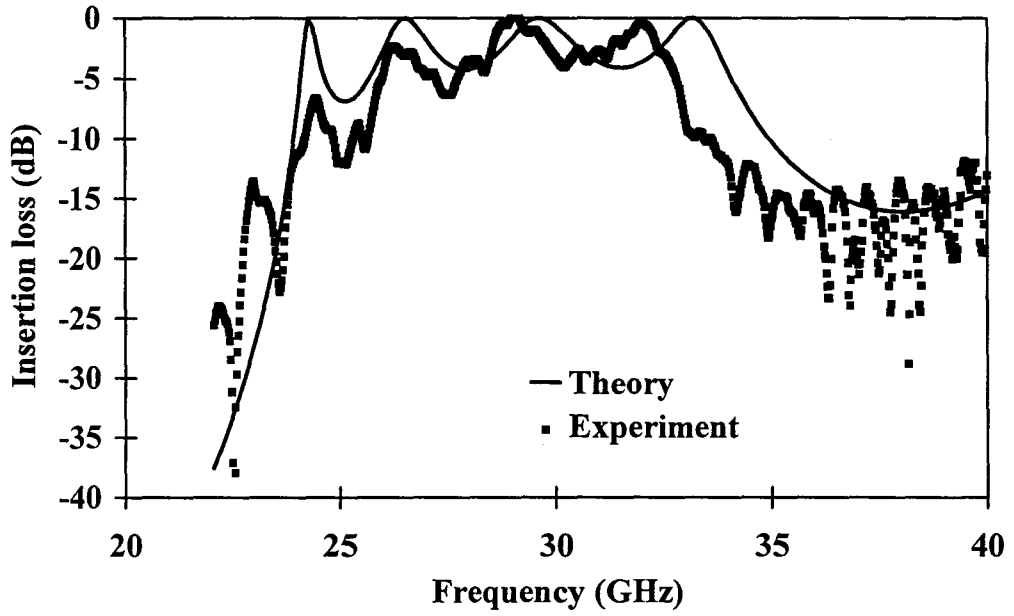

Figure 4.8: Experimental and calculated magnitudes for S_{21} for a five rows structure between 22 and 40 GHz.

For the latter structures, the characteristic frequency bands are a consequence of the geometrical dimensions of the lattice, but the general behavior is the same for both. The prototypes scale with frequency, besides the fact of having decreased the filling factor to 4 % in the second. As expected for metallic structures, we have a cut-off frequency (68 or 24 GHz), followed by a pass band with a number of resonant peaks equal to the number of rows minus one. We will see that this effect is due to localization of the E field inside the cavity formed by the interfaces air/PBG. After this first pass band, there is an abrupt reduction in the transmission of -25 dB around 87 GHz (25 GHz wide) or -16 dB around 38 GHz respectively. Finally, there is a second transmission window which starts at about 100 GHz, for the four rows structure, or beyond 40 GHz for the five rows doubled structure.

The phase of the reflection loss can also be assessed by means of a specific procedure. It is difficult to realize this type of measurement because the reference planes for the TRL calibration are located at the waveguide flanges, and thus before the horn antennas. Nevertheless, the reference plane can be shifted if an 'electrical delay' correction is applied to the measurement. As shown in Figure 4.9, the phase variations of the reflection coefficient are monotonous in the band gaps, whereas pronounced phase jumps can be observed in the pass bands.

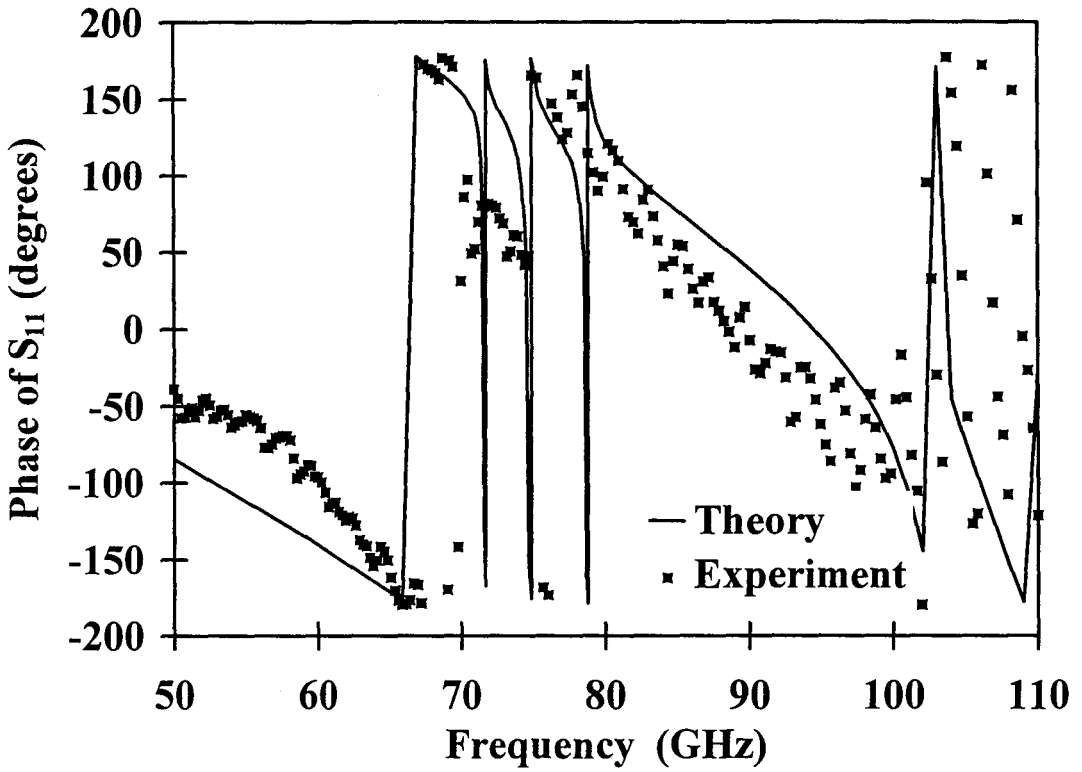

Figure 4.9: Experimental and calculated phases for S_{11} for a four rows structure between 50 and 110 GHz.

4.2.1.2 Analysis.

Figure 4.10 shows an example of simulated structure in the case of 4 rows in the propagation direction. Simulations are carried out for a vertical polarization of the electric field parallel to the wire direction and assuming a propagation direction along the [11] axis of the photonic lattice (normal incidence). For these structures, the solution of the Maxwell equations is obtained using the commercial software package HFSS. Also, we assumed that the rod array is made of perfectly conducting cylinders ($\sigma = \infty$), and the embedding space is air ($\varepsilon_r = 1$, $\mu_r = 1$). The height of the

cylinders has been chosen arbitrarily 1.5 mm. Different boundary conditions have been applied to the simulation domain, based on the image theory: top and bottom boundary regions are electric walls, whereas lateral plates are magnetic walls acting as periodic conditions to simulate an infinite medium along the transverse directions. With these conditions, a plane wave with the E field polarized parallel to the metallic cylinders is feeding the structure.

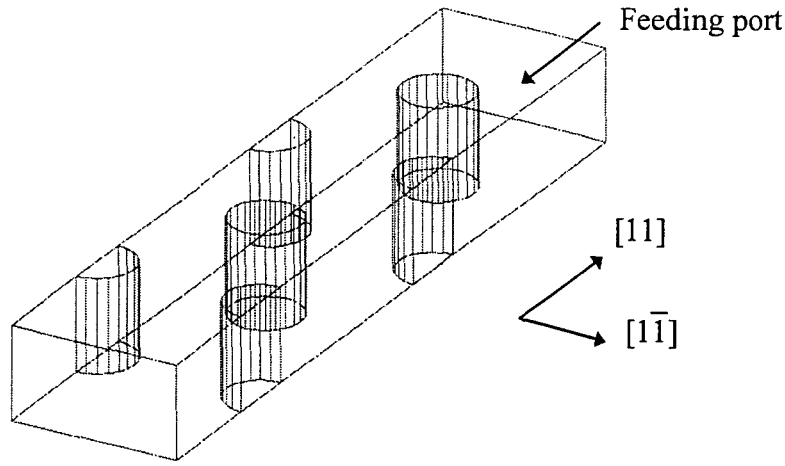

Figure 4.10: Simulated structure in HFSS, with four rows in the propagation direction.

Figures 4.6 to 4.9, permit us to make a comparison between simulation results and experimental data. Agreement is overall good for the transmission characteristics as well as for the phase of the reflection loss. Nevertheless, at low frequencies, the background noise of the measurement set up is too high compared with the extremely low transmission levels. As a consequence, a meaningful comparison is not possible under the 40 dB dynamic range of the network analyzers. For the analysis, we have considered interesting the four rows structure, because well defined peaks are visible, and at the same time, the rejection in the forbidden bands is compatible with the dynamic range of the network analyzer.

Figure 4.11 shows the E field patterns inside the structure at different frequencies, with the feeding port on top. At f_1 = 60 GHz (case a.)), we are below the cut-off frequency and in this case, the half wavelength ($\lambda/2$) of the incident wave is too large with respect to the wire spacing and the EM wave cannot propagate. However, as demonstrated in the following this is not a grid-like cut-off associated to the matching of $\lambda/2$ to the wire spacing in the transverse direction. In fact as noted before [Pendry96, Sievenpiper96] this characteristic frequency can be regarded as being analogous to a type of plasma frequency in a web-like structure.

Frequencies f_2 = 71.5 GHz and f_3 = 75 GHz (4.11 b.) and 4.11 c.)) correspond to the first two peaks of the transmission characteristic of Figure 4.6. In the first case, the E-field has a maximum in the center of the structure, and in the second, two maximums are shared between the first and the third inter-row spacings. Here, the most striking effect is the localization of the electric field in the cavity formed by the air/metallic array/air structure. The spatial evolutions of the E-field are shaped by envelop functions which correspond to the eigenmodes of the Fabry-Perot cavity. The situation is quite comparable to the one encountered in finite semiconductor superlattices where each peak observed in the transmission spectra can be attributed to the eigenstates of a finite superlattice. In order to illustrate such an analogy, we give in the next section a comparison of a PBG material with a semiconductor superlattice.

Figure 4.11 d.), corresponds to the minimum of the transmission (-30 dB) in the second band gap, f_4 = 87 GHz. This attenuation value is strongly dependent on the number of cells which compose the PBG, or alternatively the filling factor of the structure. In the propagation direction there is an exponential decay of the magnitude of electric field with a very short evanescent length.

Such a behavior is characteristic of an imaginary propagation constant, in agreement with the picture of a negative effective permittivity [Pendry96].

Finally, at f_5 = 110 GHz transmission is again maximum and there is a true propagation through the structure, i.e. more 'fluid', in contrast with the idea of eigenmodes of the first pass band. Here, $\lambda/2$ is smaller than the wire separation in the two lattice dimensions, and thus an analysis varying the phase of the incident wave proves that there are propagation phenomena in longitudinal and transverse directions inside the PBG, [Vanbésien98].

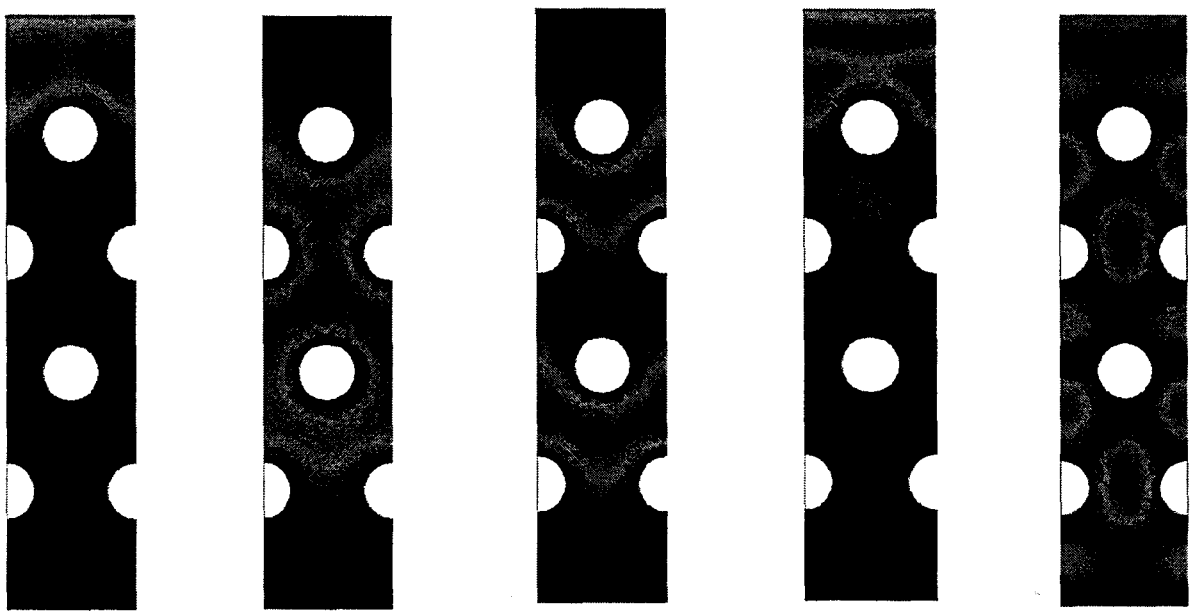

a) f_1 = 60 GHz b) f_2= 71.5 GHz c) f_3 = 75 GHz d) f_4= 87 GHz e) f_5= 110 GHz

Figure 4.11: E field patterns inside the structure at different frequencies.

We have also investigated the importance of the number of cells that form the PBG in the propagation direction as shown in Figure 4.12.

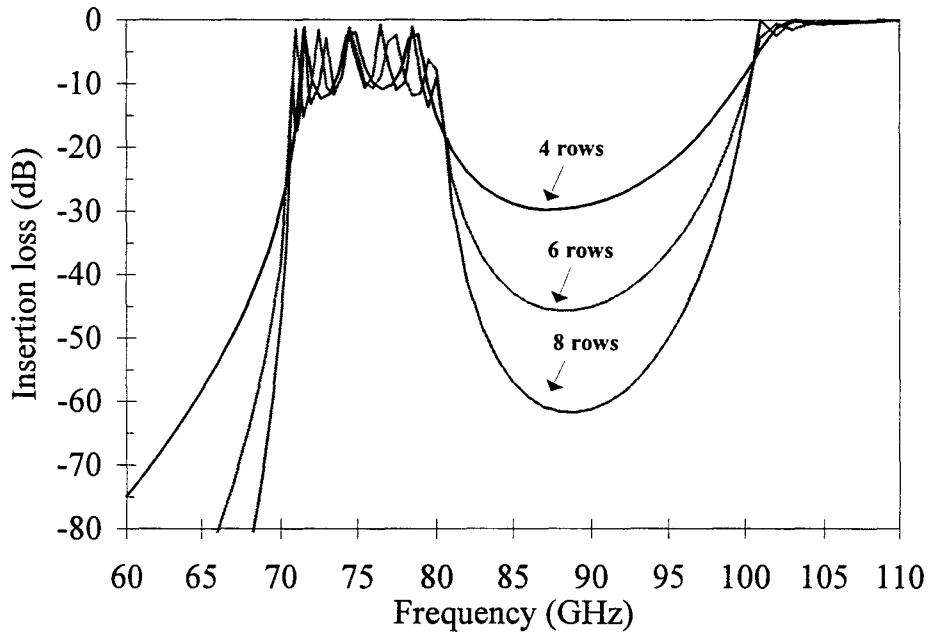

Figure 4. 12: Evolution of the transmission characteristic as a function of the number of rows of the PBG in the propagation direction.

If we double the number of rows (8), using the basic mesh dimensions, the transmission within the forbidden band gap is decreased about three orders of magnitude and we get an insertion loss of -60 dB. Results for a 6 rows structure are also reported. Approximately, each row contributes to the insertion loss with 7.5 dB of reduction in the forbidden band. Nevertheless, the bandwidths within and out of the forbidden gaps remain unchanged. This means that in the transmission windows, peaks are closer to each other.

4.2.1.3 Analogy with a semiconductor superlattice.

Under all the previous assumptions, we first calculate the insertion loss for a structure eight rows deep in the propagation direction, between 50 and 110 GHz. In order to have further insight into the reflection and transmission phenomena, let us now consider the spatial distribution of electric field magnitude within the periodic structure. Figure 4.13 shows the transmitted power versus frequency under normal incidence and the E field patterns for the first four peaks of the first pass band.

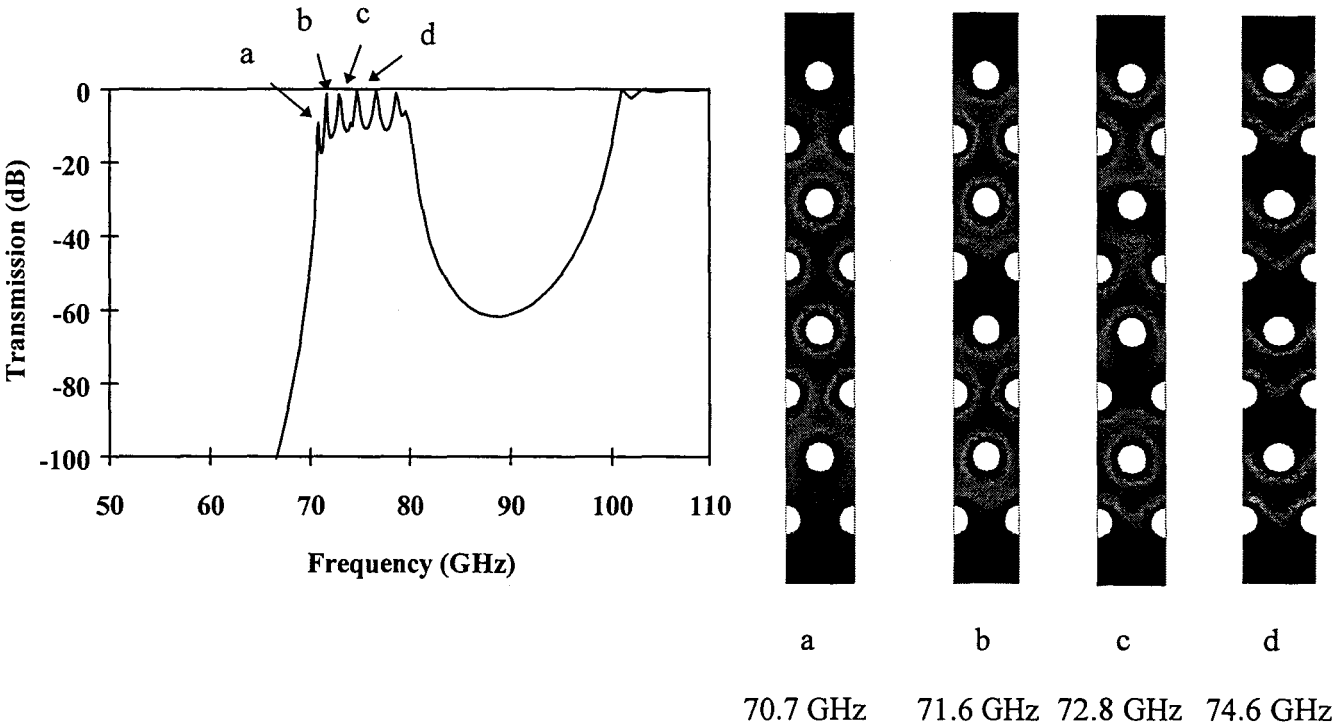

Figure 4.13: Calculated magnitude of S_{21} for an eight rows deep structure in the propagation direction and E field patterns for the first four peaks of the first transmission band.

As we noted previously, there is a striking effect of localization of the electric field in the cavity formed by the air/metallic array/air structure. The transmission characteristic and the electrical field patterns of the PBG are comparable to the quantum transmission probability and the electron wave functions of the superlattice. In order to illustrate the analogy, we give in Figure 4.14, the quantum transmission probabilities versus electron energy calculated by solving the Schrödinger equation [Vanbésien92] for a finite semiconductor superlattice (average effective mass = 0.067 m_0) with eight heterostructure barriers. The well and barrier widths (8.4 nm thick and 1.6 nm thick respectively) along with the potential discontinuity (0.16 eV) were chosen to fulfill some frequency ratios between the stop and pass-bands of the photonic crystal.

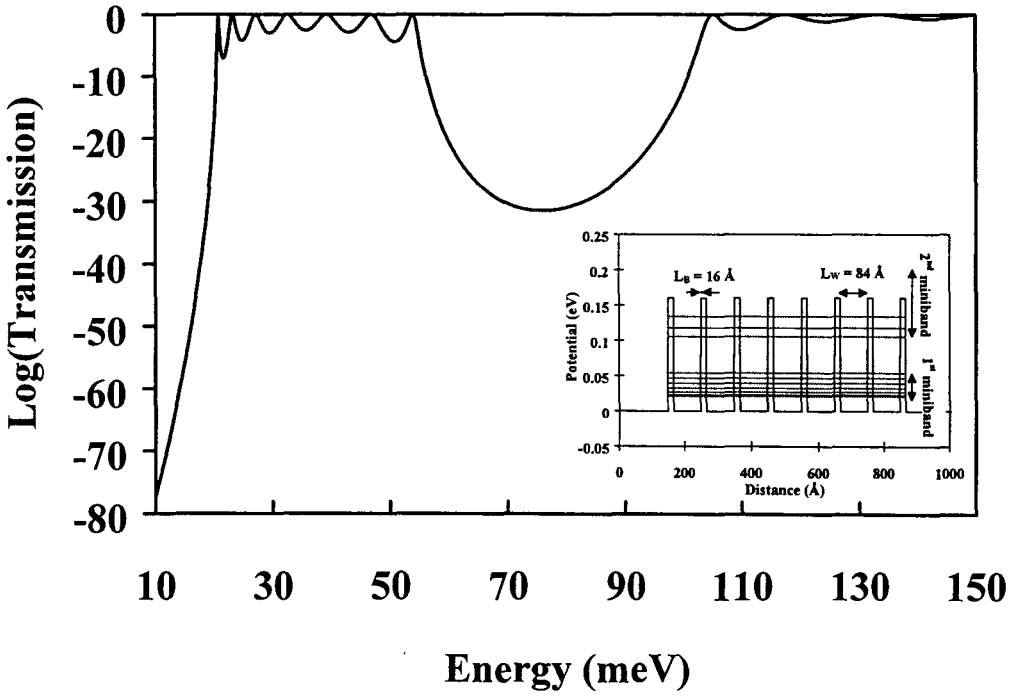

Figure 4.14: Calculated transmission coefficient for a semiconductor superlattice (structure given in inset).

The analogy between the two kinds of devices is impressive and illustrates that the localization of the electric field (wavefunction) is a direct consequence of the fact that the electromagnetic (electronic) wave is bouncing back and forth between the boundaries constituted by the homogenous air and the heterogeneous web-like media. To go further in the analogy with strongly coupled quantum well structures, each metallic row transverse to the propagation direction acts as a repelling potential (potential barrier) for the electric field whereas each inter-row gap plays the role of a quantum well. Basically, for an infinite structure the density of states is flat within the allowed band forming a mini-band. In contrast, for a finite superlattice the pass band exhibits a ripple whatever the number of rows with globally the same contrast between the transmission maxima and minima and a constant bandwidth for the transmission window.

To help clarify this issue, we give in Figure 4.15, the magnitude of the wave functions for the first four peaks of the semiconductor superlattice. Once again, the spatial distributions of electric field magnitudes for the photonic crystal can be compared to those of electron probabilities within the finite superlattice. For instance, in Figure 4.13, at 74.6 GHz the electric field is equally shared with four nodes for the fourth peak, whereas for the first peak the electric field is preferably localized in the center of the structure. For the second and third peaks, we obtain respectively two and three maxima, as it is the case in the superlattice.

Above 100 GHz, other higher order propagating modes appear with unitary transmission when λ becomes small enough for accommodating a second order eigenmode within the lattice. It is worth mentioning that the frequency behavior is somewhat different compared to the first transmission band. Indeed, above 110 GHz, other discrete propagation modes are relatively difficult to distinguish and the magnitude of S_{21} remains close to unity. The structure becomes more transparent and the electric field propagation appears more 'fluid' as for the electrons with ultra short lifetimes on the quasi bounded states in the superlattice approach. In our case, it is the distance between two wires in the [11] direction which determines the transition between the propagation modes through quasi-bounded states in the resonant cavity or through quasi-continuum states. Also,

it can be noted that the frequency selectivity of a multi-row metallic structure is quite different from a single frequency selective surface (FSS). Indeed it is now demonstrated that if just one row of wires is considered, the transmission increases monotonously from DC up to a frequency where $\lambda/2$ is smaller than the air gap (1.52 mm) between two wires.

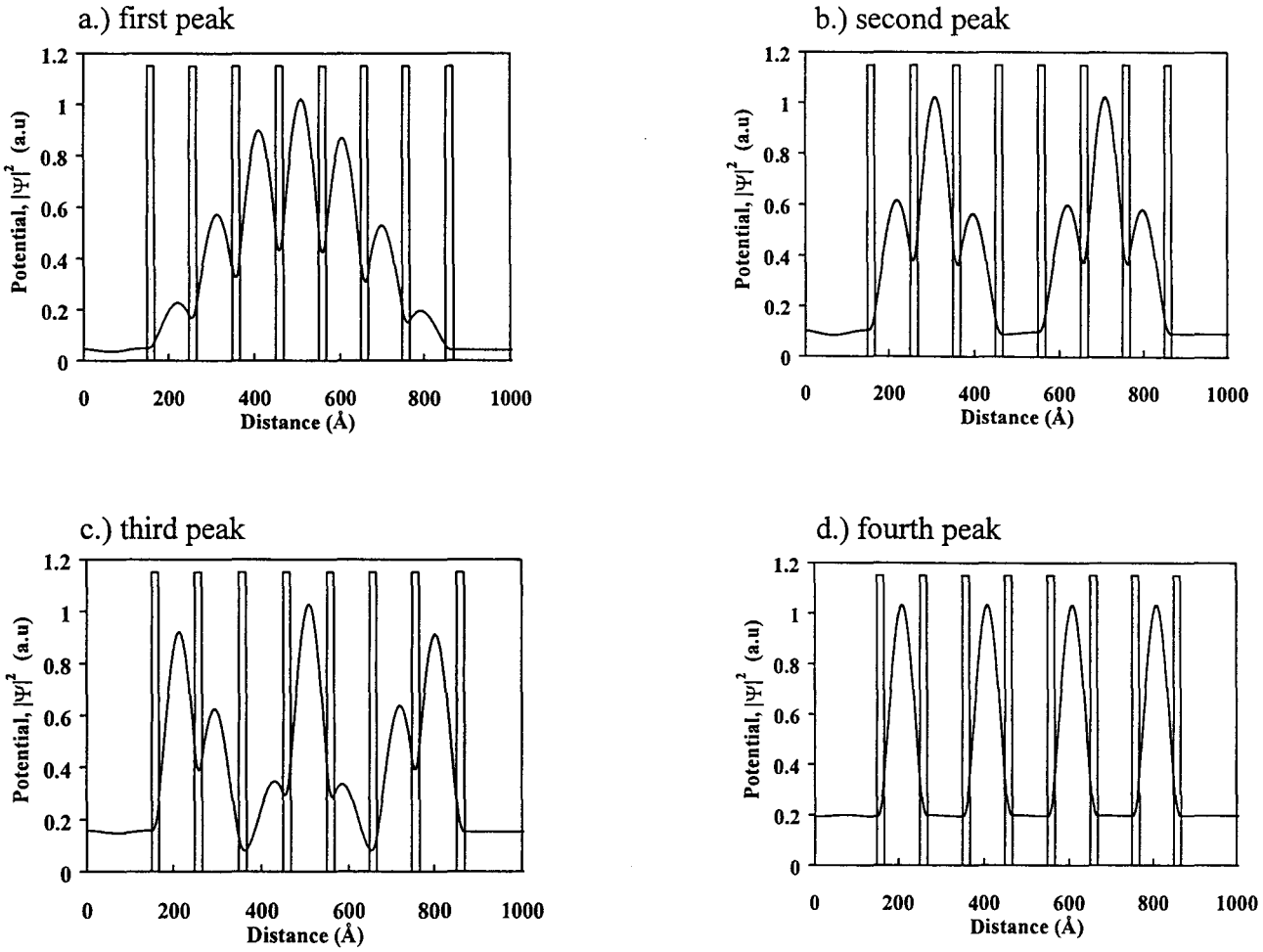

Figure 4.15: Electronic wavefunctions corresponding to the first four peaks of the first miniband of the semiconductor superlattice depicted in Figure 4.13.

A conclusion of this analysis can now be outlined, it is clear that transmission coefficient through finite photonic lattices can reflect in what extent the electromagnetic electric field is localized within the metallic structure despite the fact that we do not probe locally the electromagnetic energy.

4.2.2 Three-dimensional PBG analysis.

A three dimensional wire mesh geometry is analyzed as an extension of the previous 2D triangular design. Based on the triangular lattice dimensions, the periodicity of the structure has been outstretched to the third dimension, thus giving complete photonic band gap structures.

There is a classic separation for 3D PBG materials, consisting of whether connected or isolated scatterers are embedded in a host material, [Economou93]. The first class of materials are defined as network topology structures, with the scattering material connected. They thus form a continuous network running throughout the whole composite. The second is configured in a cermet

topology, in such a case the scattering material consists of isolated inclusions completely surrounded by the host material. Several practical examples of a network topology material have been designed and fabricated [Sievenpiper96, Özbay94]. In our study we have focused our attention in both types of topologies. We first studied, under normal incidence conditions, a network topology structure, made of crossed layers of parallel infinite cylinders. Second, a cermet topology structure made of finite dimensions vertical isolated scatterers is analyzed. Both are based on the lattice dimensions of the previous 2D structure.

4.2.2.1 Network topology.

A layer by layer PBG has been designed by assembling stacked layers consisting of rods with a layer-to-layer separation of p = 2.48 mm (equivalent to half the longitudinal lattice constant in the 2D lattice).The rods are rotated by 90° in each successive layer. Starting at any reference layer, the rods of every second neighboring layer are parallel to the reference layer, but shifted by a distance 2.69/2 mm perpendicular to the rod axis. This results in a stacking sequence that repeats every four layers and is similar to the face-centered-tetragonal (fct) proposed in [Özbay94]. Figure 4.16 illustrates the unit cell for the simulations with four stacked layers (1 unit cell ≡ 4 stacked layers) of metallic cylinders.

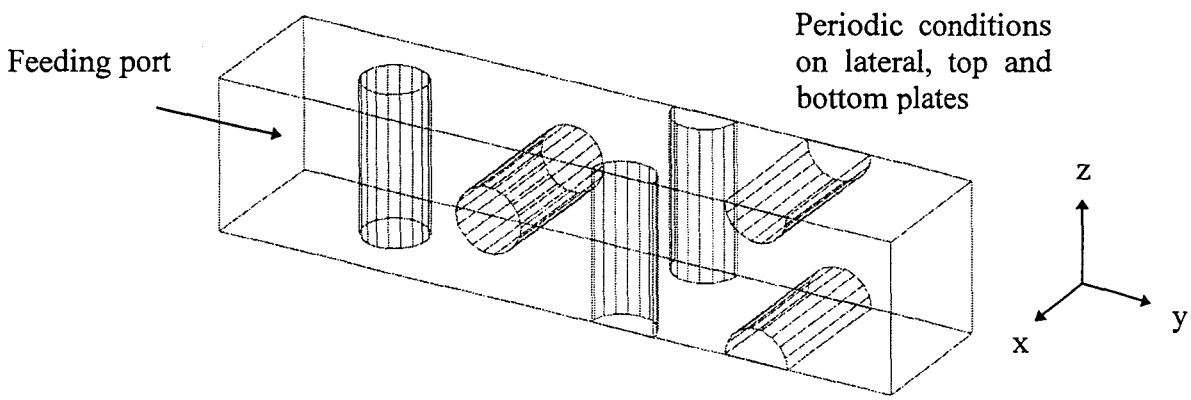

Figure 4.16: Simulated 3D PBG structure in HFSS consisting of one unit cell (four stacked layers).

Figure 4.17 shows the transmission characteristics of the PBG material for the two polarizations under normal incidence: s-polarized with the E field horizontally polarized (perpendicular to the first cylinder) and p-polarized with the E field vertically polarized (parallel to the first cylinder). In principle, and in the case of normal incidence, both polarizations have the same characteristics. For the two dimensional case with one unit cell (≡ two rows), there was only one resonant mode created in the two dimensional cavity, whereas for the 3D structure there are three resonant modes and hence three transmission maxima, in the same frequency range, at frequencies f_1 = 29 GHz, f_2 = 70.4 GHz and f_3 = 90.5 GHz. The first maximum in the transmission is at a much lower frequency than the cut-off frequency found for the 2D structure (68 GHz). The E field patterns of the resonant modes in the two representative longitudinal planes are reported in Figure 4.18 for illustration purposes.

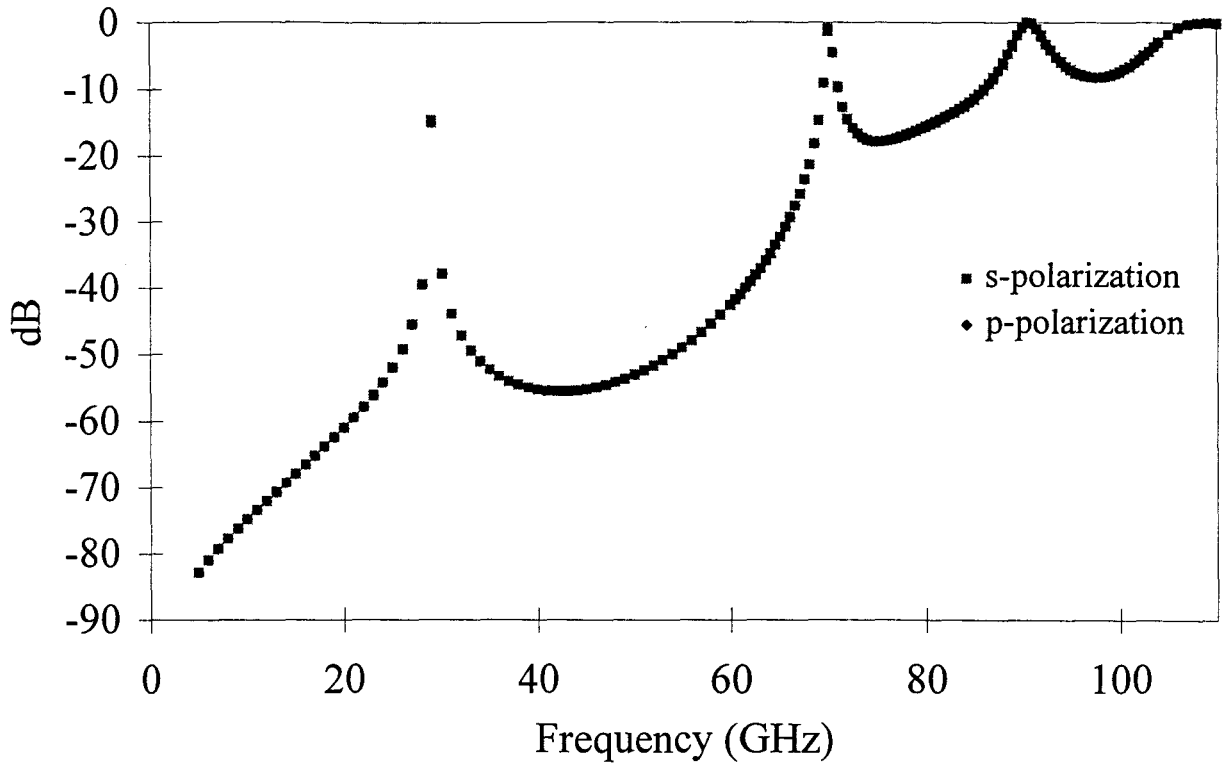

Figure 4.17: Transmission characteristics for the cross polarizations through a unit cell 3D PBG.

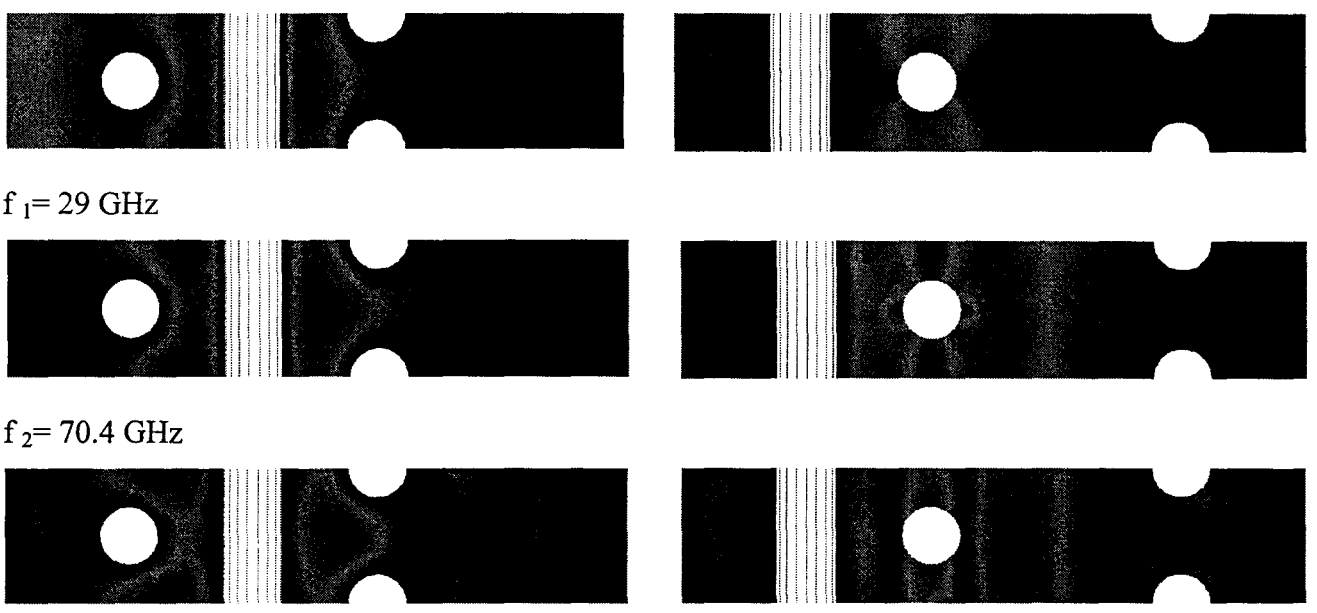

f_1= 29 GHz

f_2= 70.4 GHz

f_3= 90.5 GHz

Figure 4.18: E field patterns for the three resonant modes, left figures: top views; right figures: side views.

If we now plot the transmission characteristic for an 8 layers deep structure, we can observe more pronounced band gaps and at the same time resonant peaks that are doubled, with respect to the 4 layers case (one unit cell or two unit cells). Figure 4.19 illustrates this effect for a normal incident p-polarization.

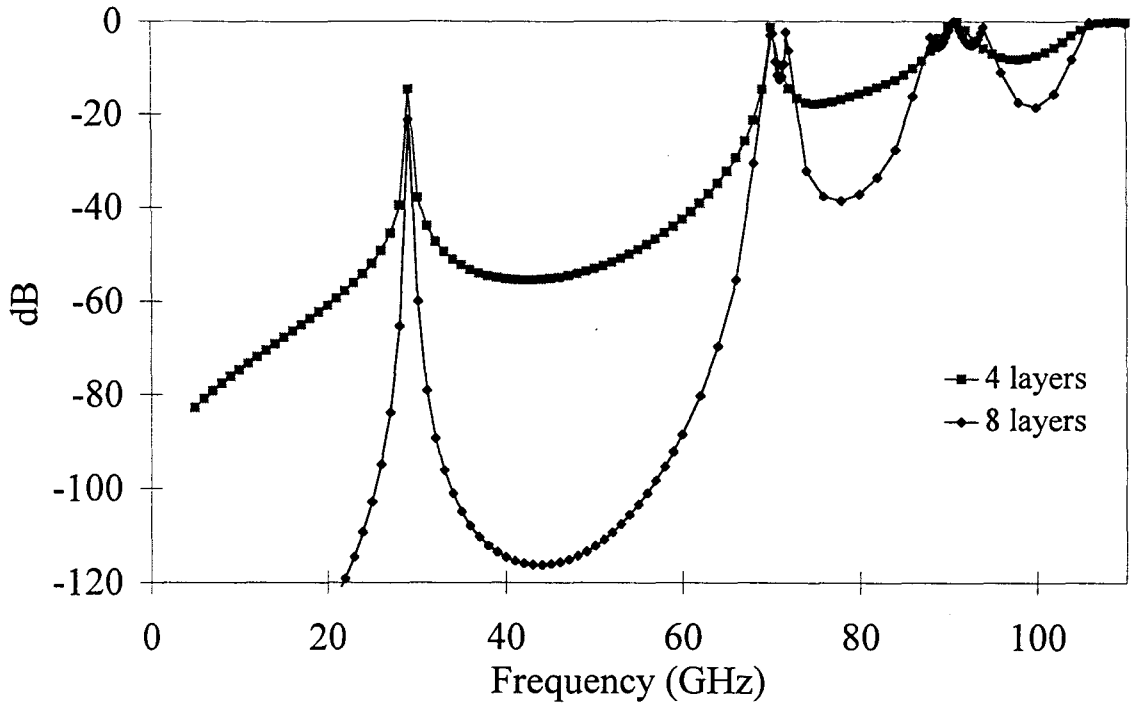

Figure 4.19: Comparison of the transmission characteristics for different thicknesses of the PBG material.

4.2.2.2 Cermet topology.

The potential interest of this kind of structure is based on the analogy with 'atoms' in a crystal. This time, each rod behaves as an individual and isolated scatterer in the artificial periodic medium. We have maintained the lattice periodicity corresponding to the 2D design in the xy plane, but in the z direction, the cylinders have a finite height and are now considered as isolated scatterers. By this means one can define a filling factor from the volume occupied by the metallic rods, and change the periodicity or the dimensions of the rods in the vertical direction. A lattice design of such structure is given in Figure 4.20.

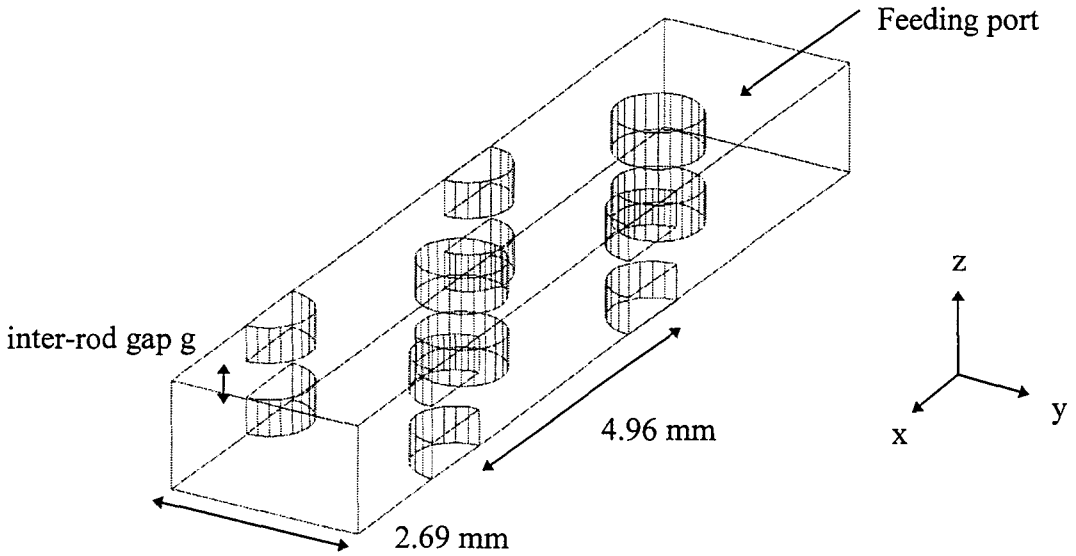

Figure 4.20: Simulated structure for a cermet topology formed of isolated cylinders.

Our analysis has consisted of varying the filling factor of this 4 rows structure in order to exchange the volume occupied by the metallic rods or the embedding air. The periodicity in the z direction is observed through the use of periodic conditions (electric or magnetic walls in the lateral, top and bottom boundaries). Figure 4.21 illustrates the transmission characteristics for a 4 rows structure for different filling factors. The heights of the rods are each time reduced (1.4, 1.2 and 1 mm), and so is the filling factor (15, 12.9 and 10.7 %), whereas the gap spacing between the scatterers is increased (0.1, 0.3 and 0.5 mm). For a lower filling factor, the structure is more transparent, as expected. The band gaps show lower attenuation and the pass bands are wider. A pass band around 80 GHz with a number of peaks equal to the number of rows minus one is again found. For a 15 % filling factor, this resonant effect becomes extremely selective and the ripple cannot be observed.

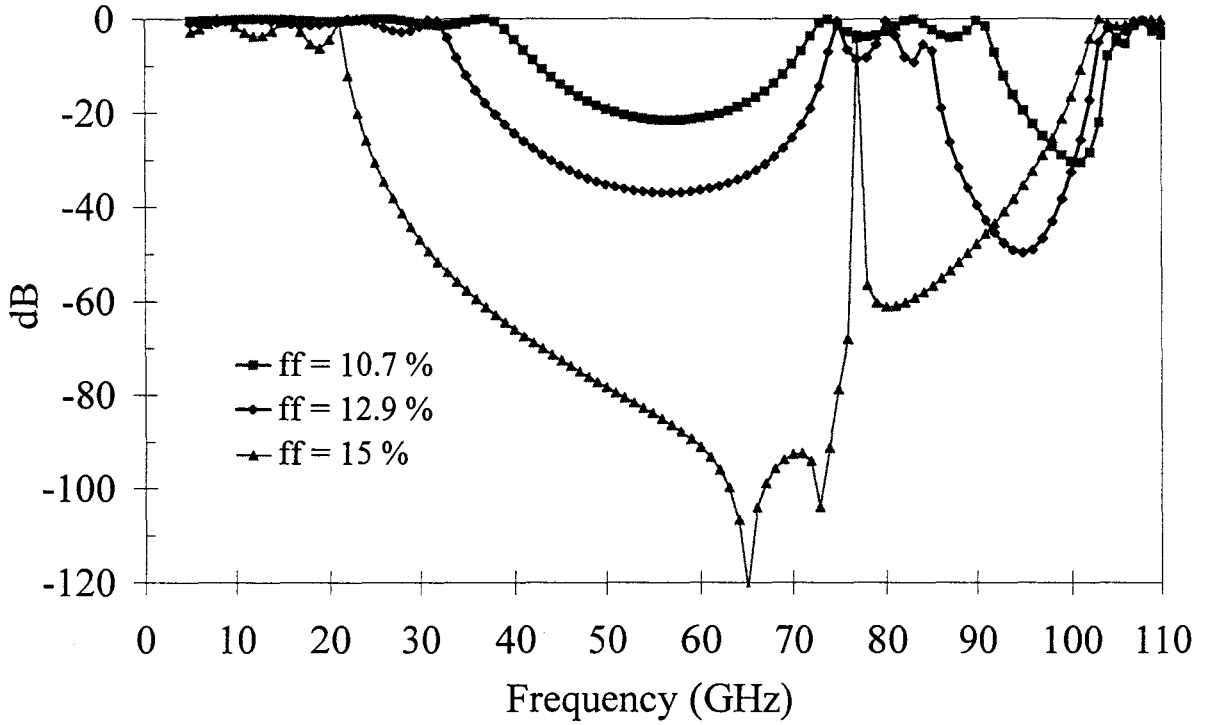

Figure 4.21: Transmission characteristics for a 4 rows structure for different gap separations between the metallic scatterers.

From this study we can conclude that 3D metallic PBG structures with network topology exhibit a cut-off frequency for both polarizations, below which there are no propagating modes. This feature puts them in the same category with the p-polarized waves propagating in 2D metallic PBGs. But, the features of 3D metallic PBG structures with isolated metallic scatterers are similar to the features of the dielectric PBG as well as to the features of s-polarized waves is 2D metallic PBGs. For all these cases there is no low frequency cut-off.

4.3 Defects in two-dimensional photonic band gaps.

The study of defects in a PBG material has also been a subject of interest for different groups [Sievenpiper96, Schultz96]. A defect is created when the periodicity of the structure is broken and thus there are defect or cavity modes created. The frequencies of these modes are generally within the forbidden band gap of the pure crystal, and the associated fields are localized around the defect. The transmission characteristics of these defect structures exhibit transmission peaks in the forbidden band gaps, that are usually very selective.

4.3.1 Cavities and resonant modes.

In practice, we have analyzed the behavior of a cavity created in our 2D metallic PBG lattice by removing several wires and hence creating a defect within the periodic structure. But, on the other hand, one may also think of creating a defect by means of a larger wire inside the lattice or just adding an 'extra implant' to the lattice. Figure 4.22 shows the schematic of different cavities formed by subtracting cylinders in the 2D lattice, for a 5 rows structure in the propagation direction.

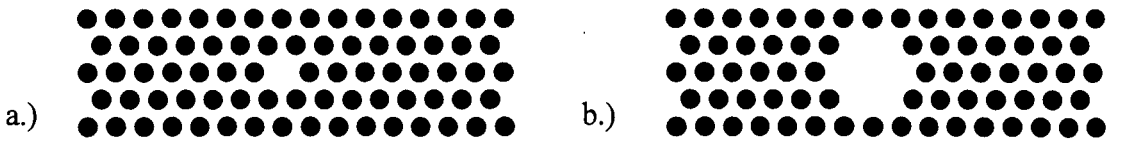

Figure 4.22: Schematics of different cavities created in the 2D lattice, by subtracting one cylinder, a.) or seven cylinders, b.).

These cavities act as microresonators, and can be compared to EM cavities in waveguide structures. The smaller the dimensions, the higher the resonant frequencies and, at the same time, the more selective resonances. For the a single wire removed on a 5 rows deep structure, our measurement set up was not able to differentiate the resonance effects created in the test frequency range, but different measurements were performed on structures with 7 or more removed cylinders. Figure 4.23 shows the transmission characteristic through a cavity structure illuminated under normal incidence. The frequency range fits in the Ka band, from 35 to 40 GHz, i.e. the first band gap of the periodic structure. A resonant peak is clearly visible in this transmission characteristic as a consequence of the creation of a cavity, and hence a localized E-field mode.

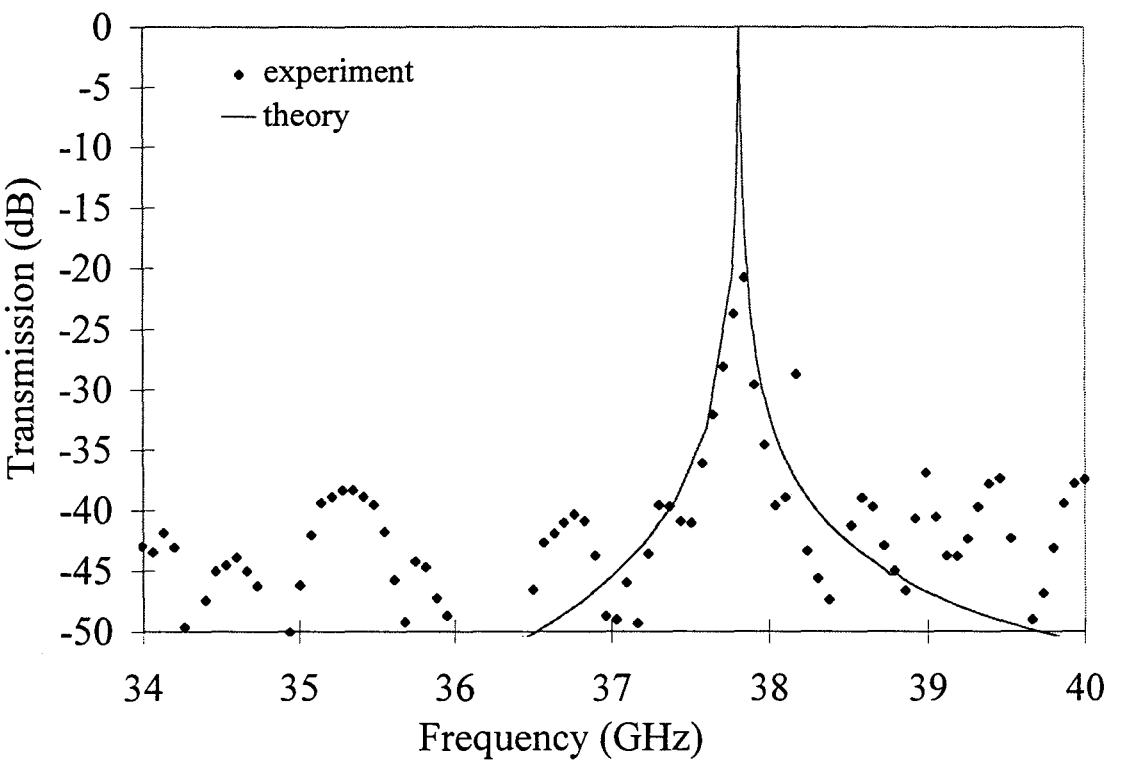

Figure 4.23: Measured and simulated transmission through a 5 rows structure with 7 cylinders removed.

In order to theoretically investigate the nature of this resonant effect, a simplified structure has been modeled to characterize the resonant modes of the cavity. The simulated structure is shown in Figure 4.24 a.). Periodic magnetic walls have been used for the lateral plates to simplify the structure and at the same time to feed it with a plane wave with vertical polarization for the E-field. In principle, and due to the strong reflective behavior of the periodic arrangement no coupling to other 'mirror' cavities may invalidate the simulation. Figure 4.24 b.) shows the E field pattern calculated at the resonant frequency of f_{21} = 37.51 GHz. From this Figure it is clear that a TE_{21} mode is excited in the cavity at this frequency. The simulation results are compared to the measurements in Figure 4.23, showing a relatively good agreement. The discrepancies between both curves may be explained by the fact that the theoretical results do not take into account losses due to diffractive phenomena in the real structure, which has been modeled assuming lossless periodic boundaries. Measurements are performed in free space conditions. Up to now, it has been very difficult, in terms of time and hardware requirements, to simulate open conditions for these types of structures. If we calculate the quality coefficients from these curves as:

$$Q=\frac{f_{res}}{\Delta f_{-3dB}}$$

where Δf_{-3dB} is the -3 dB bandwidth and f_{res} the central peak frequency in each case, we obtain the following values, 1200 (measured) and 3500 (calculated).

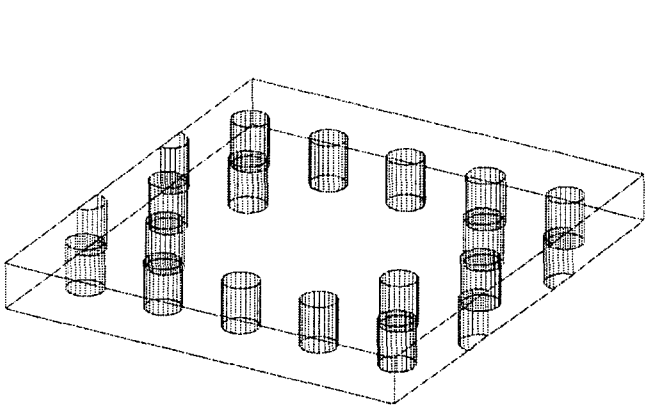

a.)

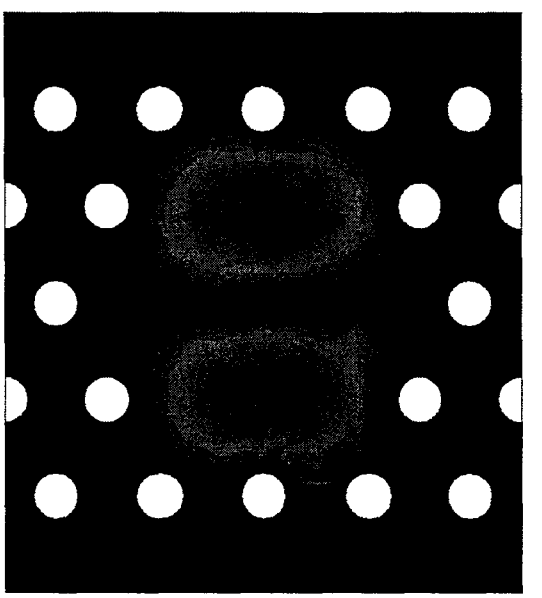

b.)

Figure 4.24: Simulated cavity structure, a.), and E field pattern of the resonant mode, b.)

With the aim of creating a more selective cavity, it may be interesting to isolate even more this resonant mode by confining it in a more compact structure. A seven rows structure has also been simulated with one row of wires added before the first row and another added after the last row. The comparison between both calculated curves shows clearly the extreme selectivity achieved with a pair of rows added to the structure. The results are reported in Figure 4.25. The new quality factor is about 10^6, calculated by means of the previous frequency definition. This extremely narrow peak, with a -3 dB bandwidth of several KHz is impossible to measure with the available equipment.

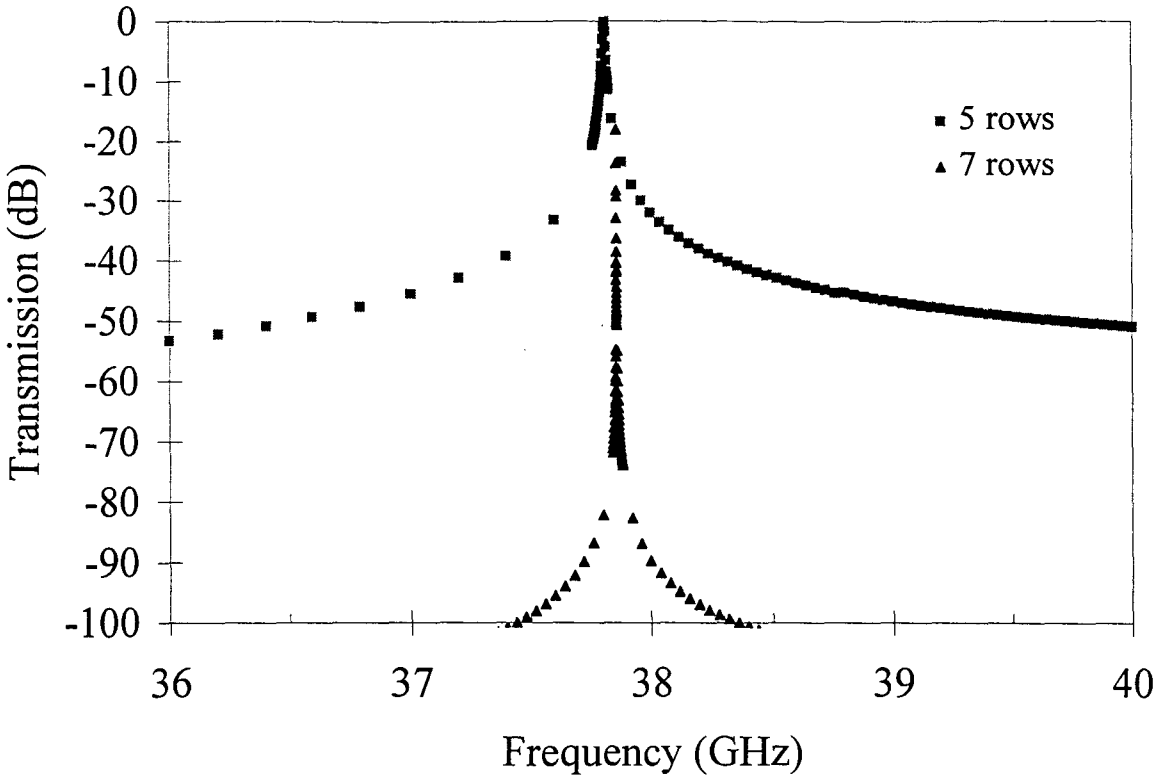

Figure 4.25: Calculated transmission characteristics through a 5 or 7 rows structure with 7 cylinders removed.

4.3.2 Comparison with a rectangular cavity.

Resonant modes in a 2D rectangular cavity have resonant frequencies that can be deduced from the following equation,

$$f_{m,n} = c\sqrt{\left(\frac{m}{2a}\right)^2 + \left(\frac{n}{2b}\right)^2}$$

where m and n are the indexes of the TE resonant mode and a and b are the cavity physical dimensions, c is the speed of light. Starting from this model, we have compared results from the following experimental procedure. A cavity can be created in a 5 rows deep structure by removing 7 cylinders, and afterwards a couple of rods is each time removed to enlarge the cavity in the b direction as shown in the schematic from Figure 4.26. In this experiment, only the width is varying.

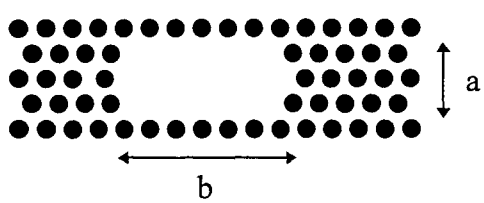

Figure 4.26: Cavity created in a 5 rows deep structure.

If we compare the resonant frequencies obtained from this theoretical analysis (for a rectangular cavity with a and b as geometrical dimensions), to the measured resonant frequencies in the experimental set up, we may also deduce the existence of a (m = 2, n = 1) excited mode. The

fundamental mode of this cavity must be in a lower frequency band, outside the frequency range of the measurements. The results of this analysis are displayed in Figure 4.27, showing a decrease in the resonant frequency with the number of removed cylinders, up to a limit value close to 33.4 GHz. This limit value is comparable to the resonant frequency of a two rows deep lattice with the same lateral periodicity and a longitudinal constant equivalent to the 5 rows thickness (4.96 x 2.5 = 12.4 mm). For the rectangular cavity, when b increases indefinitely the limit tends to a 1-D case.

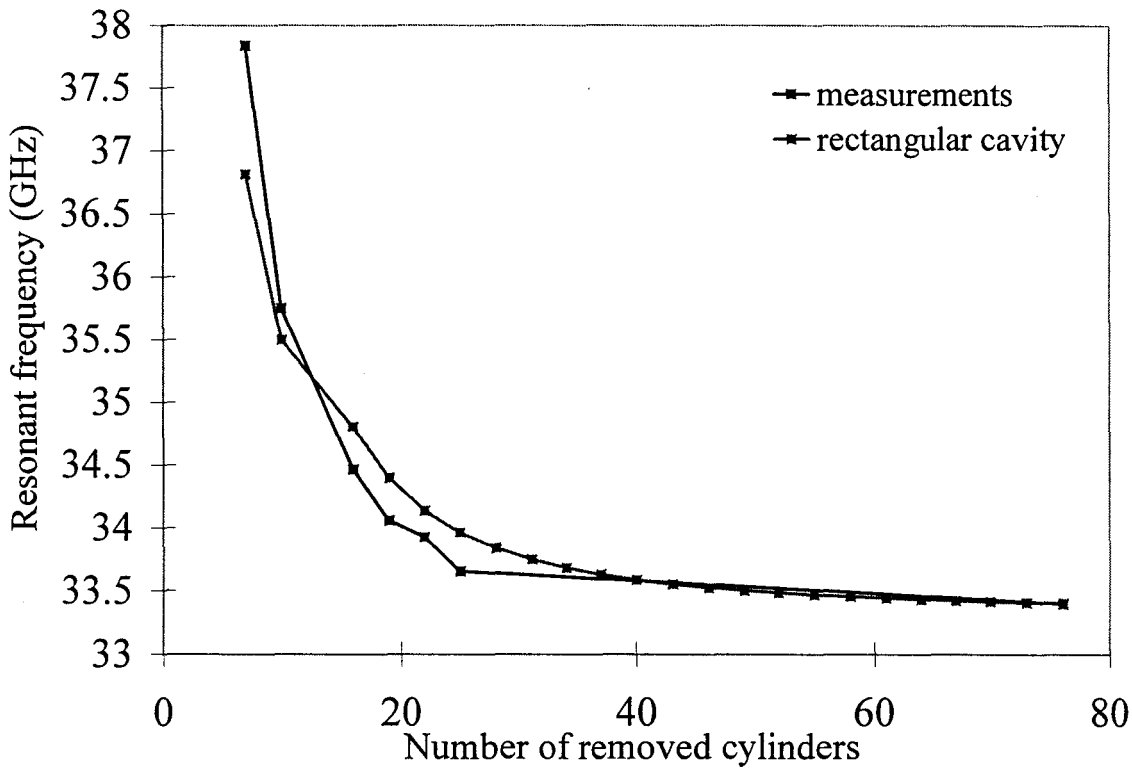

Figure 4.27: Resonant frequency versus cavity width in a 5 rows deep structure, comparison with an equivalent rectangular cavity.

4.4 Antennas on PBG materials.

Up to now, the most extensively studied application of PBG materials has been their combination with antennas in a twofold manner. As we mentioned in the first chapter, planar antennas deposited in a PBG-type substrate may alleviate the problem of trapped waves and unwanted substrate radiation [Ellis96]. Also, the combination of different types of antennas with PBG materials acting as reflectors has been widely analyzed, [Kesler96, Sigalas96]. Our study will detail some of the relevant features of the use of PBG materials combined with dipole antennas, completed by a theoretical analysis of the influence of the metallic PBG lattice already characterized in their radiation behavior.

4.4.1 General considerations.

The advantage of using Photonic Band Gap materials stems from the fact that they forbid propagation for certain frequency bands, whereas for others they may be transparent. This characteristic can be useful to tailor the radiation patterns of antennas which illuminate the periodic structure. Within the photonic band gap frequency range, the metallic PBG will act as a reflector modifying the radiation pattern of the antenna that illuminates it. On these basis, one may think of

defining a equivalent reflection plane inside the periodic medium [Kesler96]. This concept is illustrated in Figure 2.28. It is based on the quasi-linear characteristic of the reflection coefficient phase in the band gaps. The assumption of a penetration distance d(θ), which is a function of the angle of incidence, will help us to develop this concept by calculating it analytically. This distance is then compared with results from full-wave analysis and measurements.

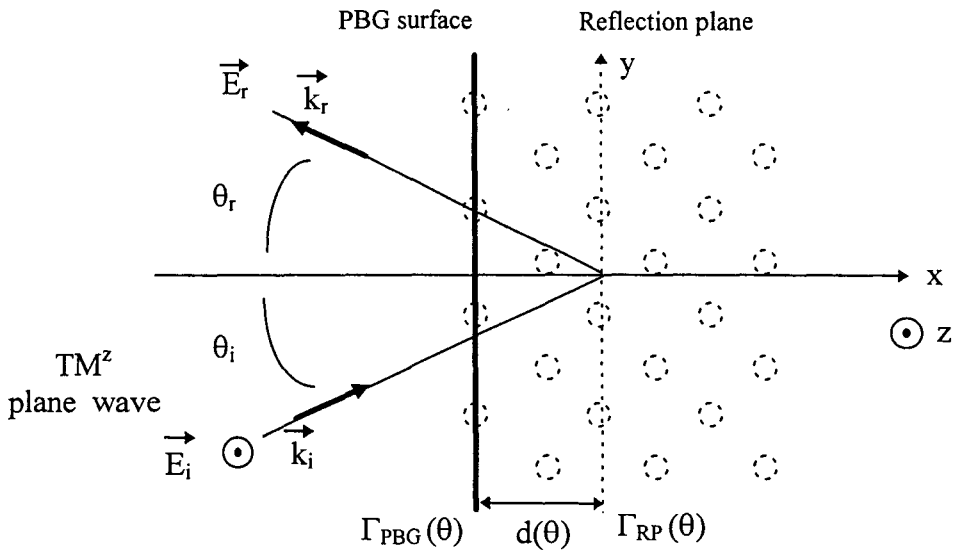

Figure 4.28: Reflection plane concept for a plane wave incident on a PBG for frequencies in the band gap.

For an incident plane wave with TM^z polarization (the E-field is parallel to the axis of the cylinders), we can define the following expression:

$$\vec{E}^i = \hat{z} E_0^i e^{-j\vec{k}_i \cdot \vec{r}}$$

with E_0^i being the magnitude of the incident electric field, and with

$$\vec{k}_i = k_0 \hat{k}_i$$
$$\hat{k}_i = \cos\theta_i \hat{x} + \sin\theta_i \hat{y},$$

hence, we can then rewrite,

$$\vec{E}^i = \hat{z} E_0^i e^{-jk_0(\cos\theta_i x + \sin\theta_i y)}$$

A similar expression can be developed for the reflected wave:

$$\vec{E}^r = \hat{z} E_0^r e^{-j\vec{k}_r \cdot \vec{r}}$$

and with

$$\vec{k}_r = k_0 \hat{k}_r$$

$$\hat{k}_r = -\cos\theta_r \hat{x} + \sin\theta_r \hat{y},$$

we can then rewrite,

$$\vec{E}^{\,r} = \hat{z} E_0^r e^{-jk_0(-\cos\theta_r x + \sin\theta_r y)}.$$

To link the expression of the reflection coefficient at the surface of the PBG with ($\Gamma_{PBG}(\theta)$) with the reflection coefficient at the reflection plane position ($\Gamma_{RP}(\theta)$), we apply the following boundary condition at x = 0 (reflection plane),

$$\vec{E}^r(x=0) = \Gamma_{RP}(\theta)\vec{E}^i(x=0),$$

$$\frac{E_0^r}{E_0^i}\frac{e^{-jk_o \sin\theta_r y}}{e^{-jk_o \sin\theta_i y}} = \Gamma_{RP}(\theta) \Rightarrow \begin{cases} \theta_r = \theta_i = \theta \\ E_0^r = E_0^i \Gamma_{RP}(\theta) \end{cases}$$

And we can deduce,

$$\vec{E}^i = \hat{z} E_0^i e^{-jk_o(\cos\theta x + \sin\theta y)}$$
$$\vec{E}^r = \hat{z} E_0^i \Gamma_{RP}(\theta) e^{-jk_o(-\cos\theta x + \sin\theta y)}$$

So, if we apply this result to calculate $\Gamma_{PBG}(\theta)$ as a function of $\Gamma_{RP}(\theta)$ we will have,

$$\vec{E}^r(x=-d(\theta)) = \Gamma_{PBG}(\theta)\vec{E}^i(x=-d(\theta))$$

$$\Gamma_{PBG}(\theta) = \frac{E^r}{E^i}(z=-d(\theta)) = \Gamma_{RP}(\theta)\frac{e^{-jk_o \cos\theta d(\theta)}}{e^{jk_o \cos\theta d(\theta)}} = \Gamma_{RP}(\theta) e^{-j2k_o \cos\theta d(\theta)} \quad \text{(i)}$$

After this analysis, we have to take into account the calculated PBG properties (for our lattice design) to obtain d(θ), in order to evaluate the location of the equivalent reflection plane. From the simulations, and within the band gap (see Figure 4.9), we can propose a simplified expression for the phase of the reflection coefficient of the PBG as:

$$\phi_{PBG}(\theta) = A(\theta) + B(\theta) f \quad \text{(ii)}$$

This expression would apply not only for normal incidence, as it was the case in Figure 4.9, but also for other incident angles, if a band gap exists for these angles. Moreover, the magnitude of the reflection coefficient is 1 in the band gaps. So, for the surface of the PBG material,

$$\Gamma_{PBG}(\theta) = e^{j\phi_{PBG}(\theta)}$$

And also, for the reflection plane,

$$\Gamma_{RP}(\theta) = e^{j\phi_{RP}(\theta)}$$

If we equate the analytical expression (i) to the empirical results from full wave analysis, (ii), we have:

$$d(\theta) = \frac{-cB(\theta)}{4\pi\cos(\theta)} \qquad \text{and} \qquad \Gamma_{RP}(\theta) = A(\theta)$$

For a normal incidence angle ($\theta = 0$), the equivalent distance for the reflection plane can be calculated as d = 3.45 mm (from Figure 4.9, for the band gap centered around 87 GHz), [Fernández98]. This value is slightly lower than the long diagonal axis of the unit cell, and is found in relative agreement with the result plotted for the E-field pattern in Figure 4.11 d).

4.4.2 Dipole antennas on PBGs.

The previous analysis is useful when a PBG material is illuminated with a plane wave and especially for frequencies within the band gap. Dipole antennas have a uniform radiation pattern in the H-plane. Therefore, a particular analysis is necessary, considering that an associated PBG material will be illuminated by cylindrical waves generated by the dipole, rather than a plane wave. Near-field effects should also be considered in the interaction dipole/PBG. In addition to the cylindrical contribution of the dipole, the rods themselves also create cylindrical scattered waves.

We have focused our attention on the interaction of a small dipole located in the close vicinity of a PBG material formed of 4 rows of perfectly conducting rods with the lattice dimensions of Figure 4.3. In the normal incidence case, a -30 dB maximum insertion loss is achieved. To this aim, an electrically small dipole has been modeled as a current source at 87 GHz in HFSS in the close proximity of the periodic structure. Figure 4.29 gives the dimensions of the dipole.

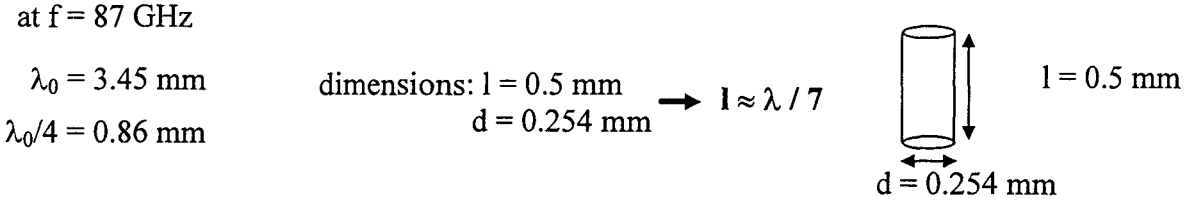

Figure 4.29: Dipole parameters.

In the Far Field approximation, field components are essentially transverse and the angular distribution is independent of the radial distance for the measurements. However, if the dipole is sufficiently close to the PBG material, not all the reactive field components will be negligible in the interaction with the PBG. It is difficult to define a Far Field limit in the case of a small dipole [Balanis82], because the usual condition, $R = 2D^2 / \lambda$, with D being the maximum dimension of the antenna, is defined for $D > \lambda$. In any case, we will assume that the dipole can have an almost uniform current along its length (small dipole). In these conditions, an isolated and vertically oriented dipole would have a uniform radiation pattern in the H-plane (horizontal plane) and virtually no radiation on its axis (vertical axis).

Various dipole configurations have been simulated in practice using the Absorbing Boundary Conditions of the software package. It was interesting to compare simulations of a combination of the dipole antenna with a metallic plane and with a PBG material used as a reflector. In the following theoretical analysis, we have only investigated the H-plane radiation patterns of the antenna combinations. Also, the position of the dipole versus the PBG surface is analyzed demonstrating that in the band gaps, the periodic structure does act like a reflector. Moreover, it can tailor the radiation pattern by creating preferential directions for radiation. In the simulations, and for sake of simplicity, we have defined the distance from the antenna to the surface of the PBG as the distance from the axis of the dipole to the axis of the first row of rods in the PBG. Figure 4.30 shows a comparison between H-plane far field patterns for different combinations. First, a free dipole is simulated in order to have a reference. In the H-plane, the free dipole has a uniform radiation pattern with a constant value around 2 dB. The slight variations that can be observed in this curve are due to the imperfections of the radiation boundaries of the problem, they do not 'absorb' all the outcoming far fields and there are some spurious reflections. The second curve stands for a dipole located at $\lambda / 4$ (at 87 GHz) from a perfect conducting reflector. The fact that radiation occurs on the backside direction from the conductor plane is due to its finite dimensions. Overall, this combination presents a broad major lobe in for the constructing interference of the wave radiated directly by the dipole and the reflected contribution from the conducting plane. Finally, the third curve represents gain for a dipole combined with a 4 row PBG material and located also at a $\lambda / 4$ distance. Hence, the PBG case offers a reduced beam for angles ranging from 230° to 300° and a slightly better gain: 9 dB compared to 8 dB. Moreover, even considering the same finite width slab of PBG material (10 wires wide) we can in principle decrease the backside radiation with respect to the perfect conducting plane. Diffraction phenomena involved in the interaction dipole/PBG are clearly demonstrated with the presence of sharp rejections in all the angular range.

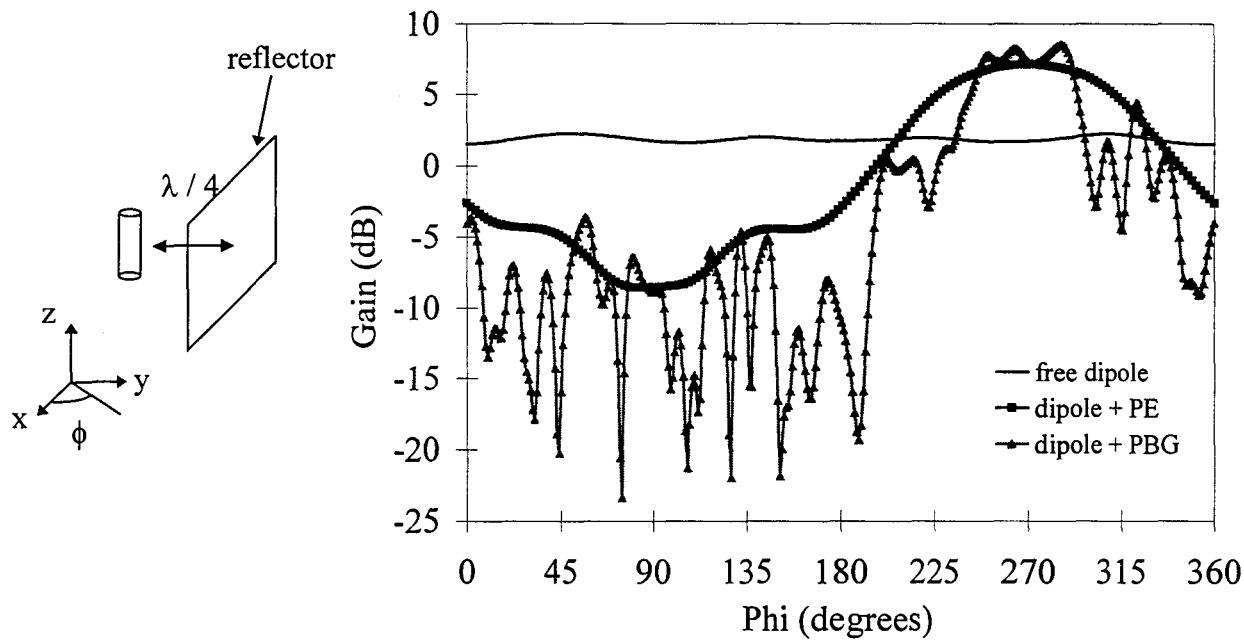

Figure 4.30: Comparison between H-plane far field patterns for different combinations.

We can expect a "lobe engineering" by varying the distance and the position of the antenna with respect to the PBG. This issue has been addressed through different simulations, see Figures 4.31 and 4.32. Two positions of the dipole have been analyzed: in front of a rod or in front of the

space between two rods. Also, two distances have been analyzed: λ / 4 or λ distances from the surface of the PBG.

(a) dipole at λ distance in front of a rod.

Figure 4.31 displays the E field pattern for the dipole antenna located at d = 3.45 mm (~λ at 87 GHz) and in front of a first row rod. Also the Far Field pattern is depicted showing, as expected, poor radiation in the backward direction. In the front direction, six lobes point at the improved directions (see Figure 4.30 for the phi-reference): 190, 230, 260 , 280, 310 and 340 degrees. The preferential directions are 230 and 310 degrees with the stronger lobes. In general the simulation preserves correctly the symmetry of the system. A quick inspection of the E field pattern on the left hand side offers the possibility of advancing several interesting remarks. The preferential directions can already be seen in this near field pattern. Also, there is a part of the dipole's radiated energy that penetrates the periodic structure, and even propagates through it. This is a clue that for this frequency (87 GHz), the lattice design may not exhibit a complete PBG for all the incidence angles. Let us recall that in the present situation, the dipole antenna illuminates the periodic structure with a wide range of incident angles.

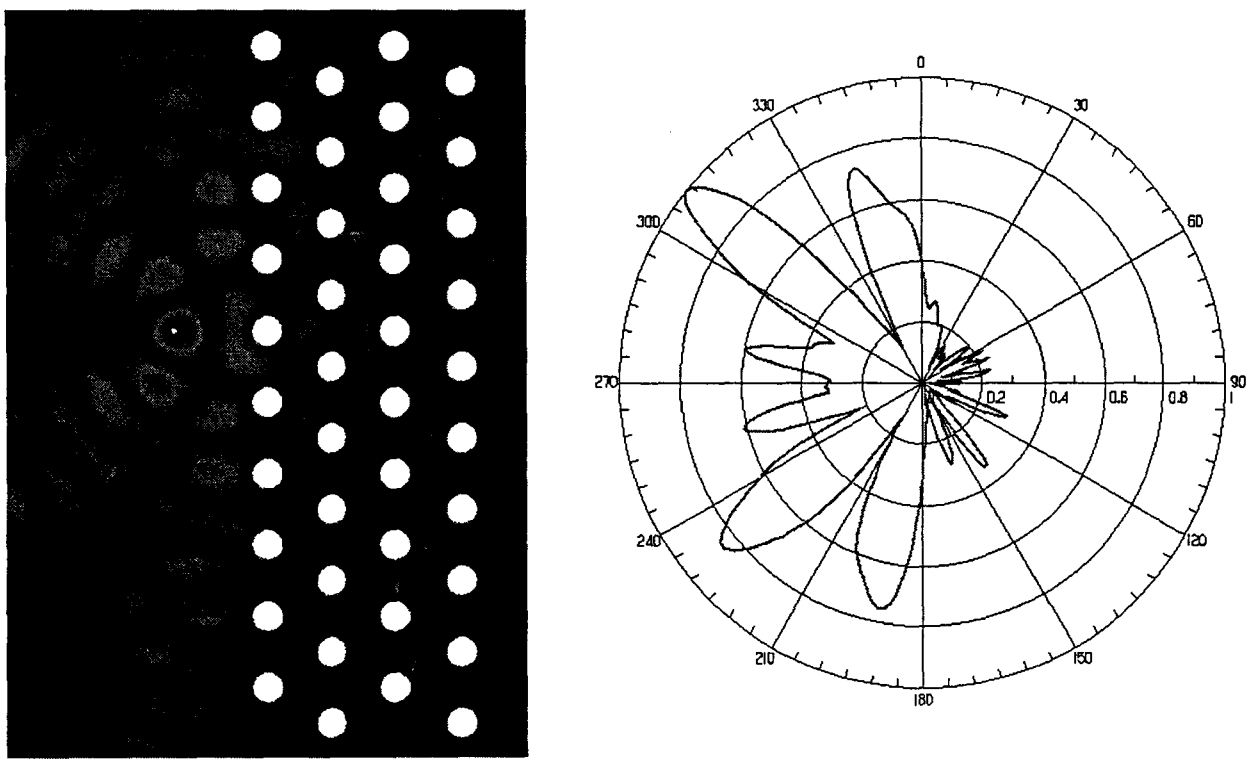

Figure 4.31: Dipole antenna at d = 3.45 mm (~λ) at 87 GHz.

(b) dipole at λ / 4 distance in front of a rod.

When the dipole is located closer to the surface of the PBG (for example λ / 4) the pattern exhibits a broad central lobe, which is the opposite behavior with respect to the λ separation case. In general it is desirable to place the dipole close to the surface to achieve strong central peak patterns.

(c) dipole at λ / 4 distance in between two rods.

Turning now to the case where the dipole is located in between two rods, the radiation pattern for a dipole located at λ / 4 away of the surface of the PBG is shown in Figure 4.32. Again are reported the E field pattern in the proximity of the radiating source and the far field radiation pattern. The far field pattern exhibits a broad central lobe and minor lobes to other directions. It was stated in [Sigalas96] that the origin of these side lobes, would be the correspondence to angles of incidence for which the PBG material would not exhibit a forbidden band. The slight shift of the central lobe may be explained by numerical error in the simulation. In reality, and due to the symmetry of the problem, this lobe should exactly point to the forward direction (270° in the phi-reference).

(d) dipole at λ distance in between two rods.

In general, the patterns exhibit the same trends as for the previous position (a). It is necessary to have the antenna close to the surface for broad central peaks, separating the antenna at a certain distance (between λ / 4 and λ) produces side lobes.

As a conclusion, we find then that the antenna patterns become insensitive to the position of the dipole when the antenna is removed to a distance away enough from the PBG surface. Then, the E fields on the PBG surface are uniform, and results for positions in front of a rod or in between two rods are similar. These results are found in agreement with those published by Sigalas et al. in [Sigalas97].

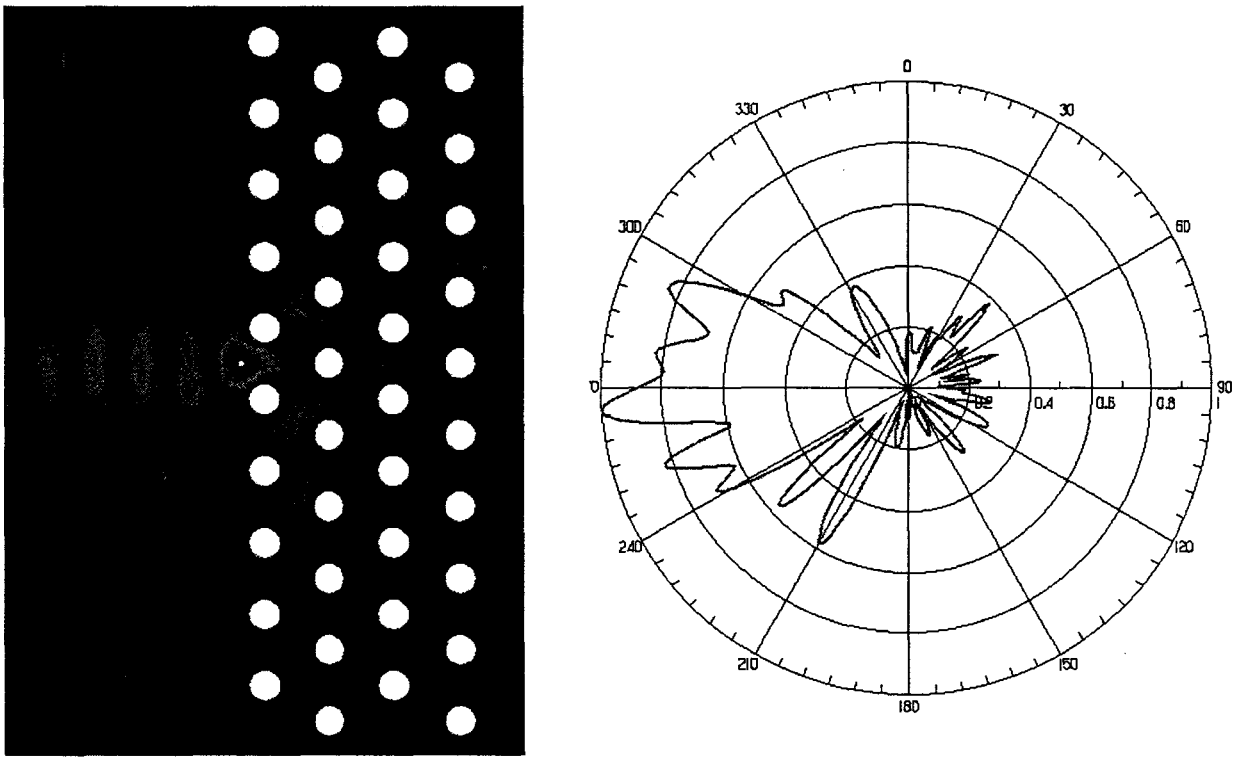

Figure 4.32: Dipole antenna at d = 0.86 mm (~λ/4) at 87 GHz.

4.5 Conclusion.

We have analyzed in this chapter some topics in connection with photonic band gap materials, which can be interesting from the point of view of microwave and millimeter wave applications. Our interest has been focused on artificial periodic materials consisting of metallic scatterers embedded in air with a 2D lattice design for operating at millimeter wave frequencies.

We have pointed out an original analogy between the EM behavior of this type of structure and the electronic behavior in semiconductor superlattices. When a finite PBG is illuminated by an EM plane wave, there are different phenomena involved in the interaction with the periodic structure. In particular, one may be able to predict the presence of allowed and forbidden band gaps for which the artificial medium becomes transparent or behaves as a reflector. By means of an extensive analysis of the localization effects based on the E field patterns inside the lattice, resonance effects were explained in terms of Bragg reflections and Fabry-Perot resonances. An experimental model was designed and the characterization conclusions support the theoretical analysis.

An extension of this full wave approach to 3D structures has shown the possibility of creating complete photonic band gaps for any incident radiation. Here, a difference exists owing to the topology employed to fabricate the artificial structure. "Cermet topology" structures behave typically as dielectric-type PBGs, whereas "network topology" structures behave like 2D metallic PBGs.

With respect to applications, the creation of defects in the periodic structure has been investigated with the aim of designing high-Q cavities and microresonators. Measurements of different cavities created by removing several cylinders in the periodic structure are in good agreement with the simulated data. Also, a preliminary analysis of the combination of dipole antennas with a metallic PBG was proposed and developed in good agreement with the conclusions of other research groups.

At the present time, the effort on this topic continues in our team with the analysis of waveguiding structures fabricated with PBG materials. In particular, the analogy with electronic devices should be extended to the field of couplers and stubs either from the electromagnetic side with PBG materials, either from the electronic side with ballistic transport electronic structures.

REFERENCES CHAPTER 4:

[Balanis82] C.A. Balanis, *Antenna theory. Analysis and design*, John Wiley & Sons Ed., 1982.

[Biswas96] R. Biswas, E. Özbay and K. M. Ho, *Photonic band gaps with layer-by-layer double-etched structures*, Jounal of Applied Physics, Vol. 80, p. 6749, 1996.

[Carbonell97] J. Carbonell, O. Vanbésien and D. Lippens, *Electric field patterns in finite two dimensional wire photonic lattices*, Superlattices and Microstructures, Vol. 22, No. 4, pp. 597-605, 1997.

[Carbonell97b] J. Carbonell, P. Mounaix, O. Vanbésien, D. Lippens, *Two dimensional wire photonic bandgap at millimeter wavelengths*, 20th ESTEC Antenna Workshop on Millimeter Wave Antenna Technology and Antenna Measurement, June 18-20 1997, ESA ESTEC, Noordwijk, The Netherlands.

[Chen97] Y. Chen, *Fabrication of two-dimensional photonic lattices in GaAs : the regular graphite structure*, Superlattices and Microstructures, Vol. 22, p. 109, 1997.

[Cheng96] C. C. Cheng, A. Scherer, V. Arbet-Engels and E. Yablonovitch, *Lithographic band tuning in photonic band gap crystals*, J. Vac. Sci. Technol. B, Vol. 14, p. 4110, 1996.

[Economou93] E.N. Econoumou and M.M. Sigalas, *Classical wave propagation in periodic structures: cermet versus network topology*, Physical Review B, Vol. 48, No. 18, pp. 13434-13438, November 1993.

[Ellis96] T. J. Ellis and G. M. Rebeiz, *MM-Wave tapered slot antenna on micromachined photonic bandgap dielectrics*, IEEE MTT-S Digest, WE4C-6, pp. 1157-1160, 1996.

[Fernández98] M. Fernández, *Modeling and charaterization of metallic Photonic Band Gap*, Training Report, IEMN, Université des Sciences et Technologies de Lille, March 1998.

[Joannopoulos96] J.D. Joannopoulos, *An introduction to Photonic Crystals*, Edited by C.M. Soukoulis, Plenum Press, New York, 1996.

[John87] S. John, *Strong localization of photons in certain dielectric superlattices*, Physical Review Letters, Vol. 58, p. 2059, 1987.

[Kesler96] M. P. Kesler, J. G. Maloney, B. L. Shirley and G. S. Smith, *Antenna design with the use of photonic band-gap materials as all-dielectric planar reflectors*, Microwave and Optical Technology Letters, Vol. 11, No. 4, pp. 169-174, March 1996.

[Meade92] R. D. Meade, K. D. Brommer, A. M. Rappe and J. D. Joannopoulos, *Existence of a photonic band gap in two dimensions*, Applied Physics Letters, Vol. 61, p. 495, 1992.

[Pendry92] J. B. Pendry and A. MacKinnon, *Calculation of photon dispersion relations*, Physical Review Letters, Vol. 69, p. 2772, 1992.

[Pendry96] J. B. Pendry, A. J. Holden, W. J. Stewart and I. Youngs, *Extremely low frequency plasmons in metallic mesostructures*, Physical Review Letters, Vol. 76, p. 4773, 1996.

[Poilasne97] G. Poilasne, J. Lenormand, P. Pouligen, K. Mahkjoubi, C. Terret and Ph. Gelin, *Theoretical study of interactions between antennas and metallic photonic bandgap materials*, Microwave and Optical Technology Letters, Vol. 15, No. 6, pp. 384-389, August 1997.

[Radisic98]V. Radisic, Y. Qian and T. Itoh, *Broad band power amplifier using dielectric photonic bandgap structure*, IEEE Microwave and Guided Wave Letters, Vol. 8, No. 1, pp. 13-14, January 1998.

[Schultz93] S. Schultz and D.R. Smith, *Measurements of localization and photonic band gap systems in two-dimensions*, Photonic Band Gaps and Localization, Edited by C.M. Soukoulis, Plenum Press, New York, 1993.

[Sievenpiper96] D. F. Sievenpiper, M. E. Sickmiller and E. Yablonovitch, *3D wire mesh photonic crystals*, Physical Review Letters, Vol. 76, No. 14, pp. 2480-2483, April 1996.

[Sigalas96] M. M. Sigalas, R. Biswas and K. M. Ho, *Theoretical study of dipole antennas on photonic band-gap materials*, Microwave and Optical Technology Letters, Vol. 13, No. 4 pp. 205-209, November 1996.

[Sigalas97] M. M. Sigalas, R. Biswas, Q. Li, D. Crouch, W. Leung, R.J.Woodbury, B. Lough, S. Nielsen, S. McCalmont, G. Tuttle and K.M. Ho, *Dipole antennas on photonic band-gap crystals - Experiment and simulation*, Microwave and Optical Technology Letters, Vol. 15, No. 3, pp. 153-158, June 1997.

[Smith94]D.R. Smith, S. Shultz, N. Kroll, M. Sigalas, K.M. Ho and C.M. Soukoulis, *Experimental and theoretical results for a two-dimensional metal photonic band-gap cavity*, Applied Physics Letters, Vol. 65, No. 5, pp. 645-647, August 1994.

[Soukoulis96] C.M. Soukoulis, *Phtotonic Band Gap Materials*, Edited by C.M. Soukoulis, Plenum Press, New York, 1996.

[Suzuki96] T. Suzuki, P. K. L. Yu, D. R. Smith and S. Schultz, *A new type of waveguide structure with photonic band structures*, IEEE MTT-S Digest, p. 911, 1996.

[Vanbésien92] O. Vanbésien, H. Leroux and D. Lippens, *Maximally flat transmission windows in finite superlattices*, Solid State Electronics, Vol. 35, p. 665, 1992.

[Vanbésien98] O. Vanbésien, J. Danglot, J. Carbonell, M. Fernández and D. Lippens, *Matériaux à gap de photons*, 5es Journées de Caractérisation Microondes et Matériaux, Le Touquet, France, May 1998.

[Winn94] J. N. Winn, R. D. Meade and J. D. Joannopoulos, *Two-dimensional photonic band-gap materials*, Journal of Modern Optics, Vol. 41, p. 257, 1994.

[Yablonovitch87] E. Yablonovitch, *Inhibited spontaneous emission in solid-state physics and electronics*, Physical Review Letters, Vol. 58, p. 2059, 1987.

GENERAL CONCLUSION

GENERAL CONCLUSION:

This work mainly concerned the analysis of active and passive devices aimed at operating at millimeter wave frequencies with a common denominator, namely the electromagnetic (EM) behavior. High operation frequencies involve problems like reduced dimensions of the devices, which are thus difficult to process, unwanted embedding effects, that may shunt the active device and degrade its performance, or dispersion phenomena. All these issues have to be considered along with the analysis of impedance matching and power considerations, when a millimeter wave system is to be operated.

To take into account all these pertinent phenomena, a Computer Aided Design (CAD) approach was found of major concern not only in the device optimization but also in the design of embedding circuits. In practice, we have used in this work a combination of different commercial software packages (HFSS, MDS and Momentum from Hewlett Packard), in order to analyze a wide variety of structures, starting from a multiplier block to open structures relying on an interference effect operation, and going through low loss transmission lines or switching devices.

The Heterostructure Barrier Varactor (HBV) has been analyzed as a promising candidate for high efficiency frequency multipliers. Starting from different samples fabricated by our group in the technological facilities and from theoretical models for the intrinsic device, EM analysis can provide a better understanding of the operation conditions when this device is planar integrated. We have proceeded with different steps in the analysis. The intrinsic device has been extensively characterized by on-wafer RF probing. Subsequently, this model has been combined with results from electromagnetic analysis to satisfactorily simulate the air-bridged device integrated in a planar configuration. Afterwards, this modelization technique has been used to predict the behavior of an HBV integrated by flip chip technology in a multiplier block. On the other hand, large signal analysis can be carried out through Harmonic Balance (HB) simulations, with conversion efficiency and power performances as output data. Also, EM analysis has been used to study the impedance matching issue, and to address the possibility of synthesizing optimum source and load impedances calculated by means of HB analysis. At the same time, it is believed that the EM analysis can be of great help to analyze the impedance measurements. By the time of this publication, we were not able to supply measured characteristics of the devices which should be tested by Matra Marconi Space at short term. However, some preliminary conclusions are in agreement with simulation data, in particular very narrow bandwidths are obtained with reactive tuning achieved with a double stub matching technique

Different technologies based on micromachining techniques have also been investigated. Coplanar waveguide (CPW) transmission lines micromachined on dielectric membranes can be an alternative guided medium with EM properties close to free space propagation conditions. An effective dielectric permittivity close to one, and hence a phase velocity practically equal to the speed of light, makes very attractive these propagation structures at very high frequencies. We have analyzed the frequency behavior of these structures, taking into account the difficulties created by the large aspect ratio in the geometrical dimensions. Thus, special care has to be taken in order to optimize the tapered transitions, key element to reduce reflection losses. Also, the application of this type of technology to filtering structures can be useful in the high millimeter wave spectrum, where filters are key elements in a receiver.

At the same time, MicroElectroMechanical Systems (MEMS) for switching or routing applications, also fabricated by micromachining techniques, have been analyzed from the EM side. The frequency limitations of these devices, fabricated in a planar technology, have been investigated demonstrating their usefulness up to the lower part of the millimeter wave band. Cantilever-type structures, rotating devices or membrane based capacitive switches have demonstrated different

advantages and drawbacks in terms of isolation or switching time, with the conclusion of parasitic fringing fields that limit the increase of operating frequencies.

Some topics dealing with Photonic Band Gap (PBG) materials have finally been analyzed as an emerging technology for applications at microwave and millimeter wave frequencies. A striking analogy of these type of structures with semiconductor superlattices has been pointed out. Localization effects inside the structures were explained in terms of Bragg reflections and Fabry-Perot resonance effects leading to forbidden frequency bands where the EM waves are not able to propagate. The analysis of finite structures was supported by measurements performed from 22 to 110 GHz, showing good agreement in terms of insertion losses and phase shift of the reflected wave. The study of this kind of artificial structures has been further investigated with the analysis of three dimensional structures and cavities created in the periodic lattice. One targeted application has been the use of PBGs as reflectors for dipole antennas. Preferential directions can be pointed out depending on the position of the antenna with respect to the artificial reflector.

The prospects for further developments are numerous. With the full description of the device in its EM embedding, it is believed that a more accurate global approach can be systematically applied to subsystems in hybrid or monolithic implementation. Towards these goals, many degrees of freedom, afforded notably by advanced micromachining techniques, can be tested prior to any technological effort. The other promising track, in our opinion, concerns the possibility to tune or to configure a device by taking advantage of the combination of electronic and electromagnetic devices. Perhaps, one of the most representative examples would be "smart PBGs" with potential applications notably for steerable antennas.

APPENDIX:

USE OF HFSS FROM HP

APPENDIX: USE OF HFSS FROM HP.

This research was carried out through the use of HP HFSS™ (High Frequency Structure Simulator) a powerful software package from Hewlett-Packard. HFSS performs a Finite Element Method (FEM) full-wave analysis for calculating the field distribution and the S-parameters of passive, high frequency 3-dimensional structures, and it has been the basic tool for doing this work.

This program can analyze open (surrounded with absorbing boundary conditions) or closed (shielded) structures made of lossy or losses metals or dielectric materials. For the later, anisotropic materials can also be simulated. The FEM is based on the division of a large, complex and three-dimensional structure into thousands of smaller regions (tetrahedra), and the calculation of the field in each sub-region with a separate equation. The E and H-fields are obtained with the solution of the well known equations:

$$\nabla \times \frac{1}{\mu_r} \nabla \times \vec{E}(r) - k_0^2 \varepsilon(r) \vec{E}(r) = 0$$

$$\vec{H}(r) = -\frac{1}{j\omega\mu_r} \nabla \times \vec{E}(r)$$

where ε_r and μ_r are the relative permittivity and permeability respectively (complex or not), and $k_0 = 2.\pi.f\ (\mu_0.\varepsilon_0)^{1/2}$ is the free space wavenumber, with f the excitation frequency. It is worth mentioning that the H-field is not solved independently, but calculated by means of the E-field curl equation.

HFSS uses an interpolation method combined with an iterative process in which a mesh is created and automatically refined in critical regions. First, the simulator creates a coarse initial mesh that is refined in areas of high error density and thus generates a new solution, using the last refined mesh. When a certain convergence level is achieved, the refinement process is stopped.

The basic steps to calculate the S-matrix associated with a structure are:

1. divide the structure into a finite element mesh (or refine the previous mesh).
2. calculate the different modes on the ports (2D surfaces) and assume that on each of the ports, the structure is excited with a wave travelling along a uniform wave-guiding structure that has the same cross section of the port.
3. compute the full-wave electromagnetic field pattern inside the structure resulting from the excitation waves from the ports.
4. compute the generalized S-matrix from the amount of reflection and transmission that occurs inside the structure.

Also, current sources can be inserted in the problem region to obtain E-field patterns or antenna parameters without the need of ports for far field calculations. This type of solution has been used in the last chapter.

In principle, ports have been designed so that only the lowest order mode is supported at the frequency of the analysis. The waveguide attached to each port should extend far enough from discontinuities in the structure where higher order and evanescent modes are generated, so that they have been attenuated at least 30 dB. During this research period, several versions of the software package have been updated, and specially the mesh and solving procedures have been accelerated, anyway, the FEM is extremely consuming in terms of time and hardware ressources. Usually, symmetry and geometric simplifications in the designs have been employed wherever it has been possible to save time in the simulations. Nevertheless, the FEM is a numerical method adapted to

solve problems with dimensions not larger than a few wavelengths. Larger structures, or with great geometric aspect ratios (>1000:1), cannot be resolved accurately. We have used a limiting criterium to evaluate the convergence between two successive meshes, $\Delta S = 0.01$, where the parameter ΔS is defined as:

$$\Delta S = \max_{i,j} | S_{i,j}^{n+1} - S_{i,j}^{n} |$$

and $S_{i,j}^{n}$ is the calculated scattering parameter in adaptive pass n. Normally, convergence and repeatability of the analysis are good, but this is not verified every time, because ΔS, in exceptional cases, is not monotonously reduced with every new mesh refinement.

The use of HFSS was accompanied by simulations with HP Momentum™ for two-dimensional structures, also from Hewlett Packard. This software package uses the Method of Moments (MoM) which is clearly faster than the FEM, but otherwise limited to 2D structures. Momentum is very efficient to calculate propagation constants and impedances for different planar transmission lines, moreover, for coplanar or microstrip technologies with planar discontinuities it has been the preferred approach, as we pointed out in the third chapter. Momentum can solve propagation structures on top of or covered with a number of substrates with different electrical properties and thicknesses.

SUMMARY

Recent advances in nanotechnology, high frequency characterization and computer aided design have strongly modified the fabrication of systems operating at millimeter- and sub-millimeter frequencies. In this context, this work deals with the electromagnetic analysis of active and passive devices for space applications. Three topics in connection with the Terahertz field are specially addressed, namely (i) an harmonic multiplier using an advanced Heterostructure Barrier Varactor (HBV) active device, (ii) micromachined transmission lines and microswitches, and (iii) metallic photonic band gap structures.

Concerning the design of an harmonic multiplier, up-converting 83 to 250 GHz, our main contribution deals with the electromagnetic analysis of the active device taking into account the embedding circuit. Starting from a high performance HBV fabricated at the IEMN, with a capacitance ratio of 5:1 and a 1 $fF/\mu m^2$ zero-bias capacitance level, special attention was paid to the influence of integration techniques on the device performance. A reverse engineering approach was successfully used by combining on-wafer probing techniques, Harmonic Balance simulations and electromagnetic analysis for a device mounted in a multiplier block.

With respect to micromachined devices, we addressed more specially the electromagnetic patterns, on one hand, for substrate-less coplanar transmission lines, and on the other hand for cantilever-type microswitches. A low-loss and dispersion-free regime is demonstrated in the first case at least up to 100 GHz, whereas cut-off frequencies for high isolation are determined in the second one.

Finally, our effort has concentrated on the analysis of metallic artificial periodic media which exhibit electromagnetic forbidden gaps, as semiconductors do for electron waves. These 'Photonic Band Gap' materials appear as an emerging technology, originally developed at optical frequencies, and show promising applications at millimeter waves as filtering, radiating and guiding elements. In the present work, we demonstrated mainly the impact of their finite dimensions and showed the striking analogy of these periodic structures with semiconductor superlattices. Also, their potential as high-Q resonant cavities or smart-reflectors is investigated.